Quantitative Diffusion Weighted Imaging: Techniques and Applications to Perinatal Asphyxia

Quyen Nguyen

Department of Medical Physics & Bioengineering
University College London

Submitted for
The Degree of Doctor of Philosophy
University of London

September 2001

Abstract

This thesis describes the results of a study to investigate early cerebral changes in a piglet model of perinatal asphyxia using quantitative diffusion-weighted imaging (DWI) and subsequent work to develop a robust DWI technique to enable similar studies to be performed in neonates.

^{31}Phophorus magnetic resonance spectroscopy and quantitative diffusion and T_2 imaging of the cerebrum were performed in a piglet model of perinatal asphyxia. A significant decline in the ratio of phosphocreatine to inorganic phosphate concentrations ([PCr]/[Pi]) was observed during the 48 hours following the transient hypoxic-ischaemic (H-I) insult. The global directionally averaged apparent diffusion coefficient (ADC_{av}) also declined significantly during the same period and a strong correlation between the [PCr]/[Pi] and ADC_{av} was found. Strong regional and temporal variations in the cerebral response were observed following the H-I insult. In the basal ganglia and parasagittal cortex, significant decline in ADC_{av} was seen approximately 8 hours after the H-I insult. In the thalamus, internal capsule, periventricular white matter and medial cortex, significant ADC_{av} decline was not observed until 32 hours following the H-I insult. A significant T_2 increase was observed in the internal capsule but not in the other regions of interest.

To enable clinical DWI to be performed in neonates a novel 'reacquisition' technique that overcomes the problem of motion artefact in DWI is presented. The reacquisition technique involves the automatic detection and reacquisition of motion-corrupted data in real-time. Computer simulations were used to demonstrate that motion-corrupted data may be detected accurately and reacquired in a time efficient manner. The reacquisition technique was implemented on a Bruker AVANCE scanner in combination with a spin-echo 2DFT DWI sequence and an interleaved EPI DWI sequence. The effectiveness of the technique was demonstrated with both a computer-controlled motion phantom and neonates from an ongoing study of perinatal asphyxia.

Contents

List of figures

List of tables

Acknowledgements

I would like to express my most sincere appreciation to my supervisor Prof. Roger Ordidge for his tireless help and guidance during my time at UCL. I would also like to thank my second supervisor, Dr. John Thornton, for his friendship and generous assistance throughout my Ph.D.

I would like to thank Prof. John Wyatt, Dr. Frances O'Brien, Dr. Mark Sellwood and Dr. Martina Noone for their invaluable assistance towards the clinical aspects of the work described here. I am indebted to Dr. Matthew Clemence for his guidance during the early stages of this project. I would also like to express my thanks to Dr. Alan Connelly, Dr. Mark Symms, Dr. Marzena Arridge, Dr. David Thomas, Dr. Fernando Calamante and Dr. Gaby Pell for their useful comments.

Finally, I would like to take this opportunity to acknowledge and thank my parents for their support, encouragement and understanding throughout my education.

1 Introduction

1.1 Introduction to chapter 1

In this chapter, a brief outline of the historical development of Nuclear Magnetic Resonance (NMR) will be presented, together with an introduction to perinatal asphyxia. The aims and objectives of the work presented in this thesis will then be given, together with an outline of the thesis contents and organisation.

1.2 Historical background

NMR describes the phenomenon whereby, in the presence of a magnetic field, the nuclei of certain atoms can undergo resonant absorption and emission of electromagnetic radiation at characteristic frequencies that are proportional to the strength of the magnetic field. NMR was first observed in bulk matter by two independent groups headed by Bloch[1] and Purcell[2] in 1946. Four years later, the discovery of the 'chemical shift' effect of NMR by Proctor and Yu[3] (and independently by Dickinson[4]) lead to the development of NMR spectroscopy (or Magnetic Resonance Spectroscopy (MRS) as it is also known), a powerful new tool for the investigation of molecular structure and concentration *in-vitro* and *in-vivo*. The development of NMR imaging (or Magnetic Resonance Imaging (MRI) as it is more commonly known) did not emerge until 1973 when, in a letter to Nature, Lauterbur[5] published the first NMR image of a heterogeneous object comprising of two tubes of water. Following the publication, the field of MRI advanced rapidly and in 1976,

Mansfield and Maudsley[6] published the first *in-vivo* image of a human finger. In the following year, the first whole body image of a thorax was reported by Damadian[7] and in 1978, the first commercial MRI scanner became available.

Of all the atomic nuclei in living tissue that are capable of undergoing nuclear magnetic resonance, by far the most abundant is that of hydrogen (^{1}H). As NMR is a very insensitive technique, clinical MRI has so far been centred on the imaging of ^{1}H in water and fat. The measurement of water content alone in human soft tissue can provide up to 15% contrast. However, by magnetically manipulating nuclei with electromagnetic radiation and field gradients it is possible to obtain image contrast based on a variety of different tissue properties and a much greater range of imaging contrast. Recent developments in MRI have meant that it is now possible to obtain *in-vivo* images depicting numerous tissue functions, including tissue perfusion and tissue water diffusion[8]. Each of these different contrast mechanisms contains unique and valuable information on the state of the tissue under study and could potentially have enormous benefit for the diagnosis and treatment of a variety of medical conditions.

1.3 Perinatal asphyxia

'Acute perinatal asphyxia refers to a condition of hypoxaemia and insufficient blood perfusion to the newborn during labour and birth'[9]. The hypoxic-ischaemic (HI) insult experienced during acute perinatal asphyxia leads to disturbances in cellular oxidative metabolism in the perinatal brain, which, if severe, eventually result in permanent brain injury. Despite advances in

obstetric and neonatal care, perinatal asphyxia remains a major cause of acute perinatal brain injury. Neonates who have suffered HI brain injury present with a characteristic syndrome known as Hypoxic-Ischaemic Encephalopathy (HIE). The incidence of HIE at birth in full term infants has been estimated to be between four to eight per 1,000 deliveries in the UK[10]. The mortality of term infants with HIE is approximately 11%, whilst of the surviving neonates, approximately 20-30% go on to develop neurological sequelae.

Neurological evaluation of newborn suspected of having suffered HI brain injury has been shown to be effective in differentiating neonates with favourable outcome from those with a poor prognosis[11]. Unfortunately, clinical assessment is often complicated by necessary anticonvulsion or sedative medication, which can masks clinical signs of encephalopathy. Furthermore, many babies with HIE require intensive care and artificial ventilation during the first few days of life, which makes clinical assessment virtually impossible. To improve diagnostic and prognostic power, numerous non-invasive methods of brain investigations have been applied in perinatal asphyxia including cranial ultrasound, Computer Tomography (CT), MRI and MRS.

Cranial ultrasound has the advantages of being relative cheap and portable, and is capable of providing anatomical and functional information of the neonatal brain. The portability of ultrasound scanners means that scans can be performed at the bedside and thus the risk of moving critically ill neonates away from the ward is avoided. However, the image quality produced in cranial ultrasound is relatively poor and the sensitivity of ultrasound to acute cerebral changes in

term neonates with HIE is low[12]. CT x-ray is capable of providing cerebral images with good anatomical details at substantially lower cost than MRI. However, it has the considerable disadvantage of a very high radiation dose and is not as sensitive to the acute cerebral changes in HIE as MRI. MRI is expensive and can be difficult to perform on acutely ill newborn. The difficulty arises from the need firstly, to transport neonates away from the ward to the scanner and secondly, to provide intensive care support in the confine of the bore of the magnet. However, despite the difficulty, MRI has been shown to be extremely useful in depicting acute cerebral changes in perinatal asphyxia at very high spatial resolution[9]. MRS has the same disadvantages as MRI in terms of cost and difficulty of scanning since it involves similar (or indeed the same) equipment. A further disadvantage of MRS is that the scanning time can be quite lengthy and the spatial resolution is limited. However, it is unique in being able to provide *in-vivo* information on cerebral metabolism, especially the processes underlying oxidative phosphorylation, and this makes it an invaluable tool for investigating brain injury in perinatal asphyxia.

Previous work performed in our group using MRS has shown that there is a biphasic change in the cerebral energy metabolism in perinatal asphyxia: an apparently reversible energy metabolism impairment during the HI insult and a secondary derangement approximately 12 to 24 hours later[13]. The severity of the delayed energy failure in neonates with HIE has been shown to correlate with long term neurodevelopmental outcome[14]. The delay between the primary insult and secondary energy failure suggests that there may exist a window of opportunity (commonly referred to as the 'therapeutic window') during which

specific therapeutic intervention may help to protect brain cells from delayed injury. Experimental work on a piglet model of perinatal asphyxia has shown that 12 hours of mild hypothermia (33^0C) immediately following the HI insult resulted in a significant reduction in the severity of delayed energy failure[15] and a marked decreased in apoptotic cell death[16]. MRI observations in the same piglet model of perinatal asphyxia have shown that there is a significant temporal and regional variation in the cerebral response during secondary energy failure[17]. This is of significant interest clinically since it suggest that there may be a variation in the susceptibility of different brain regions to early injury during secondary energy failure and that the length of the 'therapeutic window' may vary in different cerebral regions. Comparison of MRS and quantitative MRI observations in the piglet model during secondary energy failure has demonstrated that there is a strong correlation between changes in cerebral water diffusion as measured by MRI and the ratio of phosphocreatine and inorganic phosphate concentrations, as measured by MRS[17]. As the ratio of phospocreatine to inorganic phosphate reflects cellular phosphorylation potential, the strong correlation with cerebral water diffusion suggests that cerebral water diffusion may be used as a surrogate marker of cellular energy status. Since cerebral water diffusion can be measured using MRI, the advantage of MRS as a probe of cellular energy metabolism and the advantages of MRI of high spatial resolution and relatively short scanning time may both be combined by quantifying cerebral water diffusion.

1.4 Project aims

A major shortcoming of previous MRI and MRS studies of the piglet model of perinatal asphyxia described above was that they were only able to observe a small region of the brain, namely the parietal lobes. The findings in these studies were therefore only valid for the parietal lobes and the regional and temporal variations in cerebral response during secondary energy failure were only observed in a limited area. To address this shortcoming, the first aim of this thesis was to extend the findings in the previous studies to include the whole of the brain and to explore the regional and temporal variations in cerebral response in the deep brain structures.

The findings that quantitative MRI measurement of cerebral water diffusion may be used as a high resolution marker of cerebral energy metabolism during secondary energy failure provided strong motivation for performing the same measurements in neonates. Unfortunately, initial attempts at such measurements in our laboratory using standard diffusion weighted imaging techniques were thwarted by the severe motion artefacts that resulted from the extreme sensitivity of standard techniques to motion. To address this problem, the second and main aim of this thesis was to develop a novel technique to overcome the motion sensitivity of diffusion weighted imaging in neonates.

1.5 Organisation of document

In chapter 2 of the thesis, the physics of MRS and MRI are described. The techniques for quantifying tissue T_2 and water diffusion using MRI are also

given, together with a discussion of their physiological significance. Chapter 3 presents the methods and results of the piglet study undertaken to address the first aim the thesis described above. In chapter 4, the problem of motion artefacts in the imaging of tissue water diffusion in MRI is described and a novel technique (known as the reacquisition technique) for overcoming the problem is presented. The results of two computer simulation studies designed firstly, to assess the effect of motion error in diffusion-weighted imaging and secondly, to aid the design and assess the performance of the reacquisition technique are also given. In chapter 5, an implementation of the reacquisition technique on a Bruker Avance scanner is described, together with the results of phantom and neonatal studies using the technique. Chapter 6 concludes with a summary of the results presented in the thesis and suggestions for the further development of the reacquisition technique.

Reference List

1. Bloch F, Hansen WW, Packard M. Nuclear induction. **Physical Review** 1946; **69**: 127

2. Purcell EM, Torrey HC, Pound RV. Resonance absorption by nuclear magnetic moments in a solid. **Physical Review** 1946; **69**: 37

3. Proctor WG, Yu FC. The dependence of a nuclear magnetic resonance frequency upon chemical compound. **Physical Review** 1950; **77**: 717

4. Dickinson WG. Dependence of the 19F nuclear resonance position on chemical compound. **Physical Review** 1950; **77**: 736

5. Lauterbur P. Image formation by induced local interactions: examples employing nuclear magnetic resonance. **Nature** 1973; **242**: 190-191.

6. Mansfield P, Maudsley AA. Planar and line-scan spin imaging by NMR. **Proc.19th AMPERE congress, Heidelberg** 1976; 247-252.

7. Damadian R, Goldsmith M, Minkoff L. NMR in cancer: XVI. FONAR image of the live human body. **Physiol.Chem.Phys.** 1977; **9**: 97-100.

8. Le Bihan D. Diffusion and perfusion magnetic resonance imaging : Applications to functional MRI. New York: Raven Press, 1995;

9. Martin E, Barkovich AJ. Magnetic resonance imaging in perinatal asphyxia. **Archives of Disease in Childhood** 1995; **72**: F62-F70

10. Wyatt J.S. Hypoxic ischaemic injury of the neonatal brain. **Fetal and Maternal Medicine Review** 1996; 95-108.

11. Sarnat HB, Sarnat MS. Neonatal encephalopathy following fetal distress. **Arch Neurol** 1976; **33**: 696-705.

12. Siegel M, Shackleford G, Perlman J, Fulling K. Hypoxic-ischaemic encephalopathy in term infants: diagnosis and prognosis evaluated by ultrasound. **Radiology** 1984; **152**: 395-399.

13. Hope P.L., Costello A.M.dL., Cady E.B., et al. Cerebral energy metabolism studied with phosphorus NMR spectroscopy in normal and birth-asphyxiated infants. **Lancet** 1984; 366-370.

14. Azzopardi D, Wyatt JS, Cady EB, et al. Prognosis of newborn infants with hypoxic-ischaemic brain injury assessed by phosphorous magnetic resonance spectroscopy. **Paediatric Res** 1989; 445-451.

15. Thoresen M, Penrice J, Lorek A, et al. Mild hypothermia following severe transient hypoxia-ischaemia ameliorates delayed cerebral energy failure in the newborn piglet. **Paediatric Res** 1995; **37**: 667-670.

16. Amess P, Penrice J, Thoresen M, Lorek A, Kirkbride V, Cooper CE. Mild hypothermia after severe transient hypoxia-ischaemia reduces the delayed rise in cerebral lactate in the piglet (abstract). **Paediatric Res** 1995; **38**: 423

17. Thornton JS, Ordidge RJ, Penrice J, et al. Temporal and anatomical variations of brain water apparent diffusion coefficient in perinatal cerebral hypoxic-ischemic injury: relationships to cerebral energy metabolism. **Magnetic Resonance In Medicine** 1998; **39**: 920-927.

2 Nuclear Magnetic Resonance

2.1 Introduction

The field of nuclear magnetic resonance spectroscopy and imaging in medicine has matured sufficiently that the basic theory has been reviewed comprehensively by numerous authors including Young[1], Morris[2], Leach[3], Cady[4], and Liang and Lauterbur[5]. Therefore, in this chapter, only an overview of the basic theory will be provided with attention being given to those aspects that are relevant to the work to be described later in this thesis.

2.2 Quantum Description

2.2.1 Nuclear magnetic moment

Nucleons, that is protons and neutrons, are spin ½ particles possessing spin angular momentum. This spin angular momentum **S** is quantised both in magnitude and direction. The quantised magnitude of the spin angular momentum for a spin ½ particle and its z-component are given in equation 2.01.

$$|\mathbf{S}| = \sqrt{\frac{1}{2}\left(\frac{1}{2}+1\right)}\hbar$$
$$|\mathbf{S}| = \sqrt{\frac{3}{4}}\hbar \qquad (2.01)$$
$$S_z = \pm\frac{1}{2}\hbar$$

where $\hbar$ is equal to $h/2\pi$ and h is the Planck's constant

In a nucleus, there may be an additional orbital angular momentum associated with the motion of the nucleons within the nucleus. The combined orbital and

spin angular momentum of a nucleus is known as the nuclear angular momentum (**J**). The nuclear angular momentum is also quantised and its magnitude and z-component are determined by the nuclear spin quantum number (I), as shown in equation 2.02.

$$|\mathbf{J}| = \sqrt{I(I+1)}\hbar$$
$$J_z = m_j\hbar \qquad (2.02)$$

where m_j = -I, -I+1, ..., I-1, I and I is the nuclear spin quantum number

The nuclear spin quantum number I of a nucleus is determined by its nuclear constituents. Nuclei with even mass numbers and odd charge numbers have integral nuclear spin quantum numbers. Nuclei with even mass numbers and even charge have zero nuclear spin, whilst nuclei with odd mass numbers have half integral nuclear spin quantum numbers. Associated with the nuclear angular momentum **J**, is a magnetic moment $\boldsymbol{\mu}$ given by equation 2.03.

$$\boldsymbol{\mu} = \gamma\mathbf{J} \qquad (2.03)$$

where γ is the gyromagnetic ratio. The gyromagnetic ratio depends on the internal structure of the nucleus and therefore differs for each nucleus. For hydrogen (^{1}H), the gyromagnetic ratio is 2.675×10^8 rad.s^{-1}.T^{-1}.

2.2.2 Nuclear energy in a static field

In the presence of an external uniform magnetic field ($\mathbf{B}_0$), there is an interaction energy between the field and the magnetic moment ($\boldsymbol{\mu}$), given by the Hamiltonian in equation 2.04.

$$\hat{H}\varphi = E\varphi$$
$$\hat{H}\varphi = -\boldsymbol{\mu}\cdot\mathbf{B}_0\varphi \qquad (2.04)$$
$$\therefore E = -\boldsymbol{\mu}\cdot\mathbf{B}_0$$

where E = magnetic interaction energy

Assigning the z-axis to be parallel to the $\mathbf{B}_0$ field, the interaction energy E can be rewritten as shown in equation 2.05.

$$E = -\mu_z|\mathbf{B}_0|$$
$$E = -\gamma|\mathbf{B}_0|J_z \qquad (2.05)$$
$$E = -\gamma\hbar|\mathbf{B}_0|m_j$$

where m_j = -I, -I+1, ..., I-1, I

For ^{1}H with a nuclear spin quantum number of ½, m_j can have values ±½ and thus two energy states are possible depending on the direction of $\boldsymbol{\mu}$ (see figure 2.1). The lower energy state corresponds to approximate alignment of the nuclear magnetic moment ($\boldsymbol{\mu}$) with the $\mathbf{B}_0$ field, whilst the higher energy state corresponds to approximate anti-alignment of $\boldsymbol{\mu}$. The splitting of the nuclear energy states by an external magnetic field is known as Zeeman splitting. The energy difference between the two Zeeman states is given by equation 2.06.

$$\Delta E = \gamma\hbar|\mathbf{B}_0| \qquad (2.06)$$

2.2.3 Transitions between nuclear energy levels

A transition between the two states can be induced by applying a rotating magnetic field in the xy plane at an angular frequency ω_0 given by equation 2.07.

$$|\omega_0| = \frac{\Delta E}{\hbar}$$
$$|\omega_0| = \gamma |\mathbf{B}_0| \qquad (2.07)$$

where ω_0 is the resonance (Larmor) angular frequency and ΔE is given in equation 2.06

Nuclear Magnetic Resonance (NMR) is the transition of nuclei between different magnetic states and equation 2.07 describes the condition required for NMR. From equation 2.07, it can be seen that for a given nuclear species, the resonance angular frequency ω_0, known as the Larmor frequency, is directly proportional to the applied $|\mathbf{B}_0|$ field. At conventional values of $\mathbf{B}_0$, the Larmor frequency is located in the radio frequency (RF) band.

2.2.4 Boltzman's distribution of nuclear energy states

For a bulk sample in thermal equilibrium with its surroundings, the population of nuclei in each of the Zeeman energy states is determined by the Boltzman distribution. For nuclei with nuclear spin quantum numbers of ½ (e.g. ^{1}H) the relative numbers of anti-aligned spins (N_-) to aligned spins (N_+) is given by equation 2.08.

$$\frac{N_-}{N_+} = \exp\left(-\Delta E / kT\right) \qquad (2.08)$$

where k is Boltzman's constant, T is the temperature in Kelvin and ΔE is given in equation 2.06

From equation 2.08, the differences in the population of aligned and anti-aligned spin-½ nuclei can be calculated as shown in equations 2.09.

$$N_+ - N_- = N\tanh\left(\frac{\gamma\hbar|\mathbf{B}_0|}{2kT}\right)$$

$$\text{since } \gamma\hbar|\mathbf{B}_0| << kT \qquad (2.09)$$

$$N_+ - N_- \approx \frac{N\gamma\hbar|\mathbf{B}_0|}{2kT}$$

where N is the total number of spins

The magnitude of the net magnetization **M** of a bulk sample is equal to the sum of the magnetic moments from all the nuclei in the sample and can be calculated as shown in equation 2.10.

$$|\mathbf{M}| = N_+\mu_+ + N_-\mu_-$$

$$|\mathbf{M}| = \frac{\gamma\hbar}{2}(N_+ - N_-) \qquad (2.10)$$

substituting from equation 2.09

$$|\mathbf{M}| \approx \frac{N\gamma^2\hbar^2|\mathbf{B}_0|}{4kT}$$

The NMR signal from a sample is proportional to its bulk magnetisation **M** and, as can be seen from equation 2.10, this is proportional to the population differences between the aligned and anti-aligned spins. Due to the low transitional energy involved in NMR at conventional $\mathbf{B_0}$ fields, the population differences at room temperature are very small and thus NMR is a very insensitive technique. For example, at a relatively high $\mathbf{B_0}$ field of 7T, the population difference at room temperature is only 24 spins per 10^6.

2.3 Classical Description

2.3.1 Net magnetisation vector

For a system of non-interacting spins, the net magnetisation vector obeys the classical equation of motion for a magnetic moment experiencing a torque due to an applied external magnetic field $\mathbf{B_0}$. From classical mechanics, the torque (τ) experienced by a magnetic dipole $\mathbf{M}$ in an external $\mathbf{B_0}$ field is given by equation 2.11.

$$\tau = \mathbf{M} \times \mathbf{B_0} \tag{2.11}$$

Since the rate of change of angular momentum is equal to the torque, the equation of motion of $\mathbf{M}$ can be derived as follows:

$$\frac{d\mathbf{J}}{dt} = \mathbf{M} \times \mathbf{B_0}$$

$$\text{but } \mathbf{M} = \gamma \mathbf{J}, \text{ thus} \tag{2.12}$$

$$\frac{d\mathbf{M}}{dt} = \gamma \mathbf{M} \times \mathbf{B_0}$$

where $\mathbf{J}$ is the nuclear angular momentum

2.3.2 Rotating frame of reference

Equation 2.12 can be solved using the standard method of differential equations but it is more convenient to use the rotating frame co-ordinate system. In a co-ordinate system rotating at an angular velocity Ω, it can be shown[3] that the time derivative of the magnetic moment $\mathbf{M}$, is given by equation 2.13.

$$\left(\frac{d\mathbf{M}}{dt}\right)_{rot} = \frac{d\mathbf{M}}{dt} - \boldsymbol{\Omega}\times\mathbf{M}$$
$$\left(\frac{d\mathbf{M}}{dt}\right)_{rot} = \gamma\mathbf{M}\times\mathbf{B}_0 - \boldsymbol{\Omega}\times\mathbf{M}$$
$$\text{since } \mathbf{A}\times\mathbf{B} = -(\mathbf{B}\times\mathbf{A}) \qquad (2.13)$$
$$\left(\frac{d\mathbf{M}}{dt}\right)_{rot} = \gamma\mathbf{M}\times\mathbf{B}_0 + \mathbf{M}\times\boldsymbol{\Omega}$$
$$\left(\frac{d\mathbf{M}}{dt}\right)_{rot} = \mathbf{M}\times(\gamma\mathbf{B}_0 + \boldsymbol{\Omega})$$

where $(d\mathbf{M}/dt)_{rot}$ is the time derivative of the magnetic moment **M** in the rotating frame of reference.

Comparing equations 2.12 and 2.13, it can be seen that if the actual $\mathbf{B_0}$ field were replaced by an effective field $\mathbf{B_{eff}}$ (given in equation 2.14), then the motion of **M** would be the same in the rotating frame of reference as in the laboratory frame of reference.

$$\mathbf{B}_{\text{eff}} = \mathbf{B}_0 + \frac{\boldsymbol{\Omega}}{\gamma} \qquad (2.14)$$

To solve the equation of motion for the magnetic moment in the rotating reference frame we set $\boldsymbol{\Omega}$ to $-\gamma\mathbf{B_0}$. With $\boldsymbol{\Omega}$ equal to $-\gamma\mathbf{B_0}$, $\mathbf{B_{eff}}$ is reduced to zero and the magnetic moment remains static in the rotating frame of reference. If the magnetic moment is static in the rotating frame, then in the laboratory frame, the magnetic moment must be rotating at an angular frequency of $-\gamma\mathbf{B_0}$. This angular frequency is the same as the Larmor frequency obtained quantum mechanically in equation 2.07.

2.3.3 RF pulses

Using the rotating frame of reference, the effect of a rotating magnetic field in the xy plane may be now analysed. Consider a magnetic moment in a static field $\mathbf{B_0}$, experiencing a $\mathbf{B_1}$ field rotating in the xy plane at an angular velocity ω. To remove the time dependence of the $\mathbf{B_1}$ field, we choose a frame of reference that rotates at the same angular velocity as the $\mathbf{B_1}$ field. The effective field in this case is given by equation 2.15.

$$\mathbf{B}_{\text{eff}} = \mathbf{B}_0 + \frac{\omega}{\gamma} + \mathbf{B}_1 \tag{2.15}$$

If $\mathbf{B_1}$ rotates at the Larmor frequency (i.e. $-\gamma\mathbf{B_0}$) then $\mathbf{B_{eff}}$ equals $\mathbf{B_1}$ and the magnetic moment **M**, in the rotating frame of reference, rotates about $\mathbf{B_1}$. The angular velocity of **M** about $\mathbf{B_1}$ is $\gamma\mathbf{B_1}$ and if the $\mathbf{B_1}$ field is applied for a period t, then **M** will rotate about $\mathbf{B_1}$ through an angle θ given by equation 2.16.

$$\theta = |\gamma \mathbf{B}_1| t \tag{2.16}$$

The angle through which **M** is tipped can be varied by varying $|\mathbf{B_1}|$ or t. Since, in an NMR experiment, the rotating $\mathbf{B_1}$ field is generated by an RF pulse, this corresponds to a variation in either the amplitude or the length of the RF pulse respectively. To detect the magnetic moment **M** in an NMR experiment, it has to be rotated from the z-axis into the xy plane. Such a rotation can be achieved by using a 90^0 RF pulse.

2.3.4 Relaxation

After the magnetic moment **M** has been disturbed away from its equilibrium by an RF pulse, it relaxes back via longitudinal (or spin-lattice) and transverse (or

spin-spin) relaxation. Longitudinal relaxation involves the transfer of energy from the excited nuclear spins to the surrounding molecular environment (i.e. the lattice) and is responsible for the return of the z-component of the magnetic moment to its equilibrium value. For efficient longitudinal relaxation, fluctuating magnetic fields with a component oscillating at ω_0 are required to induce transitions between the different Zeeman states. These fluctuating magnetic fields are created in the lattice by the random tumbling of molecules and their associated magnetic moments. The return of the z-magnetisation to its equilibrium value (M_0) during longitudinal relaxation is given by the Bloch equation[6] as follows:

$$\frac{dM_z}{dt} = -\frac{M_0 - M_z}{T_1} \tag{2.17}$$

Where M_0 is z-magnetisation at equilibrium and T_1 the longitudinal, or spin-lattice, relaxation time.

The solution to this differential equation is given in equation 2.18. From equation 2.18, it can be seen that the z-magnetisation returns to equilibrium in an exponential manner.

$$M_z(t) = M_0 + (M_z(0) - M_0) \cdot \exp\left(-\frac{t}{T_1}\right) \tag{2.18}$$

Where $M_z(t)$ is the z-magnetisation at time t.

Transverse relaxation is responsible for the return of the transverse (x-y) magnetisation to its equilibrium value. As there is no preferred orientation for

the magnetisation in the transverse plane, the equilibrium value is zero. The decay of the transverse magnetisation during transverse relaxation can be approximated by the following Bloch equation:

$$\frac{d\mathbf{M}_{xy}}{dt} = -\frac{\mathbf{M}_{xy}}{T_2} \tag{2.19}$$

Where $\mathbf{M}_{xy}$ is the transverse magnetisation and T_2 is the transverse, or spin-spin, relaxation time.

Transverse relaxation occurs through energy-conserving processes, whereby spin energies are exchanged between neighbouring spins. These processes do not lead to a loss of energy to the lattice but they do cause a loss of phase coherence between the spins, and consequently a decrease in the transverse magnetisation. The value of T_2 can never exceed that of T_1 because factors that cause spin-lattice relaxation also lead to transverse relaxation. In addition, low frequency magnetic field fluctuation can also lead to T_2 relaxation. In biological tissues, the low frequency component of T_2 relaxation normally dominates and hence, for any biological sample, the value of T_2 will normally be considerably shorter than that of T_1.

An additional cause of transverse magnetisation decay is the imperfection in the bulk $\mathbf{B}_0$ field homogeneity. In the presence of such imperfection, nuclei in different positions experience different $\mathbf{B}_0$ fields and precess at slightly different rates, causing loss of transverse magnetisation by dephasing of the spins. This decay process is characterised by a time T_2' and can be differentiated from T_2

relaxation by the fact that it is reversible. The combined effect of T_2 and T_2' is called T_2^* relaxation and is defined in equation 2.20.

$$\frac{1}{T_2^*} = \frac{1}{T_2} + \frac{1}{T_2'} \tag{2.20}$$

2.3.5 Free Induction Decay (FID)

Following a 90^0 pulse, the magnetic moment in the transverse plane can be detected by placing an RF receiver coil around the sample. As the magnetic moment precesses about $\mathbf{B_0}$, an oscillating voltage at the Larmor frequency can be detected due to magnetic induction. The oscillating voltage decays exponentially (see figure 2.2) with a characteristic time T_2^* due to transverse relaxation, and is known as the Free Induction Decay (FID).

2.3.6 Hahn spin echo

Unlike spin dephasing due to spin-spin relaxation, spin dephasing due to field inhomogeneity is a coherent process and, therefore, is reversible. The reversal of spin dephasing by field inhomogeneity was first observed by Hahn[7] and can be understood by considering the pulse sequence shown in figure 2.3. As can be seen, following the 90^0 RF pulse, the magnetisation **M** is first left to dephase in the transverse plane for a time TE/2 (period (ii) to (iii)). At this point an 180^0 RF pulse is applied, which reverses the phase of the spins so that spins that have acquired an extra θ phase due to $\mathbf{B_0}$ field inhomogeneity will now have effectively lost a phase θ and vice versa (period (iii) to (iv)). After a further period TE/2, the spins will have acquired exactly the required phase to cancel

out the effective loss of phase during the previous *TE/2* period (period (iv) to (v)). A spin echo is seen at this point because all the dephasing due to T_2' has been rephased, and the signal is dephased by T_2 relaxation processes alone. The NMR signal at this point is given by equation 2.21.

$$S(TE) = A\exp\left(-TE/T_2\right) \tag{2.21}$$

Where A is the NMR signal just after the 90^0 RF pulse and S(TE) is the NMR signal at the spin echo time, TE.

2.3.7 Chemical shift effect

Nuclei in matter are surrounded by clouds of atomic electrons that shield them from external magnetic fields. The level of shielding depends on the arrangement of electrons about the nuclei and thus will vary between different molecules and molecular sites. The effective magnetic field ($\mathbf{B}_{0(\text{eff})}$) experienced by nuclei in a given molecular environment can be calculated as shown in equation 2.22.

$$\mathbf{B}_{0(\text{eff})} = \mathbf{B}_0(1-\sigma) \tag{2.22}$$

Where $\mathbf{B}_0$ is the external magnetic field and σ is the magnetic shielding factor of the molecular environment of interest.

The magnetic shielding effects of molecular electrons lead to a small but significant difference in the Larmor frequencies of nuclei in different molecular environment. This difference in Larmor frequencies is known as the chemical shift[8;9] and is normally expressed as follows:

$$\delta = \frac{\upsilon - \upsilon_{ref}}{\upsilon_{ref}} \times 10^6 \qquad (2.24)$$

Where δ is the chemical shift in parts per million, υ is the Larmor frequency of a nucleus of interest in a particular molecule and υ_{ref} is a reference frequency (usually taken as the Larmor frequency of the nuclei of interest in a reference compound).

2.3.8 NMR spectroscopy

The chemical shift effect forms the basis of NMR spectroscopy, allowing NMR signals arising from nuclei at different molecular sites to be distinguished from one another. One application of NMR spectroscopy is the identification of chemical compounds in a sample. To illustrate the principle involved in this process, an example will be given. Consider a sample consisting of a number of different compounds, each containing a particular nuclear species in a number of different molecular sites. Due to the chemical shift effect, numerous slightly different Larmor frequencies will exist, each corresponding to the different chemical shift present in the sample. The Larmor frequencies, and hence chemical shift, present in the sample can be determined by exciting all the nuclei of interest with a broad-spectrum 90^0 RF pulse and acquiring the resulting FID. As the observed FID is a sum of all the NMR signals arising from the nuclei at various molecular sites, it will therefore consists of a mixture of frequency components, each representing the contribution of nuclei at a particular chemical shift. By Fourier transforming the observed FID, a spectrum with peaks corresponding to the various chemical shifts can be obtained. By

analysing the chemical shifts present, it is possible to infer the presence of particular molecular sites, and hence chemical compounds, in the sample. Furthermore, since the area under each peak in the NMR spectrum (ignoring various complication factors) is proportional to the concentration of spins in a sample experiencing that particular chemical shift, it is also possible to determine the relative concentrations of the various chemical compounds in the sample.

In the following chapter, phosphorus (^{31}P) spectroscopy will be used to determine the relative concentration of cerebral phosphocreatine (PCr) and inorganic phosphate (Pi) in a piglet model of perinatal asphyxia. The importance of these compounds in perinatal asphyxia lies in their role in cerebral energy metabolism. Under physiologic conditions, the majority of the energy in the brain is supplied by the oxidative phosphorylation of glucose; a process that leads to the generation of adenosine triphosphate (ATP) from adenosine diphosphate (ADP) and Pi. ATP is a major carrier of energy in biological systems and its hydrolysis to ADP and Pi, as shown below, is accompanied by a release of a large amount of energy.

$$ATP^{4-} + H_2O \rightarrow ADP^{3-} + HPO_4^{2-} + H^+ + \Delta G \qquad (2.25)$$

where ΔG is the energy liberated.

To prevent large fluctuations in ATP concentration, it is buffered by PCr in the following reversible reaction, catalysed by creatine kinase.

$$PCr + ADP + H^+ \rightleftharpoons ATP + Creatine \qquad (2.26)$$

Thus, when the demand for energy depletes ATP faster than it can be synthesised by oxidation phosphorylation and other catabolic pathways, the above reaction is driven forward to maintain ATP levels at the expense of the PCr level. However, this decline in PCr concentration is normally only transient, as excess ATP will eventually be used to replenish the PCr level by the reverse reaction when energy demand is below that supplied by catabolic ATP synthesis.

In situations where the energy demand exceeds supply for an extended period (e.g. during an hypoxic-ischaemic (HI) insult), the creatine kinase reaction leads to a significant decline in the PCr level, whilst the mismatch between ATP synthesis and hydrolysis leads to a significant increase in the level of Pi. The changes in PCr and Pi during a HI insult can be detected by NMR spectroscopy and the ratio of [PCr] to [Pi] has been shown to be a sensitive index of cellular energy metabolism (square brackets indicate molecular concentration of the compound). In studies of perinatal asphyxia, it has been demonstrated that there is a strong correlation between the minimum [PCr]/[Pi] between 24 and 48 hours after birth and neurodevelopmental outcome at 1 year[10].

A typical cerebral ^{31}P spectrum obtained from a newborn piglet is shown in figure 2.4. The peaks from left to right correspond to[4]: (1) phosphomonoesters, (2) inorganic phosphate, (3) phosphodiesters, (4) phosphocreatine, (5) γ-nucleotide triphosphate, (6) α-nucleotide triphosphate, (7) β-nucleotide triphosphate.

2.4 Spatial encoding

In order to form images in MRI, spatial localization techniques had to be developed to encode the distribution of the spins within a sample. Historically, many techniques were developed (see Nuclear Magnetic Resonance Imaging in Medicine and Biology[2] for a comprehensive review), but the most successful were: slice selection, frequency encoding and phase encoding. These techniques still form the basis of most MR imaging techniques today and are described in the following paragraphs. To aid the description of the techniques, a standard Spin Echo Two Dimensional Fourier Transform (SE-2DFT) sequence that uses slice selection, frequency and phase encoding, is shown in figure 2.5.

2.4.1 Slice Selection

In a non-localised NMR experiment, an RF pulse will normally excite all the spins within the field of view (FOV) of the coil. Since the sample is a three-dimensional object, spatial encoding in all three dimensions would normally be needed to resolve its spatial distribution. However, by selectively exciting a thin imaging slice, a plane through the sample can be viewed and 2D spatial encoding is sufficient. To perform slice selective excitation, a magnetic field gradient (known as a slice-selection gradient) perpendicular to an imaging plane of interest, is applied (figure 2.5, period A). The slice selection gradient causes spins in different imaging planes to precess at different frequencies. Since spins are only excited by RF pulses at their Larmor frequencies, a slice of tissue at different positions and of varying thickness can be selectively excited using shaped RF pulses. For a given slice selection gradient, the position and

thickness of the excited slice are determined by the frequency and the bandwidth of the RF pulse, respectively. Slice thickness can be reduced either by increasing the gradient strength, or by decreasing the RF bandwidth. During the application of the slice-selection gradient, spins acquire a linear phase across the thickness of the slice as they are tipped into the transverse plane. A second refocusing gradient opposite to the original slice-selection gradient is normally used to rephase the spins as shown in Fig 2.5, period B.

2.4.2 Frequency Encoding

Following a 90^0 slice-selective excitation, spins from the imaging slice will all be in the transverse plane, precessing at the same angular frequency (assuming that the $\mathbf{B_0}$ field is perfectly homogeneous and that there is no chemical shift). To localise the spins along one of the directions of the imaging plane (e.g. the x-axis), frequency encoding is normally used. Frequency encoding involves the acquisition of the NMR signal during the application of a linear magnetic field gradient (known as the read gradient) along the x-axis (see figure 2.5, period D). This linear magnetic field gradient causes spins to precess at frequencies that are proportional to their positions along the x-axis. Using the Fourier transform, the frequency components of the acquired NMR signal can be separated and assigned to the correct positions along the x-axis, to give a profile of the imaging slice. The role of the dephasing gradient along the x-axis during period B in frequency encoding is best described using the concept of k-space[11] and thus will be deferred till its introduction later in this chapter.

2.4.3 Phase Encoding

Localisation of the spins along the second axis of an imaging plane can be achieved by phase encoding. Phase encoding involves the application of a linear magnetic field gradient (phase encoding gradient) along an axis perpendicular to both the slice-selective and frequency-encoding axes (e.g. the y-axis), for a period t_{PE}, prior to the acquisition of the NMR signal (see figure 2.5, period B). During the application of the phase encoding gradient, spins at different positions along the y-axis will precess at different angular velocities and, hence, accumulate different phase angles by the end of the phase encoding period. The phase angle (ϕ) accumulated by a given spin depends on its position along the y-axis, the phase encoding gradient strength (G_{PE}), and the phase encoding period, as shown in equation 2.27.

$$\phi = \gamma \cdot y \int_0^{t_{PE}} G_{PE}(t)\, dt \qquad (2.27)$$

By varying the phase encoding gradient strength in a stepwise manner in successive NMR experiments (the exact phase encoding required will be discussed in the following section), the signal from a given spin will be modulated at a frequency that is determined by its y-position. With a number of phase-encoded NMR signals, it is possible to use the Fourier transform to unravel the position dependent phase modulation of the signal and hence, to localise spins along the y-axis. Thus, by combining phase encoding and frequency encoding, an image can be formed from a defined slice.

2.4.4 Reciprocal (K) space

Due to the qualitative description used in the preceding paragraphs, it may be difficult to see precisely how frequency and phase encoding can be combined to resolve the spins distribution within an imaging slice. In the following paragraphs a more quantitative description of the spatial encoding process will be given and the concept of k-space[11] will be introduced to help visualise the MRI acquisition process.

In a frequency and phase-encoded scan, an image of the imaging slice can be obtained by applying the 2D Fourier transform to the acquired NMR signals. Since the 2D Fourier transform connects the spatial frequency domain (k-space) to the spatial domain, the encoded NMR signal must be representing the image signal in the spatial frequency domain. To understand how this has occurred, it is necessary to analyse the effects of the linear encoding gradients on the transverse magnetisation. Consider a sample whose transverse magnetisation following a slice selective 90^0 pulse is described by the complex function M(x,y). Using the inverse 2D Fourier transform, the spatial frequency distribution $M(k_x,k_y)$ *of* M(x,y) may be calculated as shown in equation 2.28.

$$M(k_x,k_y)=\iint M(x,y)\cdot\exp(i\cdot[k_x\cdot x+k_y\cdot y])dxdy \qquad (2.28)$$

where i^2 equals -1, and k_x, k_y are the spatial frequencies along the x and y axes respectively, with units of radians per metre.

Ignoring relaxation and chemical shifts effects, the NMR signal, S(t), in the presence of an uniform external $\mathbf{B_0}$ field and a time varying linear gradient field $\mathbf{G}(t)$ can be described as shown in equation 2.29.

$$S(t)=\iint M(x,y)\cdot\exp\left(i\gamma\left[|\mathbf{B_0}|t+x\int_0^t G_x(t')dt'+y\int_0^t G_y(t')dt'\right]\right)dxdy \qquad (2.29)$$

The oscillation due to the $\mathbf{B_0}$ field can be removed from the signal *S(t)* by demodulation[12] to give a signal S′(t) as shown in equation 2.30.

$$S'(t)=\iint M(x,y)\cdot\exp\left(i\gamma\left[x\int_0^t G_x(t')dt'+y\int_0^t G_y(t')dt'\right]\right)dxdy \qquad (2.30)$$

Comparing equation 2.30 with equation 2.28, it can be seen that signal S′(t) at time t is the same as the spatial frequency $M(k_x,k_y)$, with the frequency indices k_x and k_y given by equation 2.31.

$$\begin{aligned} k_x &= \gamma\int_0^t G_x(t')\,dt' \\ k_y &= \gamma\int_0^t G_y(t')\,dt' \end{aligned} \qquad (2.31)$$

Having established the relationship between the linear encoding gradients and the spatial frequency under observation, it is now necessary to determine what spatial frequencies are needed in order to reconstruct an image of the selected slice. The required spatial frequencies can be determined from the sampling theorem[13]. It can be shown from the sampling theorem that in order to reconstruct an image of M(x,y) with a resolution of λ_x by λ_y, the spatial frequency domain $M(k_x,k_y)$ must be sampled from at least $-\pi/\lambda_x$ and $-\pi/\lambda_y$ to at least $+\pi/\lambda_x$ and $+\pi/\lambda_y$ along the k_x and k_y axes respectively. It can also be shown that, for an image whose spatial extent is described by a Field Of View (FOV) of FOV_x by FOV_y, the spatial frequency domain need only be sampled

in intervals of $2\pi/FOV_x$ and $2\pi/FOV_y$ along the k_x and k_y axes respectively to prevent aliasing in the reconstructed image.

In order to acquire the spatial frequencies of $M(k_x,k_y)$ according to the sampling theorem, the strength of the linear encoding gradients and the timing of their application need to be varied such that the frequency indices k_x and k_y, given in equation 2.31, are at the desired value during the sampling period. For a standard spin echo sequence with phase and frequency encoding as shown figure 2.5, we can show how this has been achieved by plotting the trajectory of the frequency index **K** during one phase encoding step in the sequence as shown in figure 2.6. From figure 2.6, it can be seen that both frequency and phase encoding are acting together to select the required spatial frequencies $M(k_x,k_y)$ during the acquisition period. Note that the 180^0 RF pulse inverts the phase acquired during the phase encoding period, and brings the k-space trajectory to the opposite side of k-space as shown in figure 2.6.

2.4.5 Echo Planar Imaging (EPI)

At each excitation of the sample, the spin echo sequence shown in figure 2.5 only acquires a single line of k-space, but it is equally possible to acquire as many lines of k-space as are needed to form a whole image using an Echo Planar Imaging (EPI) sequence[14]. One possible implementation of the EPI sequence, known as blipped EPI, is shown in figure 2.7. In a blipped EPI sequence, after each line of k-space has been acquired, the phase encoding gradient is blipped for a short duration to move the k-space trajectory to the next line of k-space. The read gradient is then reversed so that the next line of

k-space can be acquired and this process is repeated until the all the required lines of k-space have been obtained. Other k-space trajectories are also possible but more complicated reconstruction methods are usually required to obtain images without significant imaging artefacts[14]. The first successful implementation of EPI was demonstrated by Mansfield in 1977[15]. Although theoretically simple, EPI was, and still is, technically very demanding on the gradient system. This is because of the necessity to cover the whole of k-space accurately before substantial transverse magnetisation is lost via T_2^* decay (typically less than 100ms). If the k-space trajectory is non-ideal, image ghosting and distortion occurs. If the k-space trajectory is completed too slowly (due low gradient strength or slow gradient switching), then substantial T_2^* relaxation will occur during the acquisition period, and serious chemical shift and susceptibility artefacts will result. Therefore, in order to obtain high quality images from an EPI sequence, a gradient system with high gradient strength, fast gradient switching, and minimal eddy currents, is required. Unfortunately, a gradient system that meets all of the above requirements is very difficult to realise because the requirements are all interlinked, and optimisation of one property generally leads to degradation of the others. Thus, despite many advances in the gradient systems of modern NMR scanners, the problems of limited resolution, and susceptibility and chemical shift artefacts in EPI images, are still evident. However, because EPI is able to acquire an image within 100ms, in applications where high time resolution or motion freezing are essential, it is currently the technique of choice on systems with the required gradient capabilities.

2.4.6 Interleaved EPI

To overcome the disadvantages of the EPI sequence, a slower but less demanding interleaved EPI sequence has been proposed[16]. In the interleaved EPI sequence, a large fraction of the required k-space lines are acquired at each excitation of the sample as shown in figure 2.8. The excitation is repeated several times with the appropriate phase encoding gradients until all the necessary lines of k-space have been acquired. Since fewer lines of k-space are acquired at each excitation, fewer gradient switches are required and the data acquisition can be performed in a shorter period (typically less than 20ms). Thus, the problems of eddy currents, and susceptibility and chemical shift artefacts are much reduced in interleaved EPI. Furthermore, unlike EPI, the resolution achievable from a interleaved EPI sequence can be increased, without any additional chemical shift or susceptibility artefacts, by increasing the number of interleaves in the image.

2.5 Imaging contrast in MRI

One of the major advantages of MRI over other medical imaging modalities is its ability to select different tissue properties as the imaging contrast mechanism[17]. These tissue properties are changed in pathological tissue and the ability to measure these changes using MRI is of enormous benefit in medical diagnosis and treatment. Traditionally, imaging contrast in MRI has been based on the NMR properties of tissue, that is, its spin density, spin-lattice (T_1) and spin-spin (T_2) relaxation times. However, recent developments mean that it is now possible to obtain images with contrast based on, amongst other things,

tissue perfusion and tissue water diffusion[18]. In the following chapter, the changes in water T_2 relaxation time and water diffusion in cerebral tissue in a piglet model of perinatal asphyxia will be presented. Therefore, in the following paragraphs, the MRI techniques involved in the measurements these parameters will be discussed, together with their physiological significance.

2.5.1 T_2-weighted imaging and quantification

The use of an 180^0 RF pulse in a pulse sequence to obtain NMR signal that is dependent on the T_2 time in a sample of interest was described earlier in section 2.3.7. In addition to the T_2 time in the sample, the NMR signal was also dependent on the echo time used in the sequence (see equation 2.21). By using a long echo time, signal from regions of the sample with a short T_2 time can be made to decay significantly and thus appear dark on an image. In contrast, regions with long T_2 times will not decay by as much and, thus, will appear brighter on the image. In this way, images with T_2-weighted contrast can be obtained.

Although the signal in a T_2-weighted image is related to the T_2 in the sample, it is also related to other factors (e.g. sample spin density and RF coil sensitivity), which may make interpretation of the T_2-weighted images difficult. In order to generate images that are only related to the T_2 times in the sample alone, the T_2 needs to be quantified. T_2 quantification can be achieved by acquiring two or more T_2-weighted images with different echo times. With multiple different T_2-weighted images, the T_2 time for each pixel in the images can be obtained by fitting the signal decay in each pixel to the exponential curve described by

equation 2.21. Having obtained the T_2 time for each pixel, an image that is weighted by T_2 relaxation time alone can be generated by showing a map of the T_2 values.

One method of fitting the acquired signal to the exponential decay curve is via the log-linear fitting procedure. In this procedure, the exponential equation shown in 2.21 is first linearised by taking the log of both sides as follows:

$$\ln(\mathrm{S(TE)}) = \ln(A) - \frac{1}{T_2} \cdot TE \qquad (2.32)$$

where A is the NMR signal just after the 90^0 RF pulse and S(TE) is the NMR signal at the spin echo time, TE.

From equation 2.32, it can be seen that the log of a T_2-weighted NMR signal is directly proportional to its echo time, and that the constant of proportionality is equal to the reciprocal of the T_2 time. Thus, by performing a linear regression on the log of the observed NMR signals against their echo times, the T_2 relaxation time of the sample can be obtained.

2.5.2 Physiological significance of tissue T_2

'A detailed understanding of T_2 relaxation has not yet emerged in biological tissue'[2]. However, it has been shown that there is an approximately linear relationship between the T_2 time of tissue and the water content of tissue[19]. Furthermore, it has also been demonstrated that the T_2 of cerebral tissue increases significantly following an ischaemic event in both human patients[20;21] and animal models[22;23]. It is thought that much of the increase in T_2 following

ischaemia is due to cerebral oedema, a sequelae of tissue damage that leads to significant increases in tissue water content.

It was assumed in section 2.3.7 that the NMR signal during T_2-relaxation could be approximated by an exponential decay. In tissue, non-exponential T_2 decay is often observed. One possible cause of this non-exponential decay is due to the compartmental effect, where water in different cellular compartments has different T_2 relaxation times. Due to the limited resolution of conventional MRI, the NMR signal obtained from tissue will usually consist of water signal from a number of different cellular compartments. In such cases, the observed signal will be a sum of a number of NMR signals, each relaxing at a different T_2 time, and would therefore, be best described by a multi-exponential decay curve.

2.5.3 Diffusion weighted imaging and quantification

Due to thermal agitation, molecules are constantly moving and colliding with one another. This random microscopic, translational motion of molecules is known as Brownian motion and is the basis of molecular diffusion. Over time Brownian motions tend to lead to a displacement of molecules away from their origin. Thus, for a given molecule, there is a probability that it will have travelled a distance r away from its origin after a diffusion time of t. In a simple liquid, the probability is given by a Gaussian distribution with a mean of zero and a variance of $2Dt$ (or $6Dt$ for displacement in 3 dimensions); where D is the diffusion coefficient of the liquid. The mean distance travelled is zero because

the probability of moving in one direction is the same as that of moving in the opposite direction.

The effect of molecular water diffusion on the NMR signal can be understood by analysing the classic Stejskal-Tanner diffusion weighting sequence[24], shown in figure 2.9. In the Stejskal-Tanner sequence, following the 90^0 excitation pulse, a large linear diffusion gradient (**G**) is applied, which causes the spins to accumulate a position dependent phase angle Φ_1 as shown in equation 2.33.

$$\Phi_1 = \gamma \int_0^{\delta} \mathbf{G} \cdot \mathbf{r} dt \tag{2.33}$$

where **r** is the position of the nuclear spin, γ is the gyromagnetic ratio, and δ is the duration of the diffusion gradient.

Following the 180^0 refocusing pulse, the accumulated phase angle Φ_1 in each spin is reversed to $-\Phi_1$. A second identical linear diffusion gradient **G** is then applied, which causes the spins to accumulate another position dependent phase angle Φ_2 as shown in equation 2.34.

$$\Phi_2 = \gamma \int_{\Delta}^{\Delta+\delta} \mathbf{G} \cdot \mathbf{r} dt \tag{2.34}$$

where Δ is the duration between the rising edges of the diffusion gradients.

The net phase angle Φ accumulated during the sequence is the sum of Φ_1 and Φ_2 as shown in equation 2.35.

$$\Phi = \Phi_1 + \Phi_2 = \gamma \int_{\Delta}^{\Delta+\delta} \mathbf{G} \cdot \mathbf{r} dt - \gamma \int_0^{\delta} \mathbf{G} \cdot \mathbf{r} dt \tag{2.35}$$

From equation 2.35, it can be seen that, when the diffusion gradients are equal, the net accumulated phase angle over the whole sequence is zero for static spins and the NMR signal for these spins is unaffected. For moving spins, the net accumulated phase angle is dependent on the spins' translational motion during and in between the application of the diffusion gradients. With molecular diffusion, the random translational motion of spins leads to a spread of accumulated phase angles, which results in destructive interference of the NMR signal and an associated loss in signal amplitude. If the diffusive process is unrestricted, the relationship between the molecular diffusion coefficient and the loss in signal amplitude due to diffusion, can be calculated as follows:

$$M = M_0 \exp(-bD) \tag{2.36}$$

where M is the NMR signal with diffusion weighting, M_0 is the NMR signal without diffusion weighting, D is the molecular diffusion coefficient, and b is the diffusion weighting factor.

The diffusion weighting factor b is determined by the timing and strength of the linear magnetic field gradients during the imaging sequence and can be calculated as shown in equation 2.37[18].

$$b = \int_0^{TE} \mathbf{k}(t)\cdot\mathbf{k}(t)dt$$
$$\mathbf{k}(t) = \gamma\int_o^t \mathbf{G}(t')dt' \tag{2.37}$$

where TE is the spin echo time

For the Stejskal-Tanner sequence shown in figure 2.8, the b-value calculation can be simplified to equation 2.38.

$$b = \gamma^2 G^2 \delta^2 (\Delta - \delta/3) \tag{2.38}$$

From equation 2.36, it can be seen that the diffusion coefficient D of a sample can be obtained by log-linear regression if two or more images of a sample at different b-values are known. Such images can be obtained by using the Stejskal-Tanner sequence in combination with an imaging sequence. An example of a Stejskal-Tanner sequence combined with a SE-2DFT imaging sequence is shown in figure 2.10. Diffusion weighted images at different b-values in the sequence can be obtained by varying the linear diffusion gradient **G**. Note that because additional imaging gradients have been added to the Stejskal-Tanner sequence in figure 2.10, the b-value cannot be calculated from equation 2.38 and the whole of equation 2.37 needs to be evaluated in order to obtain an accurate b-value.

The assumption of unrestricted diffusion in equation 2.36 is rarely true for biological tissue. The complex structures in cells and the cell membranes can all act to prevent free diffusion of water in living tissue. When molecules diffuse into an obstacle, they are reflected back and thus the diffusion distance does not increase indefinitely with diffusion time but is limited by the restrictive boundaries. The measured value of the diffusion coefficient in tissue is therefore dependent not only on the diffusion coefficient of water, but also on its environment and the NMR parameters used in the diffusion sequence (e.g. the diffusion time). To reflect these and other dependencies in tissue, the concept of Apparent Diffusion Coefficient (ADC) was introduced by Le Bihan et al.[25] to describe the diffusion coefficient measured in tissue. Due to the

complexity of cellular structures in tissue, the restriction of water diffusion in tissue is often directionally dependent. For example, in white matter, diffusion restriction perpendicular to the axis of the axon is much greater than that along the axis of the axon. This anisotropy in the restriction of water diffusion causes the ADC in tissue to be directionally dependent. This property is known as diffusion anisotropy[26].

2.5.4 Physiological significance of ADC

Interest in clinical diffusion weighted imaging was greatly heightened following the demonstration by Moseley et al.[27] in 1990 showing that DWI could be used to delineate ischaemic tissue. Although conventional imaging (i.e. T_1 and T_2 weighted imaging) has been shown to be able to delineate ischaemic tissue, it was usually only effective several hours after the onset of ischaemia. By using DWI, the presence of ischaemic tissue can usually be detected within minutes following the onset of ischaemia. The ability of detecting ischaemia at such an early stage has tremendous potential for the early diagnosis and treatment of ischaemic injury such as stroke and perinatal asphyxia (see chapter 3). The precise mechanisms responsible for the ADC changes seen during the acute phase of ischaemia remain controversial but the following mechanisms are thought to have some contribution to the changes seen:

i. Redistribution of extracellular water

During the acute phase of ischaemia, there is a redistribution of extracellular water into the intracellular space, which results in cellular swelling. This

cellular swelling at the expense of extracellular water is known as cytotoxic oedema and is thought to arise from the failure of the energy-dependent sodium/potassium (Na^+/K^+) pump. The operation of the Na^+/K^+ pump involves the hydrolysis of ATP molecules to exchange intracellular Na^+ ions for extracellular K^+ ions. The operation of the Na^+/K^+ pump leads to an ion concentration gradient across the cell membrane, with a high concentration of K^+ and Na^+ on the inside and outside of the cell respectively. When the Na^+/K^+ pump fails, there is an efflux of K^+ into the extracellular space and an influx of Na^+ and osmotically-driven water into the cell. Assuming that the apparent diffusion coefficient of extracellular water is higher than that of intracellular water (due to the greater concentration of restrictive boundaries intracellularly), the redistribution of extracellular water into the intracellular space should, therefore, lead to a lower overall observed tissue water ADC.

Experimental evidence to support cytotoxic oedema as a contributory mechanism to the ADC changes in ischaemia include the demonstration of tissue water ADC reduction following the administration of ouabain, a specific inhibitor of the energy-dependent Na^+/K^+ pump and following the administration of glutamate and N-methyl-D-aspartate, both of which cause cellular swelling[28]. Further support is provided by an experiment that showed that hyponatraemia, a model of cytotoxic oedema, also causes a decline in tissue water ADC[29].

ii. Increased extracellular diffusion path tortuosity

It has been proposed that the redistribution of extracellular water causes an increase in the tortuosity of water diffusion path in the extracellular space[30]. The increased tortuosity is thought to lead to a decrease in the apparent diffusion coefficient of extracellular water and hence an overall decline in the observed tissue water ADC.

iii. Decrease in the intracellular diffusion coefficient

Using NMR spectroscopy, it has been shown that there is a decline in the ADCs of intracellular tracers (e.g. ^{133}Cs[31] and intracellular metabolites such as N-acetylaspartate, creatines, cholines and myo-inositol[32]) during ischaemia. Assuming that the changes in the apparent diffusion coefficients of these tracers reflect the changes in intracellular water ADC, then a decline in intracellular diffusion coefficient during ischaemia will contribute to the observed tissue water ADC decline. The mechanisms responsible for the decline in intracellular diffusion coefficient remain unclear. However, it is unlikely to be due to cytotoxic oedema alone, since an increase in intracellular water would be expected to lead to an increase, rather than a decrease, in intracellular ADC.

It is likely that all of the above mechanisms have some contribution to the observed acute changes in ADC during ischaemia, the exact contribution from each, however, remains to be determined.

Reference List

1. Young SW. Nuclear magnetic resonance imaging : basic principles. New York: Raven Press, 1984;

2. Morris PG. Nuclear Magnetic Resonance Imaging in Medicine and Biology. Oxford: Oxford University Press, 1986;

3. Leach MO. Spatially localised nuclear magnetic resonance. In: Webb S, ed. The physics of medical imaging, Bristol: Institute of Physics Publishing, 1988: 389-487.

4. Cady EB. Clinical Magnetic Resonance Spectroscopy. New York: Plenum Press, 1990;

5. Liang Z, Lauterbur P. Principles of magnetic resonance imaging :a signal processing perspective. New York: IEEE Press, 2001;

6. Bloch F, Hansen WW, Packard M. Nuclear induction. **Physical Review** 1946; **69**: 127

7. Hahn EL. Spin Echoes. **Physical Review** 1950; **80**: 580-594.

8. Proctor WG, Yu FC. The dependence of a nuclear magnetic resonance frequency upon chemical compound. **Physical Review** 1950; **77**: 717

9. Dickinson WG. Dependence of the 19F nuclear resonance position on chemical compound. **Physical Review** 1950; **77**: 736

10. Azzopardi D, Wyatt JS, Cady EB, et al. Prognosis of newborn infants with hypoxic-ischaemic brain injury assessed by phosphorous magnetic resonance spectroscopy. **Paediatric Res** 1989; 445-451.

11. Ljunggren S. A simple graphical representation of Fourier-based imaging methods. **Journal Of Magnetic Resonance** 1983; **54**: 338-343.

12. Hoch JC, Stern AS. NMR Data processing. New York: Wiley-Liss, 1996;

13. Gonzalez RC, Wintz P. Digital image processing. London: Addison-Wesley, 1987;

14. Schmitt F, Stehling MK, Turner R. Echo-Planar Imaging. Theory, Technique and Application. Berlin: Springer, 1998;

15. Mansfield P. Multi-planar image formation using NMR spin echoes. **Journal of Physics C** 1977; L55-L58

16. Butts K, Riederer SJ, Ehman RL, Thompson RM, Jack CR. Interleaved echo planar imaging on a standard MRI system. **Magnetic Resonance In Medicine** 1994; **31**: 67-72.

17. Foster MA, Hutchinson JMS. Practical NMR imaging. Oxford: IRL Press, 1987;

18. Le Bihan D. Diffusion and perfusion magnetic resonance imaging : Applications to functional MRI. New York: Raven Press, 1995;

19. Taylor DG, Bore CF. A review of the magnetic-resonance response of biological tissue and its applicability to the diagnosis of cancer by NMR radiology. **Journal of Computer Assisted Tomography** 1981; **5**: 122-134.

20. Bailes DR, Young IR, Thomas DJ, Straugham K, Bydder GM, Steiner RE. NMR imaging of the brain using spin-echo sequences. **Clinical Radiology** 1982; **33**: 395-414.

21. Bryan RN, Willcott MR, Schneiders NJ, Ford JJ, Derman HS. Nuclear magnetic-resonance evaluation of stroke - A preliminary-report. **Radiology** 1983; **149**: 189-192.

22. Buonanno FS, Pykett IL, Brady TJ, et al. Proton NMR imaging in experimental ischemic infarction. **Stroke** 1983; **14**: 178-184.

23. Knight RA, Dereski MO, Helpern JA, Ordidge RJ, Chopp M. Magnetic resonance assessment of evolving focal cerebral ischemia. Comparison with histopathology in rats. **Stroke** 1994; **25**: 1252-1262.

24. Stejskal EO. Use of spin echoes in a pulsed magnetic field gradient to study anisotropic, restricted diffusion and flow. **Journal of Chemical Physics** 1965; **43**: 3597-3603.

25. Le Bihan D, Breton E, Lallemand D, Grenier P, Cabanis E, Laval-Jeantet M. Separation of diffusion and perfusion in intravoxel incoherent motion MR imaging. **Radiology** 1988; **168**: 497-505.

26. Moseley ME, Kucharczyk J, Asgari HS, Norman D. Anisotropy in diffusion-weighted MRI. **Magnetic Resonance In Medicine** 1991; **19**: 321-326.

27. Moseley ME, Cohen MS, Mintorovich J, et al. Early detection of regional cerebral ischaemia in cats: comparison of diffusion- and T2-weighted magnetic resonance imaging and spectroscopy. **Magnetic Resonance In Medicine** 1990; **14**: 330-346.

28. Benveniste H, Hedlund LW, Johnson GA. Mechanism of detection of acute cerebral ischemia in rats by diffusion-weighted magnetic resonance microscopy. **Stroke** 1992; **23**: 746-754.

29. Sevick RJ, Kanda F, Mintorovich J, et al. Cytotoxic brain edema: assessment with diffusion-weighted MR imaging. **Radiology** 1992; **185**: 687-690.

30. van der Toorn A, Sykova EDRM, Vorisek I, et al. Dynamic changes in water ADC, energy metabolism, extracellular space volume, and tortuosity in neonatal rat brain during global ischaemia. **Magnetic Resonance In Medicine** 1996; **36**: 52-60.

31. Neil JJ, Duong TQ, Ackerman JJH. Evaluation of intracellular diffusion in normal and globally ischaemic rat brain via 133-Cs NMR. **Magnetic Resonance In Medicine** 1996; **35**: 329-335.

32. Wick M, Nagatomo Y, Prielmeier F, Frahm J. Alteration of intracellular metabolite diffusion in rat brain in vivo during ischemia and reperfusion. **Stroke** 1995; **26**: 1930-1934.

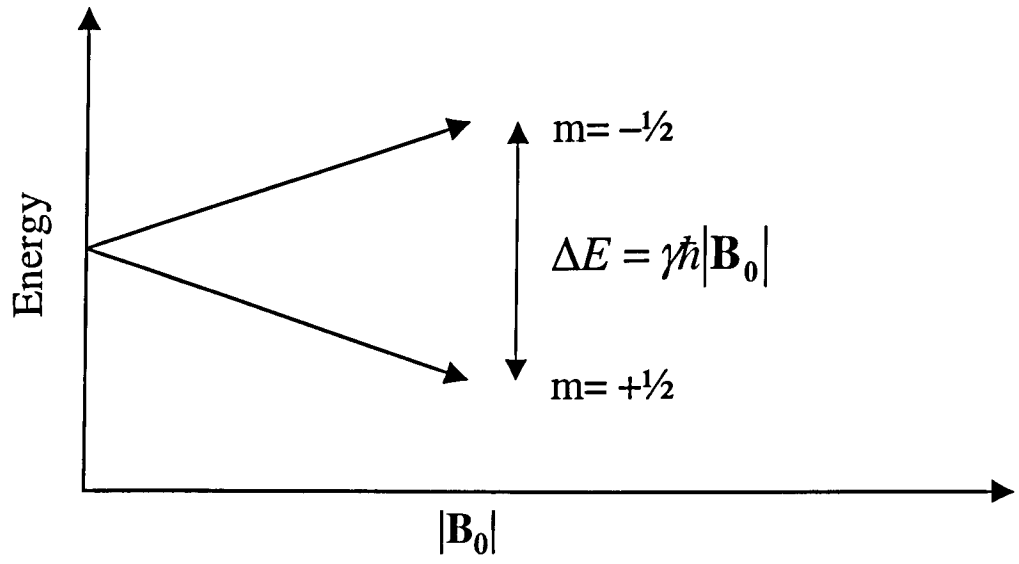

Figure 2.1 Nuclear energy levels for a nucleus with a spin quantum number of ½ (e.g. ^{1}H, ^{31}P), plotted as a function of magnetic field strength $|\mathbf{B}_0|$. The splitting of nuclear energy states by an external magnetic field is known as Zeeman splitting. The energy difference between the two Zeeman states in a spin ½ nucleus is $\gamma\hbar|\mathbf{B}_0|$. Transitions between Zeeman states can be induced by supplying photons with an energy equal to the energy difference.

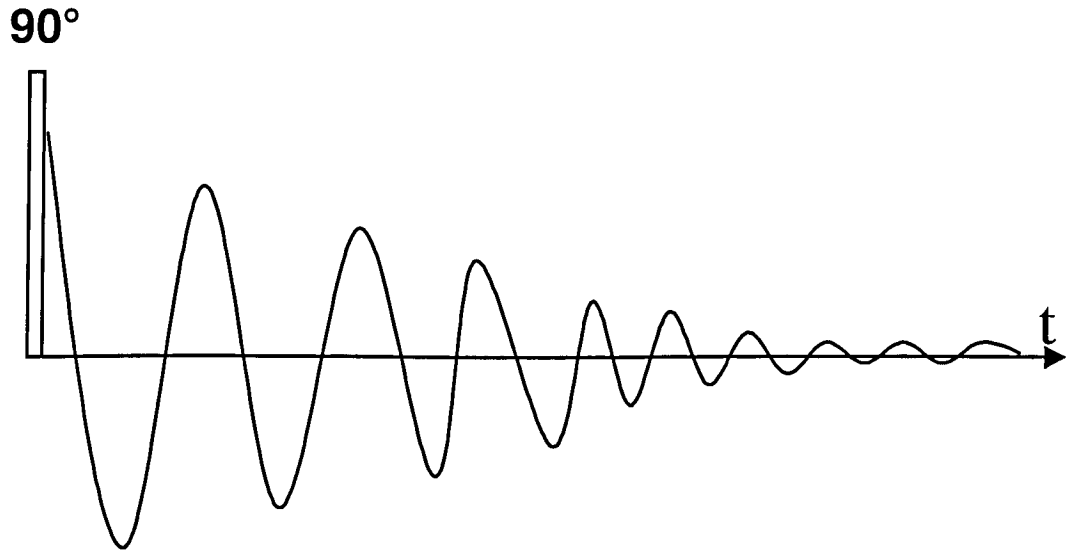

Figure 2.2 The Free Induction Decay (FID). Following a 90^0 pulse, the magnetic moment in the transverse plane can be detected by placing an RF receiver coil around the sample. The induced oscillating voltage in the coil is known as the FID. The FID oscillates at the Larmor frequency and decays exponentially with a characteristic time T_2*. N.B. The FID shown above has been demodulated (shifted down in frequency) so that it is oscillating at a only few Hertz rather than at the Larmor frequency.

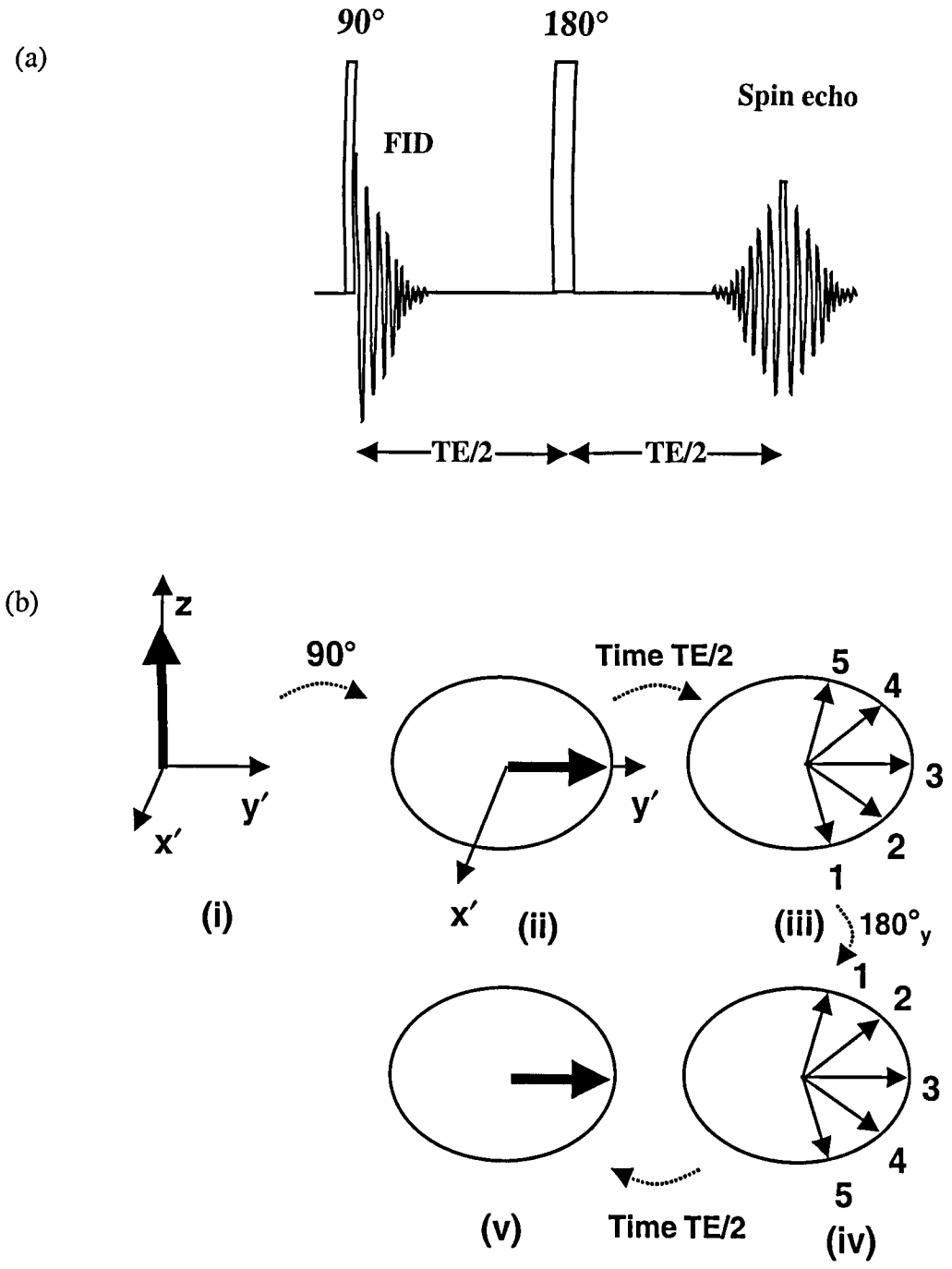

Figure 2.3 Hahn spin echo. (a) RF pulse sequence and observed signal. (b) Schematic diagram illustrating the formation of a spin echo following a 180^0 refocusing pulse.

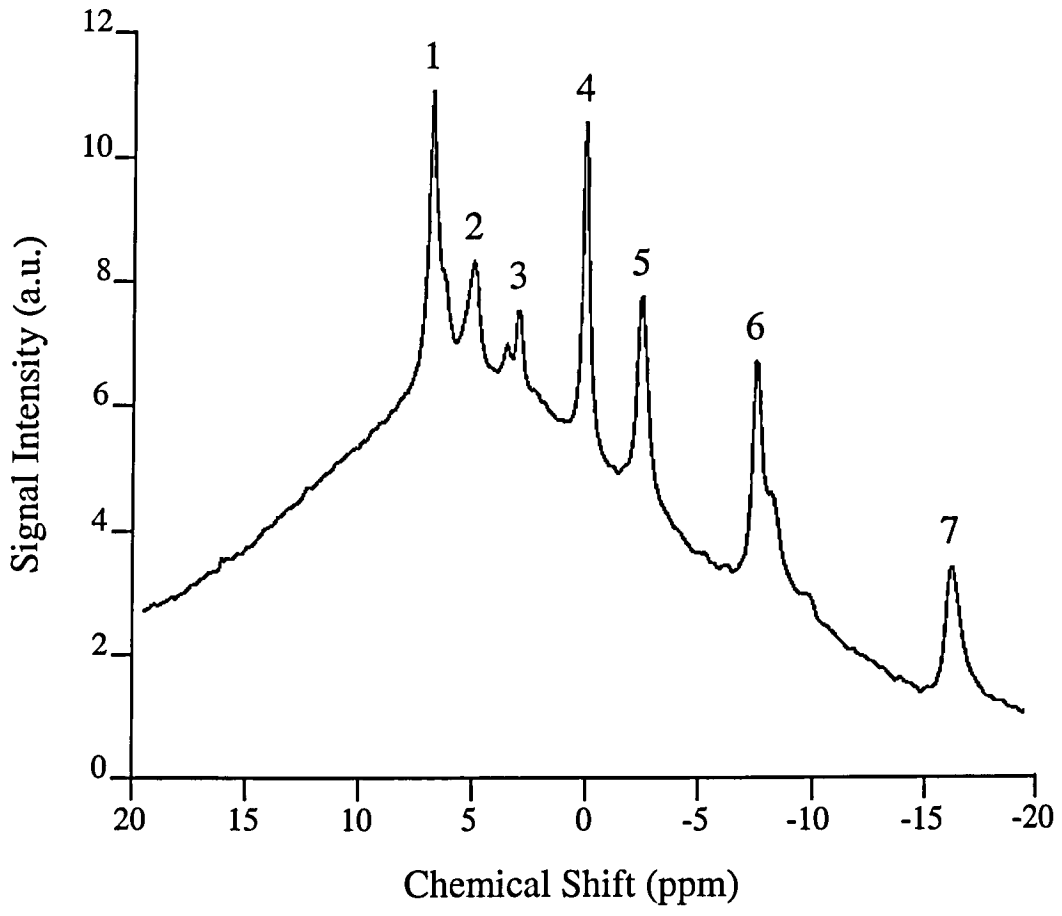

Figure 2.4 Example of a cerebral phophorus (^{31}P) spectrum obtained from a newborn piglet. Labeled peaks are as follows : (1) phosphomonoesters, (2) inorganic phosphate, (3) phosphodiesters, (4) phosphocreatine, (5) γ-nucleotide triphosphates, (6) α-nucleotide triphosphates, (7) β-nucleotide triphosphates. The broad spectral hump is due to signal from the relatively immobile phosphorus nuclei in bone and membrane phospholipids.

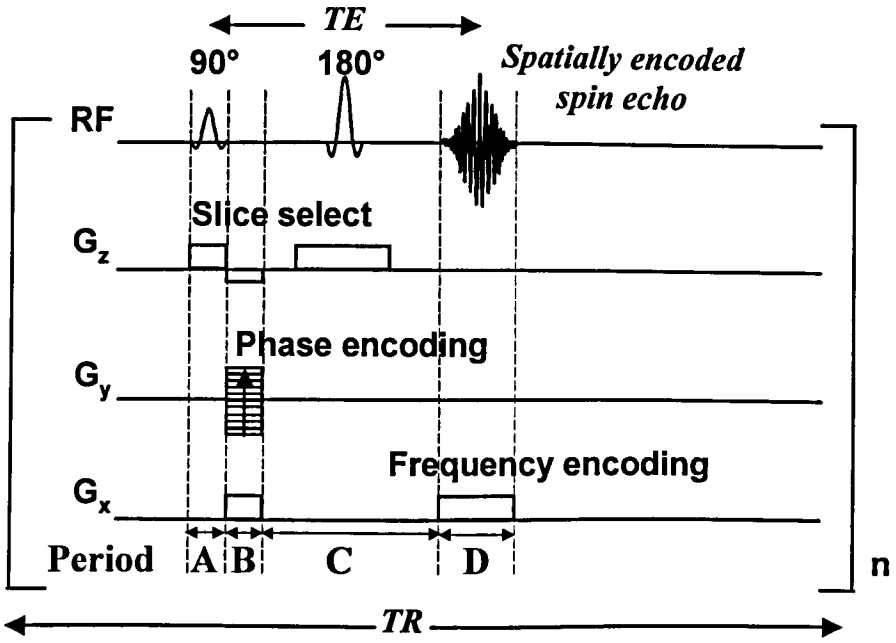

Figure 2.5 A standard spin echo 2D-FT imaging sequence. Magnetic field gradients applied along the three perpendicular directions x, y and z allow spatial encoding of the signal. The sequence is repeated for varying values of phase encoding gradien t with a repetition time of TR seconds. The resulting echoes can be reconstructed to form an image using the 2D Fourier transform.

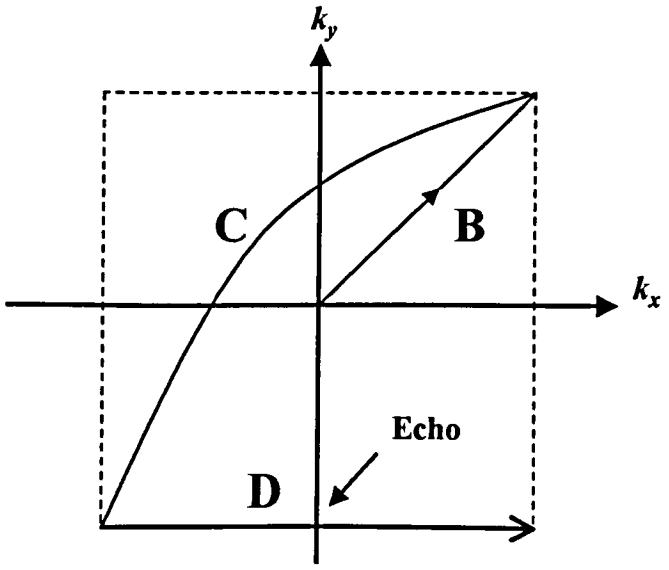

Figure 2.6 K-space trajectory of the spin echo sequence shown in figure 2.5 during one phase encoding step. The letter labels adjacent to each line refer to the corresponding period in the pulse sequence. The dash-lines illustrate a typical k-space coverage after all the phase-encoding steps have been acquired.

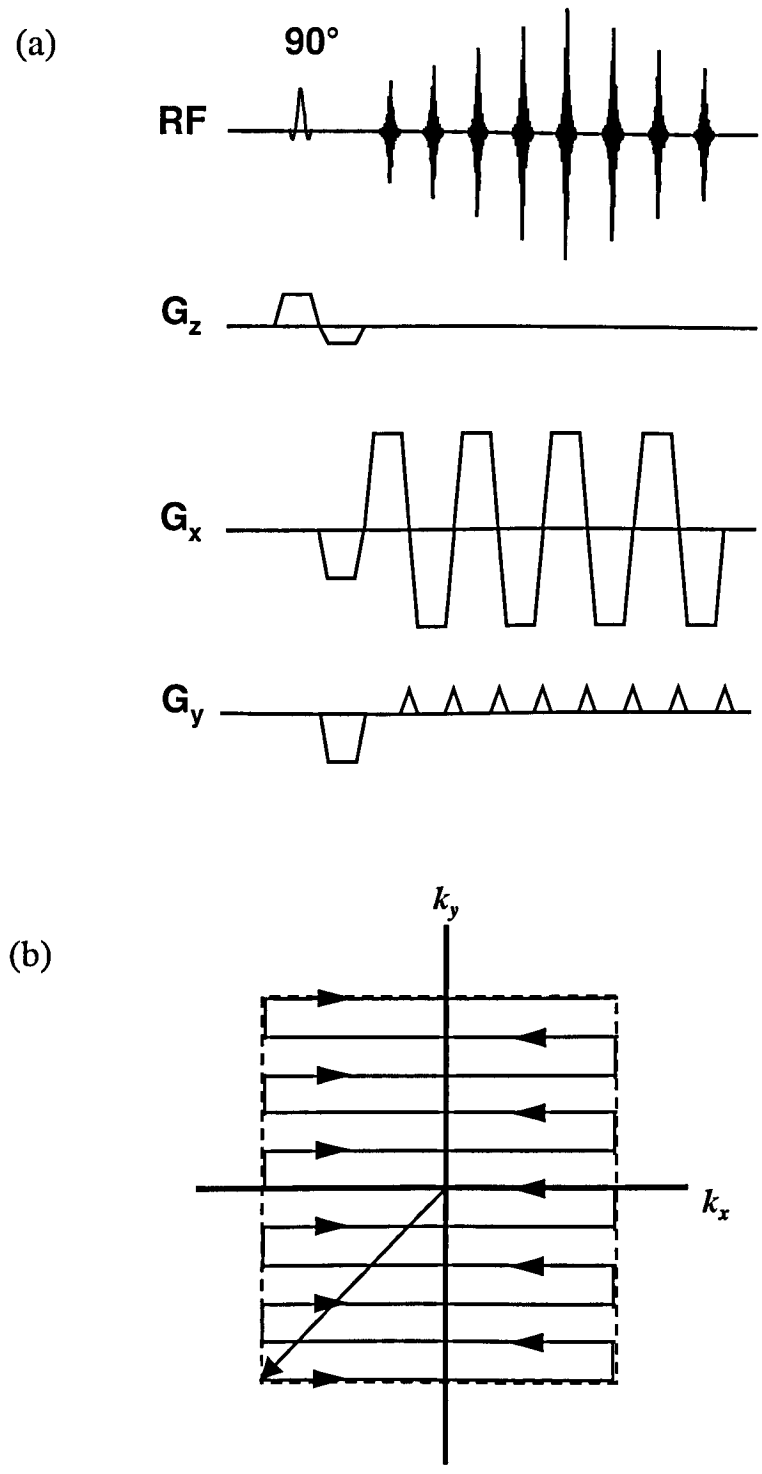

Figure 2.7 (a) Example of a blipped echo planar imaging (EPI) sequence. (b) K-space trajectory of the blipped EPI sequence shown in (a). In a blipped EPI sequence, rapid modulation of the read and phase encoding gradients following the 90^0 RF pulse enables the whole of the required k-space to be acquired in one excitation (see text).

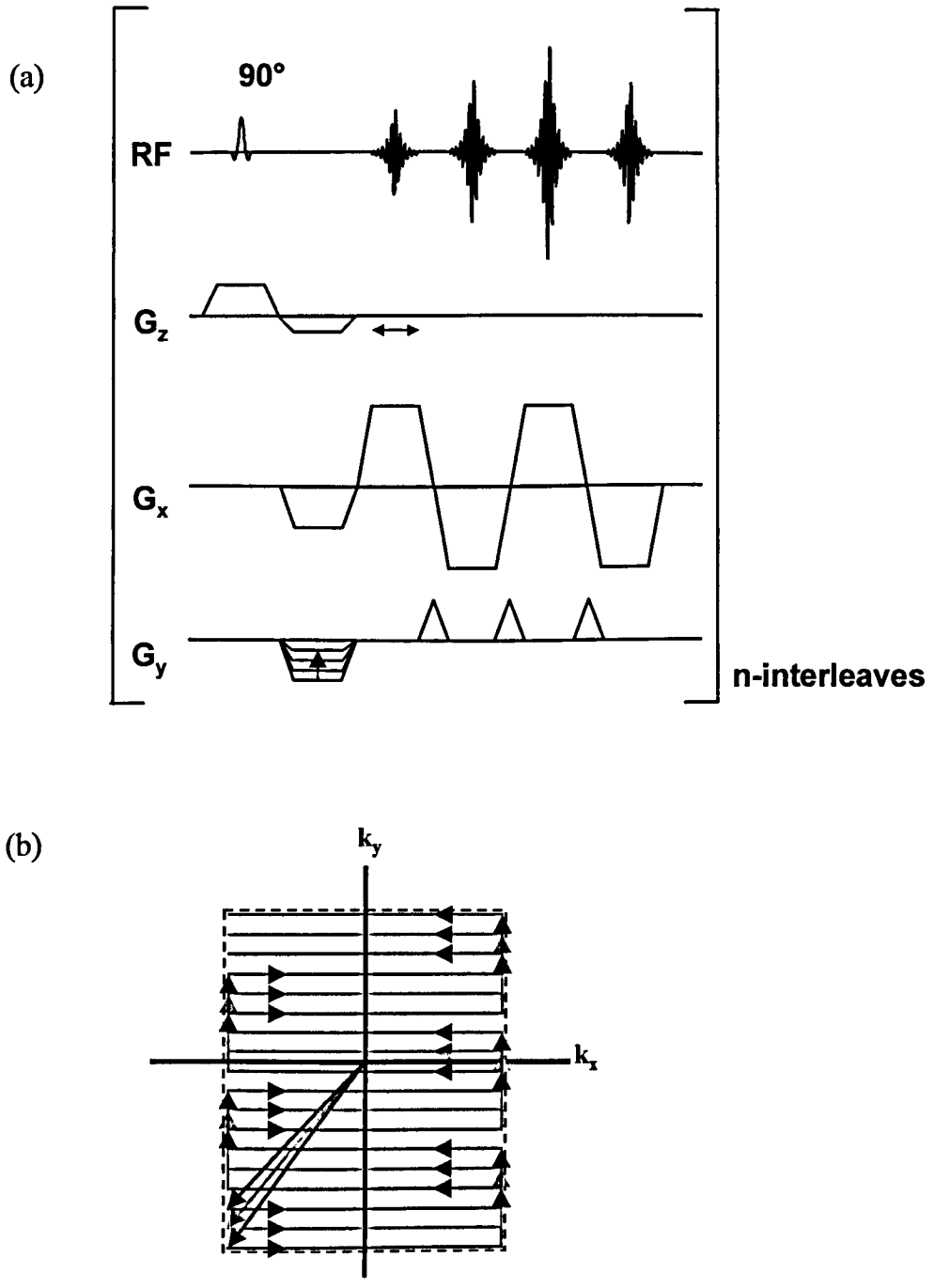

Figure 2.8 (a) Example of an interleaved echo planar imaging (EPI) sequence. (b) K-space trajectory of the interleaved EPI sequence with each phase encoding step shown as a different colour. In an interleaved EPI sequence, the modulation of the read and phase encoding gradients enables a large fraction of k-space to be acquired following each spins excitation. With a number of excitations, the whole of the k-space coverage can be completed in an interleaved fashion as shown in (b).

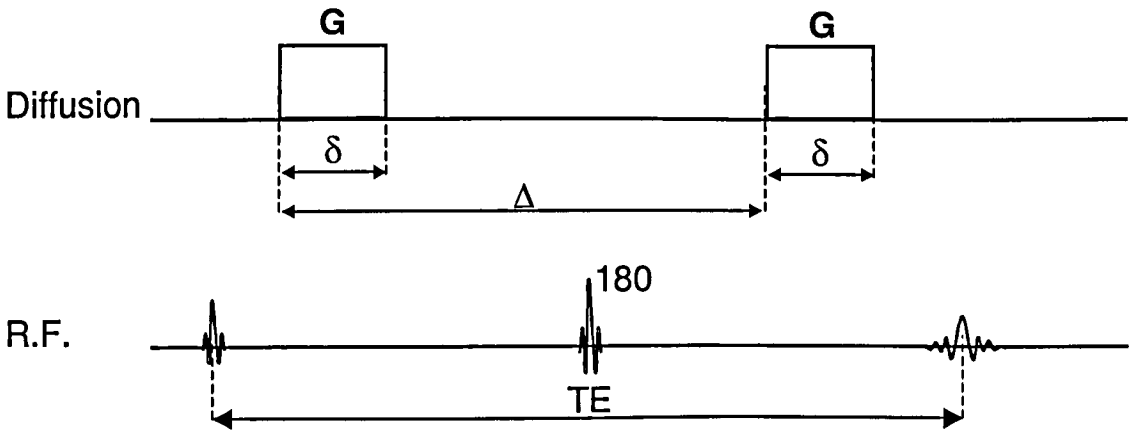

Figure 2.9 Stejskal-Tanner diffusion weighting sequence. δ is the duration of each diffusion gradient G. Δ is the period between the rising edges of the two diffusion gradients. When δ<<Δ, the diffusion time of the sequence (i.e. the time during which the diffusion effect forms) is Δ-δ/3.

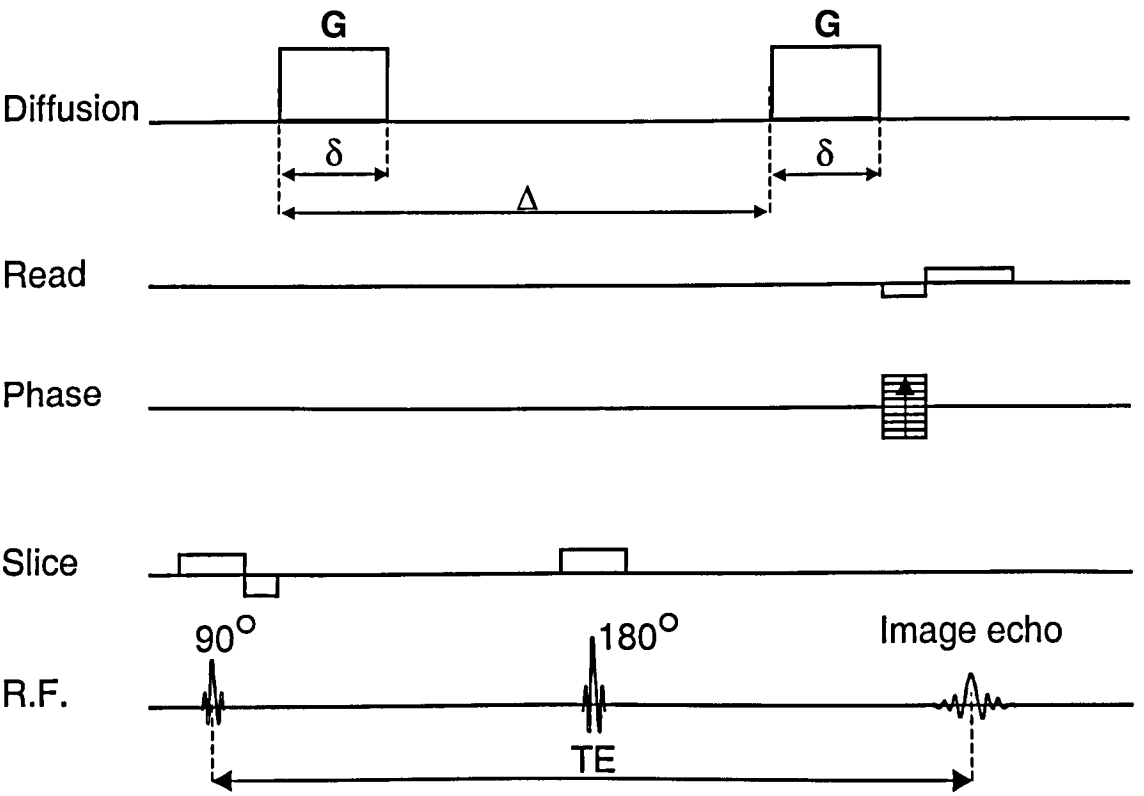

Figure 2.10 Example of a combined SE-2DFT imaging and Stejkal-Tanner diffusion weighting sequence.

3 Quantitative ADC and T_2 study in a piglet model of perinatal asphyxia

3.1 Introduction

Hypoxic-ischaemic (H-I) brain injury is recognised as the major perinatal cause of neurological morbidity in both premature and full-term infants[1]. It has been estimated that between four to eight full-term neonates per 1,000 suffer from H-I brain injury in the UK every year[2]. The aim of this work was to investigate the use of NMR techniques in the diagnoses and treatment of neonates who have suffered perinatal H-I brain injury.

Previous work performed within our group studying neonates who have suffered an acute perinatal H-I episode has shown that following an apparent initial recovery, there is a severe impairment of cerebral energy metabolism approximately 12 to 24 hours after the insult[3]. The phenomenon of an apparent recovery of cerebral energy metabolism immediately after the insult, followed by a delayed severe impairment of cerebral energy metabolism has been termed 'secondary' or 'delayed' energy failure[4]. Using phosphorus (^{31}P) and proton (^{1}H) Magnetic Resonance Spectroscopy (MRS), marked increases in cerebral concentrations of inorganic phosphates [Pi] and lactate, and reduction in phosphocreatine [PCr] and nucleotide triphosphate [NTP] concentration have been observed during 'delayed' energy failure[5]. The delayed changes in energy metabolism, especially the fall in [PCr]/[Pi], was found to correlate strongly with unfavourable long-term outcome[4]. Thus, by quantifying the delayed

changes in energetic metabolites, it was possible to provide an accurate prognosis of perinatal H-I injury within a few days of birth.

The mechanisms leading to the delayed energy failure are unclear but possibly include apoptosis[6;7], release of excito-toxic neurotransmitters[8] and cyto-toxicity caused by free radicals[9]. It has been postulated that it is the effects of the delayed phase of neuronal damage that lead to most of the mortality and morbidity associated with perinatal H-I injury. Therefore, if effective cerebro-protective intervention could be administered before the onset of delayed energy failure then the permanent brain injury with which it is associated, may be reduced or prevented altogether.

In an effort to develop effective therapies for perinatal H-I brain injury, an animal model of H-I injury was developed within the group using neonatal piglets[10]. Using ^{31}P MRS, it was shown that following a transient H-I insult, the model demonstrated a similar sequence of cerebral energy metabolism disturbances as seen in perinatally asphyxiated human neonates. The use of ^{31}P and ^{1}H MRS to monitor the neuronal damage following an H-I episode has proved to be extremely effective, but unfortunately, it has several disadvantages. Due to the low concentration of metabolites observed by MRS, the technique suffers from low signal to noise, long scanning time and poor spatial resolution. To overcome these disadvantages, we have investigated the used of Magnetic Resonance Imaging (MRI) to monitor changes in the Apparent Diffusion Coefficient (ADC)[11] and transverse relaxation time (T_2)[12] of cerebral water following H-I injury in the porcine model of birth asphyxia.

The motivation for monitoring cerebral ADC and T_2 values stem from past studies that have shown them to be effective indicators of ischaemic injury[13-15]. The ADC of cerebral tissue water has been shown to decrease significantly within minutes of the onset of an ischaemic episode[16]. The mechanisms causing the changes in ADC during and subsequent to an ischaemic event are unclear[13] but possible mechanisms include cytotoxic oedema[16], decreased extracellular space[17], restricted intracellular diffusion[18], increased tortuosity of extracellular diffusion paths[19] and temperature effects. Numerous studies of T_2 changes in ischaemic brain injury have shown that there is a significant increase in cerebral water T_2 over a period of hours and days[20]. Most of the changes in cerebral water T_2 are thought to reflect the rise in total cerebral bulk water caused by vasogenic oedema[21].

Previously, MRI studies in the porcine model of perinatal H-I injury within the group had been limited to the parietal cortex because of the use of a relatively small transmit/receive coil[11]. It is known from clinical observation that deep brain structures such as the basal ganglia and the thalami are particularly susceptible to injury in perinatal asphyxia[1]. Therefore, information from such deep structures would be of particular interest. To address this, the aim of the present study was to investigate the changes in cerebral water ADC and T_2 in the deep brain structures and to extend the findings of previous studies in the parietal cortex.

3.2 Methods

These experiments were performed under Home Office license and according to UK guidelines.

3.2.1 Animal model

Experiments were performed on 12 healthy term 'large white' piglets, aged less than 24 hours. The method described by Lorek et al.[10] was used to prepare and maintain the animals for the experiment. The animals were sedated with intramuscular midazolam (0.2mg/kg) and anaesthesia was induced with 5% isoflurane. Anaesthesia was maintained with isoflurane (1%-2%), nitrous oxide and oxygen initially via an endotracheal tube and then via a surgical tracheostomy. The carotid arteries were surgically exposed at the level of the thyroid gland and inflatable cuffs (OC2A, In Vivo Metric, Healdsburg, CA) were positioned around both common carotid arteries. Umbilical venous and arterial catheters (UVC and UAC respectively) were inserted under sterile conditions. The anaesthetised animal was positioned prone in a custom built cylindrical Perspex pod designed to fit securely in the bore of the magnet. The temperature of the animals was maintained at approximately 38.5^0C by a temperature-regulated water mattress in the pod. Their heads were restrained using a stereotatic system within the pod. Mean arterial blood pressure (MABP) and heart rate (HR) were monitored continuously via the UAC. The arterial blood gases (PaO_2, $PaCO_2$) were monitored intermittently with blood samples from the UAC and were maintained within the normal range by appropriate adjustments to the inspired oxygen concentration (FiO_2) and the ventilation

parameters. A solution containing 10% glucose and morphine (0.2mg/ml) was infused via the UVC at a rate of 60 ml/kg/day to maintain normoglycaemia and for pain relief. Antibiotics (benzylpenicillin 50mg/kg and gentamicin 25mg/kg) were administered via the UVC 12 hourly. Oxygen saturation, tympanic and rectal temperature were monitored continuously. Colloid (Gelofusine, B. Braun Medical Ltd., Emmenbrucke, Switzerland) and dopamine were infused as necessary to prevent arterial hypotension (MABP<40mmHg).

Of the 12 piglets studied, half were randomised into the sham-operated control group, whilst the other half was assigned into the experimental group where they were subjected to an H-I insult. Transient hypoxia-ischaemia was induced as previously described[10]. Briefly, the carotids arteries were clamped by inflating the carotid occluders remotely and the FiO_2 was reduced to 12% until the [NTP]/[EPP] (NTP = nucleotide triphosphate, EPP = exchangeable phosphate pool) was below approximately 30% of the baseline value for 12 to 24 minutes. The animals were resuscitated by increasing the FiO_2 to 60% and releasing the carotid occluders.

3.2.2 Data acquisition

NMR measurements were performed using a 7T Bruker Avance spectrometer system (Bruker Medical GmbH, Ettlingen, Germany). A double tuned (^{31}P and ^{1}H) 8 cm by 6 cm elliptical surface coil (with a sensitivity volume sufficient to cover the whole of the piglet brain) was used for both radio frequency transmission and reception. The coil was positioned on the intact scalp over the parietal lobes.

Fully relaxed ^{31}P spectra were obtained using a pulse acquire sequence with the following acquisitions parameters: TR=10s, spectral width 14kHz, 2048 quadrature data points. Resonance peaks were measured using a Lorentzian curve fitting procedure as described previously[10]. Following a period of stabilisation, a baseline ^{31}P spectrum was obtained from 192 summed FIDs in both the control and experimental group prior to any H-I insult. During the H-I insult in the experimental group, ^{31}P spectra from 36 summed FIDs were acquired continuously to monitor cerebral energy status. Post resuscitation in the experimental group and following baseline acquisitions in the control group, ^{31}P spectra from 384 summed FIDs were acquired at intervals of approximately every 4 hours for a period of up to 48 hours.

Following each baseline and 384 summed FIDs ^{31}P spectra acquisition, diffusion-weighted images were acquired in the coronal plane using the manufacturer's supplied diffusion-weighted STEAM (Stimulated Echo Acquisition Mode) sequence[22] shown in figure 3.1. Although the signal strength obtained from a stimulated echo is only half that obtained from a spin-echo, it was found that on the high field system used in this study (where the tissue T_1 is long and T_2 is short), the DW-STEAM sequence (with its short echo time) yielded scans that were better in terms of SNR than the conventional PGSE sequence[23]. The sequence timings were as follows: TR = 2 s, TE = 38.5 ms, TM = 186.2 ms, acquisition time 2.1 minutes per scan. The slice thickness was 2.5 mm, the FOV was 6 cm by 6 cm and the image matrix was 128 by 64. During image reconstruction the matrix was zero-filled to 128 by 128 yielding a

nominal in-plane resolution of 0.47 mm by 0.47mm. The duration (δ) and separation (Δ) of the diffusion encoding gradient pulses were 10ms and 200ms respectively. Diffusion gradient strengths of 2.3 and 25.2 mT/m were used along the x and y axes to obtain numerically calculated diffusion 'b' factors of 20 and 1000 s/mm^2 respectively. To account for the greater cross-term arising from the slice selective gradients, the diffusion gradient strengths along the z-axis were reduced to 1.8 and 24.7 mT/m so that the same diffusion 'b' factors were also obtained. Diffusion weighted imaging along the three orthogonal axes was performed after each ^{31}P MRS acquisition during baseline and up to 48 hours subsequently. Insufficient acquisition time prevented measurement of ADC data during the H-I insult. ADC maps for the three axes were calculated using a log-linear fitting procedure on a pixel-by-pixel basis.

To eliminate the confounding effects of cerebral diffusion anisotropy[13], average Apparent Diffusion Coefficients (ADC_{av}) were used in all of the diffusion data analysis. The ADC_{av} has been shown to be a good approximation of the trace of the diffusion tensor and is largely insensitive to diffusion anisotropy[24]. ADC_{av} maps were calculated by averaging the ADCs measured along the three orthogonal axes. To compare the regional variations in ADC_{av}, mean ADC_{av} from the thalamic nuclei, basal ganglia, internal capsules, periventricular white matter, parasagittal cortex and sagittal cortex were obtained using XDispUNC (D.Plummer, UCL, London, UK), a Unix based image analysis program. To aid identification of the anatomical regions of interest (ROIs), maps of a measure of 'diffusion anisotropy' were calculated as shown in equation 3.1.

$$ADC_{ani} = \frac{ADC_x - ADC_y}{ADC_x} \quad (3.1)$$

where ADC_{ani} is a simple measure of 'diffusion anisotropy', and ADC_x and ADC_y are the apparent diffusion coefficients along the x and y axes respectively.

Using the high grey-white matter contrast in the ADC_{ani} maps, the anatomical ROIs were readily identifiable by their relationship to the white matter tracts and lateral ventricles as shown in figure 3.2. To obtain a diffusion measure that was comparable with the ^{31}P MRS in terms of tissue coverage, an averaged global ADC_{av} was also calculated from the ADC_{av} maps after the CSF, scalp and bone regions were removed. The CSF was removed by eliminating all pixels above an empirically derived value of $1.2x10^{-3}$ mm^2/s. The scalp and skull regions were removed by manually defining regions with a cursor in XDispUNC.

Following the acquisition of each set of diffusion-weighted scans, T_2 measurements from the same coronal slice were obtained using the manufacture's supplied spin-echo sequence (shown in figure 3.3). The sequence timings were as follows: TR = 3 s, TE = 20 ms and 85 ms, acquisition time = 3.2 minutes per scan. Due to the poor homogeneity of the surface coil's B_1 field, the T_2-weighted images at echo times of 20 ms and 85 ms were acquired separately as two single-echo scans. The slice thickness was 2.5 mm, the FOV was 5 cm by 5 cm and the image matrix was 128 by 64, zero-filled to 128 by 128 to yield a nominal in-plane resolution of 0.4 mm by 0.4 mm. T_2 maps were

generated from the weighted images by assuming a single exponential decay and using a log-linear fitting procedure. To compare regional variations, mean T_2 values in the above-mentioned anatomical ROIs were obtained using XDispUNC. Global mean T_2 was obtained in the manner described previously for comparison with spectroscopic data. The CSF was removed from the T_2 maps by eliminating all pixels above an empirical derived value of 150ms.

3.2.3 Statistical Analysis

Data were analysed using Sigma Stat 2.00 statistical package (Jandel Scientific, San Rafael, CA). One-way Analysis Of Variance (ANOVA) was performed for each measure and where there was a statistically significant result, pair-wise comparison of all possible pairs of observations was performed using the 'Tukey' test. Unpaired t-tests were used to compare control and experimental values of [PCr]/[Pi], ADC_{av} and T_2 at baseline and various times during the experiment. The unpaired t-test was also used to investigate differences in ADC_{av} and T_2 between different ROIs at the end of the experiment. In both cases, p-values of less than 0.05 were considered to be statistically significant. The relationship between [PCr]/[Pi] and global ADC_{av} and T_2 at various observation times were investigated by calculating the Pearson's Product Moment Correlation coefficient (r) between them. Statistical significance was assumed for cases where the correlation coefficients corresponded to p-values of less than 0.05.

3.3 Results

3.3.1 Global data

Figure 3.4 and 3.5 show, respectively, the ADC_{av} and T_2 maps obtained from the control group of animals at various times during the experiments. The equivalent ADC_{av} and T_2 maps from the experimental group of animals are shown in figure 3.6 and 3.7. As can be seen most of the maps were of high quality. However, the signal to noise ratio in the ADC_{av} and particularly the T_2 maps of Control Piglet (CP) 2 and 3, and Experimental Piglet (EP) 6 was noticeably poor. Therefore, the T_2 maps from CP 2 and 3, and EP 6 were not included in the following analysis of the T_2 data. Because the ADC_{av} maps were generated by averaging three separate ADCs maps, the SNR in the ADC_{av} maps of the above-mentioned piglet were better than that seen in the T_2 maps. Therefore, only the very poor ADC_{av} maps from CP 2 and 3 were excluded from the following analysis of the ADC_{av} data.

A summary of the [PCr]/[Pi], global ADC_{av} and T_2 measurements for the control and experimental piglets at baseline and various times during the experiment are shown in tables 3.1 and 3.2 respectively. Graphical representation of the data summarised in table 3.1 and 3.2 are shown in figure 3.8 and 3.9 respectively. Of the six experimental animals studied, three (EP 3,5,6) showed severe delayed energy failure with their $min_{24\text{-}48}$ [PCr]/[Pi] (minimum [PCr]/[Pi] between 24 to 48 hours post resuscitation) all falling below 0.3. Of these three animals, the one (EP 3) that showed the most severe delayed energy failure ($min_{24\text{-}48}$ [PCr]/[Pi] <0.1) died at 24 hours post

resuscitation. Of the rest of the experimental piglets, one (EP 1) appeared to have suffered only mild delayed energy failure (min_{24-48} [PCr]/[Pi] of 0.72), whilst the other two (EP 2,4) only showed signs of moderate delayed energy failure (min_{24-48} [PCr]/[Pi] of 0.44 and 0.54) . The min_{24-48} [PCr]/[Pi] in the control group were all above 0.9.

Figure 3.10 compares the changes in mean [PCr]/[Pi], global ADC_{av} and T_2 between the experimental and control group during the course of the experiment. Time zero was defined as the start of the resuscitation process in the experimental group and as the start of the first ^{31}P spectrum acquisition following the baseline measurement in the control group.

A slight decline in mean [PCr]/[Pi] can be seen in the control group over the duration of the experiment. One-way ANOVA of the [PCr]/[Pi] data showed that this decline was statistically significant ($p=0.016$). However, a pairwise comparison of all possible pairs of observation times showed that there was no statistically significant differences in the [PCr]/[Pi] ratios observed at different times during the experiment. No significant differences in [PCr]/[Pi] between the control and experimental group was observed at baseline. During the hypoxic-ischaemic insult in the experimental group, the [PCr]/[Pi] decreased from a baseline level of 1.19 (0.11) [Mean(SD)] to 0.08(0.05) ($p<0.001$ vs control group at time zero). Upon resuscitation the [PCr]/[Pi] recovered rapidly and within approximately 4 hours post resuscitation no significant differences in [PCr]/[Pi] between the experimental and control group were seen. However, after a period of several hours, [PCr]/[Pi] started to decline again reaching a

minimum of 0.54 (0.36) at a mean measurement time of 46.3 hours. Statistical differences in [PCr]/[Pi] between the experimental and control groups were observed at approximately 18, 24, 32 and 44 hours post resuscitation.

One-way ANOVA of the global ADC_{av} and T_2 in the control group showed that there was no statistically significant differences between the global ADC_{av} and T_2 observed at different times during the experiment. No significant differences in global ADC_{av} between the control and experimental group were observed at baseline or during the period immediately following resuscitation. However, after a period of several hours following resuscitation, the global ADC_{av} in the experimental group started to decline in a similar manner to the [PCr]/[Pi]. Statistically significant differences in global ADC_{av} between the control and experimental group were observed at approximately 24, 32, and 44 hours post resuscitation. No significant differences in global T_2 between the control and experimental group were observed at any of the observation times during the experiment.

The relationship between the [PCr]/[Pi] and global ADC_{av} for each piglet in the control and experimental group is show in figure 3.11a and 3.11b respectively. No statistically significant correlation between the [PCr]/[Pi] and global ADC_{av} was found in the control group. However, a statistically significant ($p<0.001$) correlation coefficient (r) of 0.78 was observed in the experimental group. After excluding the noisy data from EP 6, the correlation coefficient (r) was found to increase to 0.86. No statistically significant correlation between the [PCr]/[Pi] and global T_2 was found in either the control or experimental group.

3.3.2 Regional Data

From figure 3.6 it can be seen that there was a general pattern of ADC_{av} reduction (darkening of the maps) in five of the experimental piglets during the course of the experiment. Whilst this general reduction was well represented by the global ADC_{av} measure shown in figure 3.9b, there were also marked variations in the time course of the ADC_{av} between different anatomical regions during experiment that were not apparent in the global measure. The variations in the time course of the ADC_{av} between different regions were most marked in the two animals that showed only moderate secondary energy failure (EP 2 and 4). In EP 2, the decline in ADC_{av} can be seen to have initiated in the basal ganglia, which then expanded slowly over the course of the experiment to affect the rest of the brain. In EP 4, a similar pattern was also observed but the decline in ADC_{av} appeared to have initiated in both the basal ganglia and parasagittal regions. In the three piglets that demonstrated severe secondary energy failure (EP 3, 5 and 6), there was an early decline in ADC_{av} in both the basal ganglia and cortical regions, which then spread rapidly throughout the rest of the brain. No obvious focal decline in ADC_{av} was seen in either the control group of animals (see figure 3.4) or the experimental piglet that showed only mild secondary energy failure (EP 1).

A summary of the ADC_{av} time course in the six anatomical ROIs for the control and experimental groups of animals is shown in table 3.3. Plots of the ADC_{av} time course in the six ROIs are shown in figure 3.12. One-way ANOVA of the ADC_{av} time courses in the control group showed that there were no significant

differences between the ADC_{av} measured at different times during the course of the experiment. The result of the unpaired t-test comparing the differences in ADC_{av} between the experimental and control groups for the various ROIs is shown in table 3.4. No significant differences in ADC_{av} between experimental and control groups were seen in any of the six ROIs at baseline and at 4 hours post-resuscitation. By 8 hours post resuscitation statistically significant differences in ADC_{av} between the experimental and control groups was seen in the basal ganglia and parasagittal cortex. By 32 hours post resuscitation, statistically significant differences in ADC_{av} between the control and experimental group were found in all but one of the anatomical ROIs. The last ROI to show a statistically significant difference in ADC_{av} between the experimental and control group was the medial cortex, at approximately 44 hours post resuscitation.

The percentage decline in ADC_{av}, from baseline, at 44 hours for the experimental group of piglets is shown in table 3.5. The largest mean percentage decline in ADC_{av} at 44 hours post resuscitation was seen in the periventricular white mater [41%(23), Mean(SD)] and parasagittal cortex [38%(20)]. The smallest decline in ADC_{av} was seen in the thalami [17%(18)] and basal ganglia [22%(21)], whilst the medial cortex and internal capsule showed intermediate decline of [33%(24)] and [30%(23)] respectively. Due to the large variation in the ADC_{av} reduction (as shown by the SD), no significant differences in ADC_{av} reduction between different anatomical ROIs was seen. However, by excluding the piglet that only showed mild secondary energy

failure (EP 1), significant differences in ADC_{av} reduction were seen between several ROIs. The results of the unpaired t-test comparing the percentage decline in ADC_{av} between the six ROIs at 44 hours are shown in table 3.6. Statistically significant differences in ADC_{av} reduction were found between the periventricular white matter ROI and the three ROIs that showed the least reduction in ADC_{av} (i.e. the thalamic nuclei, the basal ganglia and the internal capsule). Statistically significant differences in ADC_{av} reduction were also found between the ROI in the thalamic nuclei and the ROIs in the parasagittal and medial cortex.

A summary of the T_2 time course in the six anatomical ROIs for the control and experimental groups of animals is shown in table 3.7. Plots of the T_2 time course in the six ROIs are shown in figure 3.13. One-way ANOVA of the T_2 time courses in the control group showed that there were significant differences between the T_2 observed at different times during the course of the experiment in the thalamic nuclei, parasagittal cortex and medial cortex. Pairwise comparison of all possible pairs of observation times in all three ROIs showed that there was a statistically significant difference in the T_2 observed between 18 hours and baseline in the parasagittal cortex, and between 44 hours and baseline in the medial cortex. One-way ANOVA of the T_2 time courses in the experimental group showed that there were no statistically significant differences in the T_2 observed at different times during the course of the experiment in five out of the six ROIs. The ROI where the one-way ANOVA did show a statistically significant difference was in the internal capsule.

Unpaired t-test comparing the differences in T_2 between the experimental and control groups in the internal capsule showed statistically significant differences at 24 ($p<0.05$) and 32 hours ($p<0.01$) post resuscitation. No significant differences in the percentage T_2 increased between different ROIs was observed at 44 hours post resuscitation.

3.4 Discussion

From the [PCr]/[Pi] result in the experimental group it can be seen that there was a significant disturbance in the brain energy metabolism during the hypoxic-ischaemic episode. This disturbance was followed by a rapid recovery upon resuscitation and by 4 hours post resuscitation the energy metabolism appeared to have recovered completely with no significant differences seen in the [PCr]/[Pi] between the control and experimental group at this time. However, after a period of several hours the [PCr]/[Pi] was observed to have decline again and after approximately 18 hours post resuscitation, significant difference in [PCr]/[Pi] was seen between the experimental and control group. This result concurs with the findings in Lorek et al.[10], a previous study in the parietal cortex, and is consistent with the view that the H-I insult has reproduced delayed energy failure in this animal model.

With the aid of a larger surface coil, we have confirmed, and extended to the whole of the brain, previous findings in the parietal cortex showing that there was a strong correlation between the reduction in ADC_{av} and [PCr]/[Pi] during secondary energy failure. The correlation coefficient (r) obtained between the

ADC_{av} and [PCr]/[Pi] during secondary energy failure was 0.78. This is smaller than the correlation coefficient of 0.88 found in the parietal cortex previously[11] and, after a careful inspection of the global ADC_{av} data, is likely to be due to the noisy data in EP 6. From figure 3.11, it can be seen that the reduction in EP 6 global ADC_{av} with declining [PCr]/[Pi] was similar to that of the other experimental piglets. However, because the global ADC_{av} in EP 6 started at a higher value at baseline, it was nearly always higher than that of all the other global ADC_{av} at a given [PCr]/[Pi] ratio. This ADC_{av} offset was probably caused by the noisy ADC_{av} data in the deep structure of EP 6 (see figure 3.6). By excluding the noisy ADC_{av} data from EP 6, a more comparable correlation coefficient of 0.86 was obtained between the ADC_{av} and [PCr]/[Pi] ratio. The strong correlation between ADC_{av} and [PCr]/[Pi] obtained in this study further supports the view that ADC_{av} may be used as a high-resolution surrogate measure of [PCr]/[Pi] during secondary energy failure.

Marked regional variation in the ADC_{av} time course were observed in the two piglets that suffered moderate delayed energy failure (EP 2 and 4). In the three animals that demonstrated severe delayed energy failure (EP 3, 5 and 6), multiple regions in the imaging slice appeared to show a simultaneous decline in ADC_{av}. However, this apparent global decline may reflect a very rapid spread of ADC_{av} decline from a focal lesion (which was not captured by the very sparse ADC_{av} measurements performed during the experiment), rather than a true global decline. The selective early damage seen in those piglets that only suffered moderate delayed energy failure suggests that there were indeed

cerebral regions which were more prone to H-I injury than others. From the result shown in figure 3.12, it can be seen that from as early as 8 hours post resuscitation, significant differences in ADC_{av} between the control and experimental group was seen in the basal ganglia and parasagittal cortex. This is much earlier than was seen in the global measurement of either [PCr]/[Pi] or ADC_{av}, and is of considerable advantage since it allows for the possibility of a much earlier diagnosis of secondary energy failure. An earlier diagnosis of secondary energy failure should then allow earlier therapeutic intervention to be administered. Significant differences in ADC_{av} between the control and experimental group was not seen in the thalamus, internal capsule or periventricular white matter until 32 hours post resuscitation, and in the medial cortex, not until 44 hours post resuscitation. The difference in ADC_{av} time course between the parasagittal and medial cortex is consistent with the findings in a previous study[11] in the parietal cortex showing a significant earlier ADC_{av} decline in the lateral (parasagittal) grey matter than in the medial grey matter. Furthermore, the significant early ADC_{av} decline in the basal ganglia and parasagittal cortex is consistent with the clinical observation in human neonates which have shown these areas to be particularly susceptible to H-I injury[1].

At approximately 44 hours post resuscitation, the decline in ADC_{av} showed marked variations in different anatomical ROIs. Of the six anatomical ROIs analysed, the anatomical regions showing the largest percentage ADC_{av} reduction, in descending order of reduction, were as follows: periventricular

white matter, parasagittal cortex, medial cortex, internal capsule, basal ganglia and thalamic nuclei. This result is, in part, consistent with a previous study in the developing sheep brain[25] which showed that 72 hours following a transient ischaemic insult, the greatest neuronal loss was found in the parasagittal cortex. The minimum neuronal loss was found in the thalamus, whilst in the basal ganglia the degree of neuronal loss was somewhere in between the other two regions. From this result, it is clear that those ROIs that showed early decline in ADC_{av} during secondary energy failure, did not necessarily go on to show the largest decline in ADC_{av} at 44 hours post resuscitation. In particular the basal ganglia, which showed one of the earliest significant decline in ADC_{av}, demonstrated one of the smallest decline in ADC_{av} at 44 hours. The significance of this result is unclear but it may be a reflection of the different susceptibility of cells to secondary energy failure within the anatomical ROIs. For example, certain subgroups of cells in the basal ganglia may be very susceptible to secondary energy failure and thus show ADC_{av} decline very early on following resuscitation. However, if other subgroups of cells in the basal ganglia are resistant to secondary energy failure, then the overall ADC_{av} decline will not necessarily be very large. Further work using regional ADC_{av} observations with a larger experimental group, more frequent ADC_{av} observations and better methods of controlling the degree of delayed energy failure should lead to a better understanding of the susceptibility of different brain regions to transient H-I injury.

In contrast to the ADC_{av} results, very few significant T_2 changes were observed in the experimental group during the course of the experiment. No significant difference in global T_2 between the control and experimental group was observed at any observation times during the experiment. This result appears to be inconsistent with a previous study in the parietal cortex[12] which showed that there was a 30% increased in T_2 in the parietal cortex. However, because different echo times (35ms, 80ms, 120ms, 160ms) were used in the previous study, the discrepancy may have arisen because the assumption of mono-exponential T_2 decay used in the T_2 calculation, both in this and the previous study, was incorrect and that different T_2 components were being measured in the two studies. From table 3.2, it can be seen that there was a trend towards increasing global T_2 times in both EP 2 and 4 over the course of the experiment, although the rise was still very modest. In EP 5 and 3, there was a rise in global T_2 up to approximately 18 hours post resuscitation but this then started to decline again. The significance of these results is unclear at this time but it is noticeable that EP 2 and 4 were the two piglets that suffered only moderate secondary energy failure, whilst EP 3 and 5 both suffered severe secondary energy failure. Further work looking at multiple T_2 components with a larger experimental group may be helpful in elucidating the significance of these results. The lack of a significant correlation between the global T_2 and [PCr]/[Pi] in this study further supports the view that, unlike the ADC_{av}, T_2 changes during secondary energy failure does not directly reflect energy metabolism disturbances but rather its sequelae (i.e. oedema and cellular destruction).

Regional analysis of the T_2 maps showed that there was a significant T_2 increase in the internal capsule ROI in the experimental group compared to the control group. No significant T_2 increase was seen in any of the other five ROIs analysed. These results are consistent with results from previous studies in neonates showing that the earliest T_2 increases following birth asphyxia was observed in the internal capsule (<48 hours), whilst in the basal ganglia, thalamic nuclei and cerebral cortex, T_2 increases were not obvious until a week after delivery[26]. The significance of the early internal capsule T_2 changes following perinatal asphyxia is unclear but it has been suggested that it may reflect the increased susceptibility of the actively myelinating internal capsule (with its high metabolic demand) to hypoxic-ischaemic damage[27]. However, from the regional ADC_{av} data discussed previously, it would appear that the other anatomical ROIs studied were also at least as susceptible to hypoxic-ischaemic damage as the internal capsule.

Using ANOVA, a significant T_2 increase was observed in several regions of interest in the control group. The significance of this increase is unclear but it is consistent with the trend towards decreasing [PCr]/[Pi] also found in the control group and may therefore, reflect the deleterious effects of prolonged anaesthesia and intensive care support.

3.5 Conclusion

Quantitative ADC_{av} magnetic resonance imaging can provide information about H-I injury that is directly related to the cellular energy disturbances

during secondary energy failure in a fraction of the time required by ^{31}P MRS. Due to the inherently low signal to noise suffered by the ^{31}P MRS method, a high B_0 field NMR scanner is often required to acquire ^{31}P spectra in a reasonable time. In contrast, quantitative ADC_{av} MRI can be performed at standard field strength and can thus be used in the clinical environment. The spatial resolution available with MRI allows regional variation to be studied and more specific diagnosis and prognosis to be made in the clinical setting. By using quantitative ADC_{av} MRI, specific brain regions known to be susceptible to early H-I injury, rather than the whole brain, can be studied and an earlier diagnosis of secondary energy failure can be made. This should then allow therapeutic interventions to be administered to those neonates that have suffered H-I injury at the earliest stage. Although T_2 has been demonstrated to increase during secondary energy failure, its biological significance in the early stage of secondary energy failure is still unclear. Further work is necessary to assess its role in the early stage of secondary energy failure.

Measurement of ADC_{av} in neonates in the clinical setting has proven to be very difficult due to the extreme sensitivity of the DWI sequence to motion and the difficulty of keeping neonates still in the scanner over an extended period. Fast scanning techniques, such as single shot EPI, have been used to overcome the problem of motion sensitivity in adults but the high level of acoustic noise (>120dB)[28] generated in fast imaging sequences prevents them from being useful for scanning neonates. In the rest of this thesis, the novel use of selective

echo reacquisition to overcome the problem of motion sensitivity in diffusion-weighted imaging will be examined.

Reference List

1. Volpe JJ. Neurology of the newborn. Philadelphia: Saunders W.B., 1994; 279-313.

2. Wyatt J.S. Hypoxic ischaemic injury of the neonatal brain. **Fetal and Maternal Medicine Review** 1996; 95-108.

3. Hope P.L., Costello A.M.dL., Cady E.B., et al. Cerebral energy metabolism studied with phosphorus NMR spectroscopy in normal and birth-asphyxiated infants. **Lancet** 1984; 366-370.

4. Azzopardi D, Wyatt JS, Cady EB, et al. Prognosis of newborn infants with hypoxic-ischaemic brain injury assessed by phosphorous magnetic resonance spectroscopy. **Paediatric Res** 1989; 445-451.

5. Cady EB. Magnetic resonance spectroscopy in neonatal hypoxic-ischaemic insults. **Child's Nervous System** 2001; 145-149.

6. Mehmet H, Yue X, Squier MV, et al. Increased apoptosis in the cingulate sulcus of newborn piglets following transient hypoxic-ischaemia is related to the degree of high energy phosphate depletion during the insult. **Neurosci-lett** 1994; 121-125.

7. Edwards AD, Yue X, Squier MV, et al. Specific inhibition of apoptosis after cerebral hypoxic-ischaemia by moderate post-insult hypothermia. **Biochem.Biophys.Res.Commun.** 1995; 1193-1199.

8. Marret S, Gressens P, Gadisseux J-F, Evrard P. Prevention by magnesium of excitotoxic neuronal death in the developing brain: an animal model for clinical intervention studies. **Dev.Med.Child.Neurol.** 1995; 473-484.

9. Thordstein M, Bagenholm R, Thiringer K, Kjellmar I. Scavengers of free oxygen radicals with magnesium ameliorate perintal hypoxic-ischemic brain damage in the rat. **Paediatric Res** 1993; 23-26.

10. Lorek A, Takei Y, Cady EB, et al. Delayed ("secondary") energy failure after acute hypoxia-ischaemia in the new-born piglet : continuous 48 hours studied by phosphorous magnetic resonance spectroscopy. **Paediatric Res** 1994; 699-706.

11. Thornton JS, Ordidge RJ, Penrice J, et al. Temporal and anatomical variations of brain water apparent diffusion coefficient in perinatal cerebral hypoxic-ischemic injury: relationships to cerebral energy metabolism. **Magnetic Resonance In Medicine** 1998; 39: 920-927.

12. Punwani, S. The use of quantitative magnetic resonance imaging in perinatal brain injury. 57-71. 1997. University College London.

13. Baird AE, Warach S. Magnetic resonance imaging of acute stroke. **Journal Of Cerebral Blood Flow And Metabolism** 1998; **18**: 583-609.

14. Hoehn-Berlage M. Diffusion-weighted NMR imaging: Application to Experimental Focal Ischaemia. **NMR In Biomedicine** 1995; **8**: 345-358.

15. Hoehn-Berlage M, Eis M, Back T, Kohno K, Yamashita K. Changes of relaxation times (T_1, T_2) and apparent diffusion coefficient after permanent middle cerebral artery occlusion in the rat: temporal evolution, regional extent, and comparison with histology. **Magnetic Resonance In Medicine** 1995; **34**: 824-834.

16. Moseley ME, Cohen MS, Mintorovich J, et al. Early detection of regional cerebral ischaemia in cats: comparison of diffusion- and T_2-weighted magnetic resonance imaging and spectroscopy. **Magnetic Resonance In Medicine** 1990; **14**: 330-346.

17. Hasegawa Y, Formato JE, Latour LL, et al. Severe transient hypoglycemia causes reversible change in the apparent diffusion coefficient of water. **Stroke** 1996; **27**: 1648-1656.

18. Neil JJ, Duong TQ, Ackerman JJH. Evaluation of intracellular diffusion in normal and globally ischaemic rat brain via 133-Cs NMR. **Magnetic Resonance In Medicine** 1996; **35**: 329-335.

19. Nicholson C. Diffusion of ions and micromolecules in the brain. In: SMRM, ed. Workshop Book of Abstracts, Berkley: Society of Magnetic Resonance in Medicine, 1993: 1-7.

20. Quast MJ, Huang NC, Hillman GR, Kent TA. The evolution of acute stroke recorded by multimodal magnetic resonance imaging. **Magnetic Resonance Imaging** 1993; **11**: 465-471.

21. Kato H, Kogure K, Ohtomo H, et al. Characterization of experimental ischemic brain edema utilizing proton nuclear magnetic resonance imaging. **Journal Of Cerebral Blood Flow And Metabolism** 1986; 212-221.

22. Merboldt K-D, Hanicke W, Frahm J. Diffusion imaging using stimulated echoes. **Magnetic Resonance In Medicine** 1991; **19**: 233-239.

23. Stejskal EO, Tanner JE. Spin diffusion measurements: spin echoes in the presence of a time dependent field gradient. **Journal of Chemical Physics** 1965; **42**: 288-292.

24. Basser PJ, Mattiello D, Le Bihan D. MR diffusion tensor spectroscopy and imaging. **Biophysical Journal** 1994; **66**: 259-267.

25. Williams CE, Gunn AJ, Mallard C, Gluckman PD. Outcome after ischemia in the developing sheep brain : an electroencephalographic and histological study. **Annals of Neurology** 1992; 14-21.

26. Rutherford, M. A., Pennock, J. M., Schweiso, J. E., Cowan, F. M., and Dubowitz, L. M. S. Hypoxic-ischaemic encephalopathy: early and late magnetic resonance imaging findings in relation to outcome. Archives of Disease in Childhood (75), F145-F151. 1996.

27. Rutherford, M. A., Pennock, J. M., Counsell, S. J., Mercuri, E., Cowan, F. M., Dubowitz, L. M. S., and Edwards, A. D. Abnormal magnetic resonance signal in the internal capsule predicts poor neurodevelopmental outcome in Infants with hypoxic-ischemic encephalopathy. Pediatrics 102(2), 323-328. 1998.

28. Foster, J. R., Hall, D. A., Summerfield, A. Q., Palmer, A. R., and Bowtell, R. W. Sound level measurements and calculations of safe noise dosage during EPI at 3T. Journal of Magnetic Resonance Imaging (12), 157-163. 2000.

(a)

	[PCr]/[Pi]						
Time (h)	CP 1	CP 2	CP 3	CP 4	CP 5	CP 6	Mean (SD)
Baseline	1.52	1.57	1.28	1.25	1.39	1.09	1.35(0.18)
0.0 - 0.0	1.22	1.69	1.70	1.17	1.18	1.34	1.38(0.25)
2.2 - 5.5	1.17	1.58	1.57	1.20	1.40	1.47	1.40(0.18)
6.2 - 9.6	1.23	1.82	1.66	1.21	1.14	1.39	1.41(0.28)
11.9 - 13.6	1.22	1.61	1.59	1.21	1.05	1.18	1.31(0.23)
16.7 - 18.9	1.14	1.78	1.47	1.04	0.95	1.08	1.24(0.32)
22.9 - 24.4	1.30	1.60	1.36	1.08	0.93	1.09	1.23(0.24)
30.6 - 32.7	1.14	1.80	1.45	1.03	1.07	1.17	1.28(0.30)
41.0 - 46.0	1.11	1.50	1.23	1.01	1.12	1.10	1.18(0.17)
$Min_{24\text{-}48}$ [PCr]/[Pi]	1.08	1.50	1.23	1.01	0.93	1.10	1.14(0.20)

(b)

	Global ADC_{av} (10^{-3} mm^2/s)				
Time (h)	CP 1	CP 4	CP 5	CP 6	Mean (SD)
Baseline	0.83	0.87	0.85	0.96	0.89(0.05)
1.5 - 2.5	0.83	0.89	0.90	0.94	0.89(0.04)
4.0 - 5.4	0.81	0.90	0.83	0.95	0.88(0.06)
7.0 - 8.1	0.81	0.91	0.84	0.91	0.88(0.06)
10.8 - 12.3	0.84	0.91	0.87	0.94	0.89(0.04)
16.7 - 20.3	0.85	0.93	0.89	0.92	0.90(0.04)
22.4 - 25.5	0.83	0.93	0.87	0.90	0.87(0.04)
30.9 - 33.0	0.86	0.95	0.92	0.92	0.89(0.04)
38.5 - 45.2	0.85	0.93	*	0.94	0.90(0.05)

(c)

	Global T_2 (ms)				
Time (h)	CP 1	CP 4	CP 5	CP 6	Mean (SD)
Baseline	63.9	67.6	61.8	63.0	64.2(1.9)
1.2 - 1.9	65.3	70.6	61.4	62.3	65.4(3.6)
3.7 - 4.7	*	69.3	63.3	59.1	64.8(3.9)
7.0 - 9.2	64.8	69.4	62.6	61.0	66.3(4.5)
10.7 - 13.9	66.6	73.4	63.2	59.7	67.9(6.8)
16.5 - 19.9	68.7	64.9	64.0	62.6	68.5(5.2)
22.9 - 28.5	66.5	67.9	65.7	59.9	63.2(5.2)
31.8 - 33.8	67.2	69.0	65.5	62.7	66.2(2.3)
40.3 - 44.4	69.9	72.1	63.3	64.7	67.6(3.9)

Table 3.1 Individual and averaged (a) [PCr]/[Pi], (b) global ADC_{av} and (c) global T_2 in the control animals observed at baseline and various times during the experiment. $Min_{24\text{-}48}$ [PCr]/[Pi] is the minimum [PCr]/[Pi] between 24 and 48 h post resuscitation. T_2 and ADC_{av} data from CP 2 and 3 have not been included due to poor scan quality from those animals. * Scan not acquired during experiment.

(a)

	[PCr]/[Pi]						
Time (h)	EP 1	EP 2	EP 3	EP 4	EP 5	EP 6	Mean (SD)
Baseline	1.11	1.27	1.22	1.36	1.07	1.11	1.19(0.11)
0	0.04	0.15	0.08	0.05	0.03	0.15	0.08(0.05)
2.8 - 5.0	0.67	1.34	1.30	1.37	1.14	1.04	1.14(0.26)
6.9 - 9.1	1.02	1.37	1.31	1.29	0.70	0.79	1.08(0.29)
10.1 - 15.2	0.88	1.53	1.12	1.23	0.40	0.55	0.95(0.43)
16.9 - 19.5	0.83	1.23	0.66	1.17	0.28	0.43	0.77(0.39)
22.9 - 25.9	1.17	1.07	0.08	0.91	0.32	0.36	0.65(0.45)
28.6 - 33.3	1.14	0.92	*	0.58	0.16	0.36	0.63(0.40)
45.0 - 47.7	1.10	0.58	*	0.45	0.12	0.45	0.54(0.36)
$Min_{24\text{-}48}$ [PCr]/[Pi]	0.72	0.54	0.08	0.44	0.12	0.26	0.36(0.25)

(b)

	Global ADC_{av} (10^{-3} mm^2/s)						
Time (h)	EP 1	EP 2	EP 3	EP 4	EP 5	EP 6	Mean (SD)
Baseline	0.80	0.89	0.87	0.91	0.94	0.97	0.90(0.06)
1.5 - 2.5	0.80	0.88	0.84	0.87	0.89	0.96	0.87(0.05)
3.9 - 5.3	0.80	0.84	0.85	0.89	0.87	0.94	0.87(0.05)
7.0 - 8.7	0.79	0.84	0.78	0.89	0.79	0.88	0.83(0.05)
10.9 - 12.6	0.80	0.84	0.80	0.92	0.66	0.81	0.81(0.09)
17.1 - 20.5	0.80	0.79	0.54	0.90	0.64	0.79	0.74(0.13)
21.2 - 24.7	0.80	0.79	*	0.85	0.60	0.73	0.76(0.10)
27.1 - 32.3	0.81	0.76	*	0.71	0.50	0.73	0.70(0.12)
44.2 - 46.3	0.84	0.66	*	0.66	0.53	0.68	0.67(0.11)

(c)

	Global T_2 (ms)					
Time(h)	EP 1	EP 2	EP 3	EP 4	EP 5	Mean (SD)
Baseline	66.0	63.1	62.5	67.4	60.7	63.5(2.7)
3.4 - 4.3	65.1	62.9	66.6	66.6	59.8	64.3(2.6)
5.8 - 9.1	64.8	63.3	66.0	68.0	62.1	65.0(2.1)
11.1 - 11.8	65.6	66.7	66.0	67.8	68.0	67.3(1.4)
15.2 - 19.1	66.0	66.6	65.7	66.0	69.3	66.7(1.3)
21.0 - 24.7	66.3	65.5	61.6	67.5	68.7	67.3(4.2)
30.1 - 32.0	66.5	69.5	*	70.2	66.4	71.3(7.3)
41.5 - 42.8	66.6	70.5	*	74.0	62.9	71.9(8.7)

Table 3.2 Individual and averaged (a) [PCr]/[Pi], (b) global ADC_{av} and (c) global T_2 in the experimental animals observed at baseline and various times during the experiment. $Min_{24\text{-}48}$ [PCr]/[Pi] is the minimum [PCr]/[Pi] between 24 and 48 h post resuscitation. *Exp 3 died at 24 hours post resuscitation. T_2 data from EP 6 were not included due to poor scans quality.

(a)

Time (h)	Mean (SD) ADC_{av} (10^{-3} mm^2/s)					
	Basal Ganglia	Thalamus	Internal Capsule	Peri-ventricular WM	Para-sagittal cortex	Medial Cortex
Baseline	0.89(0.06)	0.83(0.10)	0.76(0.07)	0.89(0.06)	0.88(0.00)	0.89(0.04)
4.1 - 5.1	0.85(0.06)	0.84(0.15)	0.75(0.09)	0.83(0.06)	0.85(0.07)	0.85(0.05)
7.2 - 7.8	0.85(0.06)	0.81(0.11)	0.72(0.09)	0.86(0.06)	0.90(0.02)	0.87(0.02)
10.8 - 11.6	0.88(0.04)	0.84(0.10)	0.75(0.05)	0.84(0.04)	0.88(0.04)	0.84(0.04)
16.7 - 20.3	0.90(0.05)	0.88(0.11)	0.78(0.08)	0.87(0.05)	0.90(0.02)	0.86(0.03)
22.4 - 25.0	0.87(0.03)	0.85(0.08)	0.74(0.05)	0.87(0.07)	0.90(0.03)	0.88(0.04)
30.9 - 32.9	0.92(0.04)	0.92(0.07)	0.81(0.07)	0.86(0.05)	0.90(0.03)	0.90(0.04)
38.5 - 44.4	0.90(0.05)	0.94(0.13)	0.77(0.11)	0.87(0.06)	0.89(0.02)	0.92(0.06)

(b)

Time (h)	Mean (SD) ADC_{av} (10^{-3} mm^2/s)					
	Basal Ganglia	Thalamus	Internal Capsule	Peri-ventricular WM	Para-sagittal cortex	Medial Cortex
Baseline	0.87(0.05)	0.86(0.06)	0.78(0.07)	0.86(0.04)	0.86(0.03)	0.89(0.04)
3.9 - 5.3	0.81(0.03)	0.83(0.08)	0.74(0.07)	0.82(0.04)	0.81(0.05)	0.84(0.05)
7.0 - 8.7	0.76(0.05)	0.80(0.10)	0.68(0.10)	0.75(0.13)	0.75(0.10)	0.81(0.06)
10.9 - 12.6	0.77(0.08)	0.80(0.10)	0.66(0.13)	0.72(0.18)	0.69(0.17)	0.75(0.14)
17.1 - 20.5	0.68(0.15)	0.72(0.21)	0.56(0.18)	0.65(0.20)	0.65(0.22)	0.70(0.18)
21.2 - 24.6	0.67(0.11)	0.72(0.17)	0.56(0.14)	0.67(0.17)	0.68(0.19)	0.73(0.17)
29.7 - 32.3	0.65(0.15)	0.70(0.15)	0.54(0.15)	0.56(0.18)	0.63(0.21)	0.67(0.21)
44.2 - 46.3	0.67(0.16)	0.72(0.15)	0.55(0.16)	0.51(0.19)	0.53(0.16)	0.60(0.20)

Table 3.3 Summary of ADC_{av} values observed in the six anatomical ROIs in the control (a) and experimental (b) groups of animals at baseline and various times during the experiment.

Time (h)	p-values					
	Basal Ganglia	Thalamus	Internal Capsule	Peri-ventricular WM	Para-sagittal cortex	Medial Cortex
Baseline	0.64	0.67	0.71	0.43	0.21	0.94
3.9 - 5.3	0.18	0.89	0.92	0.95	0.28	0.67
7.0 – 8.7	**0.05**	0.85	0.50	0.13	**0.02**	0.07
10.8 – 12.6	**0.04**	0.60	0.25	0.21	0.07	0.26
16.7 - 20.5	**0.02**	0.20	0.06	0.07	0.06	0.14
21.2 - 25.0	**0.01**	0.19	0.05	0.07	**0.05**	0.12
29.7 - 32.9	**0.01**	**0.03**	**0.01**	**0.01**	**0.04**	0.07
38.5 - 46.3	0.06	0.07	0.09	**0.02**	**0.01**	**0.04**

Table 3.4 p-values of two tailed unpaired t-tests comparing the differences in ADC_{av} between experimental and control groups in the various anatomical regions of interest.

EP	Percentage change in ADC_{av} from baseline					
	Basal Ganglia	Thalamus	Internal Capsule	Peri-ventricular WM	Para-sagittal cortex	Medial Cortex
1	12	12	9	-1	-5	8
2	-29	-16	-42	-58	-42	-40
4	-18	-23	-28	-43	-46	-35
5	-45	-37	-44	-51	-58	-57
6	-31	-22	-44	-54	-40	-40
Mean (SD)*	-22(21)	-17(18)	-30(23)	-41(23)	-38(20)	-33(24)
Mean (SD)#	-31(11)	-25(9)	-39(8)	-52(6)	-46(8)	-43(10)

Table 3.5 Percentage decline in ADC_{av} from baseline at 44 hours in the six anatomical regions of interest in the experimental group of piglets. * Mean percentage decline in all five piglets. # Mean percentage decline in the four piglets that showed moderate to severe secondary energy failure (EP 2, 4-6).

	Basal Ganglia	Thalamic Nuclei	Internal Capsule	Peri-ventricular W.M.	Parasagittal cortex	Medial Cortex
Basal Ganglia	-	0.416	0.271	**0.018**	0.068	0.157
Thalamic Nuclei	0.416	-	0.051	**0.003**	**0.012**	**0.034**
Internal Capsule	0.271	0.051	-	**0.048**	0.256	0.568
Peri-ventricular W.M.	**0.018**	**0.003**	**0.048**	-	0.343	0.195
Parasagittal cortex	0.068	**0.012**	0.256	0.343	-	0.628
Medial Cortex	0.157	**0.034**	0.568	0.195	0.628	-

Table 3.6. p-values of two tailed unpaired t-tests comparing percentage decline in ADC_{av} between different anatomical regions of interest at 44 hours following resuscitation from an H-I insult.

(a)

Time (h)	Mean (SD) T_2 (ms)					
	Basal Ganglia	Thalamus	Internal Capsule	Peri-ventricular WM	Para-sagittal cortex	Medial Cortex
Baseline	60.1(1.3)	55.8(3.9)	45.5(2.7)	56.9(1.2)	58.5(1.7)	59.7(3.5)
3.7 - 4.7	60.1(2.3)	55.8(5.3)	47.1(3.5)	57.6(2.6)	58.0(4.9)	61.6(5.4)
7.0 - 8.2	58.9(2.8)	55.2(5.1)	45.6(3.4)	55.7(2.0)	59.4(2.7)	61.5(2.3)
10.7 - 13.9	62.9(7.2)	58.3(9.0)	47.7(6.2)	60.3(6.4)	63.4(7.0)	64.8(7.3)
16.5 - 19.9	64.9(3.5)	60.5(6.6)	49.0(5.8)	59.8(4.8)	64.3(6.6)	64.6(5.5)
22.9 - 28.5	61.4(4.1)	58.1(3.9)	46.2(2.1)	58.3(3.0)	61.3(5.1)	64.8(3.8)
31.8 - 33.8	61.0(3.7)	58.8(2.3)	46.2(2.9)	57.8(1.7)	61.3(4.6)	66.6(3.4)
40.9 - 44.4	61.9(3.0)	59.6(4.5)	47.5(3.8)	59.3(1.7)	62.8(4.4)	68.6(5.1)

(b)

Time (h)	Mean (SD) T_2 (ms)					
	Basal Ganglia	Thalamus	Internal Capsule	Peri-ventricular WM	Para-sagittal cortex	Medial Cortex
Baseline	62.3(2.2)	58.6(6.0)	47.4(5.6)	60.6(4.4)	58.9(5.5)	61.5(3.2)
3.4 - 4.3	63.6(3.8)	59.9(4.8)	47.7(3.5)	60.7(3.7)	60.9(2.7)	61.3(3.3)
5.8 - 9.1	65.0(4.1)	62.4(3.2)	48.7(3.3)	61.2(2.7)	61.8(3.4)	62.9(3.0)
11.1 - 11.8	67.5(4.2)	63.8(3.3)	50.9(2.4)	63.1(3.5)	63.8(6.0)	65.0(3.3)
15.2 - 19.1	69.1(6.2)	63.8(5.0)	53.4(2.6)	61.6(3.4)	65.0(8.4)	65.8(6.7)
21.3 - 24.7	68.9(6.0)	63.0(3.7)	54.7(2.4)	60.5(3.8)	63.7(9.8)	64.2(7.7)
30.1 - 32.0	68.5(11.3)	62.5(6.4)	56.1(7.5)	62.9(3.6)	68.2(7.8)	67.6(6.0)
41.5 - 42.8	69.5(9.3)	63.5(6.1)	56.7(8.6)	64.8(5.6)	68.3(9.4)	69.5(8.2)

Table 3.7 Summary of T_2 values observed in the six anatomical ROIs in the control (a) and experimental (b) groups of animals at baseline and various times during the experiment.

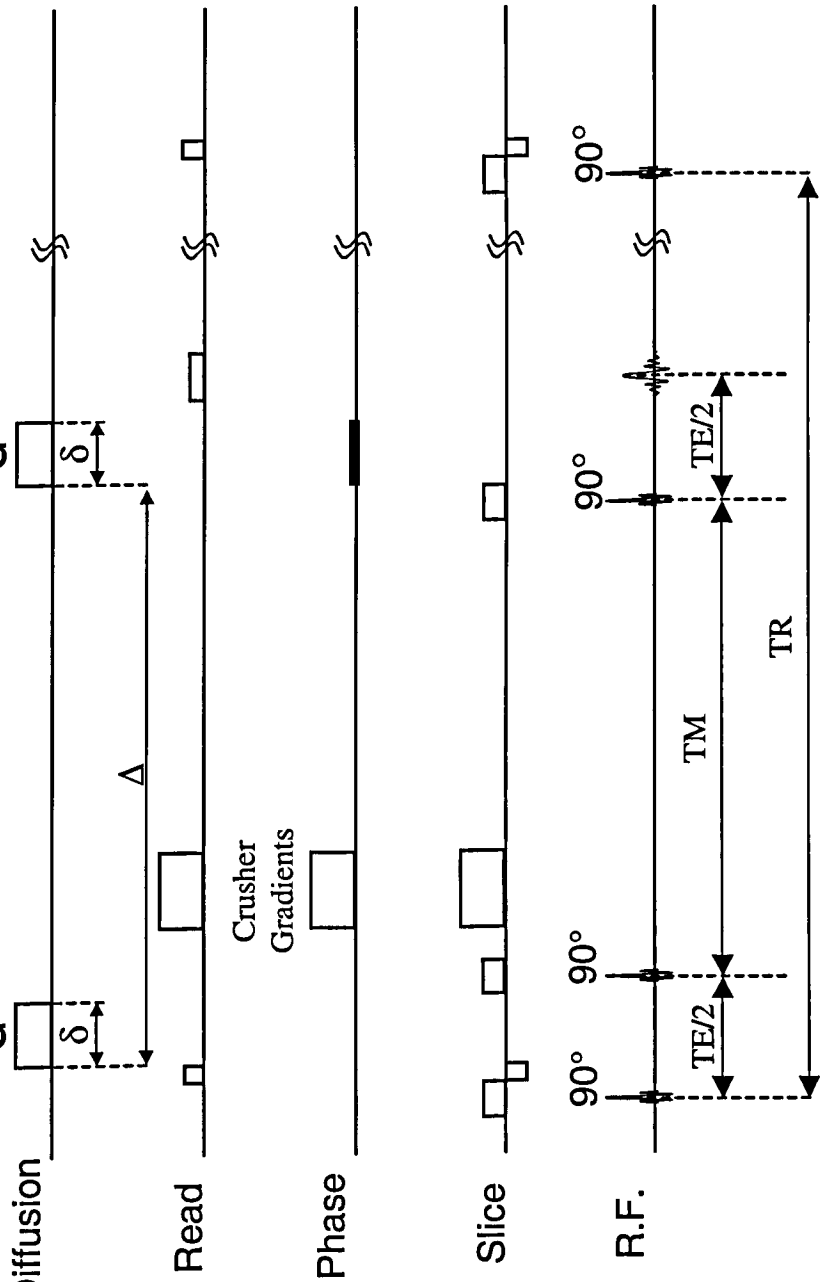

Figure 3.1 Schematic diagram of the manufacturer's supplied diffusion-weighted STEAM (Stimulated Echo Acquisition Mode) sequence used in study of the piglet model of perinatal asphyxia. The sequence timings were set as follows: δ=10ms, Δ=200ms, TM=186.2ms, TE=38.5ms, TR=2s.

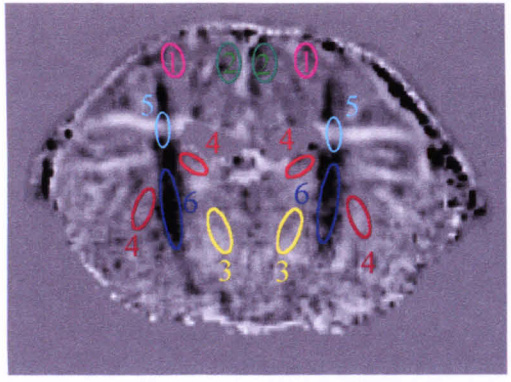

ADC_{ani} Map

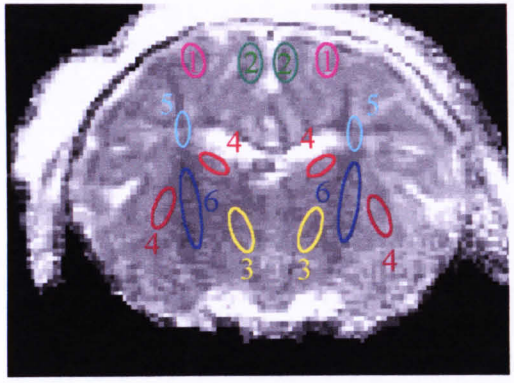

ADC_{av} Map

Keys:

① Parasagittal Cortex
② Sagittal Cortex
③ Thalamic nuclei
④ Caudate Nucleus
④ Lenticular Nucleus
} Basal Ganglia
⑤ Periventricular WM
⑥ Internal Capsule

Figure 3.2. Positions of the anatomical regions of interest on the schematic diagram, ADC_{ani} and ADC_{av} map of the neonatal piglet brain.

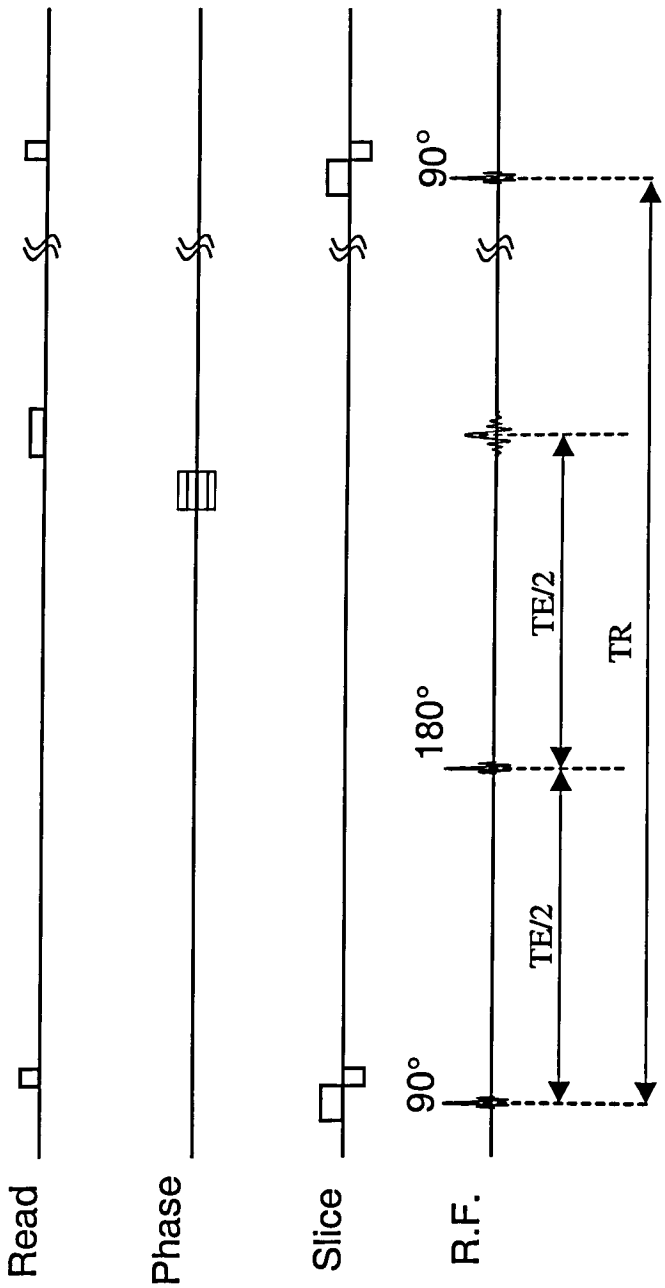

Figure 3.3 Schematic diagram of the manufacturer's supplied spin-echo sequence used in the T_2 study of the piglet model of perinatal asphyxia.

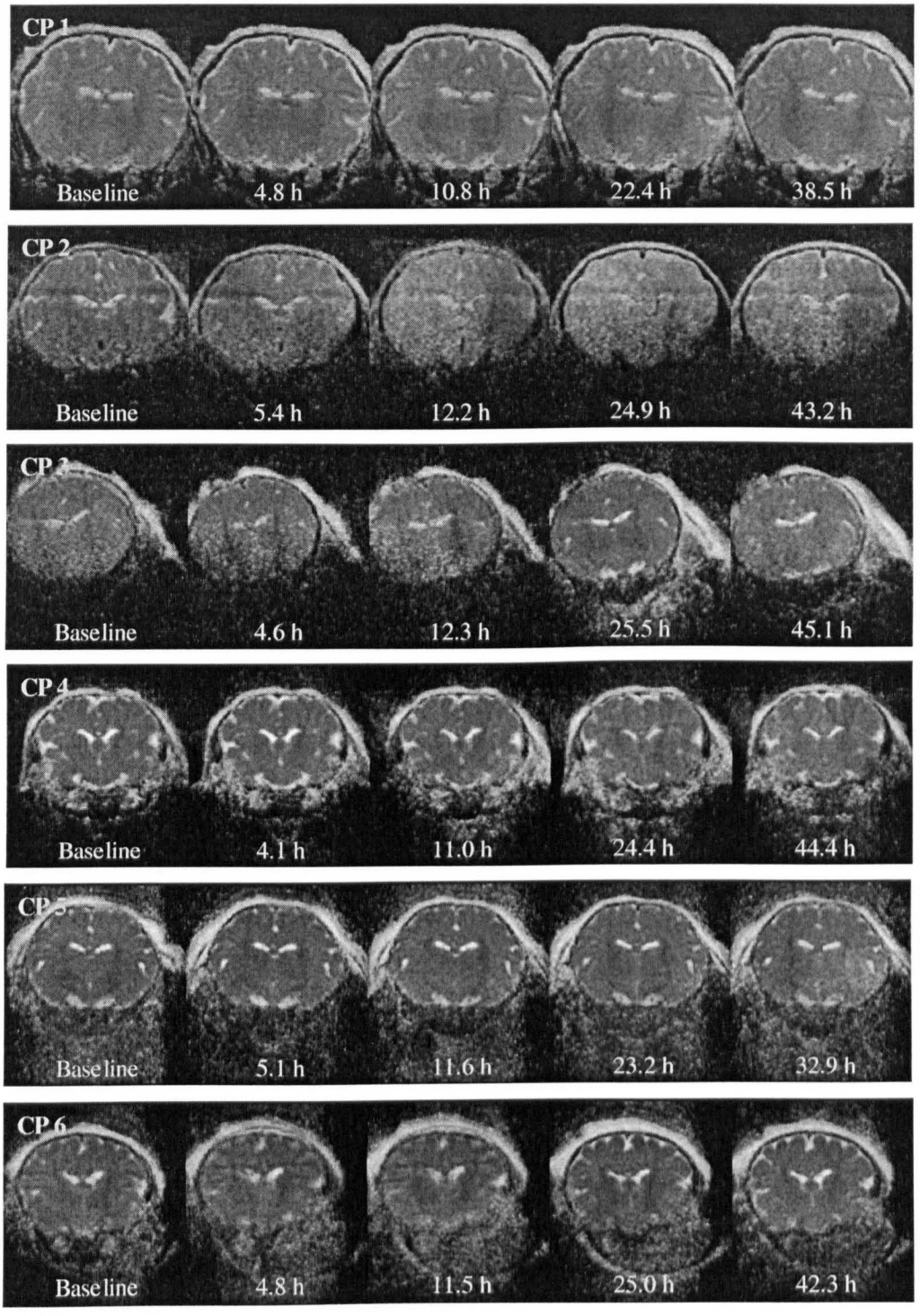

Figure 3.4 ADC_{av} maps of the control group of piglets at baseline and various times during the experiment. Control piglets (CP) are shown in ascending order from 1 to 6. Acquisition times are shown at the bottom of each map in hours after the start of the first ^{31}P MRS following the baseline.

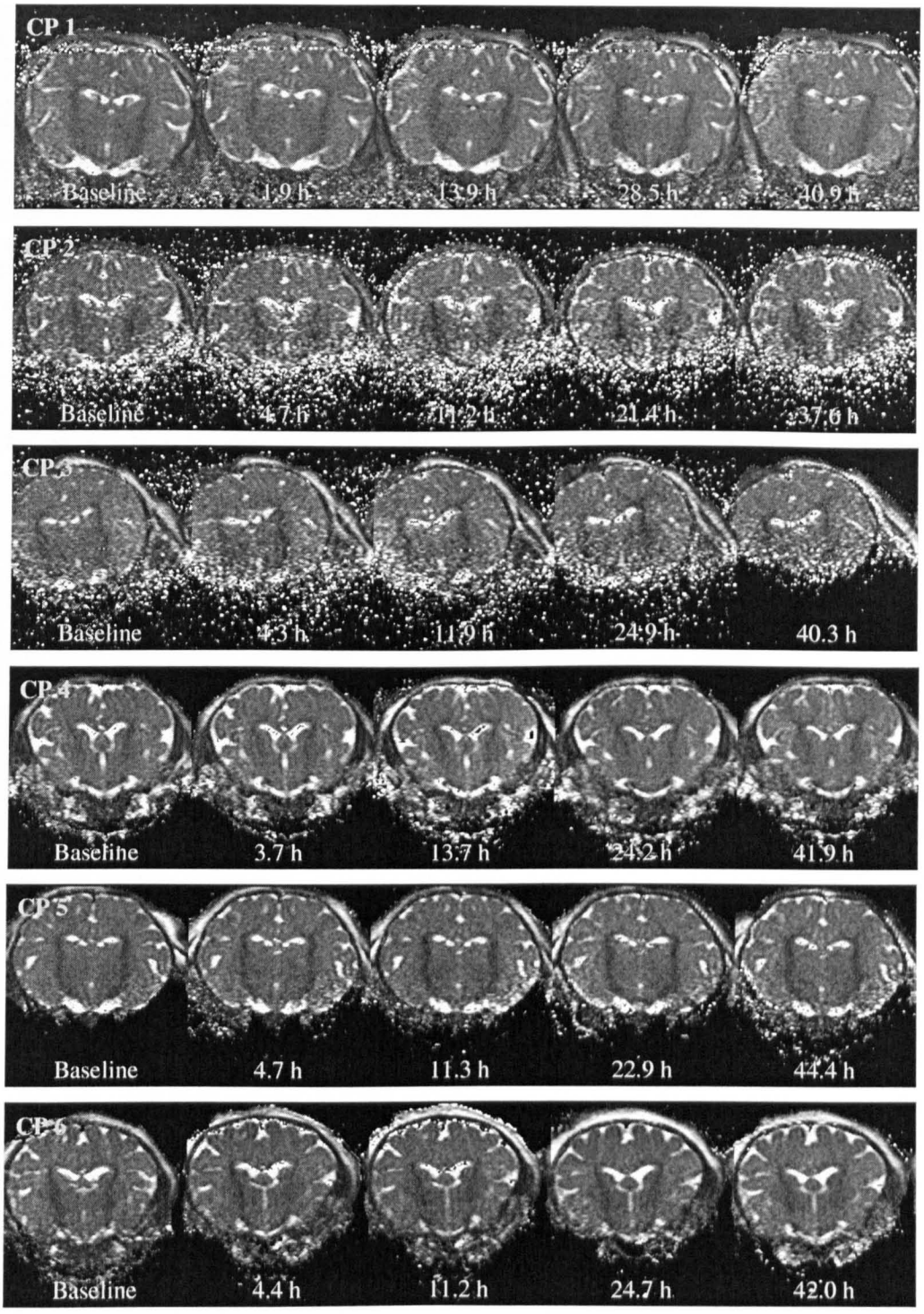

Figure 3.5 T_2 maps of the control group of piglets at baseline and various times during the experiment. Control piglets (CP) are shown in ascending order from 1 to 6. Acquisition times are shown at the bottom of each map in hours after the start of the first ^{31}P MRS following the baseline.

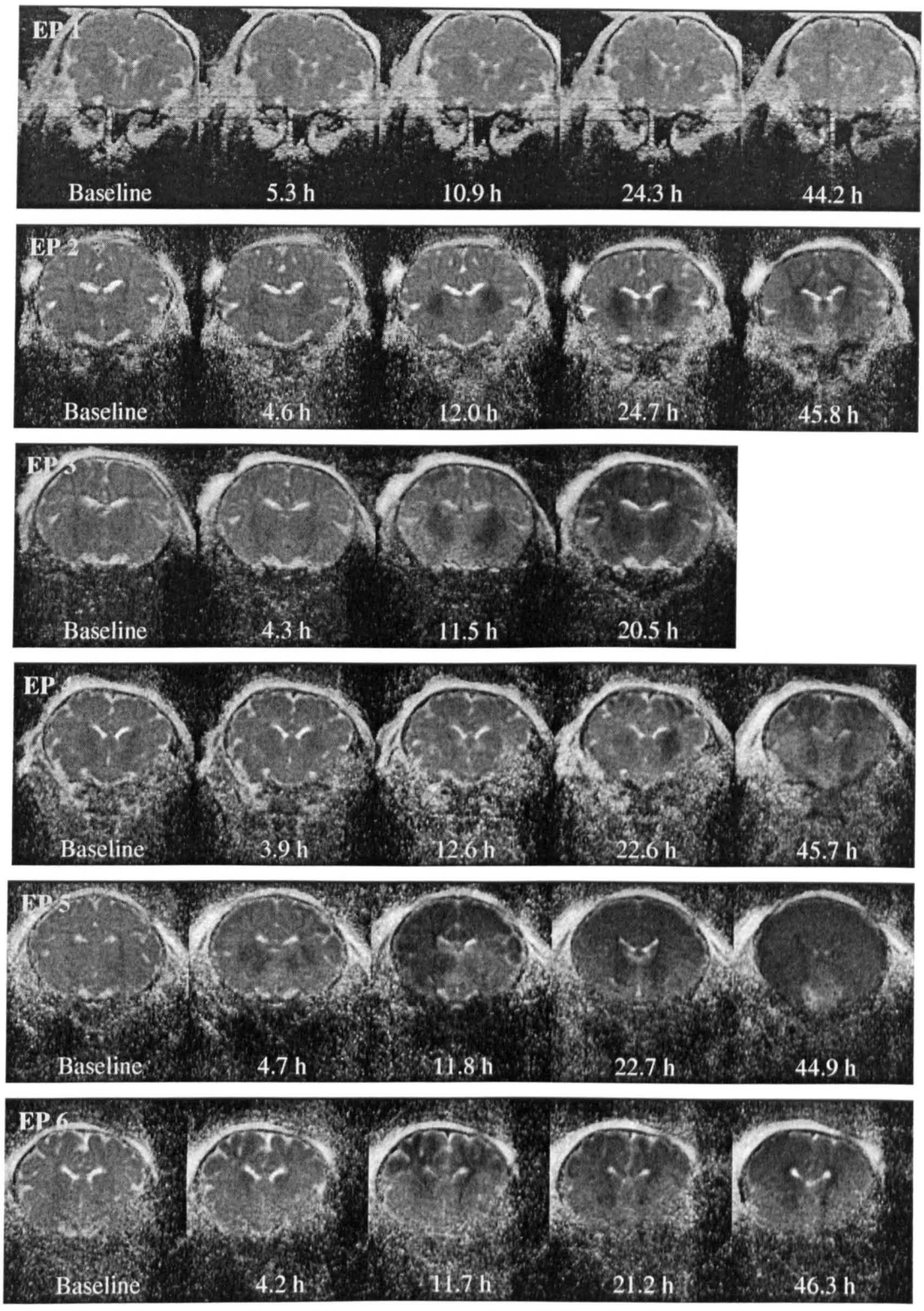

Figure 3.6 ADC_{av} maps of the experimental group of piglets at baseline and various times during the experiment. Experimental piglets (EP) are shown in ascending order from 1 to 6.

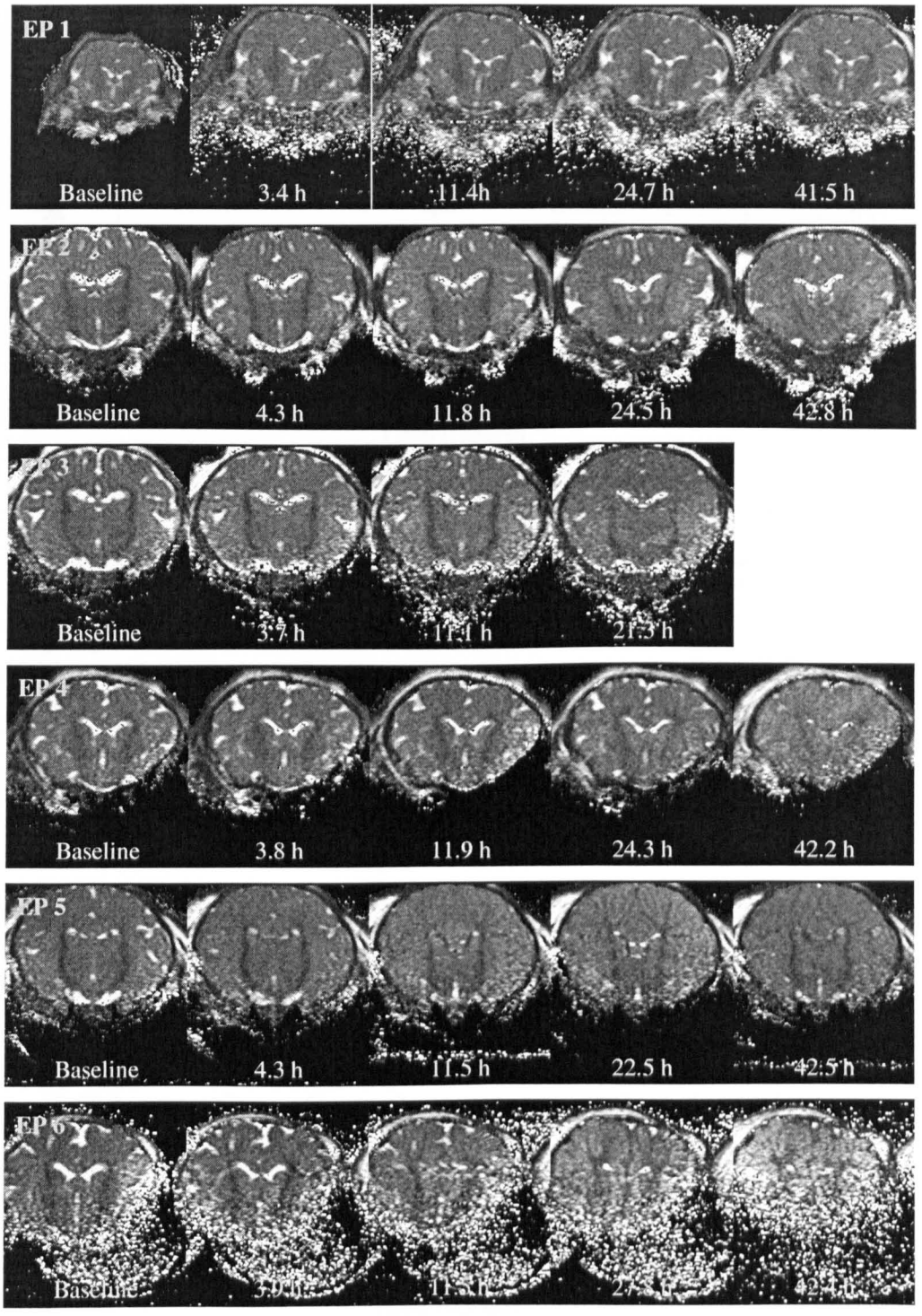

Figure 3.7 T_2 maps of the experimental group of piglets at baseline and various times during the experiment. Experimental piglets (EP) are shown in ascending order from 1 to 6.

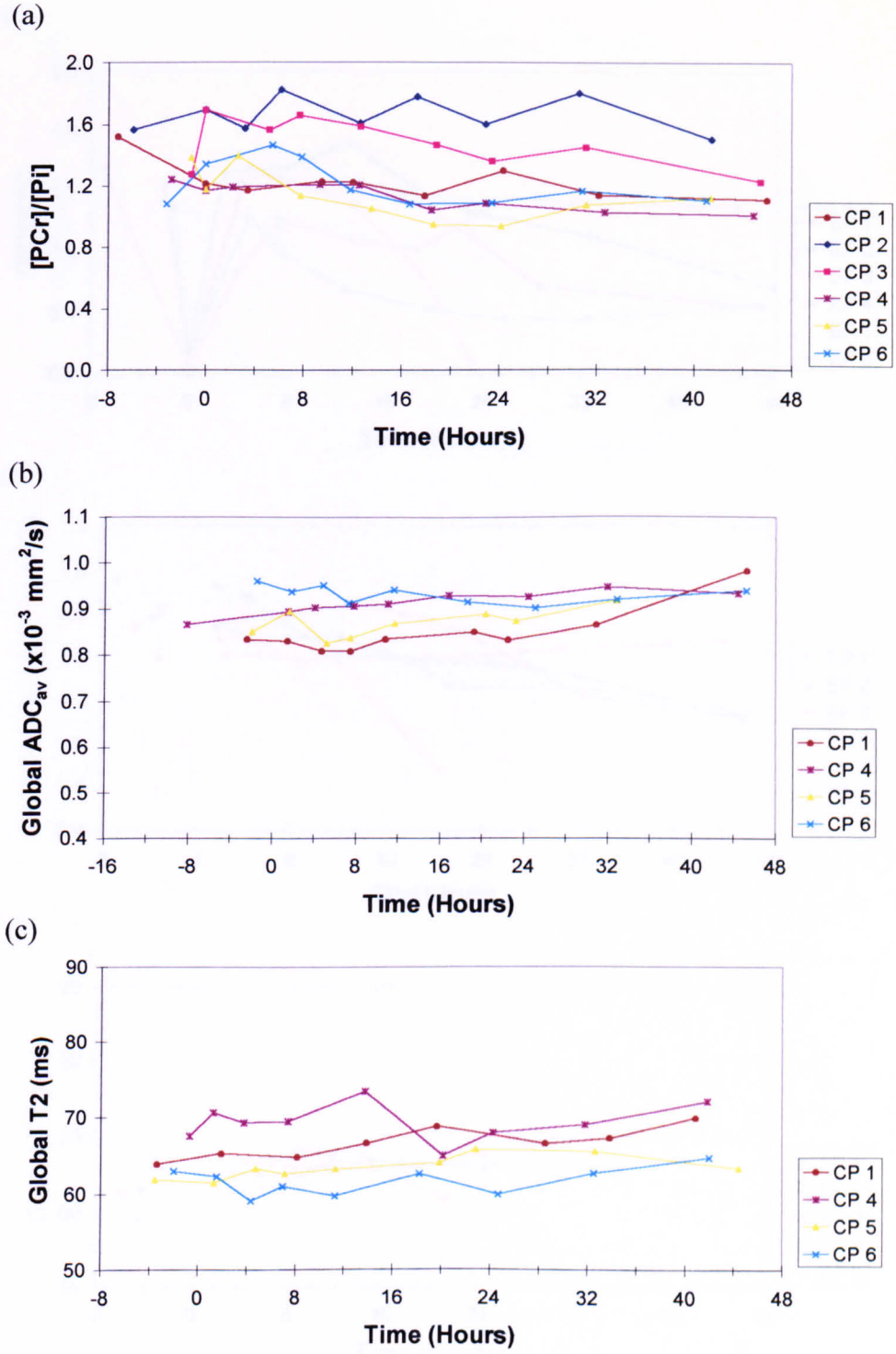

Figure 3.8 Time course of [PCr]/[Pi] ratio (a), global ADC_{av} (b) and global T_2 (c) for individual piglets in the control group.

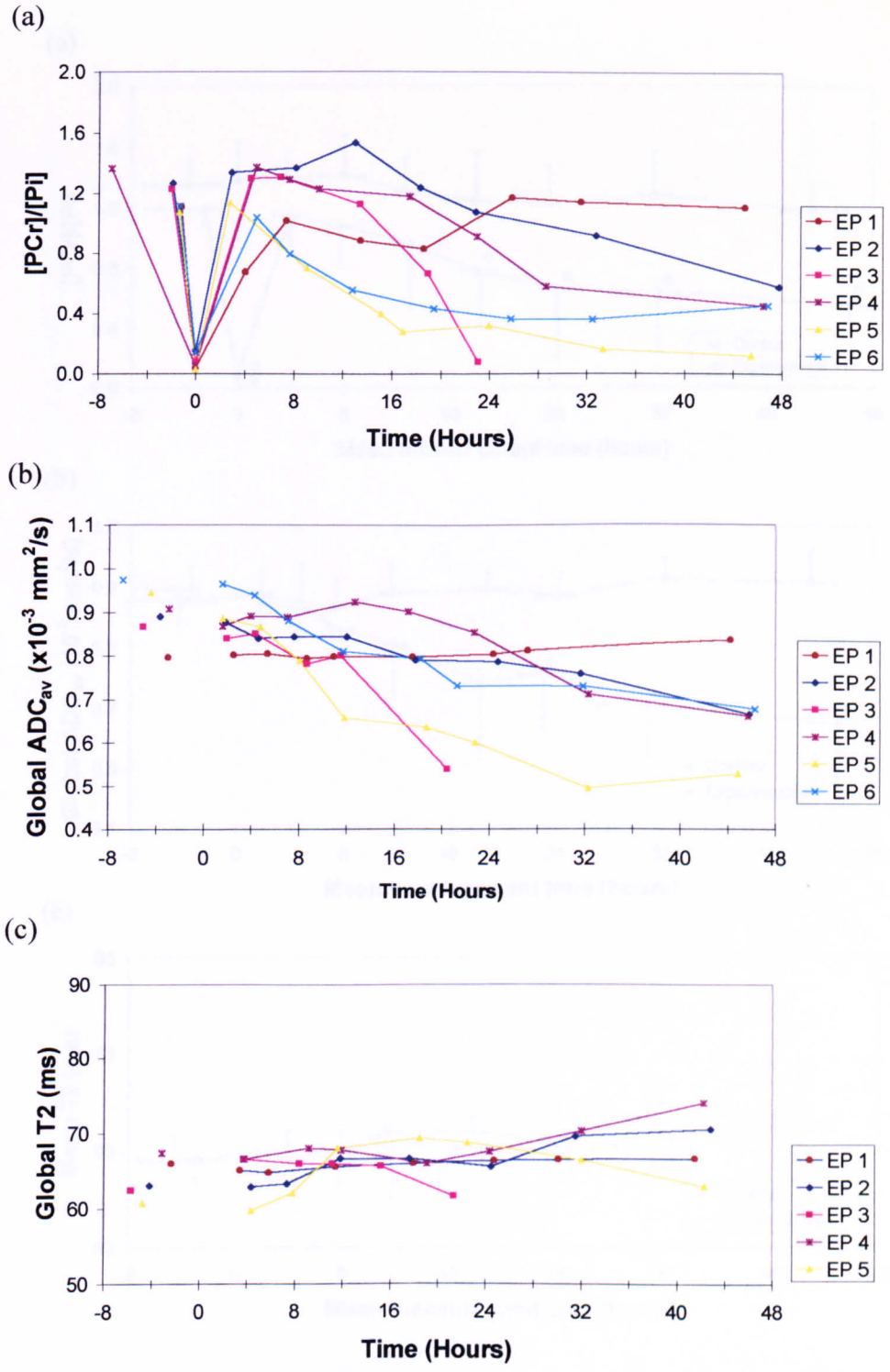

Figure 3.9 Time course of [PCr]/[Pi] ratio (a), global ADC_{av} (b) and global T_2 (c) for individual piglets in the experimental group.

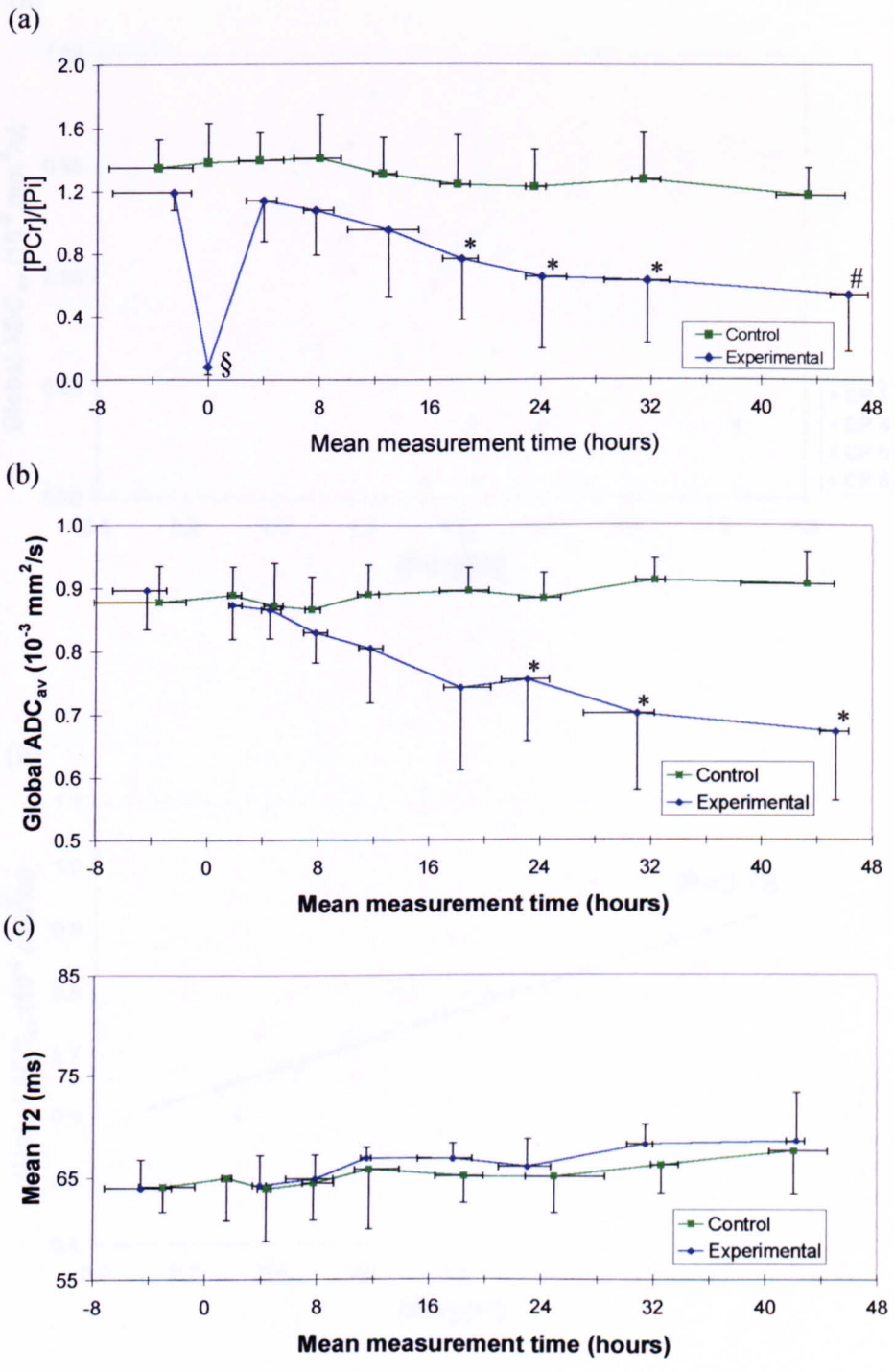

Figure 3.10 Time course of mean [PCr]/[Pi] ratio (a), global ADC_{av} (b) and global T_2 (c) for the control and experimental groups. Error bars are SD (observations) and range of measurement times. * $p<0.05$, # $p<0.01$, § $p<0.001$ control vs. experimental group.

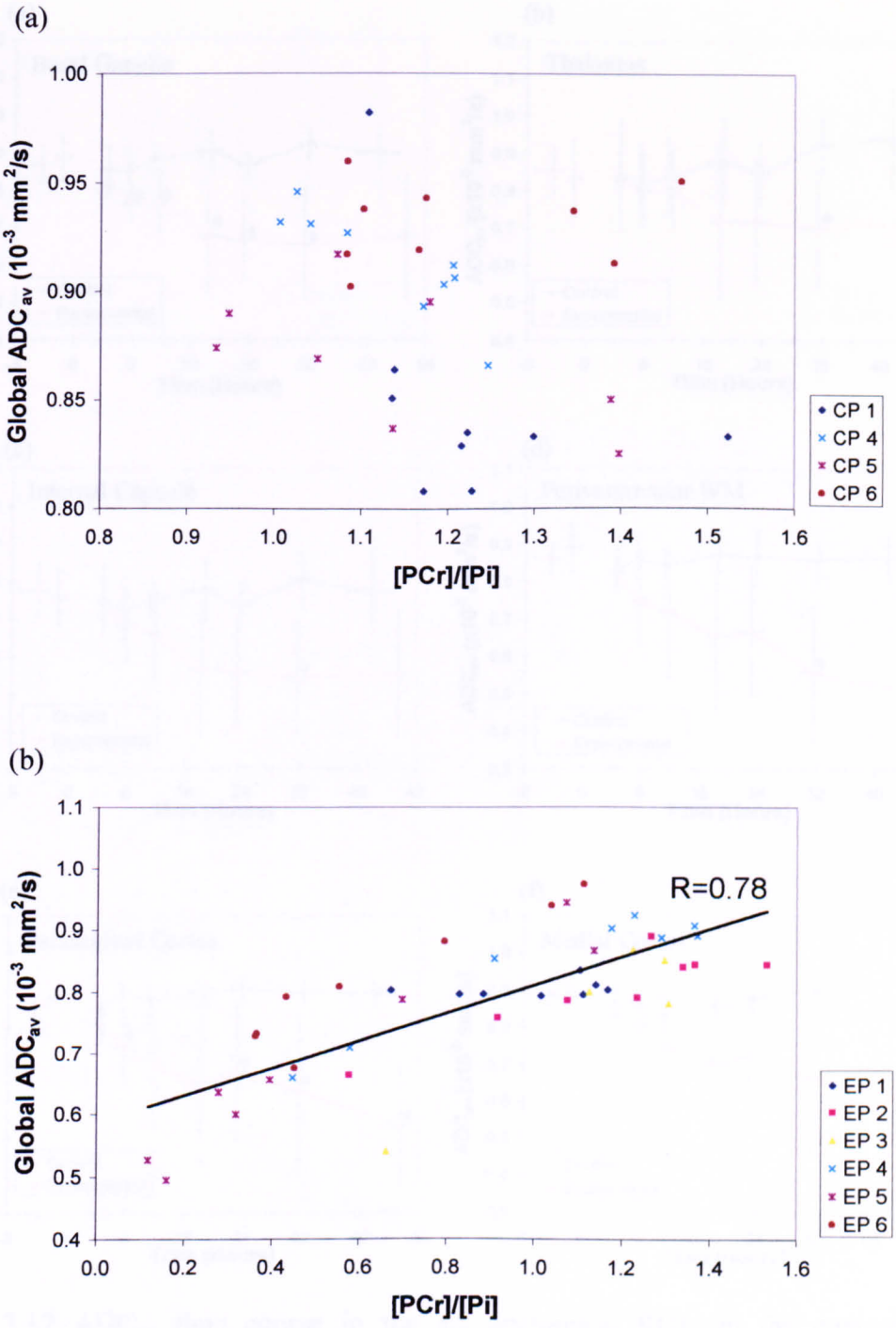

Figure 3.11 Relationship between [PCr]/[Pi] ratio and global ADC_{av} observed consecutively in the control (a) and experimental (b) groups. No significant correlation was found for the control group but a significant ($p<0.001$) correlation coefficient (r) of 0.78 was observed in the experimental group. If the noisy data from EP 6 is excluded, the correlation coefficient (r) can be increased to 0.86.

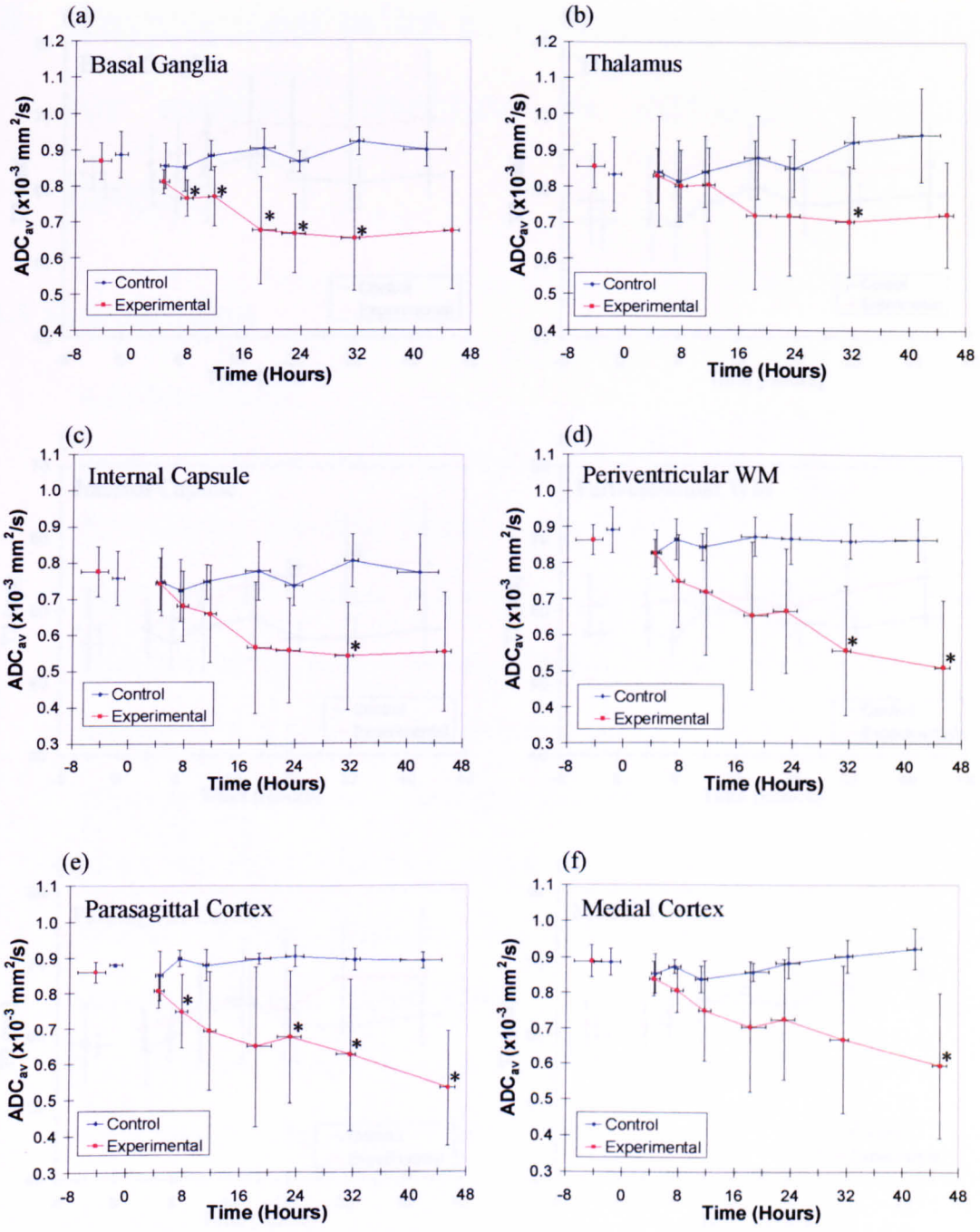

Figure 3.12 ADC_{av} time course in the six anatomical ROIs in the control and experimental groups of piglets. ROIs shown are (a) basal ganglia, (b) thalamus, (c) internal capsule, (d) periventricular white matter, (e) parasagittal cortex, (f) medial cortex. * $p<0.05$ experimental vs. control.

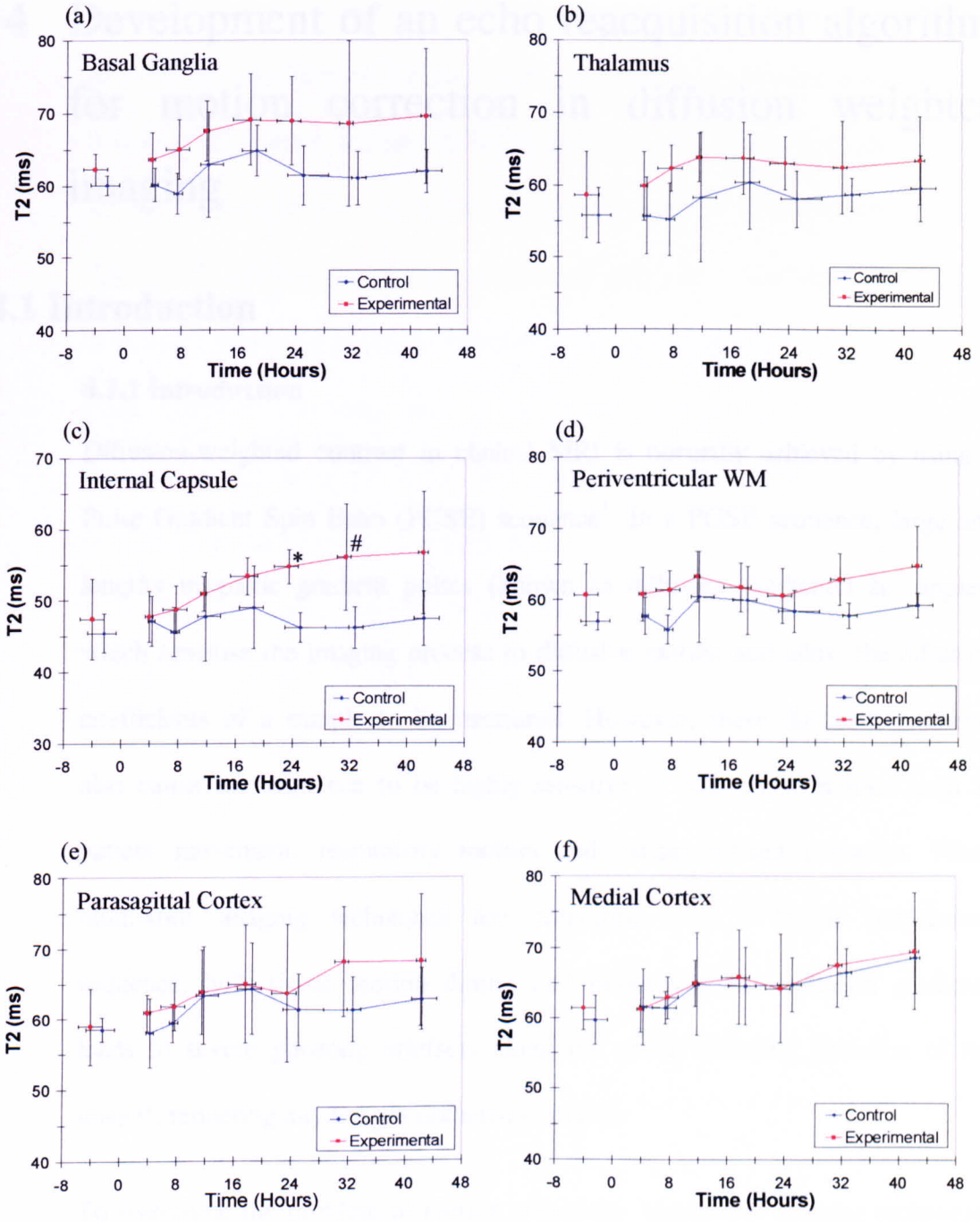

Figure 3.13 Local T_2 at baseline and various times during the experiment. ROIs shown are (a) basal ganglia, (b) thalamus, (c) internal capsule, (d) periventricular white matter, (e) parasagittal cortex, (f) medial cortex. * $p<0.05$ experimental vs. control. # $p<0.01$ experimental vs. control.

4 Development of an echo reacquisition algorithm for motion correction in diffusion weighted imaging

4.1 Introduction

4.1.1 Introduction

Diffusion-weighted contrast in clinical MRI is normally achieved by using a Pulse Gradient Spin Echo (PGSE) sequence[1]. In a PGSE sequence, large and lengthy magnetic gradient pulses (known as diffusion gradients) are applied which sensitise the imaging process to diffusive motion and allow the diffusion coefficients of a sample to be measured. However, these diffusion gradients also cause the sequence to be highly sensitive to bulk tissue motion such as patient movement, respiratory motion and cardiac-related pulsation. When multi-shot imaging techniques are combined with a PGSE preparation sequence, bulk tissue motion during and in-between the diffusion gradients leads to severe ghosting artefacts along the phase encoding direction of the image[2], rendering any images obtained unusable.

To overcome the problem of motion sensitivity, single-shot imaging techniques such as single-shot Diffusion-Weighted Echo Planar Imaging (DWEPI)[3], Line Scan Diffusion Imaging (LSDI)[4], and single-shot diffusion-weighted Stimulated Echo Acquisition Mode (STEAM) imaging[5;6] have been used and shown to be effective. Unfortunately, these solutions have several disadvantages. Single-shot DWEPI requires expensive specialist gradient hardware that is not

available on many scanners in use today, suffers from limited resolution and susceptibility artefacts and it generates a great deal of acoustic noise. On our Bruker 2.4T Avance scanner, DWEPI with typical imaging parameters (Field Of View (FOV) = 160 mm x 160 mm, image matrix = 64 x 64 and b-value = 900 s/mm^2) leads to peak sound pressure in excess of 120 dBA. The high level of acoustic noise is a particular problem in our laboratory, as it could potentially cause permanent hearing loss[7] in our newborn patients. Due to the one-dimensional nature of the LSDI technique, it is a very inefficient method for two-dimensional imaging. Consequently, the images it generates have much lower Signal to Noise Ratios (SNR) than those obtained from two-dimensional imaging sequences[4]. Single-shot diffusion-weighted STEAM imaging suffers from limited resolution, low SNR and generates a great deal of acoustic noise due to the short TR time.

Multi-shot imaging sequences do not suffer from the above-mentioned disadvantages and if a method of overcoming the problem of motion artefacts in multi-shot Diffusion Weighted Imaging (DWI) sequences could be developed, clinically acceptable diffusion-weighted images may be obtained using standard hardware. The aim of this work was to investigate the possibility of developing such a motion tolerant multi-shot DWI technique using computer simulation.

4.1.2 Motion errors

In the following paragraphs, the effects of motion in DWI will be discussed. As this work is specifically concerned with diffusion imaging in the brain, only the effects of rigid body motion shall be considered. Non-rigid motion, such as

cardiac pulsations, shall be assumed to be negligible or can be ameliorated by cardiac gating[8]. In the absence of diffusion sensitising gradients, relatively large motions are tolerated before motion artefacts are apparent. In this work, it will be assumed that these larger subject motions can be effectively suppressed using gentle restraints and only those motion artefacts arising from the presence of the diffusion gradients shall be considered.

It has been shown that rigid translational motion during DWI gives rise to a constant phase shift error in the NMR signal[9]. The value of the phase shift, α, is dependent on both the strength of the diffusion gradient and the translational motions during the diffusion sensitising period. The constant phase, α, can be calculated as follows:

$$\alpha = \gamma \cdot \int \mathbf{G}(t) \cdot \mathbf{r}(t) dt \tag{4.1}$$

where $\mathbf{G}$ is the diffusion gradient vector, $\mathbf{r}$ is the position vector of the subject and γ is the gyromagnetic ratio.

It has also been shown that rigid rotational motions give rise to a linear phase shift in the macroscopic magnetisation of the sample[10]. Using the Fourier shift theorem, it can be shown that such linear phase shifts lead to a displacement of the spin echo away from its intended position in k-space. The k-space displacement error depends on the direction and timing of the diffusion gradients and the subject's rotational motions[10;11]. If the rotational motions are small, then the k-space displacement error can be calculated as follows[10]:

$$\begin{aligned}
\mathbf{dk}_x &= \gamma \int [\mathbf{G}_y(t)\cdot\boldsymbol{\theta}_z(t) - \mathbf{G}_z(t)\cdot\boldsymbol{\theta}_y(t)]dt \\
\mathbf{dk}_y &= \gamma \int [\mathbf{G}_z(t)\cdot\boldsymbol{\theta}_x(t) - \mathbf{G}_x(t)\cdot\boldsymbol{\theta}_z(t)]dt \\
\mathbf{dk}_z &= \gamma \int [\mathbf{G}_x(t)\cdot\boldsymbol{\theta}_y(t) - \mathbf{G}_y(t)\cdot\boldsymbol{\theta}_x(t)]dt
\end{aligned} \tag{4.2}$$

where **dk** is the k-space displacement error vector, $\boldsymbol{\theta}$ is the subject's rotational angle and **G** is the diffusion gradient vector.

In the above equation, the k-space displacement error vector (**dk**) was expressed as three orthogonal components along the x, y and z axes. However, in the analysis of motion errors in DWI, it is often more convenient to express the k-space displacement error vector as components along the read, phase encoding and slice-selection axes. Thus, for the sake of clarity, equation 4.2 will be rewritten as follows:

$$\begin{aligned}
\mathbf{dk}_r &= \gamma \int [\mathbf{G}_p(t)\cdot\boldsymbol{\theta}_s(t) - \mathbf{G}_s(t)\cdot\boldsymbol{\theta}_p(t)]dt \\
\mathbf{dk}_p &= \gamma \int [\mathbf{G}_s(t)\cdot\boldsymbol{\theta}_r(t) - \mathbf{G}_r(t)\cdot\boldsymbol{\theta}_s(t)]dt \\
\mathbf{dk}_s &= \gamma \int [\mathbf{G}_r(t)\cdot\boldsymbol{\theta}_p(t) - \mathbf{G}_p(t)\cdot\boldsymbol{\theta}_r(t)]dt
\end{aligned} \tag{4.3}$$

where the subscripts *r*, *p* and *s* signify vector components along the read, phase encoding and slice-select axes respectively.

4.1.3 Motion Correction

The errors described above give rise to ghosting artefacts because they destroy the phase integrity between the spin echoes acquired during different phase encoding steps in a multi-shot imaging sequence. To overcome this problem, the use of navigator correction[9;10] and of radial scan data acquisition with projection reconstruction[12] have been suggested and shown to be partially effective. In projection reconstruction, the problem of view-to-view phase

variation is overcome by using only the magnitude of the projection data to reconstruct the image. However, in order to obtain the correct projection data, the k-space trajectories of all the spin echoes must intersect the centre of k-space. Subject motion causing **dk** displacement errors that shift the k-space trajectories of spin echoes perpendicularly away from their intended paths will cause incorrect projection data to be acquired, and lead to imaging artefacts. Thus, projection reconstruction is only partially effective in overcoming the problem of motion error in DWI. Navigator correction overcomes the problem of view-to-view phase variation in DWI by acquiring an extra non-phase encoded 'navigator' echo at each phase encoding step in the DWI sequence. As the navigator echoes are not phase-encoded, they should all sample the same central line of k-space at each phase encoding step and should all contain the same phase information. However, in the presence of subject motion, phase errors will be introduced and there will be phase variations between the navigator echoes. The phase variations between the navigator echoes can be used to determine and correct for the motion errors in the image echoes. For purely translational motions, it has been shown that the constant phase shift error, α, in a motion-affected image echo can be determined by subtracting the phase of a motion-free navigator echo from that of the motion-affected navigator echo. Given the phase shift errors, the phase integrity of a scan can be restored by appropriate phase correction of the image echoes' signal. Where a motion-free navigator echo cannot be identified then any navigator echo may be used as the reference echo instead. However, in such cases, all the echoes in the scan will contain the same phase shift error as the reference echo following the

phase-correction process. Fortunately, this residue phase error is of no consequence as only the magnitude image is required in DWI.

By Fourier transforming the navigator and image echoes along the read direction prior to navigator correction, it has been shown[10] that the navigator correction technique can also be used to correct for rotational motions that cause linear phase error along the read direction (i.e. $\mathbf{dk}_r$ displacement error). For reasons to be outlined in the following section, rotational motions leading to linear phase error along the phase encoding and slice-selection directions (i.e. $\mathbf{dk}_p$ and $\mathbf{dk}_s$ displacement errors) cannot be corrected for using the navigator correction technique and therefore it is not always effective.

4.1.4 Irreparable spin echoes

A diagram illustrating the k-space displacement errors and their effects on the spin echo's signal is shown in figure 4.1. Constant phase shift errors and $\mathbf{dk}_r$ displacement errors lead to correctable spin echoes because they don't alter the information content of the echoes significantly. The echoes' information is still derived from the intended line of k-space despite these errors. Although $\mathbf{dk}_r$ displacement errors will shift the spin echoes along the intended k-space line and cause a partial loss of the echoes signal through displacement of the echoes outside the k-space coverage of the experiment, this will not alter the information content of the echoes significantly until the errors are very large.

In contrast, $\mathbf{dk}_p$ and $\mathbf{dk}_s$ displacement errors shift spin echoes perpendicularly away from their intended position in k-space and cause spin echoes to be acquired from completely erroneous regions of k-space. These errors cause

complex changes to the information content of the spin echoes and it is generally not possible to recover the desired echoes by using the navigator correction technique. In this work, where a spin echo has been altered beyond the ability of the navigator correction technique to correct, it shall be described as an 'irreparable' echo. Motion errors that lead to irreparable echoes shall be described as 'irreparable' errors.

To overcome the problem of the irreparable $\mathbf{dk}_p$ and $\mathbf{dk}_s$ displacement errors, it has been suggested that the diffusion gradients in DWI sequences should be restricted to the phase encoding direction[10]. From equation 4.3, it can be seen that such an arrangement would prevent the occurrence of $\mathbf{dk}_p$, but not $\mathbf{dk}_s$, displacement errors. However, because the thickness of an imaging slice is generally of the order of a few millimetres, relatively large $\mathbf{dk}_s$ displacement errors are required before significant phase variation across the slice will occur. Thus, in most cases, the effect of $\mathbf{dk}_s$ displacement errors on the echoes signal is small and may be neglected. Experimental results have shown that restriction of the diffusion gradients to the phase encoding direction in combination with navigator correction is indeed effective in reducing much of the ghosting artefacts seen in DWI[10]. Unfortunately, because of the restriction imposed on the direction of the diffusion gradient, this solution limits the diffusion information that can be obtained and, in particular, it cannot be used to acquire diffusion trace maps. In order to acquire diffusion trace maps, the diffusion gradients need to be applied in all three orthogonal axes. This would not be possible if the diffusion gradient was restricted to the phase encoding direction.

Diffusion trace maps have been shown to be necessary to eliminate the confounding effects of diffusion anisotropy (especially in the white matter) when assessing cerebral ischaemia using DWI[13]. Therefore, the ability to acquire a diffusion trace map is essential in the clinical environment.

4.1.5 Reacquisition rationale

Since irreparable displacement errors are unavoidable in the clinical environment, it is proposed here that by detecting and reacquiring irreparable echoes, navigator correction can be used to obtain high quality diffusion weighted images. Whilst it is disadvantageous to have to reacquire echoes in order to eliminate motion artefacts, since this will increase scanning time, it will be shown that the scanning time need not increase significantly if the occurrences of irreparable displacement errors are not too frequent. For example, consider an imaging experiment where the occurrence of irreparable displacement error is R per echo, with $R<1$. After the first scan, there will be a fraction R of echoes with irreparable errors. Reacquiring the irreparable echoes only should leave R^2 fraction of echoes with irreparable errors. By repeated reacquisition of irreparable echoes in this manner, eventually all irreparable echoes will be removed from the image. The total number of echo acquisitions (N) required to achieve this can be calculated as follows:

$$N = N_0\left(1 + R + R^2 + R^3 + \ldots R^{\infty}\right)$$
$$\text{Since } R < 1$$
$$N = N_0\left(\frac{1}{1-R}\right) \tag{4.4}$$

where N_0 is the total number of echo acquisitions in a normal scan

From equation 4.4, it can be seen that even with an error rate of 50% (i.e. R=0.5), the total number of echo acquisitions required to remove all irreparable echoes is only twice that required for a normal scan. This would be a vast improvement over the present method, where the whole image is rescanned in the hope that no error will occur. At an error rate of 50%, the chances of no error occurring in an image with 128 phase encoding steps are very low indeed (1 in 2^{128}).

4.2 Effects of irreparable displacement errors

4.2.1 Introduction

Although the relationship between subject's motion and the phase errors produced in DWI is well understood, the relationship between the phase errors and the ghosting artefacts they produce and the consequence of the ghosting artefacts on the quantification of the Apparent Diffusion Coefficient (ADC) remains unclear. In order to develop an effective reacquisition algorithm it is desirable that these phenomena are first understood. To this end, the following simulation study was set-up to examine the effects of irreparable displacement errors on image ghosting and ADC quantification.

4.2.2 Method

The simulation used in the following study is based on the PGSE DWI sequence shown in figure 4.2. The simulation was implemented on a Windows NT system using the 'Delphi' integrated development environment (Inprise Corporation, 100 Enterprise Way, Scotts Valley, CA, USA). The navigator and image echoes were simulated as shown in equation 4.5.

$$N(m,j) = S(m\cdot\delta k_r + dk_r, dk_p, dk_s)e^{i\alpha} + \eta(\sigma)$$
$$F(m,n_j) = S(m\cdot\delta k_r - dk_r, n\cdot\delta k_p - dk_p, -dk_s)e^{-i\alpha} + \eta(\sigma) \quad (4.5)$$

where N(m,j) and F(m,n_j) are the navigator echo and the image echo at the j^{th} phase encoding step respectively. S(k_r,k_p,k_s) is the three dimensional k-space representation of the selected imaging slice. δk_r and δk_p are the intervals between k-space samples along the read and phase encoding axes and are equal to $2\pi/FOV_r$ and $2\pi/FOV_p$ respectively. FOV_r and FOV_p are the Field Of View along the read and phase encoding axes respectively. m and n_j are the integer indicies of the time data matrix. α is as defined in equation 4.1. **dk** is as defined in equation 4.3. η is a zero mean Gaussian noise signal with a Standard Deviation (SD) of σ. Note that the α phase error and the **dk** displacement error in the image echoes are opposite to that in the navigator echoes because of the 180^0 RF pulse in between their acquisition.

The k-space signal S(k_r,k_p,k_s) of the imaging slice in the simulation study was generated by using a diffusion-weighted image of a neonatal brain collected in our laboratory in a previous study. The time data and its corresponding image data are shown in figure 4.3. Unwanted background noise outside the imaging slice was removed by performing a masking operation on the image. The mask was generated automatically by using a high quality proton-weighted image of the same slice and thresholding it to 10%. The masking process is illustrated in figure 4.4. Following the masking operation, the remaining image was assumed to be free of noise and that the residual noise signal inside the imaging slice was part of the true imaging slice signal. The two dimensional image was extrapolated into a three-dimensional slice by assuming that it was homogenous

along the slice axis and that the profiles of the RF pulses in the imaging sequence were perfectly rectangular. With these assumptions, the relationship between the k-space signal $S(k_r,k_p,k_s)$ of the imaging slice and the k-space signal $W(k_r,k_p)$ of the 2D image is as follows:

$$S(k_r,k_p,k_s)=W(k_r,k_p)\cdot\tau\cdot\mathrm{Sinc}(\tau\cdot k_s) \tag{4.6}$$

where $W(k_r,k_p)$ is the time data of the cerebral image, τ is the slice thickness and $Sinc(x) = sin(x)/x$.

To convert the discrete time data of the cerebral image into a continuous function as required in equation 4.6, sinc interpolation was used with the assumption that the regions outside the FOV were void[14]. The following imaging parameters were used in the simulation. Δ = 50 ms, δ = 40 ms, G_{diff} = 13 mT/m along the read direction, FOV = 160 mm x 160 mm, matrix size = 128 x 128, slice thickness = 5 mm. The values of the $\mathbf{dk_p}$ and $\mathbf{dk_s}$ displacement errors were calculated using equation 4.2. Typical values of $\mathbf{dk_p}$ and $\mathbf{dk_s}$ displacement errors at various rotational velocities for the above parameters are illustrated in table 4.1. From table 4.1, it can be seen that, for the imaging parameters used in this simulation (where the highest sampled k-space point (k_{max}) is 2.5 rad/mm), a modest rotational motion of 1 rad/s was sufficient to displace a spin echo up to a 1/4 of the k-space coverage away from its intended position. This is an enormous error, especially if it is along the k_p axis, and demonstrates how sensitive DWI is to subject motion.

4.2.2.1 Objective measures of ghosting artefacts and ADC quantification error

In order to study the level of ghosting artefacts in a corrupted scan, objective measures of ghosting artefacts were required. In this study, two objective measures of ghosting artefacts were defined. The first, known as the Signal to Artefact Ratio (SAR), is based on the signal differences between the corrupted image and the true image. The second, known as the Signal to Ghost Ratio (SGR), is based on the ghost signal seen outside the boundary of the imaging slice. The definitions and methods used in calculating the SAR and the SGR in this study are described in the following paragraphs.

The SAR was defined as the ratio of the true mean signal of the imaging slice to the mean artefact signal within the imaging slice, the artefact signal being defined as the magnitude of the difference between the true and the corrupted signal. For simplicity, no attempts were made to account for the noise signal measured as part of the artefact signal. Thus, in the absence of any ghosting artefact, the SAR will be equal to the SNR (the SNR in this work being defined as the ratio of the mean signal in the imaging slice to the mean signal in a noise region). The SAR was calculated as follows:

$$SAR = \frac{\sum I_t(x,y)}{\sum |I_t(x,y) - I_m(x,y)|} \tag{4.7}$$

where both summations are taken over all co-ordinates inside the imaging slice. $I_t(x,y)$ is the true image signal without noise. $I_m(x,y)$ is the motion and noise corrupted image signal.

The extent of the imaging slice was defined as all co-ordinates where the mask image (see section 4.2.2) was non-zero.

The SGR was defined as the ratio of the mean signal in the Region Of Interest (ROI) that contained the imaging slice to the mean signal in the ROI that contained ghost signal. The ROIs used were determined automatically by using the mask image described previously. The ROI that contained the imaging slice was defined as all co-ordinates where the signal in the mask image was non-zero. The ROI containing the ghost signal was defined by drawing two lines horizontally and vertically at the extremities of the imaging slice as shown in figure 4.5. The ROI labelled *'G'* in figure 4.5 (on either sides of the imaging slice along the phase encoding direction) were taken as the ROI that contained the ghost signal.

To analyse the effects of ghosting artefacts on the accuracy of ADC quantification, an objective measure of ADC quantification error was required. In this study, the mean ADC error (ADC_{error}) was defined for this purpose. The ADC_{error} was defined as the mean of the magnitude difference between the true ADC_{map} and the corrupted ADC_{map} inside the imaging slice. It was assumed in the simulation study that the ADC_{map} would be calculated by using a two point log-linear fit as described previously (see Chapter 2). The 'zero' diffusion-weighted image used in the fitting procedure was assumed to be uncorrupted and only the ghosting artefacts in the diffusion-weighted image were considered in the assessment of the ADC quantification error. The true ADC map was obtained in the simulation study by performing a two point log-linear fit

between the 'zero' diffusion-weighted image and the true diffusion-weighted image (I_t as defined in equation 4.7). The corrupted ADC map was obtained in exactly the same way but with the corrupted diffusion-weighted image (I_m as defined in equation 4.7) instead of the true diffusion-weighted image. The ADC_{error} was calculated as follows:

$$ADC_{error} = \frac{1}{n}\sum\left|ADC_t(x,y) - ADC_m(x,y)\right| \tag{4.8}$$

where the summation is taken over all co-ordinates inside the imaging slice. $ADC_t(x,y)$ and $ADC_m(x,y)$ are the true and corrupted ADC maps respectively. n is the number of ADC values inside the imaging slice.

4.2.2.2 Relationship between the SAR, the SGR and the ADC_{error}

Although it is trivial to calculate the SAR and the ADC_{error} within the simulation environment, such calculations are not possible in the real world environment where the true diffusion-weighted image, I_t, is not known. However, it may be possible to estimate the SAR and the ADC_{error} from the SGR, which is readily obtainable from the corrupted diffusion-weighted image alone. To estimate the underlying SAR and ADC_{error} from the SGR, an understanding of the relationship between the SAR, SGR and ADC_{error} is required. To this end, a simulation study was set-up to generate scans that contained a random number of irreparable echoes in the time data. The positions of the irreparable echoes in each scan were randomly distributed and the size of the motion errors was normally distributed with a SD of 0.31 rad/mm. Both $\mathbf{dk}_p$ and $\mathbf{dk}_s$ displacement errors were included in the simulation. The SD of the noise signal in the simulation ($\eta(\sigma)$) was such that the SNR in

the simulated images was 25. One thousand scans were simulated. For each scan the SAR, SGR and ADC_{error} were recorded for analyses.

4.2.2.3 Effects of a single irreparable echo

To analyse the ghosting effects of a single irreparable echo in the scan time data, a simulation study was set-up to generate scans with only one irreparable echo in the time data. The value of the motion error and the phase encoding position of the irreparable echo were systematically varied until all of the echoes in the time data were simulated with $\mathbf{dk}_p$ and $\mathbf{dk}_s$ displacement error of between –0.31 rad/mm to 0.31 rad/mm. The simulated noise signal was set such that the SNR in the simulated images was 25. The SAR, SGR and ADC_{error} from each simulated scan were recorded for analyses.

4.2.2.4 Effects of multiple irreparable echoes

To extend the ghosting effects of a single irreparable echo to that of multiple irreparable echoes seen in a typical scan, a simulation study was set-up to analyse their relationship. The simulation program was set-up to generate scans that contained multiple irreparable echoes. The positions of the irreparable echoes in the time data were randomly distributed, whilst the size of the irreparable displacement errors was normally distributed with a SD of 0.31 rad/mm. The noise level was set so that the SNR in the simulated images was 25. The motion error rates (i.e. R as defined in equation 4.4) were set to 30%, 50% and 70% in consecutive simulation runs. One hundred scans were simulated for each run. For each scan, the true SAR, SGR and ADC_{error} due to the presence of all the irreparable echoes were recorded together with the SAR,

SGR and ADC_{error} due to the presence of 1, 2, 4, and 8 of the most significant irreparable echoes. In this work, the significance of an irreparable echo was defined as the level of ghosting artefacts produced by the irreparable echo acting individually as described in the above paragraph.

4.2.3 Results and discussions

4.2.3.1 Relationship between the SAR, the SGR and the ADC_{error}

The relationship between the SAR and the SGR is shown in figure 4.6. As can be seen, for scans with modest ghosting artefacts (SGR>5), there was a strong correlation between the SAR and the SGR. For scans with greater ghosting artefacts (SGR<5), the correlation was not as strong. Overall, there was a tendency for the SGR to underestimate the true level of ghosting artefacts in the imaging slice as measured by the SAR. The underestimate is particularly noticeable for scans with high level of ghosting artefacts (SGR<5).

The underestimate of the ghosting artefact by the SGR could have arisen either because of lesser ghosting artefacts outside the imaging slice than inside it, or because of higher imaging slice signal in the corrupted scan (as measure by the SGR) than in the true scan (as measured by the SAR). To exclude the latter possibility, the SGR was recalculated using the true imaging slice signal and the relationship was reassessed as shown in figure 4.7. For scans with modest ghosting artefacts, the relationship shown in figure 4.7 is very similar to that shown in figure 4.6. However, for scans with high level of ghosting artefacts (SGR<5), the underestimate of the ghosting level by the SGR was even more marked. The result therefore suggests that the ghosting artefact underestimation

is mostly due to the differences between the artefact signal within and without the imaging slice. An illustration of this phenomenon is shown in figure 4.8, where typical error images (i.e. images of the difference between a true image and a corrupted image) at different SGR are shown. From figure 4.8, it can be seen that, for scans with high SGR, the signal in the error images tended to be evenly distributed along the phase encoding direction. For scans with low SGR, the signal in the error images tended to have more structure and a greater amount of the signal was concentrated within the imaging slice.

The relationship between the SAR and the ADC_{error} is shown in figure 4.9a. From the shape of the graph, an inverse linear correlation was inferred. To linearise the relationship, the Artefact to Signal Ratio (ASR) (defined as the reciprocal of the SAR) was plotted against the ADC_{error} as shown in figure 4.9b. As can be seen, there was a strong linear correlation between the ASR and the ADC_{error} ($r=0.81$) overall. However, the correlation between the ASR and ADC_{error} for scans with high ASR was significantly weaker that those with low ASR. After excluding those scans with ASR of greater than 0.2 (i.e. SAR<5), the correlation coefficient (r) between the ASR and the ADC_{error} increased to 0.96, as shown in figure 4.9c. Also shown in figure 4.9c is the ADC_{error} measured from scans without motion artefacts but with varying amount of white noise. As can be seen, there was a strong correspondence between the ADC_{error} caused by a given level of ghosting artefacts and a similar level of white noise at these low ghosting artefacts level.

The relationship between the Ghost to Signal Ratio (GSR), defined as the reciprocal of the SGR, and the ADC_{error} is shown in figure 4.10a. The relationship is very similar to that between the ASR and the ADC_{error} but with one notable exception. For scans with high GSR, there was a tendency for the GSR to underestimate the ADC_{error} more often than to overestimate it. This phenomenon reflects the differences between the artefact signal inside and outside the imaging slice at high level of ghosting artefacts, as described previously. The overall correlation coefficient (r) between the GSR and the ADC_{error} was 0.82. After excluding those scans with GSR of greater than 0.2 (i.e. SGR<5), the correlation coefficient increased to 0.90, as shown in figure 4.10b. Also shown in figure 4.10b is the ADC_{error} measured from scans without ghosting artefacts but with variable SNR. Again, it can be seen that there was a strong correspondence between the ADC_{error} caused by a given level of ghosting artefacts (as measured by the GSR) and a similar level of white noise.

The above results suggest that for scans with modest ghosting artefacts, the ADC_{error} introduced by the ghosting artefacts is similar to that of white noise. The even distribution of artefact signal in scans with modest ghosting artefacts (see figure 4.6) further supports the idea that modest ghosting artefacts may be viewed as a pseudo noise signal. Therefore, it should be possible to treat diffusion-weighted images with modest ghosting artefacts (SGR>5) as noisy images and use them for ADC quantification accordingly. For scans with more substantial ghosting artefact (SGR<5), the effects of the ghosting artefacts were more complex and thus, they could not be viewed as pseudo noise signal. The ADC_{error} caused by these artefacts were also generally large and unpredictable.

Therefore, in general, scans with high level of ghosting artefacts (SGR<5) should not be used for ADC quantification, as the quantification error is not quantifiable.

4.2.3.2 Effects of a single irreparable echo

The ghosting effects, as measured by the SGR and ADC_{error}, of a single irreparable echo at different phase encoding positions with varying values of $\mathbf{dk_p}$ error are shown in figure 4.11 and 4.12 respectively. As can be seen, there was a general decline in the SGR and a corresponding increase in the ADC_{error} as the magnitude of the $\mathbf{dk_p}$ error in the irreparable echo was increased. For a given $\mathbf{dk_p}$ error, the decline in SGR were significantly greater when echoes with small phase encoding were affected compared to when echoes with larger phase encoding were affected. There was also a significant difference in the level of ghosting artefacts associated with negative and positive values of $\mathbf{dk_p}$ displacement error. This difference reflects the fact that the signal energy around a phase-encoded echo is usually asymmetrical. The asymmetry leads to differential changes in the echo signal depending on the sign of the $\mathbf{dk_p}$ error and hence differences in the level of ghosting artefacts. Consider for example an echo with an intended phase encoding of (k_p=) 5 rad/mm. If a motion error caused a $|\mathbf{dk_p}|$ error of 5 rad/mm during the diffusion sensitising period then the echo could be phase-encoded erroneously to either k_p = 0 rad/mm or k_p = 10 rad/mm depending on the sign of the error. In the former case, the echo signal would be much greater than it should be (as it is now in the centre of k-space) and the ghosting artefact would be correspondingly large. In the latter case, the signal would be smaller than expected but not by the same amount and the

ghosting artefact would be correspondingly less. This difference was not observed with the central echo ($k_p = 0$ rad/mm), as the signal energy around the centre of k-space is symmetrical.

The ghosting effects, as measured by the SGR and ADC_{error}, of a single irreparable echo at different phase encoding positions with varying values of $\mathbf{dk_s}$ displacement error are shown in figure 4.13 and 4.14 respectively. As can be seen, the ghosting effects of an echo with $\mathbf{dk_s}$ displacement error show the same characteristic dependency on phase encoding position and error size as that demonstrated by an echo with $\mathbf{dk_p}$ error. However, for a given error size and phase encoding position, the ghosting effects of an echo with a $\mathbf{dk_s}$ error was much smaller than that of an echo with a $\mathbf{dk_p}$ error. This difference was because of the small dimension of the slice thickness, which required a very large $\mathbf{dk_s}$ error to create a significant phase variation through the slice. No asymmetrical changes in the ghosting artefact were seen with positive and negative values of $\mathbf{dk_s}$ error, as the slice phase encoding position was in the centre of k-space (i.e. $k_s = 0$ rad/mm).

The relationship between the phase encoding position of a corrupted echo and the amount of artefact that it generates has been studied previously in abdominal T_2-weighted imaging in association with respiratory motion[15]. It was found that the amount of artefact generated by a corrupted echo increased with increasing level of respiratory motion, and with decreasing phase encoding level of the corrupted echo. Although the changes in spin echo signal due to subject motion in abdominal T_2-weighted imaging and in DWI are very

different, the general relationship between the phase encoding position of a corrupted echo and the amount of artefact that it generates in both cases appears to be very similar. It has been shown previously that the information content of an MR image is concentrated mainly in the centre of k-space[16]. Therefore, when echoes near the centre of k-space are corrupted, it is likely that much more of the scan information is lost than when echoes in the periphery are corrupted. The greater lost of scan information should in general lead to greater ghosting artefacts, and therefore would account for the greater amount of artefact generated by corrupted echoes with low levels of phase encoding.

4.2.3.3 Effects of multiple irreparable echoes

The relationship between the true ghosting artefact with all simulated irreparable echoes in the scan and the ghosting artefacts with only the most significant 1, 2, 4 and 8 irreparable echoes in the scan is shown in figure 4.15. As can be seen, the ghosting artefacts in the synthetic images with only a few of the most significant irreparable echoes were mostly less than that in the true corrupted images. The differences between the true ghosting artefact level and that obtained from the synthetic images tended to increase with increasing level of ghosting artefact and with decreasing numbers of irreparable echoes in the synthetic images. However, even when only one irreparable echo was used in the synthetic images, the level of ghosting artefact obtained from the synthetic images was, on average, 65% of that in the true corrupted images. When eight irreparable echoes were included in the synthetic images, the level of ghosting artefact was, on average, 95% of that in the true corrupted images. The result thus suggests that a very significant proportion of the true ghosting artefact is

attributable to just eight of the most significant irreparable echoes. If these echoes could be identified then significant reduction in ghosting artefact could be achieved by just reacquiring these few echoes alone.

4.2.4 Summary and conclusions

The results from the first simulation study demonstrated that the SGR and its related measure the GSR are effective objective measures of ghosting artefact in a corrupted image. For scans with modest ghosting artefact, the SGR accurately reflected the level of ghosting artefact in the imaging slice, whilst the GSR correlated well with the level of ADC quantification error obtained from those scans. For scans with substantial ghosting artefact (SGR<5), neither measures correlated well with the level of ghosting artefact in the imaging slice or the ADC quantification error. However, it is generally true that when the SGR of a scan was very low, the amount of ghosting artefact in the scan was usually large and unpredictable. Therefore, a low SGR could be used as a marker to exclude scans from further analysis.

The results of the second simulation study showed that the level of ghosting artefact due to a single irreparable echo is a function of both the intended phase encoding position of the echo, as well as the type, sign and size of the k-space displacement error. Although the exact function is complex and dependent on the exact image being analysed, there was a general trend showing an increased level of ghosting artefact with increasing error size and with decreasing phase encoding level of irreparable echo.

The results of the third simulation study demonstrated that the ghosting effects of multiple irreparable echoes in a scan were mainly determined by a few of the most significant irreparable echoes. Therefore, in the clinical environment, where it may not be possible to reacquire all the irreparable echoes due to scanning time constraints, it is likely that the greatest improvement in image quality would be achieved by reacquiring the most significant irreparable echoes first. In cases where not all of the corrupted echoes are reacquired, it is expected that residual ghosting artefact will inevitably persist. However, if the residual level of ghosting artefact is low (i.e. SGR>5) then, from the results of the first simulation study, the scan may still be usable.

4.3 Simulation of the reacquisition algorithm

4.3.1 Introduction

From the results of the previous simulation studies, it was concluded that the ghosting artefact in a corrupted scan was mostly due to the effects of only a few of the most significant irreparable echoes in the scan. By identifying and reacquiring these echoes in descending order of their significance, it is postulated here that an optimal or near optimal rate of image quality improvement should be achieved during the reacquisition process. In the following paragraphs, the design and implementation of an algorithm to identify and reacquire irreparable echoes on such a basis is discussed and tested in simulation studies.

4.3.2 Theory

The acquisition of an uncorrupted diffusion-weighted image using the reacquisition technique involves six main steps. They are as follows:

i) Obtain a standard corrupted diffusion-weighted scan for reacquisition

ii) Identify, from within the scan, a reference navigator echo that has not been corrupted by irreparable errors (i.e. dk_p and dk_s errors).

iii) Use the reference echo to identify all echoes that have been corrupted by irreparable errors.

iv) Select an irreparable echo for reacquisition.

v) Reacquire and replace the selected echo.

vi) Repeat from step (iii) until the stopping conditions are met.

A flowchart of the steps outlined above is illustrated in figure 4.16. The initial step of acquiring a corrupted scan for reacquisition can be achieved by merely running a standard navigated DWI sequence and thus will not be expanded upon any further. The theory and implementation of the other steps in the reacquisition process are more involved and, thus, are described below.

4.3.2.1 Identification of the reference navigator echo

In order to identify navigator echoes with irreparable errors, the reacquisition algorithm must first identify a reference navigator echo that has not been corrupted by irreparable errors (i.e. a correctable navigator echo). Under ideal imaging conditions, correctable navigator echoes are always obtained from the centre of k-space (i.e. $k_p = 0$ rad/mm, $k_s = 0$ rad/mm), where the time data signal is greatest. Subject motion leading to $\mathbf{dk_p}$ and $\mathbf{dk_s}$ displacement errors acts to

shift the navigator echoes away from the centre of k-space and thus reduces their signals. Therefore, in principle, it should be possible to identify the required reference navigator echo by searching for the navigator echo with the largest signal. An illustration of this principle is shown in figure 4.17.

Unfortunately, under realistic imaging conditions, the navigator echoes often have some unintended phase encoding due to gradient eddy currents arising from the large and lengthy diffusion gradients[17]. The unintended phase encoding means that correctable navigator echoes without motion induced $\mathbf{dk}_p$ or $\mathbf{dk}_s$ displacement errors are no longer acquired from the centre of k-space, but somewhere off-centre. Under such circumstances, subject motion leading to $\mathbf{dk}_p$ and $\mathbf{dk}_s$ errors can shift a navigator echo either closer to or further away from the centre of k-space and thus increase or decrease its signal. An illustration of this phenomenon is shown in figure 4.18. Therefore, it is not possible to identify a reference navigator echo by selecting the navigator echo with the largest signal as suggested above. It is conceivable that with the use of self-shielded gradients[18], gradient pre-emphasis[19], optimised diffusion sensitising sequence[20], and/or additional trimming gradients the unintended phase encoding due to eddy currents can be reduced to such an extent that it would have negligible effects on the navigator echoes signal. However, due to the rapid decline in time data signal with increasing phase encoding[16], the eddy currents induced phase encoding must be reduced to a very small amount indeed to avoid significant decline in the navigator echoes signal. After some experimentation, it was found that such a feat was not practical on our scanner

and the following alternative technique of identifying the reference navigator echo, known as the 'clustering method', was proposed.

The principle of the 'clustering' identification technique relies on the following assumptions being true.

i) The percentage of irreparable echoes in a corrupted scan never exceeds 70%.

ii) Following correction for motion induced dk_r and α phase error, correctable navigator echoes are all very similar to one another but very different to irreparable navigator echoes.

iii) Irreparable navigator echoes are dissimilar to one another due to the presence of different dk_p and dk_s displacement errors during their acquisition.

The validity of these assumptions in the clinical environment will determine the accuracy with which the 'clustering' identification method will be able to correctly identify the required reference navigator echo. The validity of the first assumption depends entirely upon the movement of the subject during the scan acquisition. Therefore, it cannot be guaranteed. However, if the subject were going to be moving so frequently during a scan that this assumption could not be met then the theoretical increase in scanning time (see section 4.1.5) alone would render the use of the reacquisition technique impractical. Thus, the validity of the first assumption should not be the limiting factor to the feasibility of the 'clustering' identification technique. The validity of the second assumption will be tested empirically in a simulation study and will be

described later. The validity of the third assumption depends on the exact subject motion present during the scan acquisition. However, it is very unlikely that motion errors from one phase encoding step to the next are going to be the same. Thus, the third assumption is very likely to be true.

Given that the above assumptions are true, the identification of the required reference navigator echo can be achieved by assessing the similarities of the navigator echoes against one another. From the first assumption, it is known that at least 30% of the navigator echoes in the scan are correctable. From the second and third assumptions, it is known that correctable navigator echoes are similar to one another but that irreparable navigator echoes are not. Therefore, it follows that the required reference navigator echo will be the one that is most similar to 30% of the navigator echoes in the scan.

In this work, the following algorithm was used to identify the reference navigator echo based on the above principle.

i) Remove the dk_r and α phase error from all navigator echoes in the scan.

ii) For each navigator echo, calculate its differences to 30% of the most similar navigator echoes in the scan.

iii) Select the navigator echo with the minimum total differences as the reference echo.

To remove the $\mathbf{dk_r}$ and α phase error from the navigator echoes as required in step (i) of the algorithm, the $\mathbf{dk_r}$ displacement error was first converted into a linear phase error by Fourier transforming the navigator echoes into the projection domain[10]. The phase errors were then removed by retaining only the

magnitude component of the navigator projection signal. To calculate the differences between the navigator echoes as stated in step (ii) of the algorithm, a method of measuring the differences between two navigator echoes was required. In this work, the differences between a pair of navigator echoes were measured by calculating the Euclidean distance between their corresponding navigator projections. The Euclidean distance between two navigator projections was calculated as follows:

$$S_{ab}^2 = \sum^{N} \left(A(x) - B(x)\right)^2 \tag{4.9}$$

where S_{ab} is the Euclidean distance between navigator echo a and navigator echo b. A is the magnitude projection signal of navigator a. B is the magnitude projection signal of navigator echo b. N is the numbers of data points in the navigator projection.

4.3.2.2 Identification of irreparable echoes

From the assumptions and discussions in the previous section, it can be inferred that the Euclidean distance between two correctable navigator echoes should be much smaller than that between an irreparable navigator echo and a correctable one. Since the reference navigator echo is a correctable navigator echo, it should be possible to identify irreparable navigator echoes by calculating their Euclidean distances to the reference navigator echo. Those navigator echoes that are further than a predetermined distance away from the reference navigator echo can be classified as irreparable, whilst the rest can be classified as correctable. The predetermined distance will depend on the exact level of signal to noise present during the acquisition of the navigator echoes. By

assuming that the only difference between correctable navigator echoes is their noise signal, the required distance may be determined automatically by calculating the distance between two correctable navigator echoes. To account for the random variation in noise signal that can lead to distances greater than the calculated value, a multiplication factor of greater than unity should also be applied. In this work, the distance between two correctable echoes was obtained by calculating the distances between the reference navigator echo and its closest match. This was valid since the reference navigator echo, if correctly identified, must be a correctable echo, whilst its closest match, from the assumptions in the previous section, must also be another correctable echo. A systematic bias will be introduced by the use of the closest match, but this can be accounted for by applying a larger multiplication factor to the result.

The choice of multiplication factor will be critical to the accuracy with which irreparable echoes can be identified and therefore must be selected carefully to prevent poor reacquisition performance. If the chosen multiplication factor is too large, irreparable echoes may be erroneously classified as correctable and be retained in the final image. If the chosen multiplication factor is too small, correctable echoes will be classified erroneously as irreparable and valuable scanning time will be wasted reacquiring correctable echoes. No multiplication factor can be expected to give 100% accuracy in all cases and the choice of multiplication factor will have to be a compromise between minimising the size of the irreparable errors retained in the scan and minimising the numbers of correctable echoes erroneously classified as irreparable. The value used in this work was determined by using a simulation study that will be described later.

4.3.2.3 Selection of irreparable echoes

In order to remove all motion errors from a corrupted diffusion-weighted scan, all irreparable echoes in the scan must be reacquired. If all irreparable echoes are to be reacquired then the order in which they are done should not affect the final image quality. Therefore, in such cases, the task of selecting an irreparable echo for reacquisition is simplified to selecting at random an irreparable echo for reacquisition. If all the irreparable echoes have been correctly identified then it will not matter which is chosen. However, since such identification accuracy cannot be guaranteed, there is always the possibility that some correctable echoes will have been erroneously classified as irreparable. Therefore, to ensure that genuinely irreparable echoes are reacquired first, the navigator echo that is most dissimilar to the reference echo should be selected instead. This then allows for the possibility of the scan being terminated early (e.g. based on image quality criteria) before a significant amount of time was wasted on reacquiring correctable echoes. To differentiate this selection method from the other methods to be discussed in the following paragraphs, it will hereafter be referred to as the 'simple' selection method.

Due to time constraints in the clinical environment, it may not be possible to reacquire all the irreparable echoes in a corrupted scan as described. Under such circumstances, a compromise between scanning time and image quality has to be made. From the results of the previous simulation studies (see section 4.2.4), it was hypothesised that by identifying and reacquiring the irreparable echo that caused the greatest amount of ghosting artefact first, optimal or near optimal image quality should be achieved for any given reacquisition time.

Unfortunately, identifying such an irreparable echo is not a trivial process since the ghosting effect of an echo cannot be determined without knowledge of both the image being scanned and the irreparable error in the echo. However, by noting that the ghosting artefact due to irreparable echoes in the centre of k-space is generally much greater than that due to irreparable echoes at the periphery, it follows that irreparable echoes at the centre of k-space are much more likely to cause the most significant ghosting artefact than their peripheral counterparts. Therefore, by selecting irreparable echoes from the centre of k-space for reacquisition first, an approximation to the desired selection method can be achieved. However, to account for the fact that the ghosting effect of an irreparable echo is dependent on both the size of the motion error and its phase encoding position, a compromise between these two factors must also be considered. In this work, the following selection method, called the 'centric' selection method, was devised based on the above principles.

i) Initialise the selection pool to the central 16 echoes.

ii) Search for all irreparable echoes that are within the selection pool.

iii) If there is no irreparable echo in the pool then widen the selection pool to include 16 more peripheral echoes and repeat from step (ii), otherwise continue with step (iv).

iv) Select the irreparable echo in the selection pool that is most dissimilar to the reference navigator echo for reacquisition.

The compromise between the importance of motion error size and phase encoding position to the ghosting effect of an irreparable echo was achieved in the above algorithm by ensuring that the echo with the largest error (assumed to

be the one most dissimilar to the reference echo) in the selection pool was reacquired first. However, at the same time, the selection pool was set so that the peripheral echoes, regardless of their error size, were only reacquired after all irreparable echoes in the centre of k-space have been removed. The relative importance of the central echoes can be crudely adjusted by varying the initial number of central echoes in the selection pool and the number of peripheral echoes that are added to the pool when no more irreparable echoes are in the pool. The larger the number in both cases, the lower the importance of the central echoes and vice versa.

To assess the performance of the 'centric' selection method, two theoretically better, but practically unrealisable, selection methods were also proposed. The first of these selection methods, called the 'artefact' selection method, is based on the hypothesis that by reacquiring irreparable echoes based on their ghosting effects, optimal or near optimal image quality improvement in a given reacquisition time could be achieved. The 'artefact' selection method involves selecting the irreparable echo that produces the greatest amount of ghosting artefact for reacquisition first. In the simulation environment, identification of such an echo can be achieved by using simulation methods such as that described in section 4.2.2.3. The second theoretically better selection method, called the 'optimum' selection method, involves selecting the echo that will lead to the best improvement in image quality following the next echo reacquisition. In order to achieve such a feat, the 'optimum' selection process has to know in advance the motion error that will be present in the following echo acquisition and the consequence of reacquiring a specific irreparable echo

given the motion error. Although impossible in the real world, this feat is trivial in the simulation environment since all the parameters are known and the consequence of each choice can be simulated.

4.3.2.4 Reacquisition of irreparable echoes

Reacquisition of a selected echo in the simulation environment is a simple matter of simulating the reacquired echo under the given simulation parameters. However, once the echo has been reacquired, it should only be used to replace the current echo if it has less motion error than the current echo. Unfortunately, there is no reliable way of assessing the exact motion error that has occurred during a navigator echo acquisition from its signal alone. However, if it is assumed that the navigator echo signal becomes increasingly distorted with increasing motion error then it may be surmised that the navigator echo will also become increasingly dissimilar to the reference echo with increasing motion error. In which case, the reacquired echo should only be used to replace the current echo if it is more similar to the reference echo than the current echo.

4.3.2.5 Stopping conditions

The decision whether to terminate the reacquisition process or not can be automated by using various predefined criteria, such as a maximum total scanning time, a minimum image quality or a maximum number of irreparable echoes in the scan. Alternatively, the reacquisition process can be terminated interactively by the operator using feedback information from the reacquisition algorithm. In the following simulation study, no scanning time constraints were

imposed and the reacquisition process was only halted when all identified irreparable echoes were removed.

4.3.3 Method

Much of the computer software required to simulate the reacquisition process was present in the simulation software used to study the ghosting effects of irreparable echoes described in section 4.2.2. Therefore, the simulation of the reacquisition algorithm was implemented on top of the previous simulation software using the same development environment. The imaging data and parameters used in the previous simulation studies were also retained.

One of the assumptions used in the development of the reacquisition algorithm was that the signal of correctable navigator echoes were all very similar to one another but very different to that of irreparable navigator echoes. Furthermore, it was assumed that this difference could be measured adequately using the Euclidean distance between the magnitude signals of the navigator echo projections. To assess the validity of these assumptions, navigator echoes with varying amount of phase encoding along the three orthogonal axis and with varying amount of a phase errors were simulated and the Euclidean distances between them were calculated. To assess the effects of additive noise on the validity of the assumptions, the simulation was ran twice, once with the noise parameters set for high SNR (SNR = 25) and once for low (SNR = 6).

To assess the accuracy of the 'clustering' method in identifying the required reference echo from a corrupted scan, 100 corrupted scans were simulated under each of the following combinations of scanning conditions:

i) Motion-induced dk_r and α phase error rate of 100%.

ii) Motion-induced dk_p and dk_s error rates of 30%, 50% and 70%.

iii) Eddy currents induced dk_p and dk_s errors of zero, 0.04 and 0.16 rad/mm.

iv) SNR in an uncorrupted image of 25, 12, and 6.

The values of the motion induced displacement errors (**dk**) and phase errors (α) were set so that they were normally distributed with a SD of 0.31 rad/mm and π radian respectively. For each simulated scan, the 'clustering' method was used to identify the reference navigator echo in the scan. The accuracy of the 'clustering' method was measured by noting the presence of motion error in the identified reference echo.

To assess the accuracy of the reacquisition algorithm in identifying irreparable echoes in a corrupted scan, the reacquisition algorithm identification process was tested with all the simulated scans described above. The sensitivity and specificity of the identification process was measured for each scan using various noise multiplication factors (see section 4.3.2.2). The sensitivity of the identification process was defined as the ratio of the number of correctly identified irreparable echoes to the number of irreparable echoes in the scan. The specificity of the identification process was defined as the number of correctly identified correctable echoes to the number of correctable echoes in the scan. The sensitivity and specificity of the identification process was calculated as follows:

$$Sensitivity = \frac{True\ positives}{True\ positives + False\ negatives}$$
$$Specificity = \frac{True\ negatives}{True\ negatives + False\ positives} \quad (4.10)$$

where 'true positives' is the number of echoes correctly identified as irreparable, 'false negatives' is the number of irreparable echoes erroneously identified as correctable, 'true negatives' is the number of echoes correctly identified as correctable, and 'false positives' is the number of correctable echoes erroneously identified as irreparable.

The performance of the reacquisition algorithm during the reacquisition process was analysed by using the algorithm to acquire scans at motion error rates of 30%, 50% and 70%. Subject motion leading to normally distributed $\mathbf{dk}_p$ and $\mathbf{dk}_s$ displacement errors with SD of 0.31 rad/mm was simulated during the scans. For each error rate, six scans were acquired using all the four different selection methods. The SAR, SGR and ADC_{error} were all recorded for analyses after each echo reacquisition.

4.3.4 Results and discussions

4.3.4.1 Differences between correctable and non-correctable navigator echoes

The assumption that correctable echoes are all very similar to one another requires that the differences between two navigator echoes with different level of correctable motion errors (i.e. $\mathbf{dk}_r$ and α phase error) to be small and independent of the motion error. The Euclidean distances between two navigator echoes with varying amount of α phase error and $\mathbf{dk}_r$ displacement error are shown in figure 4.19 and 4.20 respectively. As can be seen, the

Euclidean distances between the two correctable navigator echoes were indeed small and independent of the motion error. When the $|\mathbf{dk}_r|$ displacement error in one of the navigator echoes (e.g. navigator A) was a significant fraction of k_{max}, it began to differ significantly from the other navigator echo (e.g. navigator B). This result appears to contradict the previous statement and the assumption mentioned above. However, when the $|\mathbf{dk}_r|$ error in navigator A was very large, it was no longer correctable because a significant amount of its signal would have been lost through echo truncation. If the navigator echo was no longer correctable, its dissimilarity to correctable echoes was apt and thus the assumption above is still valid.

In the development of the 'clustering' method for identifying the reference echo (see section 4.3.2.1), it was assumed that correctable navigator echoes were always more dissimilar to irreparable echoes than to one another. Furthermore, it was assumed that this dissimilarity could be adequately measured using the Euclidean distance. In order for these assumptions to be true, the Euclidean distance between a correctable navigator echo and an irreparable navigator echo must always be greater than that between two correctable navigator echoes. The Euclidean distances between a correctable navigator echo, with varying amount of eddy current induced $\mathbf{dk}_p$ and $\mathbf{dk}_s$ displacement error, and a test navigator echo, with varying amount of additional motion induced $\mathbf{dk}_p$ and $\mathbf{dk}_s$ displacement errors are shown in figure 4.21 and 4.22 respectively. As can be seen, when the test navigator echo was a correctable echo (i.e. when it had no additional motion induced $\mathbf{dk}_p$ or $\mathbf{dk}_s$ error), the Euclidean distances between the navigator echoes was, with one notable exception, always less than when

the test echo was an irreparable echo. Thus, apart from the exception, the result confirms that the 'clustering' method assumptions were valid. The exceptional case occurred when the motion-induced $\mathbf{dk}_p$ and $\mathbf{dk}_s$ error in the irreparable echo was exactly double in magnitude but opposite in sign to that of the eddy-current induced $\mathbf{dk}_p$ and $\mathbf{dk}_s$ error. The reason for this phenomenon lies in the fact that the signal in an imaging slice is real and consequently it has conjugate symmetry in its time data[14]. Thus, when subject motion displaces an irreparable echo to an equal but opposite position in k-space to that of the correctable echoes, conjugate symmetry in the time data meant that the magnitude component of their projection signals were identical. An example of this phenomenon is illustrated in figure 4.23. To separate the two projections, the phase information must also be compared. Unfortunately, the phase comparison is not trivial as the presence of any $\mathbf{dk}_r$ and α phase errors in both navigator echoes must be accounted for. To determine the absolute values of the $\mathbf{dk}_r$ and α phase errors in the navigator echoes, a navigator echo without motion error has to be known *a priori*[9;10]. However, if such *a priori* information were available then the 'clustering' method would not be necessary. Therefore, in this work, it shall be assumed that the occurrences of subject motion leading to irreparable echoes with equal and opposite phase encoding to that of correctable echoes will be very rare and thus shall not alter the validity of the 'clustering' method assumptions significantly.

Similar comparisons to those of figure 4.21 and figure 4.22, but with additional noise signal, are shown in figures 4.24 and 4.25 respectively. As can be seen, the additional noise signal has increased the minimum Euclidean distances

between the correctable navigator echoes. However, this increase has not affected the ability of the Euclidean distances to resolve irreparable echoes from correctable echoes to any significant extent.

It was assumed in the development of the 'simple' and 'centric' selection methods (see section 4.3.2.3) that the differences between a correctable echo and an irreparable echo would increase monotonically with increasing motion induced $|\mathbf{dk}_p|$ and $|\mathbf{dk}_s|$ errors. The same assumption was also made in step (v) of the reacquisition process in deciding whether to accept or reject a reacquired echo (see section 4.3.2.4). From figure 4.21b and 4.22b, it can be seen that the increase in Euclidean distances with increasing motion-induced $\mathbf{dk}_p$ and $\mathbf{dk}_s$ error is only monotonic and symmetric over a small range of motion error size. Thus, in general, the above assumption is false. The implication of this result for the selection methods is that the irreparable echo with the largest motion error will not always be selected first, as had been assumed. However, this should not affect the image quality of the reacquired image as long as all the irreparable echoes are reacquired. If not all of the irreparable echoes are reacquired then the image quality of the scan may be inferior to that which would have been achieved had the echoes with the largest motion error been reacquired first as intended. The implication of the invalidity of the above assumption for the process of deciding whether to accept or reject reacquired echoes is that it may sometimes make a wrong decision. Reacquired echoes with large motion error may sometimes be accepted over echoes with smaller motion error. In such cases, the image quality of the reacquired scan may deteriorate temporarily. However, because correctable echoes are always more

similar to the reference echo than irreparable echoes (apart from one rare exception discussed earlier), correctable echoes will always be accepted over irreparable echoes. Thus, as increasing numbers of correctable echoes are acquired, the image quality of the scan should continue to improve. In the rare event that an irreparable navigator echo with opposite phase encoding to the reference navigator echo is acquired then, due to its similarity with the reference echo, it will be erroneously accepted and retained in the scan. In such cases, the image quality of the reacquired scan will be compromised by the residual irreparable echo in the scan. However, it is expected that such events will be very rare and thus should not affect the overall performance of the reacquisition algorithm significantly.

4.3.4.2 Reference echo identification accuracy

Figure 4.26 shows the accuracy of the 'clustering' method in identifying correctable navigator echoes as the reference navigator echo under various simulation conditions. As can be seen, the 'clustering' method was successful in identifying a correctable navigator echo as the reference navigator echo at least 99% of the time under all the simulated conditions. On the rare occasions when the 'clustering' method did fail to identify a correctable echo as the reference echo, the reference echo had either very small motion error or motion error that caused its phase encoding position to be opposite to that of the correctable echoes. In either case, the reference echo signal was still very similar to that of the correctable echoes. Therefore, the motion error in the reference echo should not affect the accuracy of the irreparable echoes identification process significantly. However, because the reference echo is

assumed to be perfect, it will not be reacquired and thus its motion error will always be retained in the final scan. In the case where the motion error is small, this is unlikely to cause significant image degradation in the final scan. However, in the case where the motion error caused the reference's phase encoding position to be opposite to that of the correctable echo, the motion error can be quite large (double that of the eddy current effects) and significant ghosting artefacts may occur. This is particularly true if that large motion error had occurred in an image echo with low phase encoding. However, the chance of such a combination of events occurring is very small.

4.3.4.3 Irreparable echoes identification accuracy

The sensitivity and specificity (see section 4.3.3, equation 4.10 for definition) of the reacquisition algorithm in identifying irreparable echoes at different multiplication factors are shown in figure 4.27a. The mean motion induced $\mathbf{dk}_p$ and $\mathbf{dk}_s$ errors in the echoes that were erroneously classified as correctable at different multiplication factors are shown in figure 4.27b. The results shown in figure 4.27 were obtained from 100 scans simulated without any eddy currents effects and with the noise level set such that the SNR in an uncorrupted scan was 25. From figure 4.27a, it can be seen that the sensitivity of the identification process was greater than 99% for all multiplication factors less than 4. The specificity of the identification process was poor at low multiplication factors but it increased rapidly with increasing multiplication factor and was virtually 100% at a multiplication factor of two. From figure 4.27b, it can be seen that the mean motion induced $|\mathbf{dk}_p|$ and $|\mathbf{dk}_s|$ displacement error in those echoes that were erroneously classified as correctable increased

monotonically with increasing multiplication factor. The increase in the $|\mathbf{dk}_s|$ error was much greater than that in the $|\mathbf{dk}_p|$ error and reflected the fact that for a given error size, the effects of a $\mathbf{dk}_s$ displacement error on the navigator echo signal are much smaller than that of a $\mathbf{dk}_p$ displacement error.

The effects of additional noise on the sensitivity and specificity of the identification process are shown in figure 4.28a. As can be seen, for a given multiplication factor, the sensitivity of the identification process decreased significantly with increasing noise signal (i.e. decreasing SNR). In contrast to the sensitivity, the specificity of the identification process was virtually independent of the noise signal. The decrease in sensitivity with decreasing SNR reflects the fact that, as the noise signal increases, it becomes increasingly difficult to determine whether the differences between a given navigator echo and the reference navigator echo is due to noise signal or motion error. In this work, the 'irreparable echo' threshold (i.e. the threshold that is used to decide whether the differences between a navigator echo and the reference echo are due to noise signal or subject motion) is calculated directly from the navigator echoes themselves. Therefore, when the noise signal in a scan is increased, the 'irreparable echo' threshold will also increase correspondingly. The increase in the 'irreparable echo' threshold causes an inevitable increase in the numbers of irreparable echoes being erroneously classified as correctable and thus decreases the sensitivity of the identification process. Unfortunately, to account for the greater differences that would be obtained between correctable echoes with greater noise signal, the increase in the 'irreparable echo' threshold is unavoidable. The lack of variation in the specificity of the identification process

with varying noise signal showed that the 'irreparable echo' threshold had successfully accounted for the variation in the noise signal. The effect of additional noise on the mean motion error in those echoes that were erroneous classified as correctable is shown in figure 4.28b. As can be seen, for a given multiplication factor, the mean motion error in those echoes that were incorrectly classified as correctable increased monotonically with increasing noise signal. This increase reflected the fact that as the noise signal and 'irreparable echo' threshold got larger, bigger motion errors were becoming indistinguishable from the noise signal.

The effect of eddy current induced phase encoding on the identification process sensitivity and specificity is shown in figure 4.29a. As can be seen, the specificity was virtually unaffected by the eddy currents induced phase encoding, whilst the sensitivity was only altered slightly. The slight change in sensitivity reflects the fact that changes in the navigator echo signal due to motion errors are dependent on both the motion induced error and the initial phase encoding position of the navigator echo (i.e. its phase encoding position without any motion error). Certain initial phase encoding positions lead to greater changes in the navigator echo signal for a given motion induced error than others. The greater the changes, the easier it is to detect the motion error and thus the better the sensitivity of the identification process. The effect of eddy current induced phase encoding on the mean motion error present in those echoes that were erroneously identified as correct is shown in figure 4.29b. Despite the fact that the sensitivity of the identification process was largely unchanged, the mean $|\mathbf{dk}_p|$ and $|\mathbf{dk}_s|$ errors in those echoes that were

erroneously identified as correctable were markedly increased. The increase was due to the fact the initial navigator echo position was no longer in the centre of k-space, which allowed the following two phenomena to occur. Firstly, it was possible for a navigator echo with phase encoding position opposite to that of the reference echo to appear similar to the reference echo and thus be erroneously identified as correctable. Secondly, it was possible for certain combinations of $\mathbf{dk}_p$ errors (that increased the navigator signal) and $\mathbf{dk}_s$ errors (that decreased the navigator signal) to appear to cancel out each other effects. In such cases, the navigator echo can appear to be similar to the reference echo and be erroneously identified as correctable.

The effects of eddy currents induced phase encoding along the slice-selective direction on the identification process are shown in figure 4.30. The changes in sensitivity with increasing eddy current induced slice-selective phase encoding are similar to that shown in figure 4.29a and are due to the same reason. The mean $|\mathbf{dk}_p|$ and $|\mathbf{dk}_s|$ errors in those echoes that were erroneously identified as correctable were also markedly increased and occurred for similar reasons.

From the results shown in figure 4.27 to 4.30, it was decided that a noise multiplication factor of two should be used to determine the 'irreparable echo' threshold in the identification process. At a value of two, it can be seen that the specificity of the identification process was virtually 100%, whilst the sensitivity was at least 98% for all the noise and eddy currents conditions analysed. Thus in the worst-case scenario, where 70% of the 128 navigator echoes in the scan were irreparable, the mean numbers of irreparable echoes

that would be expected to be erroneously identified as correctable is only two. Furthermore, the mean $\mathbf{dk}_p$ and $\mathbf{dk}_s$ error in these corrupted echoes would be expected to be only a fraction of the spacing between adjacent k-space samples (i.e. 2π/FOV = 0.03 rad/mm).

4.3.4.4 Reacquisition performance: a comparison between different selection methods

A typical example of the performance of the reacquisition algorithm using the optimum selection procedure at motion error rates of 30%, 50% and 70% is shown in figure 4.31. As can be seen, the total scanning time required to remove all the irreparable echoes from a scan (i.e. to achieve minimum ASR) increased dramatically with increasing error rate. With 128 phase encoding steps and a TR of 2s, the theoretical scanning times required to acquire an image without irreparable echoes at motion error rates of 30%, 50% and 70% are 6.1, 8.5 and 14.2 minutes respectively. Inspection of the graph showed that for each of the motion error rates, the ASR was indeed asymptotic at these times and the residue artefact signal was equal to the noise signal, indicating that all irreparable echoes have been removed from the scan. From figure 4.31, it can be seen that the use of the 'optimum' selection method has lead to an extremely rapid decline in ghosting artefacts during the initial phase of the reacquisition procedure, with more than 50% of the ghosting artefacts in the scan being eliminated during the first 10% of the reacquisition period. The rapid decline in ghosting artefacts during the reacquisition process lends further support the hypothesis that most of the ghosting artefacts in a corrupted scan is due to a few of the most significant irreparable echoes.

A comparison of the reacquisition performance of the four different selection methods at error rates of 30%, 50% and 70% is shown in figure 4.32. From figure 4.32, it can be seen that at all error rates, the 'optimum' selection method yielded the greatest decline in ghosting artefact at all times during the reacquisition process. However, the performance of the 'artefact' selection method was very close to that of the 'optimum' selection method and at times was equal to it. This result, therefore, supports the hypothesis that by identifying and reacquiring irreparable echoes based on their ghosting effects, near optimal improvement in ghosting artefact per unit time can be achieved. The performance of the 'centric' selection method was inferior to that of the 'artefact' selection method. However, the difference was not substantial. In contrast, the performance of the 'simple' selection method was very poor for much of the reacquisition period. Whereas the others selection methods achieved most of the ghosting artefact improvement during the initial phase of the reacquisition process, the 'simple' selection method demonstrated very variable improvement throughout the process. Consequently, its performance lagged that of the other selection methods up until the theoretical scanning time required to remove all irreparable echoes from the scan was reached.

Despite its relative simplicity, the performance of the 'centric' selection method has been shown to be almost equal to that of the much more demanding and practically unrealisable 'artefact' selection method. The reason for the inferior performance of the 'centric' selection method in comparison with the 'artefact' selection method lies in the fact that the 'centric' selection method could not always select the irreparable echo that caused the greatest ghosting artefact for

reacquisition first. This can be seen in the performance of the 'centric' selection method during the initial reacquisition period (see figure 4.32c). The ASR of the scan during the initial reacquisition period showed a characteristic successions of rapid decline followed by a period of slower decline. The period of rapid decline corresponds to those times when echoes with large motion errors from the centre of k-space (i.e. those that caused a large amount of ghosting artefact) were selected and reacquired. The period of slower decline corresponds to those times when echoes that, although centrally located, had only been affected by small motion errors, were selected and reacquired. The selection of these echoes had occurred because of two reasons. Firstly, it was not possible for the 'centric' selection method to determine accurately the size of the motion error in each echo (see section 4.3.4.1). Secondly, the 'centric' selection method was designed to select centrally located irreparable echoes, regardless of their motion errors, before more peripheral echoes. These shortcomings of the 'centric' selection method could be overcome if, firstly, it was possible to determine the size of the motion error in an irreparable echo with greater accuracy, and secondly, the relative importance of the phase encoding position and motion error size to the genesis of ghosting artefact could be better accounted for. However, given that the performance of the 'centric' selection method is only slightly inferior to that of the 'artefact' and 'optimum' selection method, any increase in reacquisition performance by a more advanced selection procedure is unlikely to be justified by the necessary increase in complexity.

4.3.5 Summary and conclusion

Using computer simulation, it was demonstrated that the identification and selective reacquisition of irreparable echoes in diffusion-weighted imaging was possible under most scanning conditions. By selectively reacquiring irreparable echoes, it was demonstrated that high quality diffusion-weighted images could be obtained in the theoretical time shown in equation 4.3. It was also shown that by using a reacquisition algorithm that identified and reacquired echoes in descending order of their ghosting effects (hereafter known as the 'artefact' reacquisition algorithm), near optimal improvement in ghosting artefact per unit time could achieved. Although the 'artefact' reacquisition algorithm is not realisable outside the simulation environment, an approximation of the 'artefact' reacquisition algorithm (hereafter known as the 'centric' reacquisition algorithm) that could be implemented in the real world was demonstrated to be almost as good. A 'simple' reacquisition algorithm that reacquired irreparable echoes without consideration of their ghosting effects was also demonstrated. It was shown that although the 'simple' reacquisition algorithm was able to remove all irreparable echoes from a scan and could achieve high quality images by the end of the reacquisition process, the improvement in ghosting artefact during much of the reacquisition process was far poorer than that achieved by the 'centric' reacquisition technique. In the clinical environment where scanning time is limited, it may not be possible to wait until all irreparable echoes are reacquired and a compromise between scan image quality and scanning time may sometimes be necessary. Thus, in the clinical

environment, the 'centric' reacquisition algorithm should be superior as it offers near optimal improvement in ghosting artefact for a given reacquisition period.

Reference List

1. Le Bihan D, Breton E, Lallemand D, Grenier P, Cabanis E, Laval-Jeantet M. MR imaging of intravoxel incoherent motions: application to diffusion and perfusion in neurologic disorders. **Radiology** 1986; **161**: 401-407.

2. Le Bihan D, Breton E, Lallemand D, Grenier P, Cabanis E, Laval-Jeantet M. Separation of diffusion and perfusion in intravoxel incoherent motion MR imaging. **Radiology** 1988; **168**: 497-505.

3. Turner R, Le Bihan D, Maier J, Vavrek R, Hedges LK, Pekar J. Echo-Planar imaging of intravoxel incoherent motion. **Radiology** 1990; **177**: 407-414.

4. Gudbjartsson H, Maier J, Mulkern RV, Morocz IA, Patz S, Jolesz FA. Line Scan Diffusion Imaging. **Magnetic Resonance In Medicine** 1996; **36**: 509-519.

5. Merboldt K-D, Hanicke W, Bruhn H, Gyngell ML, Frahm J. Diffusion imaging of the human brain *in vivo* using high speed STEAM MRI. **Magnetic Resonance In Medicine** 1992; **23**: 179-192.

6. Yongbi MN, Ding S, Dunn JF. A modified sub-second fast-STEAM sequence incorporating bipolar gradients for in vivo diffusion imaging. **Magnetic Resonance In Medicine** 1996; **35**: 911-916.

7. Brummett R, Talbot M, Charuhas P. Potential hearing loss resulting from MR imaging. **Radiology** 1988; **169**: 539-540.

8. Dietrich O, Heiland S, Benner T, Sartor K. Reducing motion artefacts in diffusion-weighted MRI of the brain: efficacy of navigator echo correction and pulse triggering. **Neuroradiology** 2000; **42**: 85-91.

9. Ordidge RJ, Helpern JA, Qing ZX, Knight RA, Nagesh V. Correction of motional artifacts in diffusion-weighted MR images using navigator echoes. **Magnetic Resonance Imaging** 1994; **12**: 455-460.

10. Anderson AW, Gore JC. Analysis and correction of motion artifacts in diffusion weighted imaging. **Magnetic Resonance In Medicine** 1994; **32**: 379-387.

11. Trouard TP, Sabharwal Y, Altbach MI, Gmitro AF. Analysis and comparison of motion-correction techniques in diffusion-weighted imaging. **Journal of Magnetic Resonance Imaging** 1996; **6**: 925-935.

12. Gmitro AF, Alexander AL. Use of a projection reconstruction method to decrease motion sensitivity in diffusion-weighted MRI. **Magnetic Resonance In Medicine** 1993; **29**: 835-838.

13. van Gelderen P, de Vleeschouwer MHM, Despres D, Pekar J, van Zijl PCM, Moonen CTW. Water diffusion and acute stroke. **Magnetic Resonance In Medicine** 1994; **31**: 154-163.

14. Bracewell RN. The Fourier transform and its applications. New York: MC Graw-Hill, 1986;

15. Weiger M, Bornert P, Proksa R, Schaffter T, Haase A. Motion-adapted gating based on k-Space weighting for reduction of respiratory motion artifacts. **Magnetic Resonance In Medicine** 1997; **38**: 322-333.

16. Fuderer M. The information content of MR images. **IEEE Transactions of Medical Imaging** 1988; **7**: 368-380.

17. Liu Q, Hughes D, Allen PS. Quantitative characterization of the eddy-current fields in a 40 cm bore superconducting magnet. **Magnetic Resonance In Medicine** 1994; **31**: 73-76.

18. Carlson JW, Derby KA, Hawryszko KC, Weideman M. Design and evaluation of shielded gradient coils. **Magnetic Resonance In Medicine** 1992; **26**: 191-206.

19. Terpstra M, Andersen P, Gruetter R. Localized eddy current compensation using quantitative field mapping. **Journal Of Magnetic Resonance** 1998; **131**: 139-143.

20. Reese TG, Weisskoff RM, Wedeen VJ. Diffusion NMR facilitated by a refocused eddy-current EPI pulse sequence. **Proc.Sixth Annual Meeting of the Society of Magnetic Resonance in Medicine** 1998; 663

ω_r (rad/s)	ω_p (rad/s)	ω_s (rad/s)	$\mathbf{dk_p}$ (rad/mm)	$\mathbf{dk_s}$ (rad/mm)
0.0	0.0	0.0	0.00	0.00
0.0	0.0	0.2	-0.24	0.00
0.0	0.0	0.4	-0.47	0.00
0.0	0.0	0.6	-0.71	0.00
0.0	0.0	0.8	-0.94	0.00
0.0	0.0	1.0	-1.18	0.00
0.0	1.0	0.0	0.00	1.18
1.0	0.0	0.0	0.00	0.00

Table 4.1 Typical values of $\mathbf{dk_p}$ and $\mathbf{dk_s}$ displacement errors at various rotational velocities (ω) for the diffusion parameters described in section 4.2.2. N.B. k_{max} = 2.51 rad/mm for the imaging parameters described.

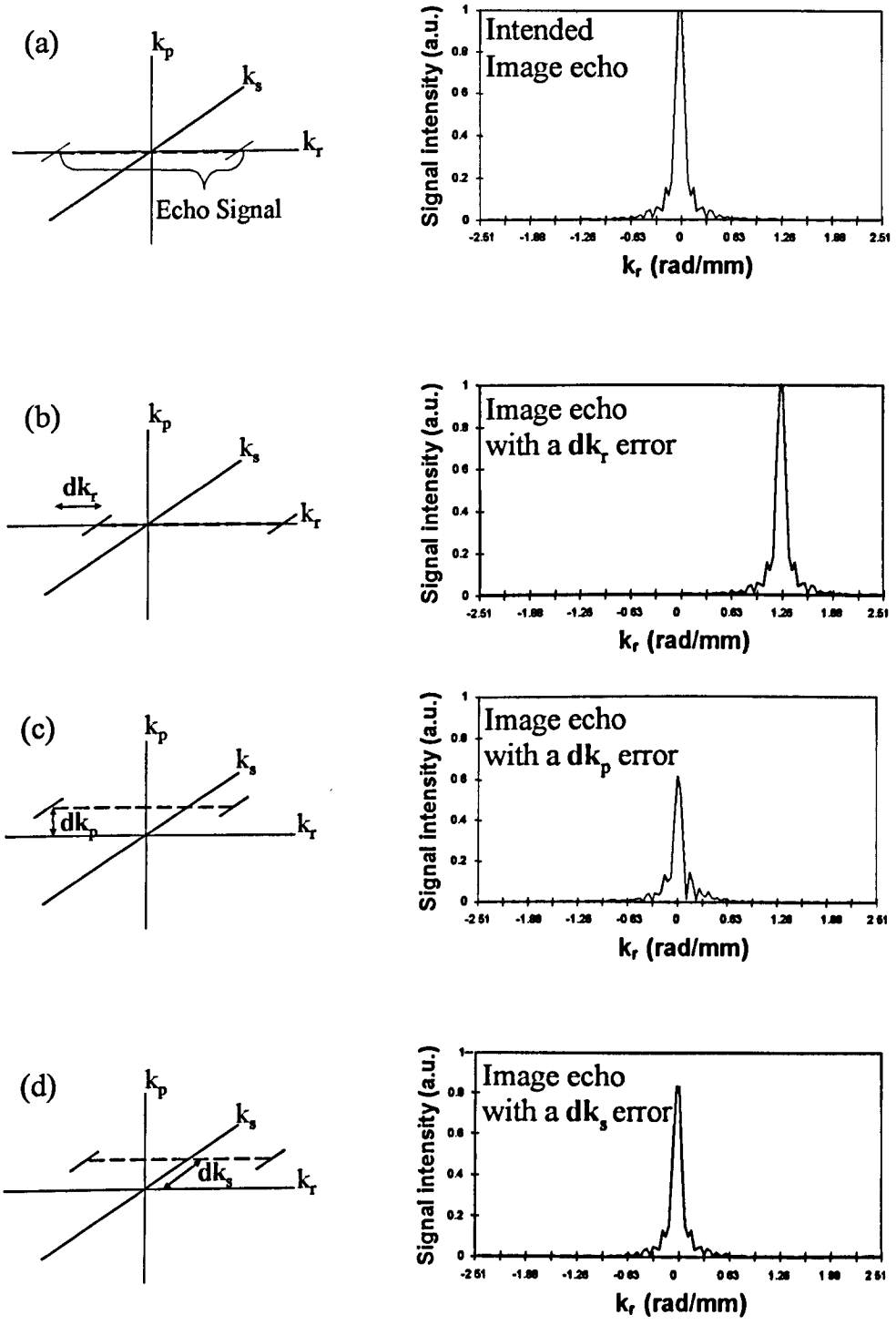

Figure 4.1 Examples of k-space displacement errors and their effects on a spin echo. (a) A typical spin echo at its intended position in k-space and its amplitude signal. The same spin echo following (b) a dk_r error, (c) a dk_p error and (d) a dk_s error.

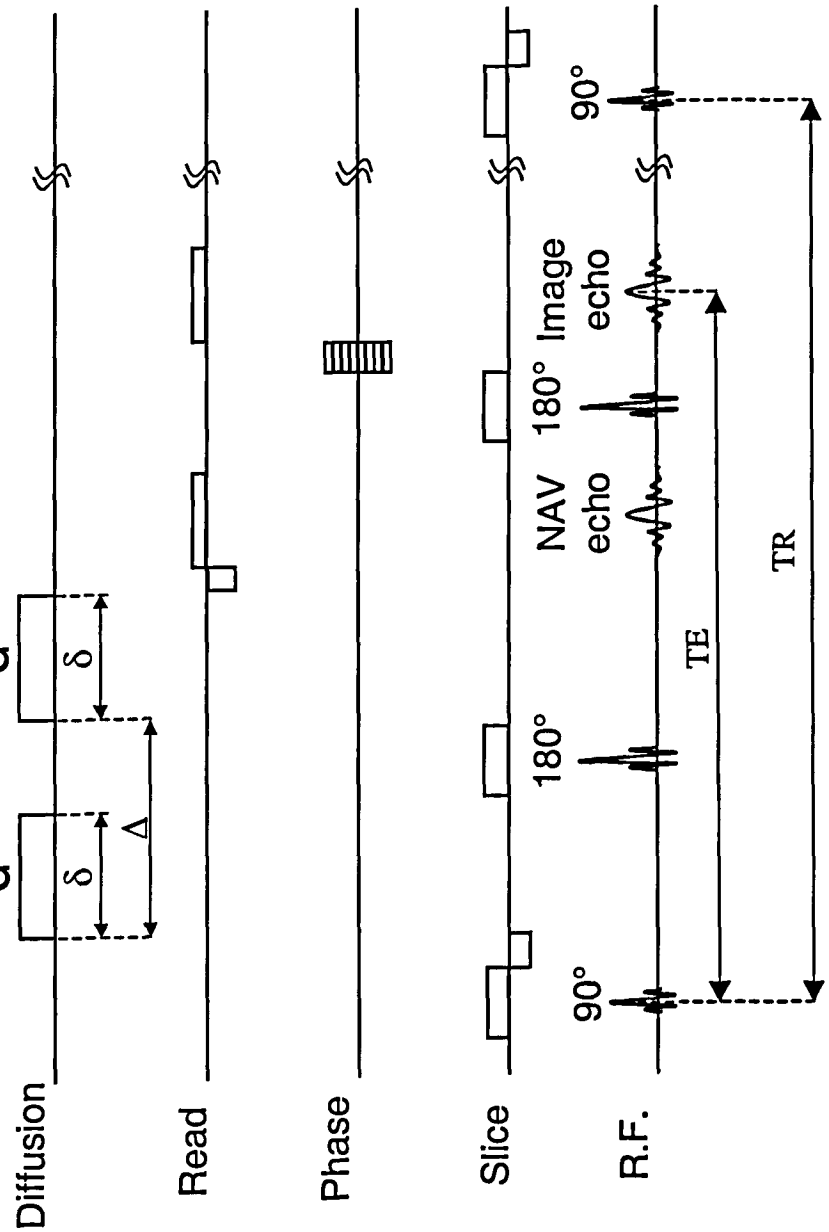

Figure 4.2 Navigated PGSE DWI sequence used in the simulation study of irreparable displacement errors. **G** is the diffusion gradient strength, δ is the diffusion gradient duration, and Δ is the separation between the rising edges of the two diffusion gradients.

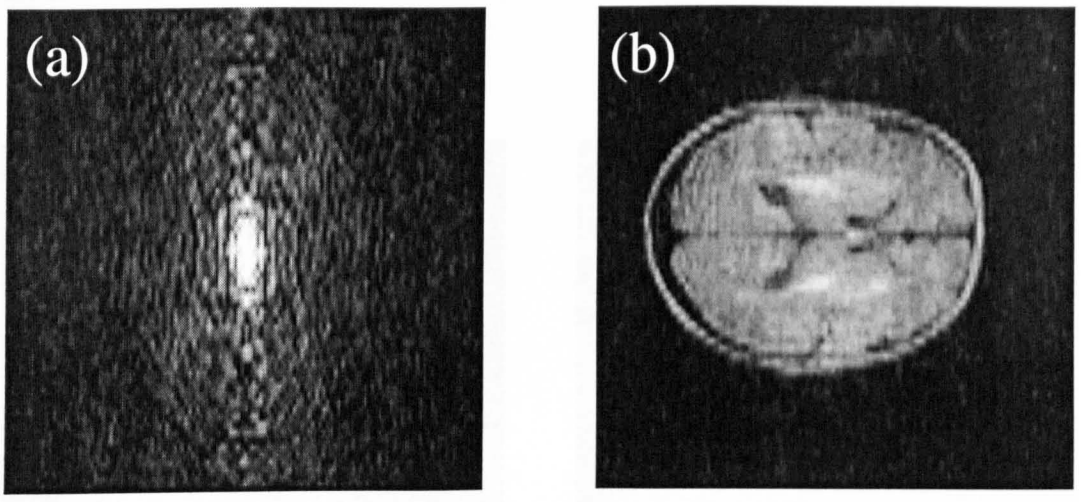

Figure 4.3 Imaging slice data used in the simulation study of irreparable displacement errors. (a) Raw time data and its corresponding (b) reconstructed image data.

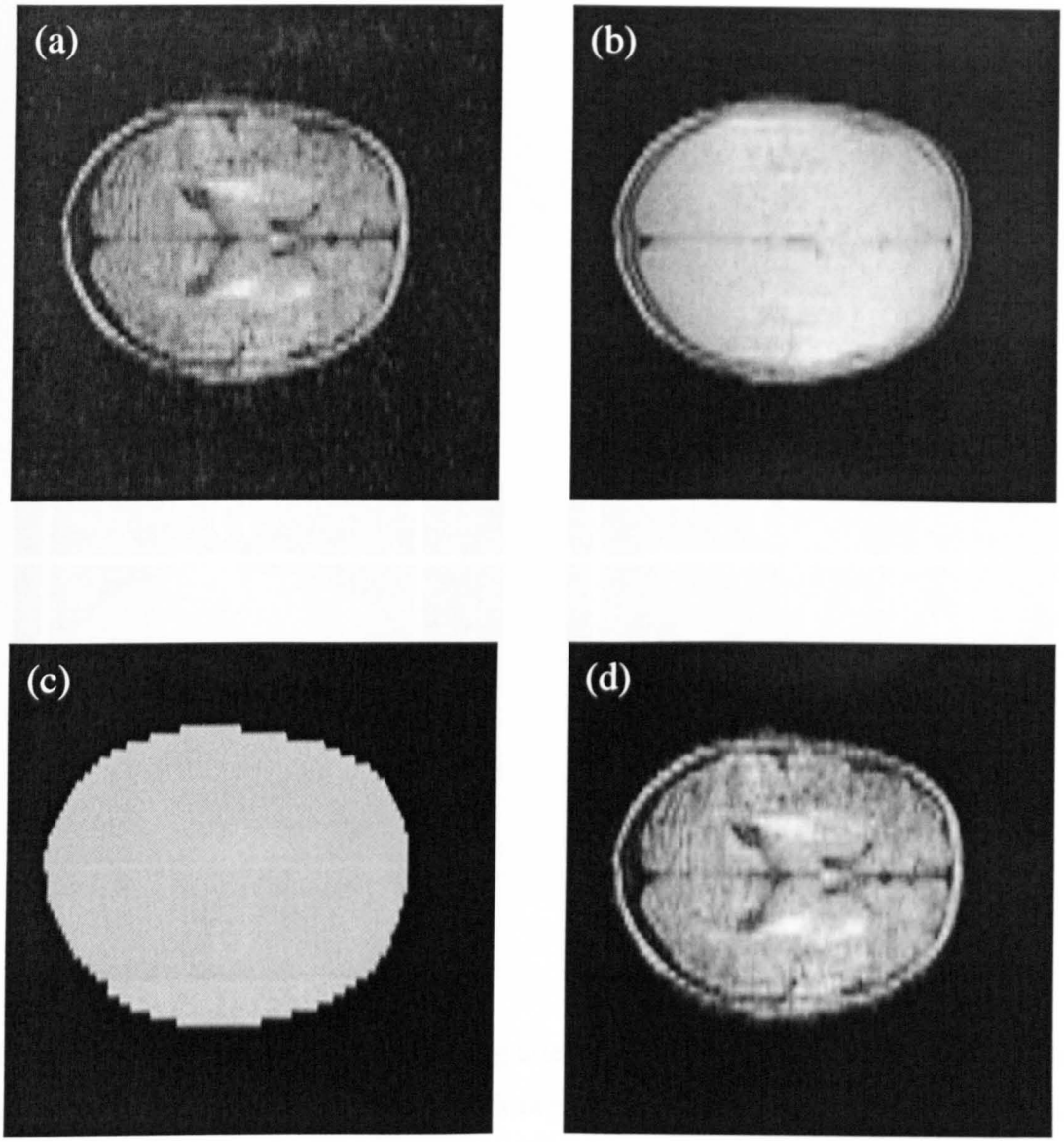

Figure 4.4 Removal of background noise from the diffusion-weighted image used in the simulation study. (a) Diffusion-weighted image of a neonatal brain obtained from a previous study. (b) Proton-weighted image of the same patient obtained at the same time. (c) Mask image of the imaging slice generated by thresholding the proton-weighted image signal at 10%. (d) Diffusion-weighted image used in the simulation study formed by the product of the raw diffusion-diffusion image (a) and the mask image (c).

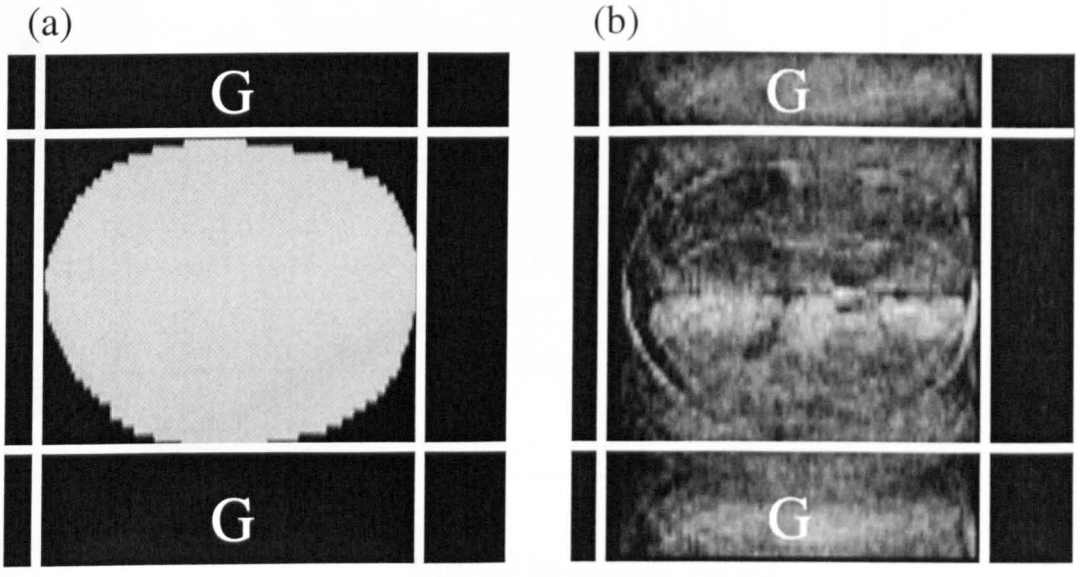

Figure 4.5 Determination of the ghosting artefact Region Of Interest (ROI). (a) Mask image of imaging slice with two lines drawn horizontally and vertically at the edges of the imaging slice. The areas labeled G, on either sides of the imaging slice along the phase-encoding direction, are taken as the ROI containing the ghosting artefact. (b) Overlay of the ghosting artefact ROI on a motion corrupted scan.

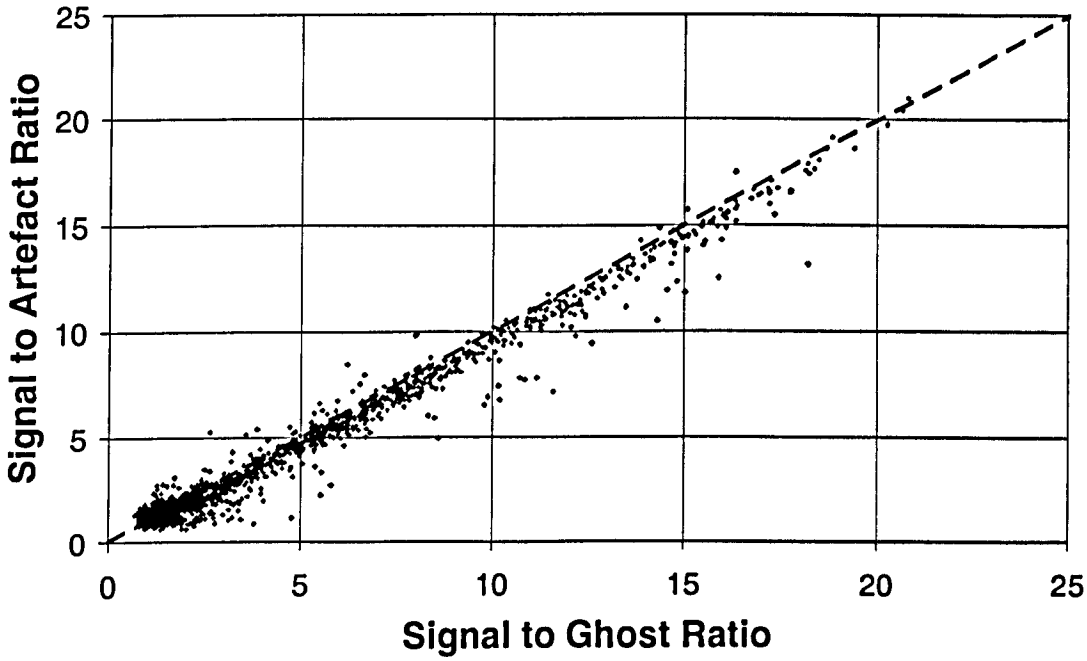

Figure 4.6 Relationship between the signal to ghost ratio and the signal to artefact ratio. The signal to ghost ratio was calculated as the ratio of the mean corrupted signal within the imaging slice to the mean signal in the ghosting ROIs. The signal to artefact ratio was calculated as the ratio of the mean true image signal to the mean signal differences between the true and the corrupted image within the imaging slice.

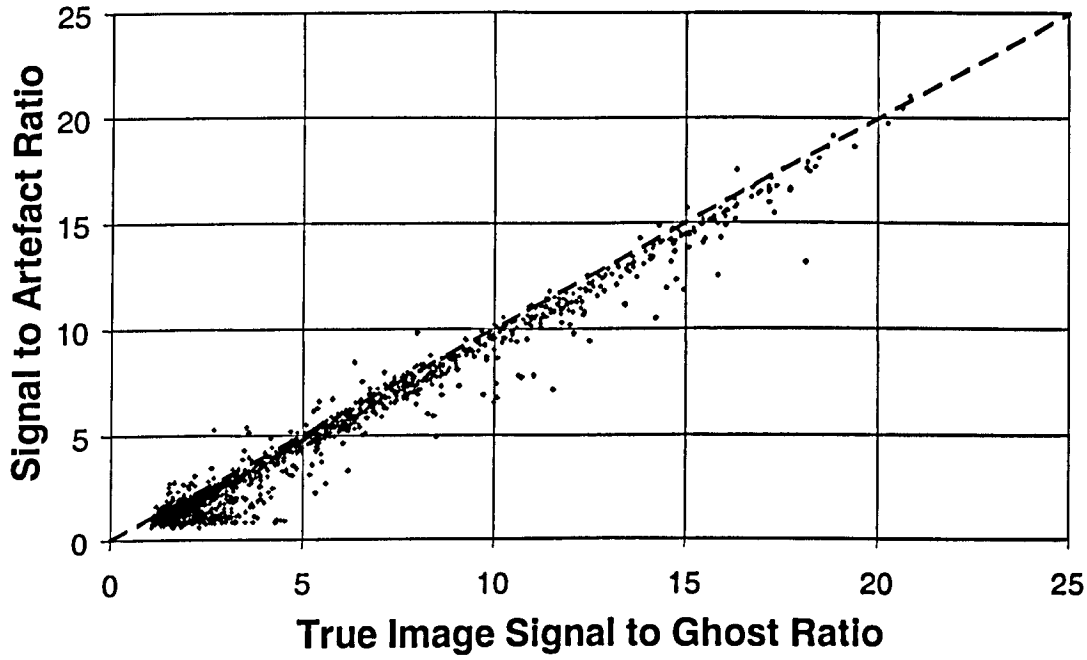

Figure 4.7 Relationship between the true image signal to ghost ratio and the signal to artefact ratio. The signal component in calculation of both ratios was measured from the true image. The ghost component was measured from ghost ROIs in the corrupted image, whilst the artefact component was measured from the difference image between the true image and the corrupted image.

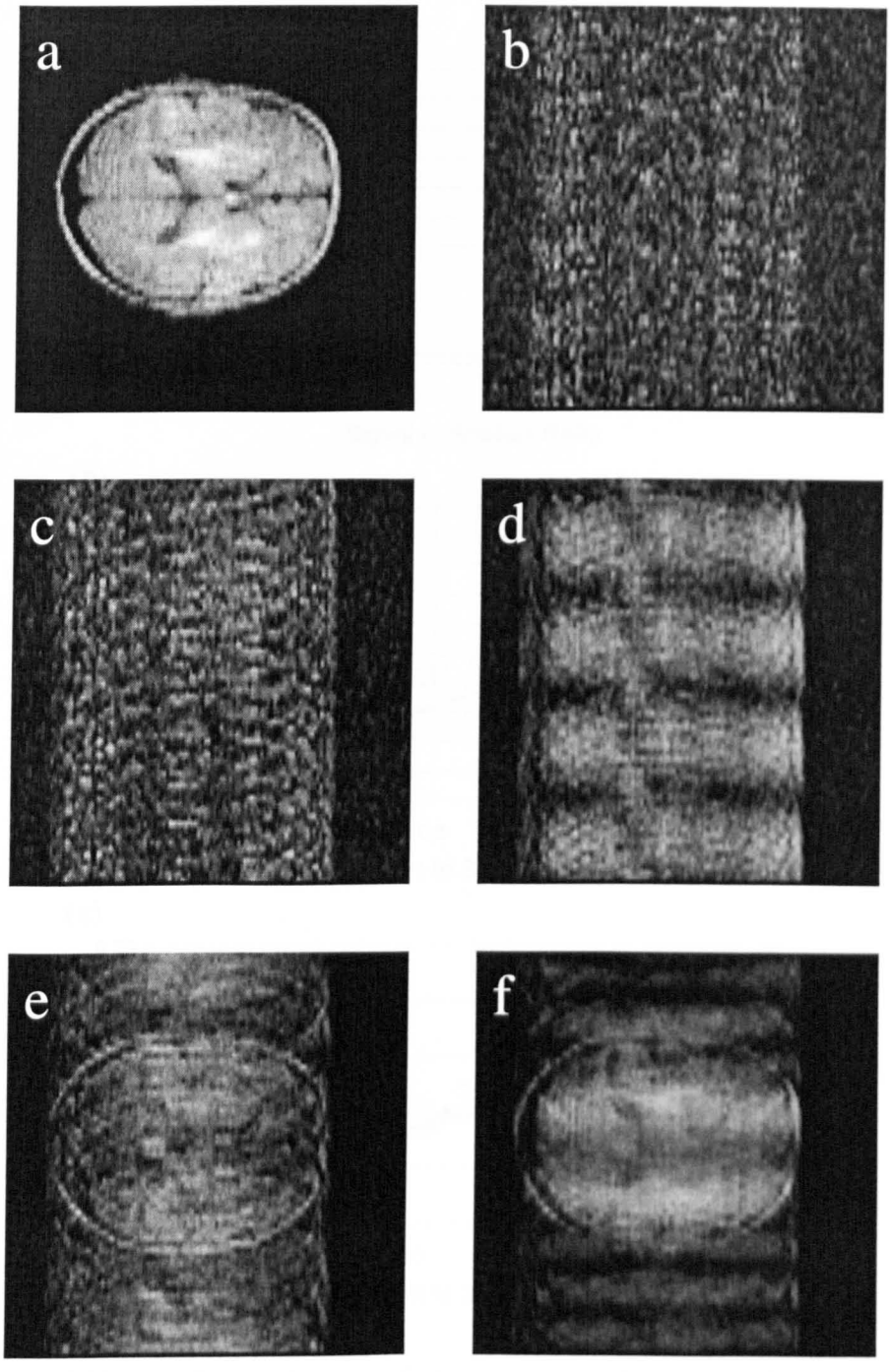

Figure 4.8. Spatial relationship between the true scan image and the error images at different Signal to Ghost Ratio (SGR). An error image being defined here as the difference image between the true image and a motion corrupted image. (a) True scan image. Typical error image at SGR of (b) 15, (c) 10, (d) 5, (e) 2 and (f) 1.

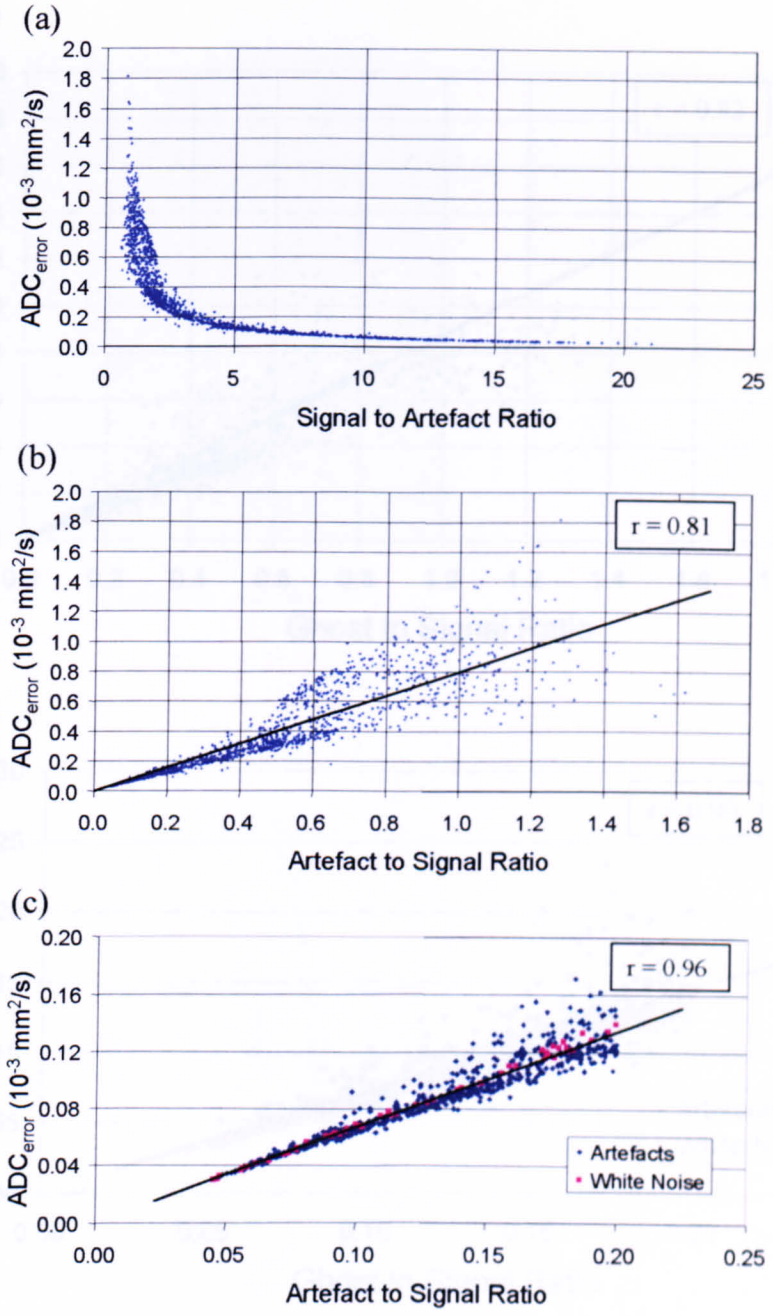

Figure 4.9 Effects of ghosting artefacts on the ADC quantification process. (a) Relationship between the Signal to Artefact Ratio (SAR) and the ADC_{error}. (b) Relationship between the Artefact to Signal Ratio (ASR) and the ADC_{error}. (c) Relationship between the ASR and the ADC_{error} at low ghosting artefact level. The effects of white noise on the ADC quantification process are also shown for comparison. Note that, in the absence of ghosting artefacts, the ASR is equivalent to the reciprocal of the SNR.

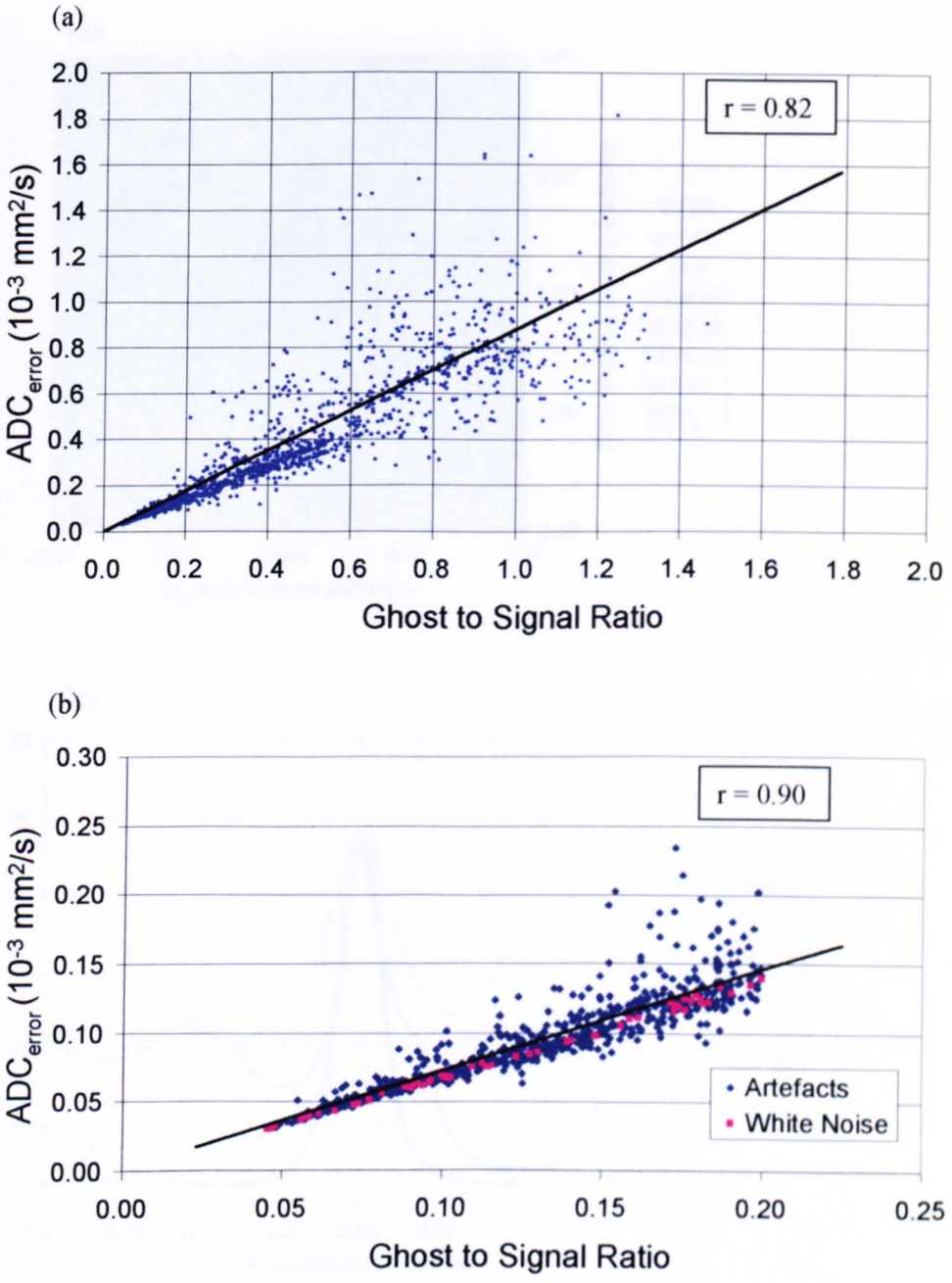

Figure 4.10 Effects of ghosting artefacts on the ADC quantification process. (a) Relationship between the Ghost to Signal Ratio (GSR) and the ADC_{error}. (b) Relationship between the GSR and the ADC_{error} in scans with modest ghosting artefacts (GSR<0.2). The effects of white noise on the ADC quantification process are also shown for comparison. Note that, in the absence of ghosting artefacts, the GSR is equivalent to the reciprocal of the SNR.

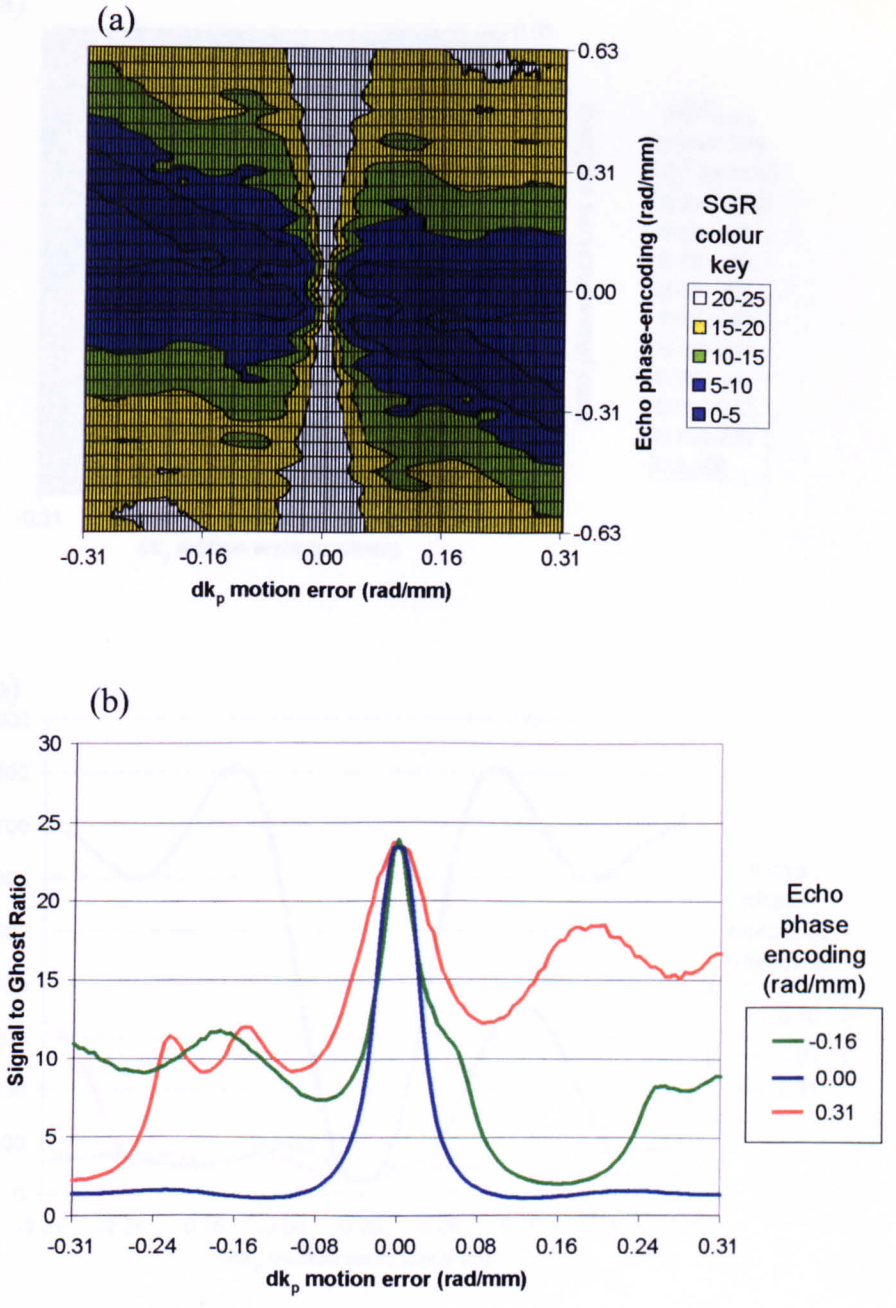

Figure 4.11 (a) Contour plot showing an overview of the ghosting artefact due to an irreparable echo at different phase-encoding positions with varying values of $\mathbf{dk_p}$ error. The ghosting artefact was measured using the Signal to Ghost Ratio (SGR) (see text). A low SGR indicates poor image quality with high level of ghosting artefact and vice versa. (b) Line plot showing the ghosting artefact due to an echo with $\mathbf{dk_p}$ error at a few selected phase-encoding positions.

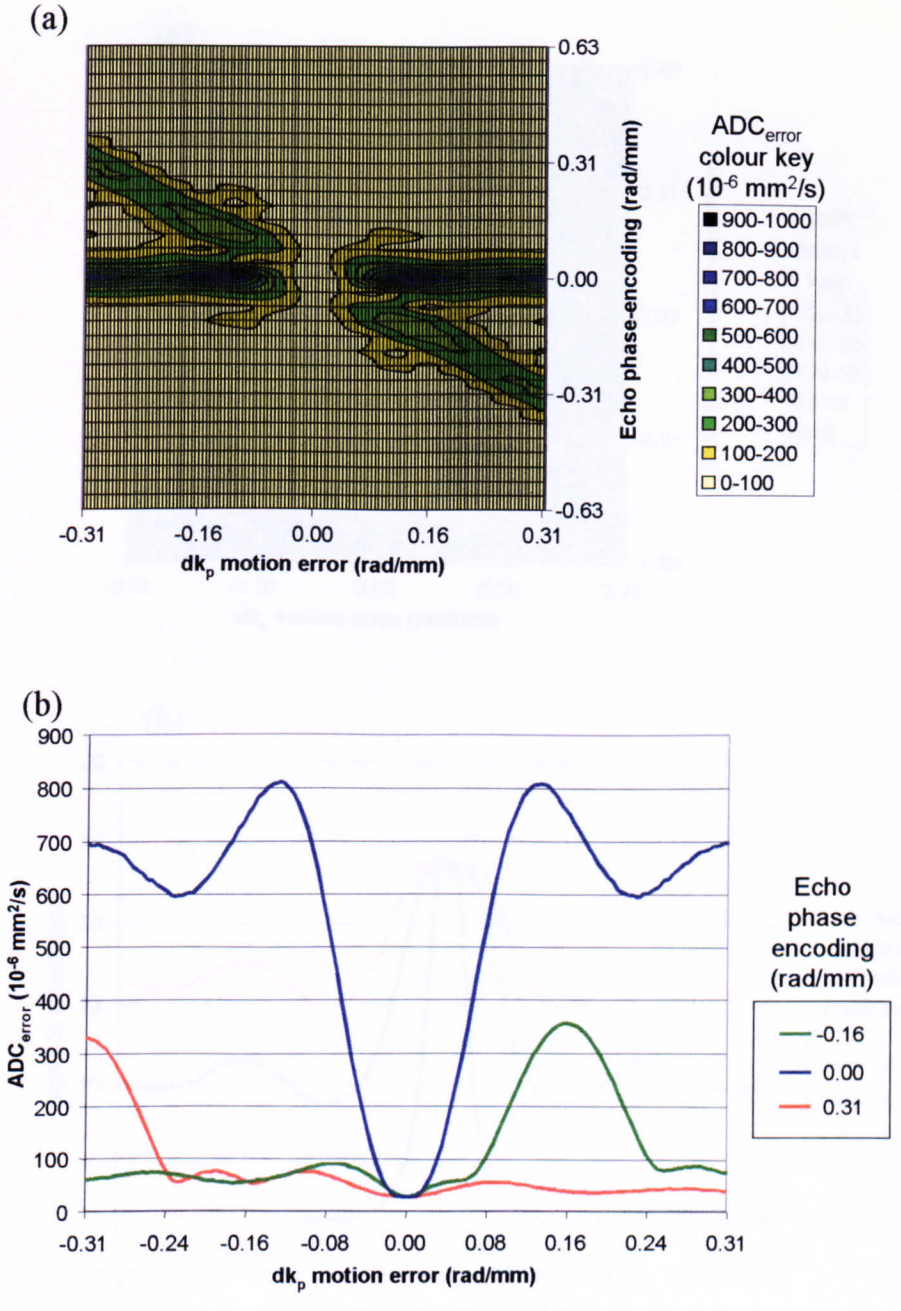

Figure 4.12 (a) Contour plot showing an overview of the ADC quantification error due to an irreparable echo at different phase-encoding positions with varying values of $\mathbf{dk_p}$ error. The ADC quantification error was measured using the ADC_{error} (see text). A high ADC_{error} indicates poor ADC quantification accuracy with high level of quantification error and vice versa. (b) Line plot showing the ADC quantification error due to an echo with $\mathbf{dk_p}$ error at a few selected phase-encoding positions.

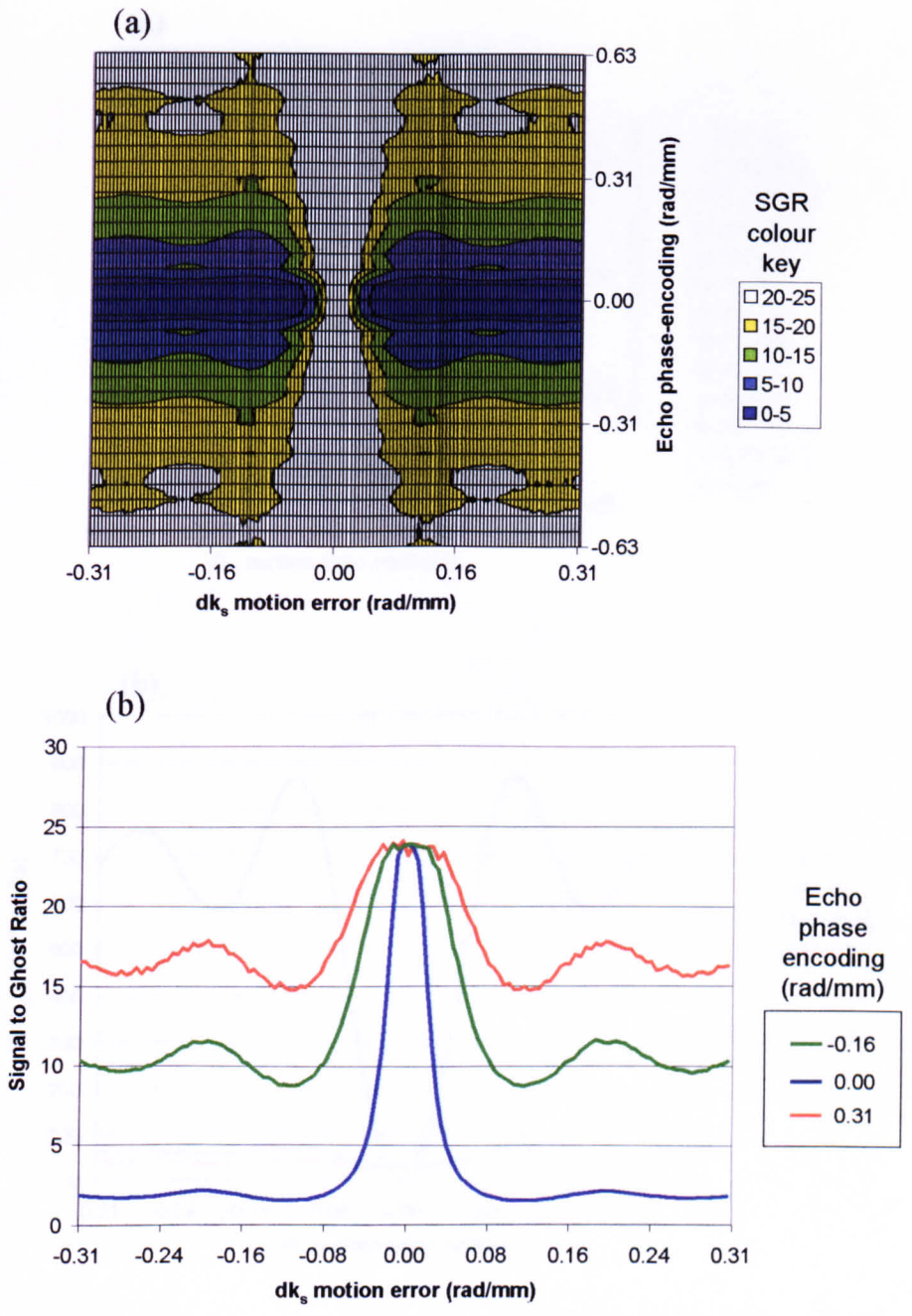

Figure 4.13 (a) Contour plot showing an overview of the ghosting artefact due to an irreparable echo at different phase-encoding position with varying values of $\mathbf{dk}_s$ error. The ghosting artefact was measured using the Signal to Ghost Ratio (SGR) (see text). A low SGR indicates poor image quality with high level of ghosting artefact and vice versa. (b) Line plot showing the ghosting artefact due to an echo with $\mathbf{dk}_s$ errors at a few selected phase-encoding positions.

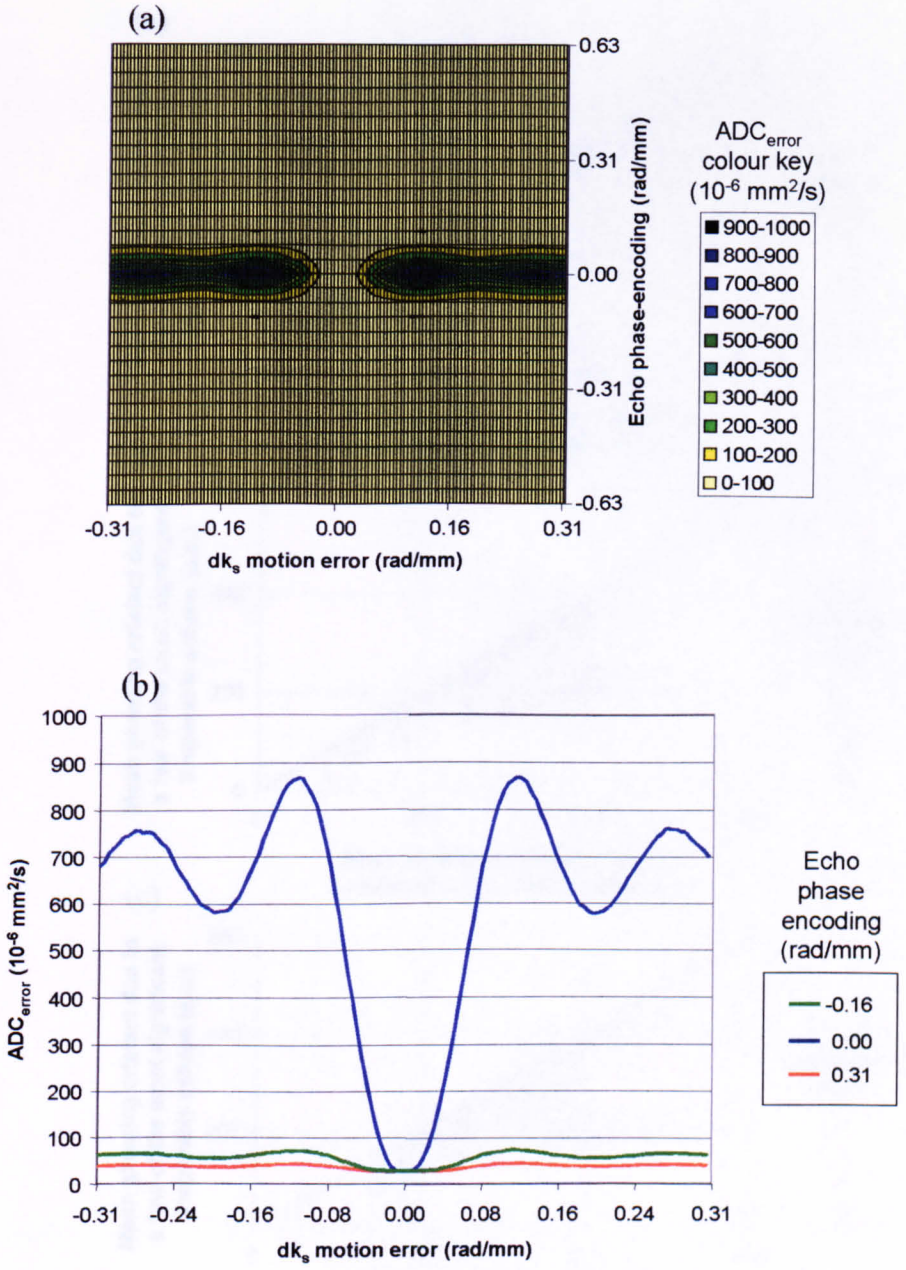

Figure 4.14 (a) Contour plot showing an overview of the ADC quantification error due to an irreparable echo at different phase-encoding positions with varying values of $\mathbf{dk}_s$ error. The ADC quantification error was measured using the ADC_{error} (see text). A high ADC_{error} indicates poor ADC quantification accuracy with high level of quantification error and vice versa. (b) Line plot showing the ADC quantification error due to an echo with $\mathbf{dk}_s$ motion error at a few selected phase-encoding positions.

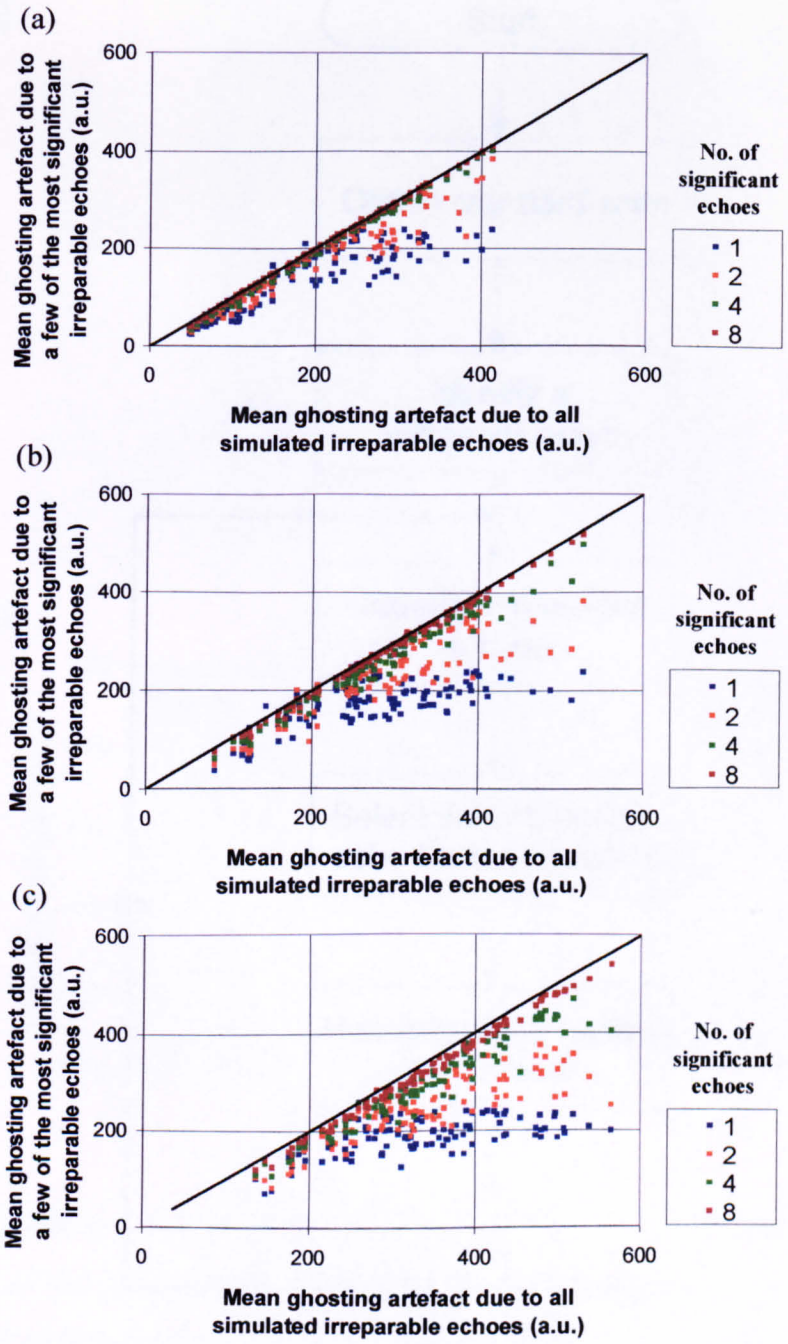

Figure 4.15 Relationship between the mean ghosting artefact due to multiple irreparable echoes and that due to 1 (blue), 2 (orange), 4 (green) and 8 (brown) of the most significant irreparable echoes in the scan. The significance of an irreparable echo was defined as the level of ghosting artefact it produced when acting individually. Motion error rates of 30% (a), 50% (b) and 70% (c) were simulated.

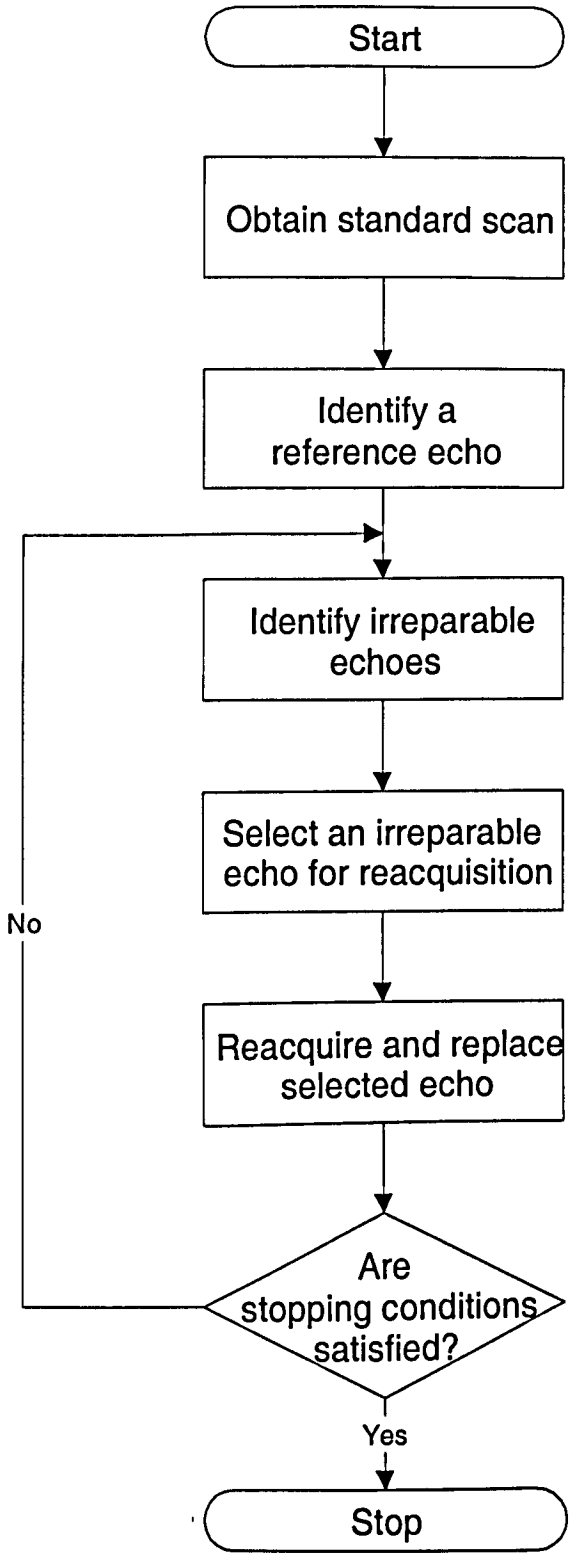

Figure 4.16 Flowchart of the reacquisition algorithm.

(a)

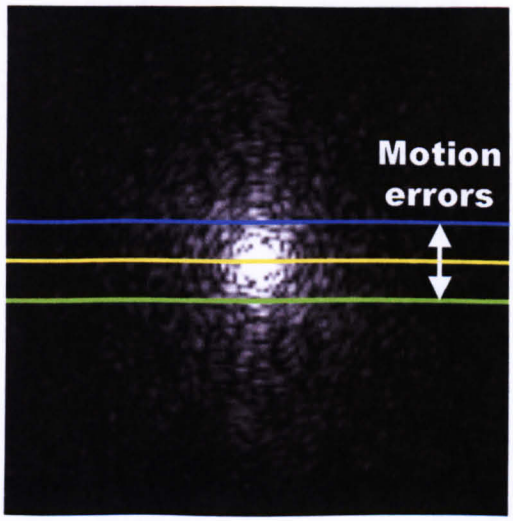

(b)

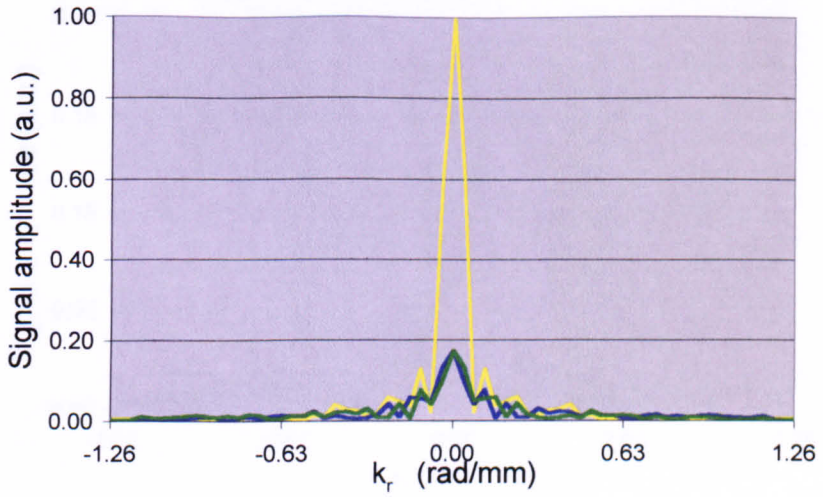

Figure 4.17 Effects of an irreparable error on the navigator echo signal. (a) Time data signal of the imaging slice used in the simulation study. Also shown are the positions of navigator echoes with (green and blue lines) and without (yellow line) irreparable errors under ideal imaging conditions. (b) Amplitude signal of the navigator echoes shown above. Note that, because the navigator echo without irreparable errors was acquired from the centre of k-space, it had the largest echo signal. Therefore, in principle, it should be possible to identify a reference navigator echo (i.e. a navigator echo without irreparable errors) from within a scan by virtue of its signal size.

(a)

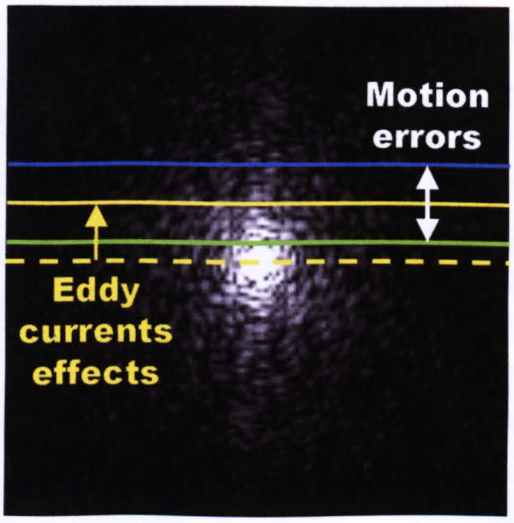

(b)

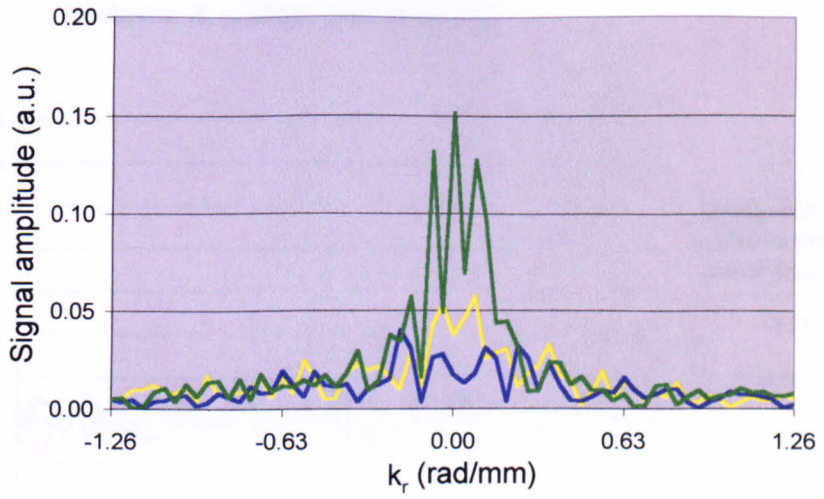

Figure 4.18 Effects of eddy currents on the navigator echo signal. (a) Time data signal of the imaging slice used in the simulation study. Also shown are the positions of navigator echoes with (green and blue lines) and without (solid yellow line) motion errors under realistic imaging conditions, where eddy currents can lead to unintended phase-encoding. (b) Amplitude signal of the navigator echoes shown above. Note that the navigator echo without motion errors is no longer the one with the largest signal and that the navigator echo that was displaced closer to the centre of k-space is now much larger than the motion-free navigator echo.

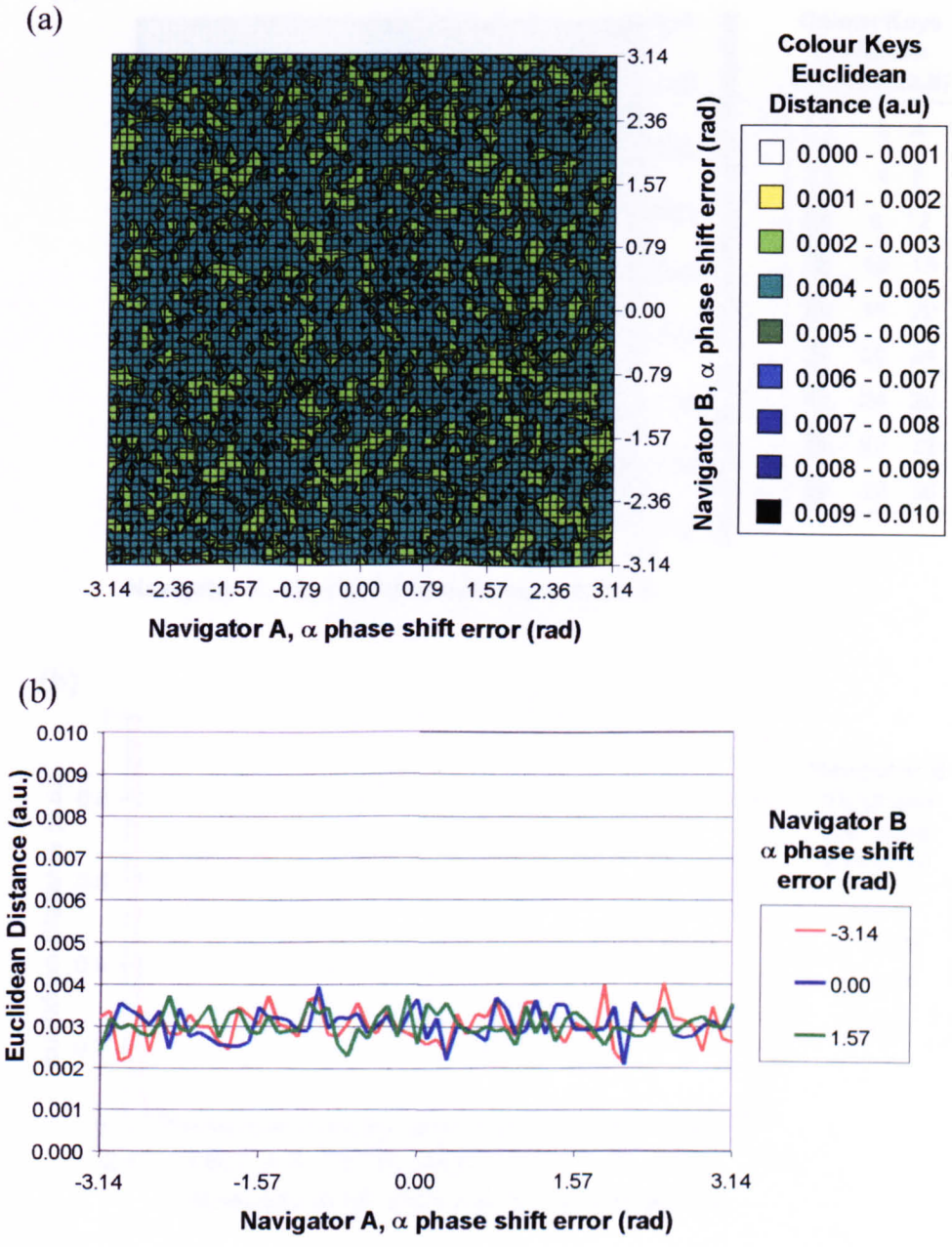

Figure 4.19 (a) Contour plot showing an overview of the differences between two navigator echoes (A and B) with varying amount of α phase shift error. The navigator echoes differences were measured using the Euclidean distance (see text). A large Euclidean distance indicates large differences between the two navigator echoes and vice versa. (b) Line plot showing the differences between navigator echoes A and B with different α phase shift errors. Ideally, the differences should be small and independent of the phase shift in both echoes.

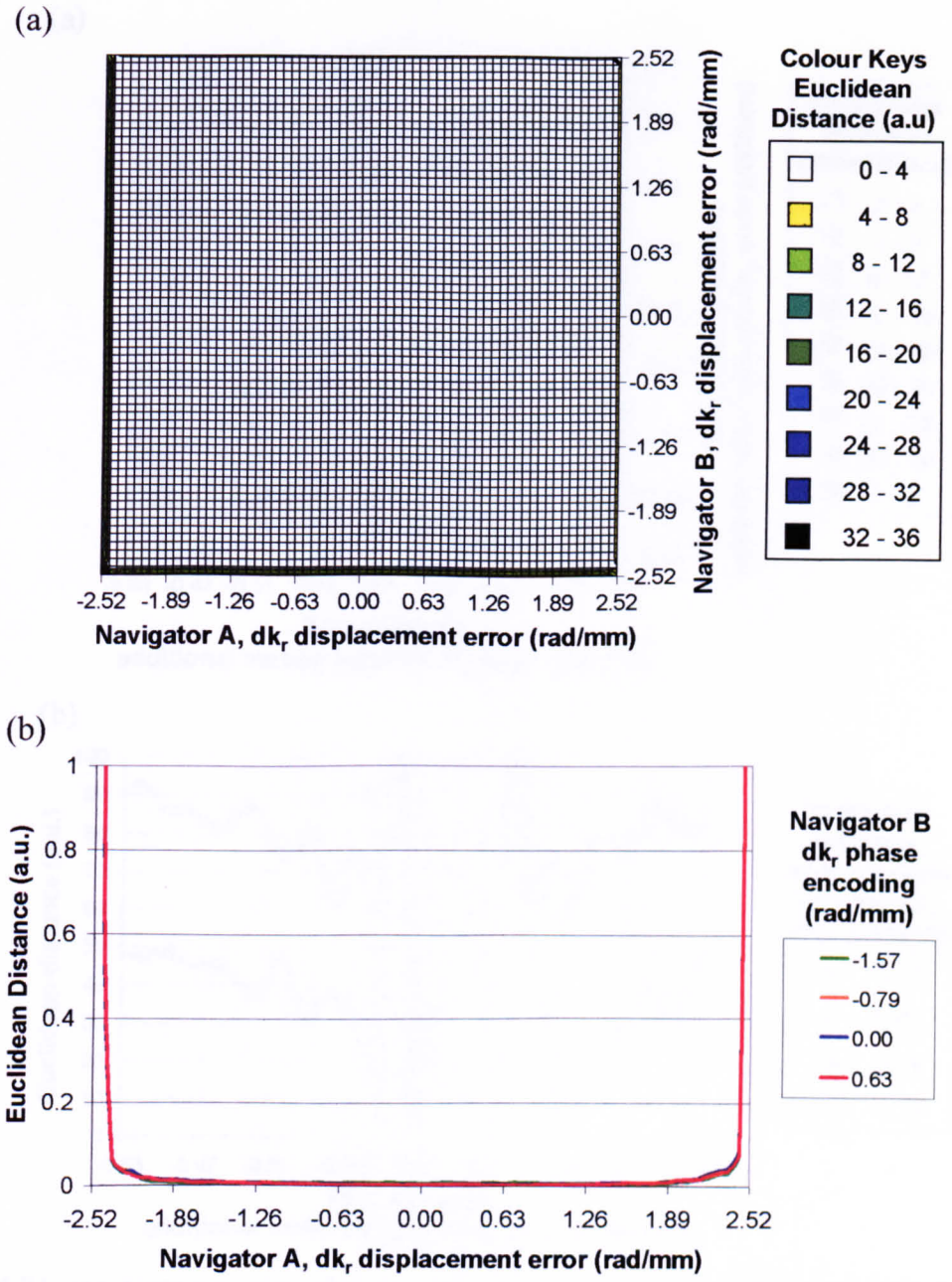

Figure 4.20 (a) Contour plot showing an overview of the differences between two navigator echoes (A and B) with varying amount of $\mathbf{dk_r}$ displacement error. The navigator echoes differences were measured using the Euclidean distance (see text). A large Euclidean distance indicates large differences between the two navigator echoes and vice versa. (b) Line plot showing the differences between navigator echoes A and B with different $\mathbf{dk_r}$ displacement errors. N.B. The scale in the contour plot shown here is different to that used in the previous figure.

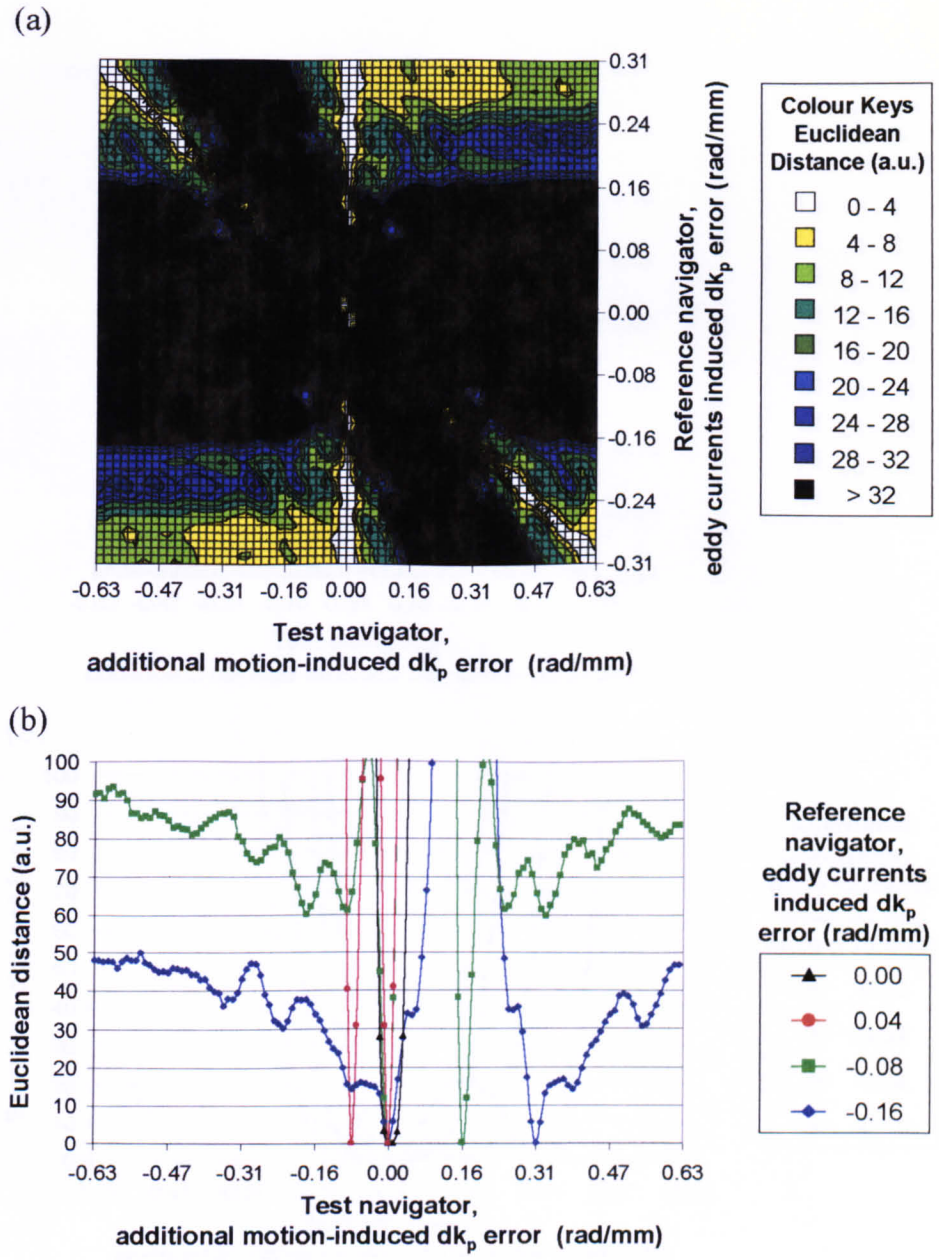

Figure 4.21 (a) Contour plot showing an overview of the differences between a correctable (reference) navigator echo, with varying amount of eddy currents induced $\mathbf{dk_p}$ error, and a test navigator echo, with varying amount of additional motion induced $\mathbf{dk_p}$ error. (b) Line plot showing the differences between the correctable navigator echo and the test navigator echo at selected eddy currents induced $\mathbf{dk_p}$ errors. N.B. Although it appears on the contour plot that the differences between the reference echo and some test navigator echoes without motion error are very large, this is in fact an artefact of the contour plotting process. The line plot shows that differences between the reference echo and all test navigator echoes without motion error are indeed always very low.

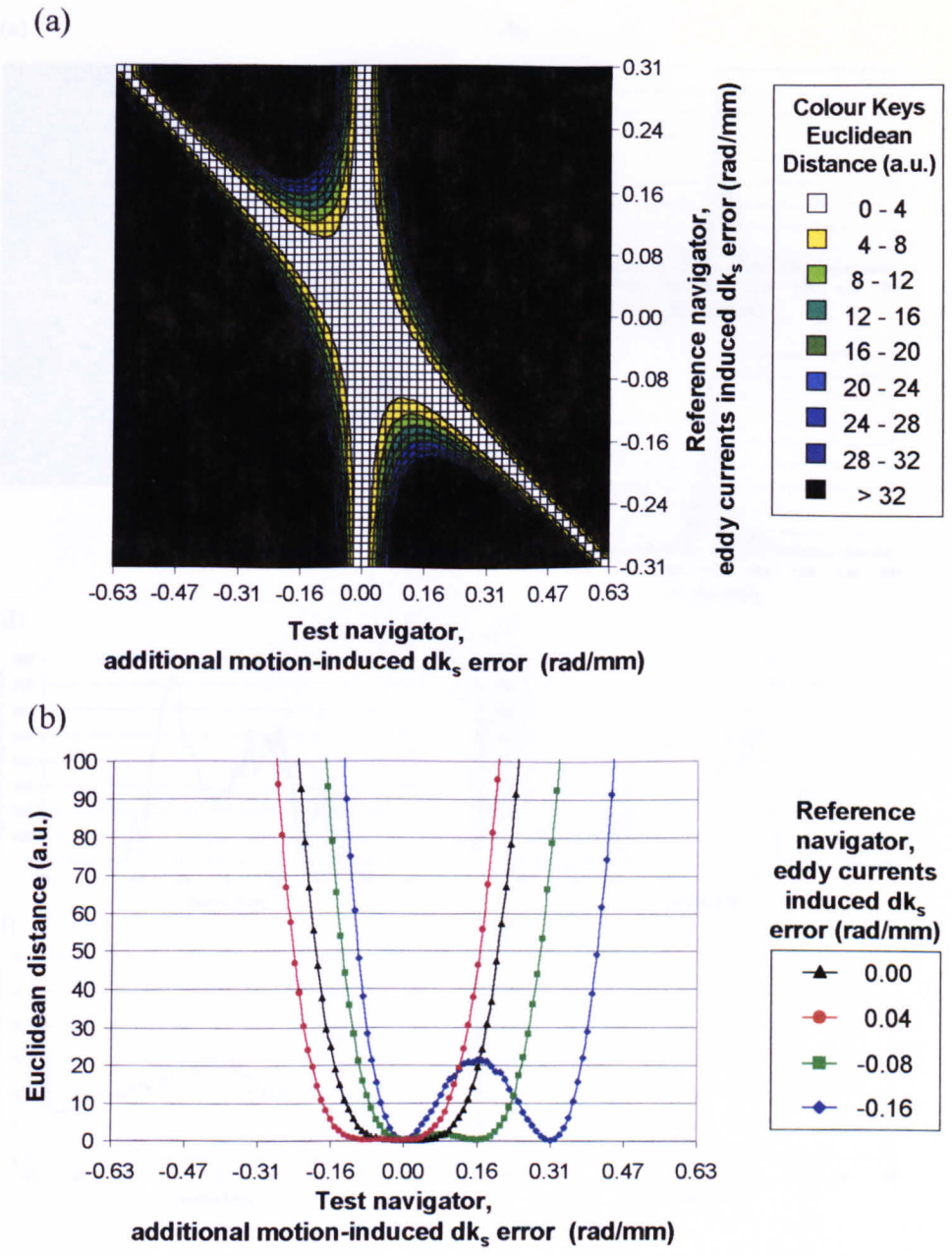

Figure 4.22 (a) Contour plot showing an overview of the differences between a correctable (reference) navigator echo, with varying amount of eddy currents induced $\mathbf{dk}_s$ error, and a test navigator echo, with varying amount of additional motion induced $\mathbf{dk}_s$ error. (b) Line plot showing the differences between the correctable navigator echo and the test navigator echo at selected eddy currents induced $\mathbf{dk}_s$ errors.

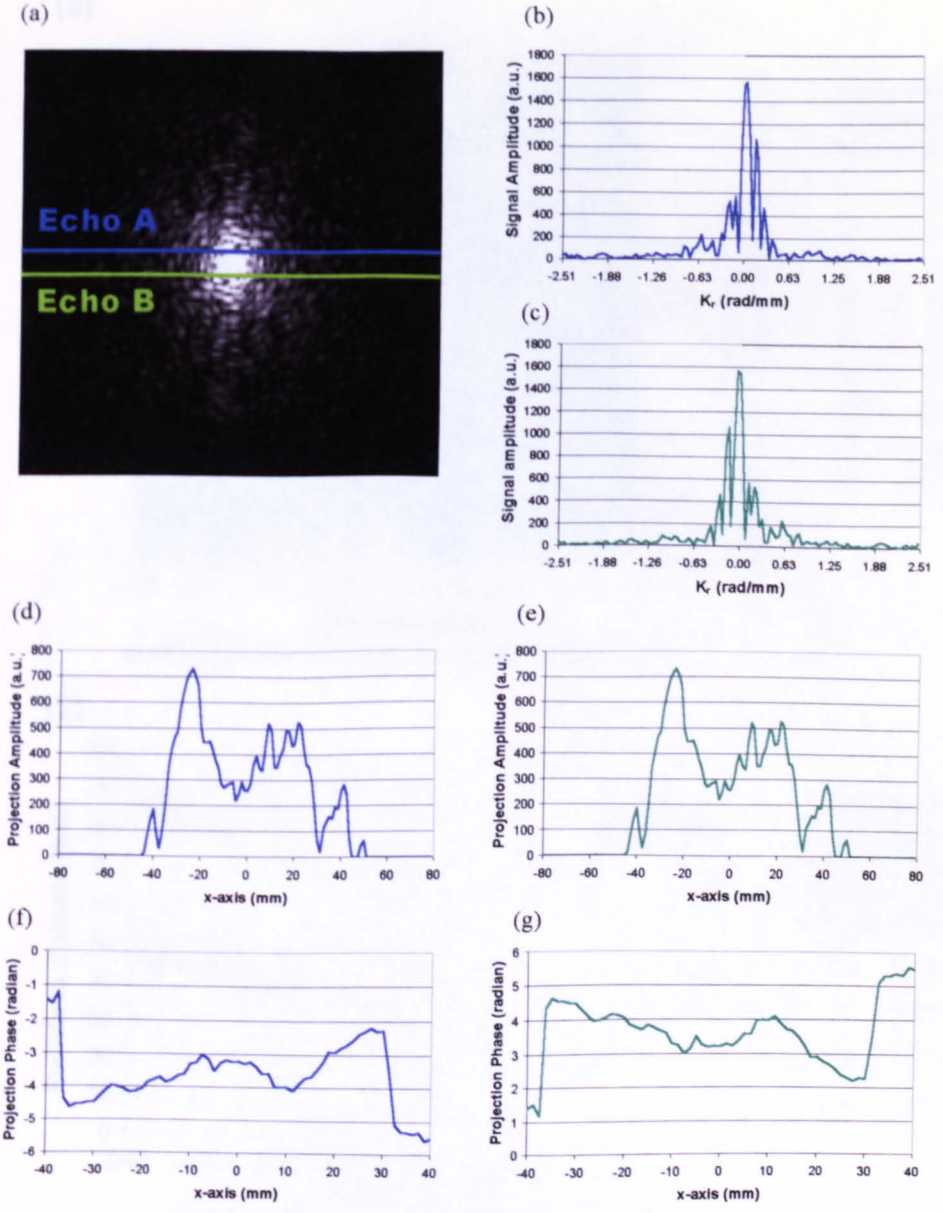

Figure 4.23 Conjugate symmetry in an MRI scan time data. (a) K-space positions of echo A and B superimposed on the time data signal used in the simulation study. (b) Echo A magnitude signal. (c) Echo B magnitude signal. (d) Echo A projection, magnitude signal. (e) Echo B projection, magnitude signal. (f) Echo A projection, phase signal. (g) Echo B projection, phase signal. Echo A and B were taken from opposite positions in k-space. Conjugate symmetry in the time data give rise to equal magnitude signal in the echoes projection, as shown in (d) and (e), but opposite phase signal, as shown in (f) and (g).

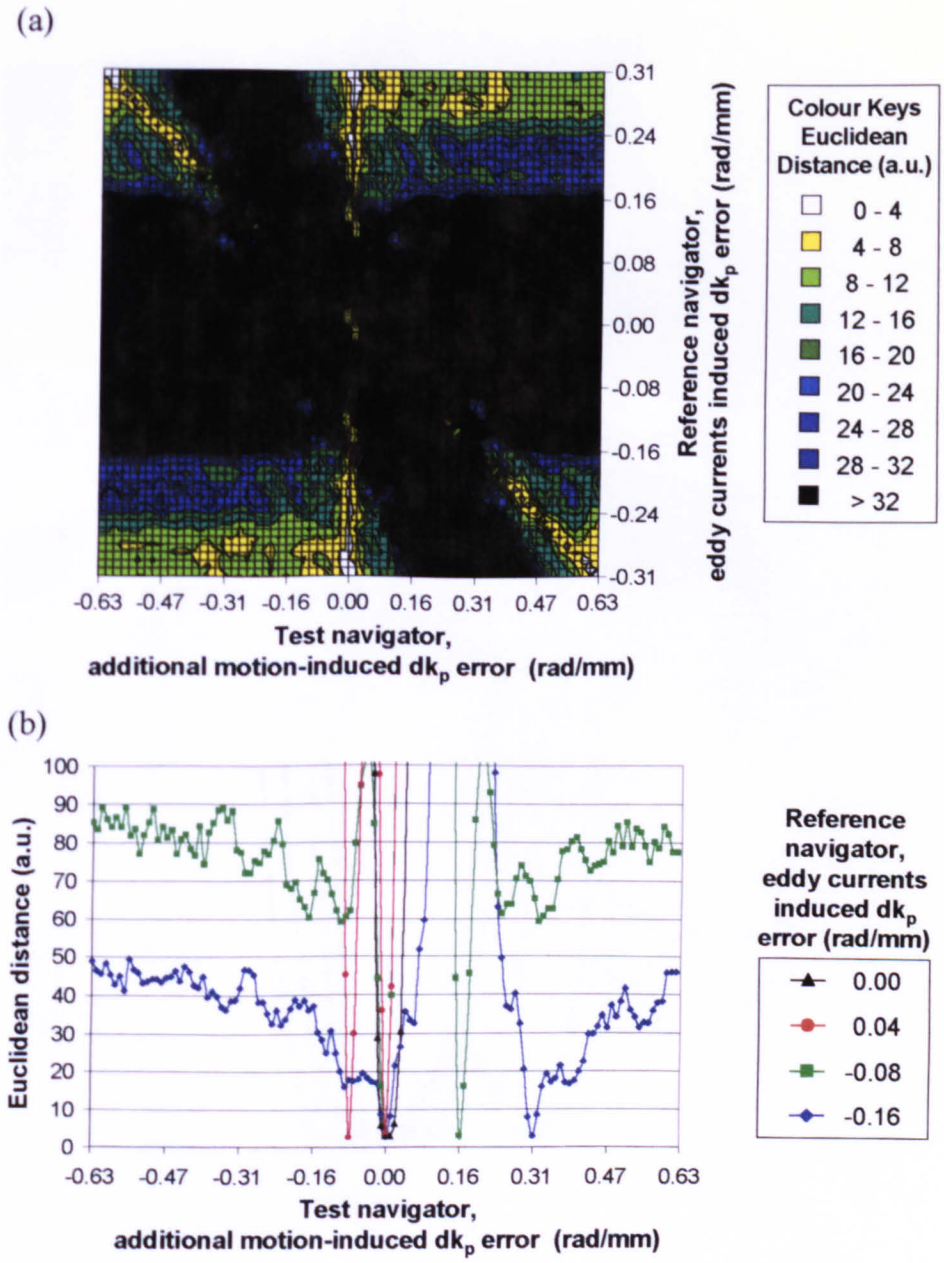

Figure 4.24 (a) Contour plot showing an overview of the differences between a correctable (reference) navigator echo, with varying amount of eddy currents induced $\mathbf{dk_p}$ error, and a test navigator echo, with varying amount of additional motion induced $\mathbf{dk_p}$ error. (b) Line plot showing the differences between the correctable navigator echo and the test navigator echo at selected eddy currents induced $\mathbf{dk_p}$ errors. The noise level in the simulation was set such that the SNR in the simulated images was 6.

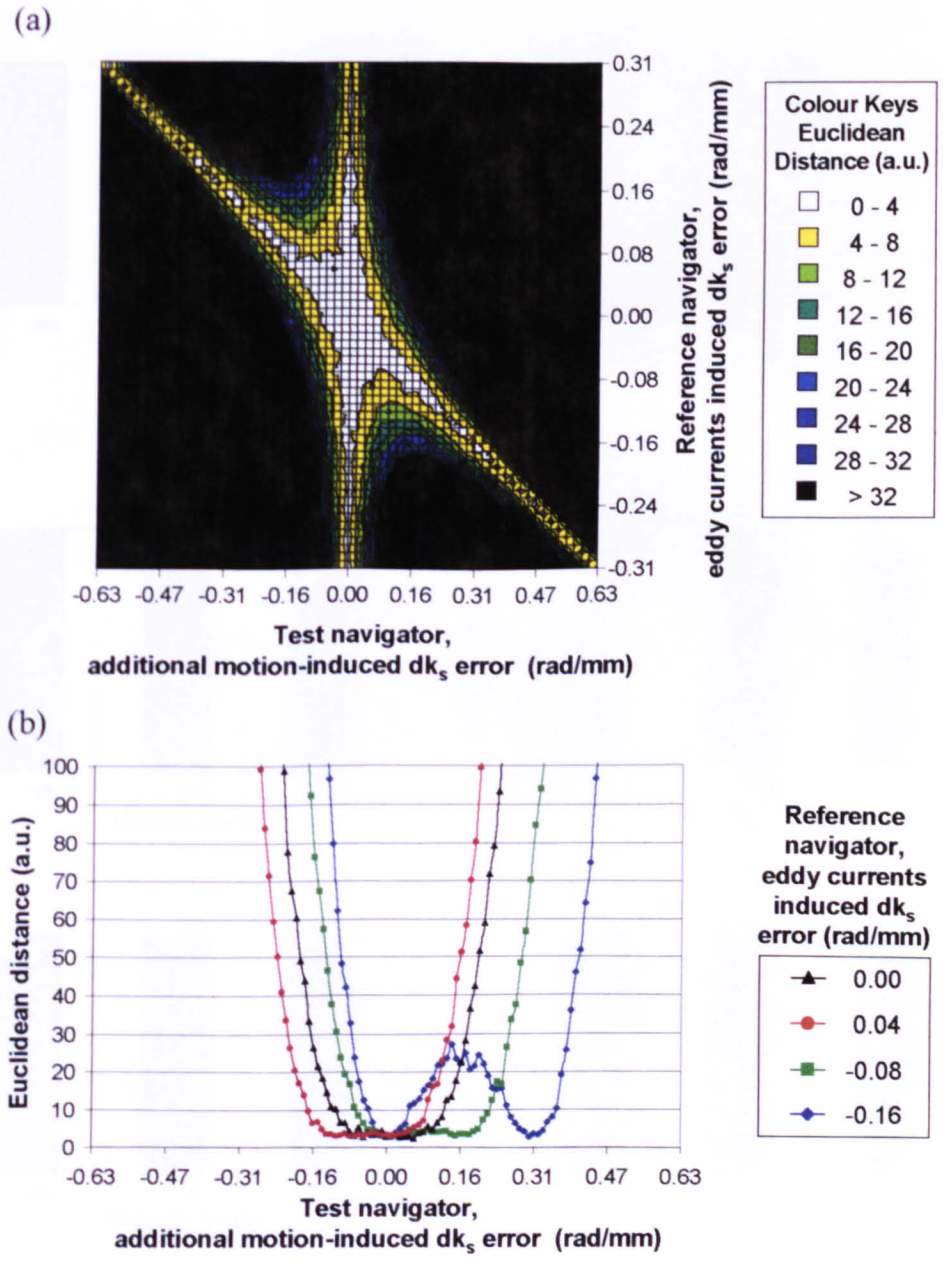

Figure 4.25 (a) Contour plot showing an overview of the differences between a correctable (reference) navigator echo, with varying amount of eddy currents induced $\mathbf{dk}_s$ error, and a test navigator echo, with varying amount of additional motion induced $\mathbf{dk}_s$ error. (b) Line plot showing the differences between the correctable navigator echo and the test navigator echo at selected eddy currents induced $\mathbf{dk}_s$ errors. The noise level in the simulation was set such that the SNR in the simulated images was 6.

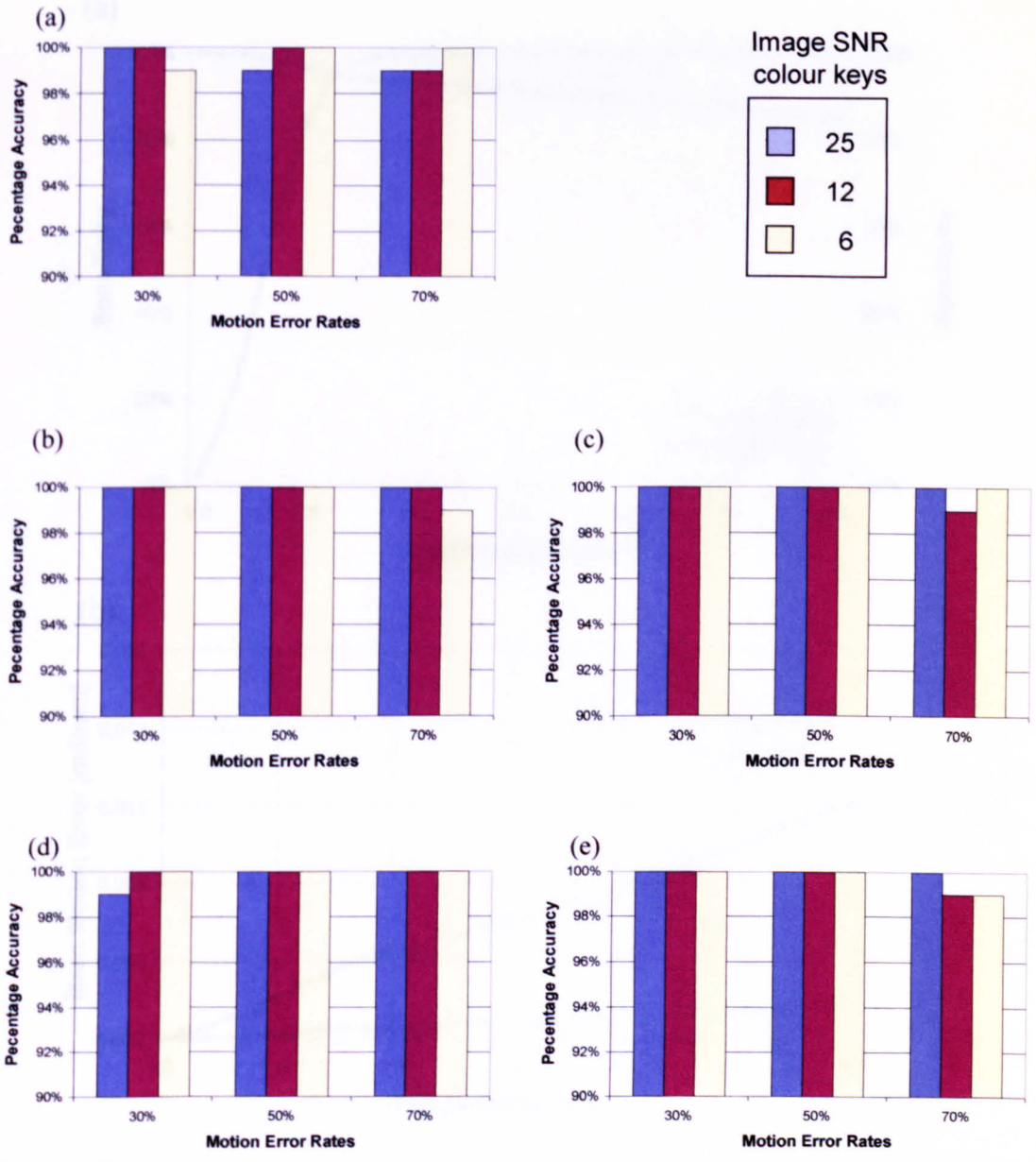

Figure 4.26 Accuracy of the 'clustering' method in identifying the correct reference navigator echo from corrupted scans that were acquired under various eddy current conditions, SNR and motion error rates. (a) No eddy currents effects. (b) Eddy currents causing k_p phase-encoding of 0.04 rad/mm, (c) Eddy currents causing k_p phase-encoding of 0.16 rad/mm. (d) Eddy currents causing k_s phase-encoding of 0.04 rad/mm. (f) Eddy currents causing k_s phase-encoding of 0.16 rad/mm. For comparison, k_{max} and δk_p (i.e. the spacing between two k-space samples) in the simulated image were 2.51 and 0.04 rad/mm respectively.

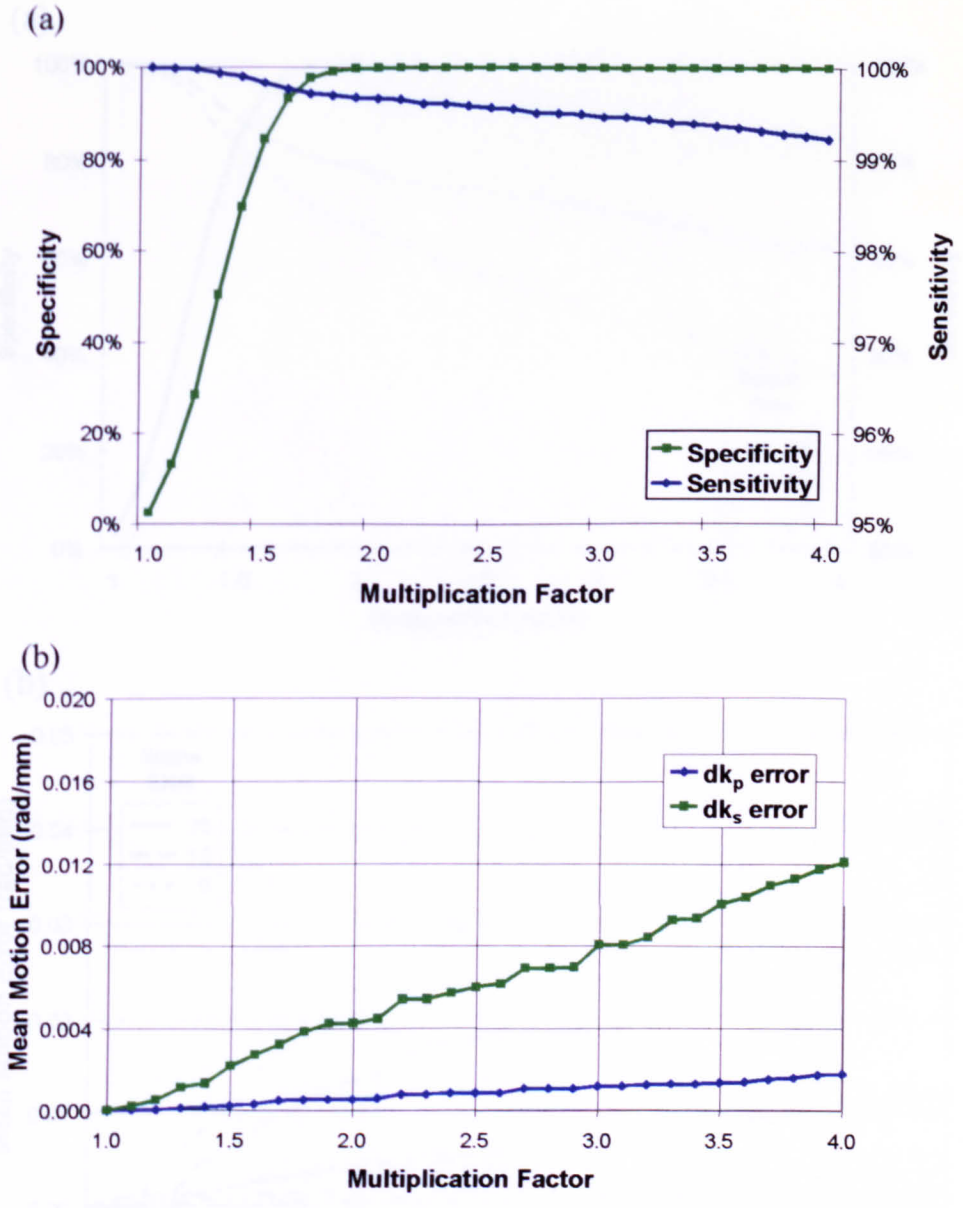

Figure 4.27 Accuracy of the reacquisition algorithm in identifying irreparable echoes. (a) Sensitivity and specificity of the identification process at various multiplication factor. (b) Mean $\mathbf{dk}_p$ and $\mathbf{dk}_s$ errors in those echoes that were erroneously classified as correctable. Result obtained from 100 scans simulated without eddy currents effects and with noise level set such that the SNR in an uncorrupted simulated scan was 25. N.B. The sensitivity of the identification process is a measure of its accuracy in recognising irreparable echoes, whilst the specificity of the identification process is a measure of its accuracy in recognising correctable echoes (see section 4.3.3, equation 4.10).

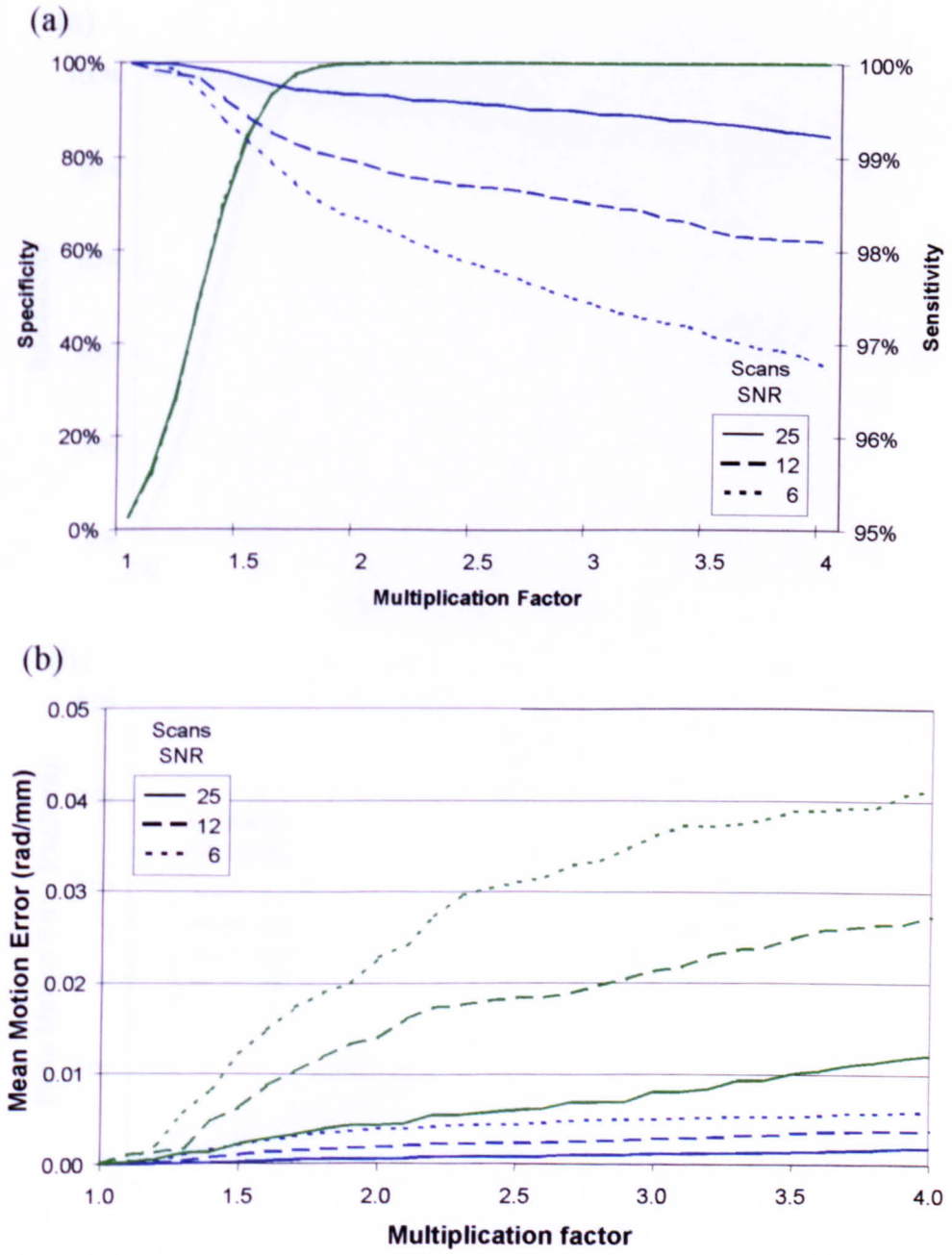

Figure 4.28 Effects of additive noise signal on the identification of irreparable echoes. (a) Sensitivity (blue lines) and specificity (green lines) of the identification process at various noise levels. (b) Mean $\mathbf{dk}_p$ (blue lines) and $\mathbf{dk}_s$ (green lines) errors in those echoes that were erroneously classified as correctable. Noise levels leading to SNR of 25 (solid lines), 12 (coarse dashed lines) and 6 (fine dashed lines) were simulated.

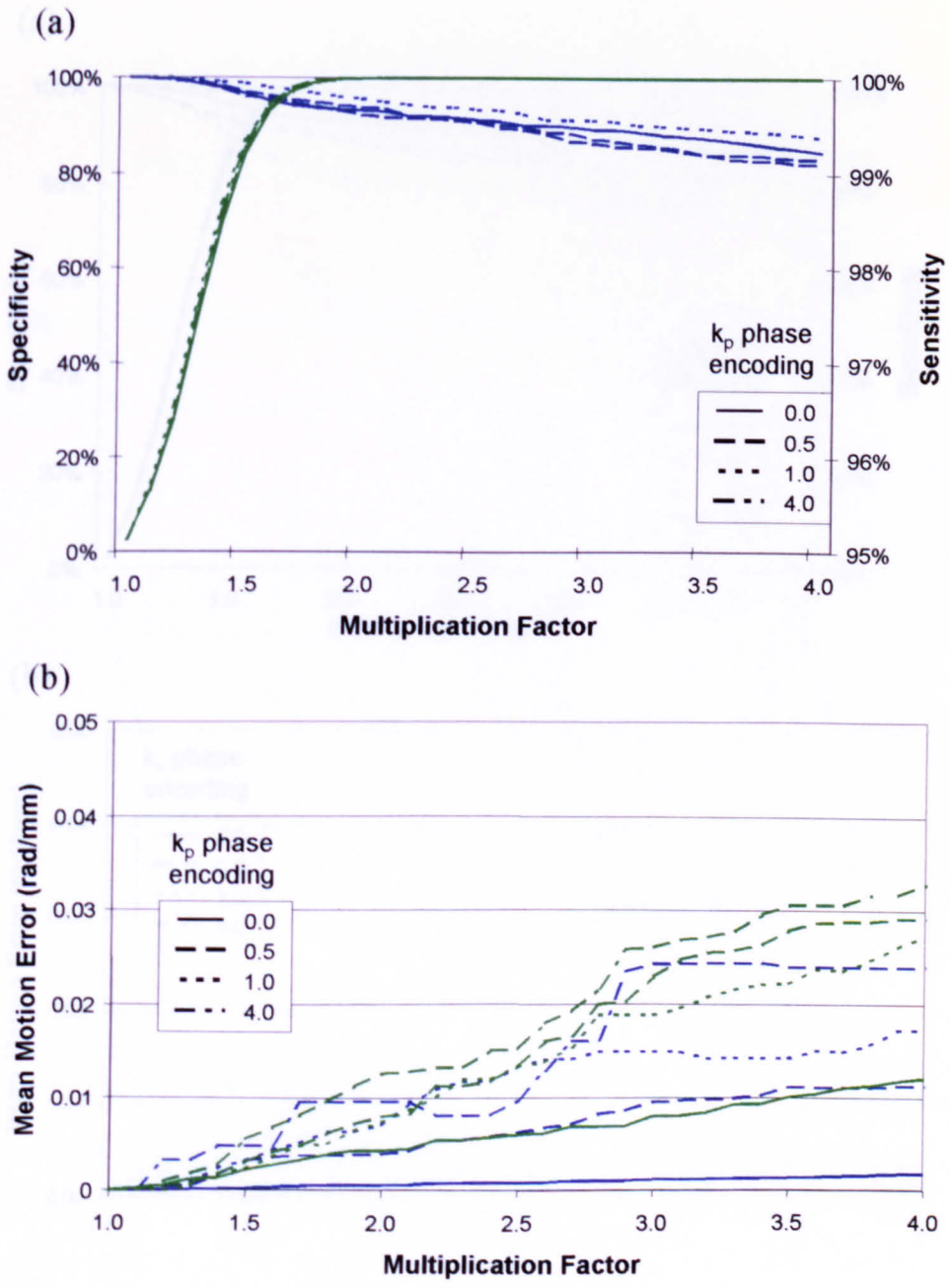

Figure 4.29 Effects of eddy currents induced k_p phase encoding on the identification of irreparable echoes. (a) Sensitivity (blue lines) and specificity (green lines) of the identification process at various eddy currents induced k_p phase encoding. (b) Mean $\mathbf{dk_p}$ (blue lines) and $\mathbf{dk_s}$ (green lines) errors in those echoes that were erroneously classified as correctable. Eddy currents causing k_p phase encoding of zero (solid lines), 0.02 (dashed lines), 0.04 (dotted lines) and 0.16 rad/mm (dot-dashed lines) were simulated.

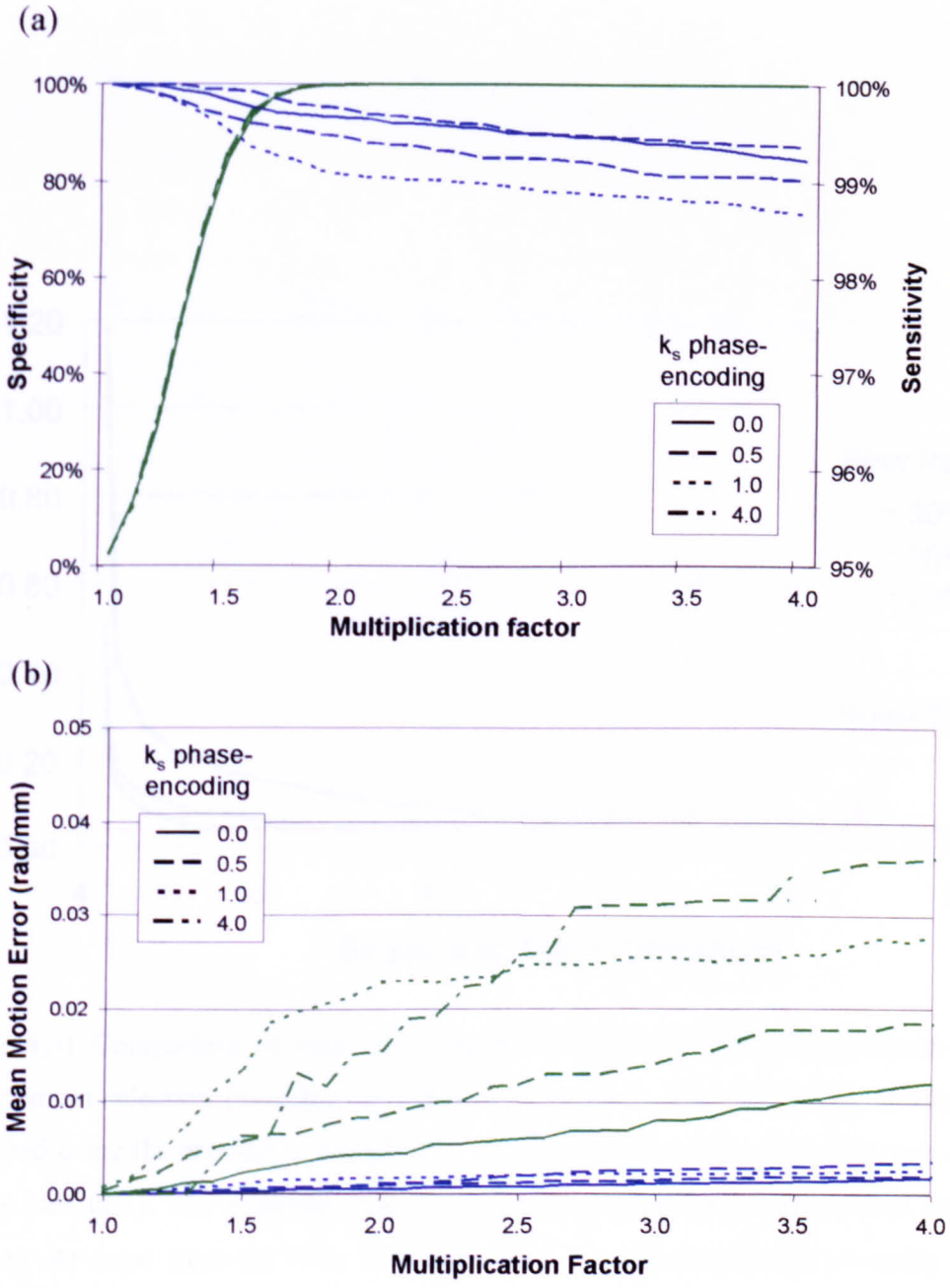

Figure 4.30 Effects of eddy currents induced k_s phase-encoding on the identification of irreparable echoes. (a) Sensitivity (blue lines) and specificity (green lines) of the identification process at various eddy currents induced k_s phase-encoding. (b) Mean $\mathbf{dk}_p$ (blue lines) and $\mathbf{dk}_s$ (green lines) errors in those echoes that were erroneously classified as correctable. Eddy currents causing k_s phase encoding of zero (solid lines), 0.02 (dashed lines), 0.04 (dotted lines) and 0.16 rad/mm (dot-dashed lines) were simulated.

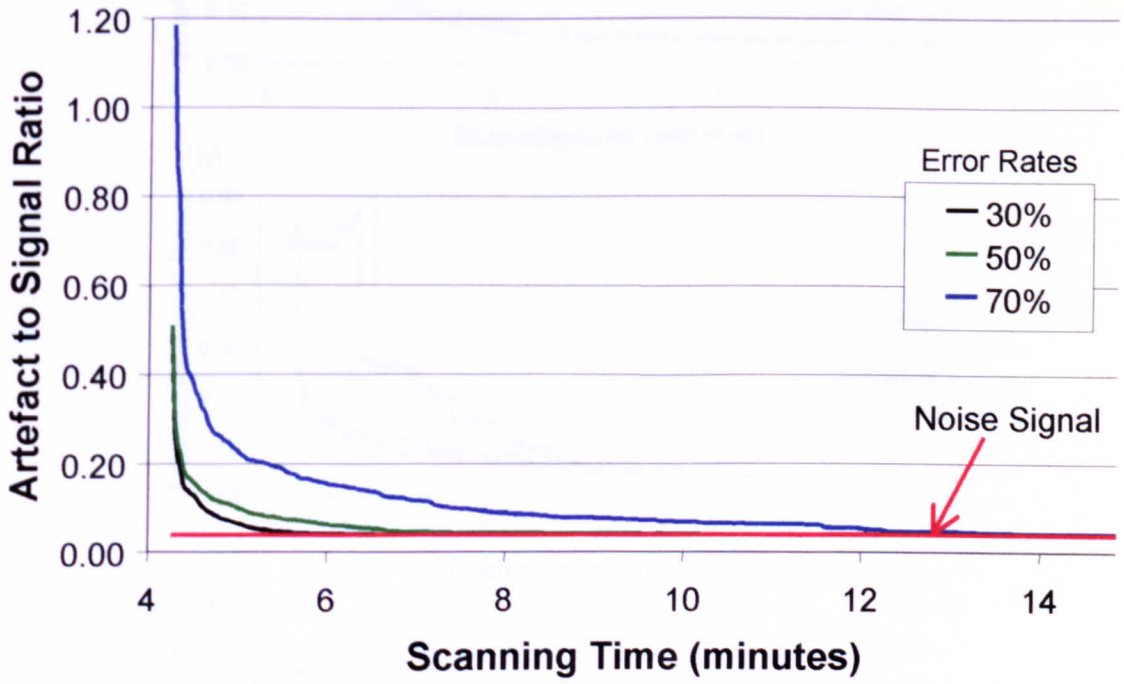

Figure 4.31 Comparison of scan image quality during the reacquisition process using the optimum selection procedure at different error rates. The scan image quality was measured using the artefact to signal ratio, which decreases with increasing scan image quality (see text). The scanning time for a normal scan without reacquisition was 4.3 minutes. At error rates of 30%, 50% and 70%, the theoretical total scanning times required to obtain an error-free image were 6.1, 8.5 and 14.2 minutes respectively. As can be seen, at these times the scan image quality was asymptotic for each of the different error rates and the artefact signal was equal to the noise signal.

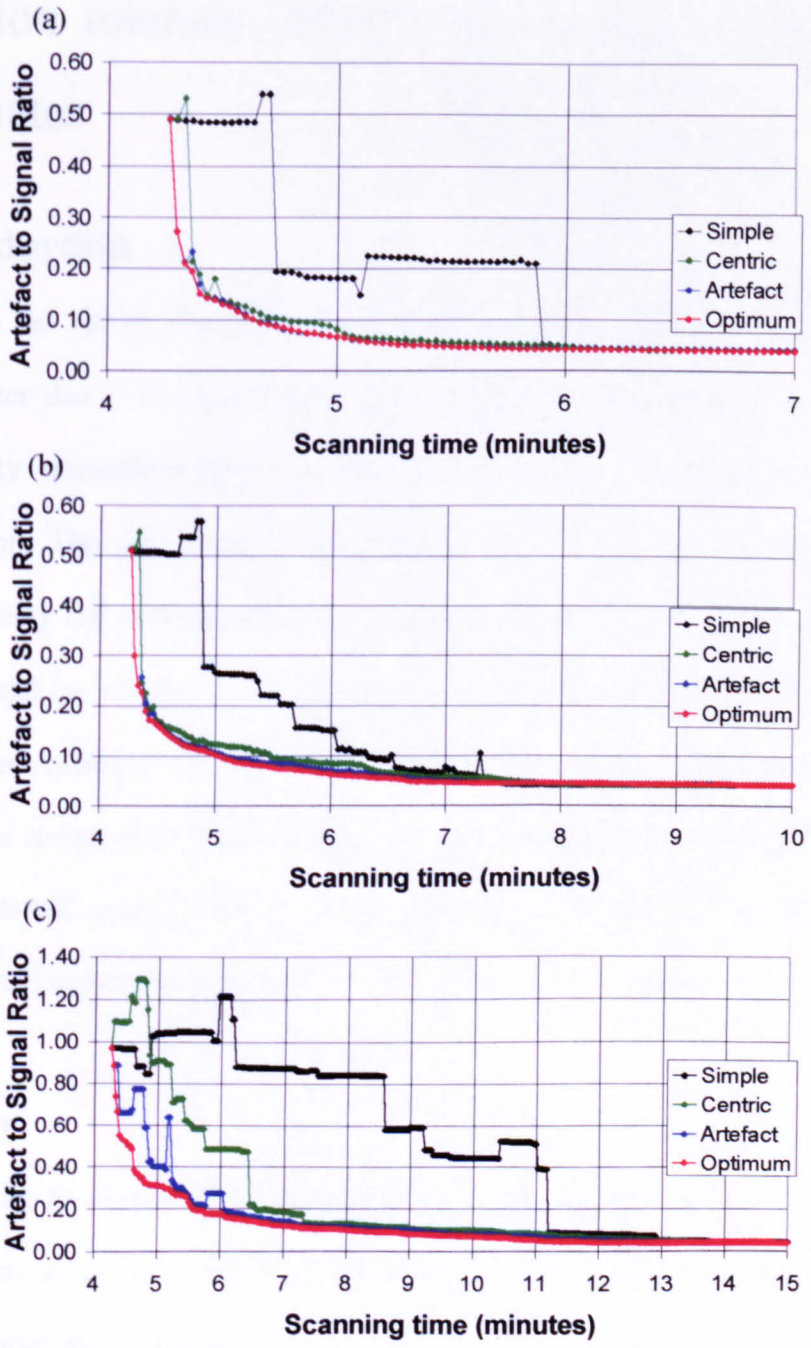

Figure 4.32 Comparison of scan image quality during the reacquisition process using the four different selection methods. The comparison was performed at error rates of (a) 30%, (b) 50% and (c) 70%. The normal scanning time was 4.3 minutes. The theoretical scanning times required to remove all irreparable echoes from a scan at an error rate of 30%, 50% and 70% were 6.1, 8.5 and 14.2 minutes respectively. The scan image quality was measured using the artefact to signal ratio, which decreases with increasing scan image quality (see text).

5 Motion tolerant diffusion weighted imaging in neonates

5.1 Introduction

With the aid of computer simulations, it was demonstrated in the previous chapter that it was possible to use the reacquisition technique to obtain high quality diffusion-weighted images in the presence of intermittent subject motion. The aim of the work presented in this chapter was to assess the feasibility and performance of the reacquisition technique on a real scanner. To this end, a version of the reacquisition technique was implemented on the Bruker Avance 24/40 scanner and its performance was assessed systematically with a computer controlled motion phantom. Its feasibility and performance in the clinical environment was also assessed by using it to obtain diffusion-weighted images from neonates in an on-going clinical study.

5.2 Theory

In order to support the reacquisition technique as described in the previous chapter, a scanner must be capable firstly, of processing all acquired data in 'real-time' (i.e. process a current data set before the next set is acquired) and secondly, of changing the phase encoding gradient within the pulse sequence 'on the fly' (i.e. according to the result of the previous data acquisition). With its 'pipeline filter' processing method, the Bruker Avance scanner was capable of supporting 'real-time' user-defined processing of acquired scan data, and therefore was able to meet the first requirement. However, the Avance scanner

was not capable of altering the phase encoding gradients during a scan acquisition, and thus was not able to meet the second requirement.

In order for the Avance scanner to selectively acquire a user-defined combination of phase-encoded echoes, the phase encoding values of the echoes must be programmed into the scanner prior to the start of the scan. With such a limitation, any implementation of the reacquisition algorithm would have involved stopping the scan after every few echo acquisitions so that the phase encoding gradients could be reprogrammed. Such an implementation would not have been feasible as the time lost to scanner initialisation and dummy scans at each restart would have been too prohibitive (typically >10s).

Fortunately, the Avance scanner had a 'set-up' mode that allowed certain scanning parameters to be altered during the scanning process. With the scanner in 'set-up' mode, it was found that by altering the appropriate gradient trim value, it was possible to vary the phase encoding gradient in between echo acquisitions. However, because the scanner's 'set-up' mode was designed to allow the user to optimise a sequence prior to a scan acquisition, rather than to acquire scan data, there were some difficulties in using the 'set-up' mode to reacquire data. The most obvious difficulty was the fact that no data were saved to disk when the scanner was acquiring data in 'set-up' mode, thus all reacquired data would be lost unless they were saved explicitly. To overcome this problem, a program was incorporated into the 'pipeline filter' to save any acquired data to disk as the scan proceeded during 'set-up' mode. A less obvious, but more serious difficulty, was that there was a delay of two phase

encoding steps before the changes in the gradient trim values were implemented and it was only possible to change one gradient trim value once every two phase encoding steps. To overcome these limitations, the reacquisition algorithm (as described in the previous chapter) was modified slightly so that it could be implemented using the scanner in its 'set-up' mode. The modified reacquisition algorithm involved acquiring a normal diffusion-weighted scan (i.e. the first step of the reacquisition algorithm) using the scanner's standard acquisition mode, followed by selective reacquisition of corrupted echoes using the scanner's 'set-up' mode. To reacquire corrupted echoes using the scanner's 'set-up' mode, a 'pipeline filter' was implemented to carry out the following tasks in 'real-time':

i) Identify all corrupted echoes in the scan using the criteria described in section 4.3.2.2

ii) Select a corrupted echo for reacquisition using one of the methods described in section 4.3.2.3

iii) Update the appropriate gradient trim value so that the selected echo will be reacquired.

iv) As selected echoes are reacquired, accept or reject them according to the criteria outlined in section 4.3.2.4

v) Store any updated scan data to disk as no data are saved by the scanner software in 'set-up' mode

vi) Determine whether to continue with the reacquisition process or stop using the criteria outlined in section 4.3.2.5

To account for the delay between the changes in the gradient trim and the actual implementation of the change, the gradient trim values were buffered so that the correct phase encoding value could be assigned to each acquired echo. To account for the fact that the trim values could be altered only once every two phase encoding steps, the reacquisition algorithm was modified so that each selected echo was reacquired twice. Identification of the reference echo was performed automatically following the acquisition of the normal diffusion-weighted scan using the 'clustering' method as described in section 4.3.2.1. As it was not possible to alter the phase encoding gradient trim value between slice acquisitions, support for multi-slice acquisitions was not implemented.

The requirement to reacquire each selected echo twice in the modified reacquisition algorithm meant that scanning time was wasted whenever the first reacquired echo was correctable, thus lowering the overall efficiency of the reacquisition technique. However, the loss of efficiency is minimal as will be shown in the following calculation. Consider an imaging session where the rate of irreparable motion error was R per echo, with $R<1$. The number of echo acquisitions required to obtain an error-free scan using the modified reacquisition algorithm in such a circumstance can be determined by noting that, after the initial scan (N_0 echo acquisitions), there will be N_0R echoes to reacquire. Then in reacquiring each N_0R echo twice, $2N_0R$ echo acquisitions will have been performed and there will be N_0R^3 echoes to reacquire. By continuing this process all erroneous echoes will eventually be removed and the total number of echo acquisitions required to obtain an error-free scan can be calculated as follows:

$$N = N_0 + 2N_0\left(R + R^3 + R^5 + ...R^{\infty}\right)$$
$$\text{Since } R < 1$$
$$N = N_0\left(1 + \frac{2R}{1-R^2}\right) \quad (5.1)$$

By dividing equation 5.1 by equation 4.4, it can be shown that the maximum increased in scanning time due to the double acquisitions of selected echoes is only 17% and that this occurs when R=0.414.

5.3 Materials and Method

5.3.1 Pulse sequences

To assess the performance of the reacquisition technique, two diffusion-weighted imaging sequences with echo reacquisition capability were implemented on the Bruker 24/40 (2.4 Tesla) scanner. The first sequence, shown in figure 5.1, is a navigated bipolar PGSE diffusion-weighted imaging sequence. It is based on a standard navigated PGSE DWI sequence[1] but with an extra 180^0 RF pulse and bipolar gradient[2] to minimise unwanted eddy currents. The second sequence, shown in figure 5.2, is an isotropic diffusion-weighted interleaved EPI sequence. It is based on the isotropic diffusion-weighted imaging sequence by Cercignani and Horsefield[3] and is designed to minimise the effects of eddy currents from the large diffusion-encoding gradients, whilst maximising the diffusion weighting. It was important to minimise the eddy currents induced by the diffusion-encoding gradients because unwanted phase encoding of the navigator echoes can lead to imaging artefacts for the following reasons: Firstly, when a navigator is phase-encoded, the Fourier transform of its signal no longer represents a linear projection of the object being imaged but a

projection of the object with phase encoding information along an axis perpendicular to the projection axis. In contrast to the linear projection, a phase-encoded projection is not always guaranteed to contain a 'non-zero' signal in all parts of the object. Where the signals in the phase-encoded projection are below the noise signal, it will not be possible to obtain phase information from those points. As the navigator correction technique relies on the phase signal from the navigator echo projection to restore a scan's phase integrity, loss of phase signal in part of the navigator echo projections will lead to imaging artefacts. An example of such artefacts is shown in figure 5.3. Secondly, it was shown in the simulation work in the previous chapter (see section 4.3.4.5) that when navigator echoes are phase-encoded, an increased number of residual motion errors are retained in the required scan. Since residual motion errors lead to ghosting artefacts, an increased level of residual motion errors will inevitably lead to greater ghosting artefacts and therefore should be avoided.

The navigator echo in both sequences was acquired immediately following the diffusion-encoding period. In the navigated PGSE DWI sequence, a further single phase-encoded spin echo was then acquired to form the imaging echo. In the isotropic diffusion-weighted interleaved EPI sequence, a spin-echo interleaved EPI readout followed the navigator echo acquisition. Seven echoes were acquired in the interleaved EPI readout with the spin-echo time (TE) centred on the fourth echo. Trapezoidal gradient waveforms with a relatively lengthy rise time of 840μs were used during the readout period. Linear sampling of the imaging echoes was performed on the plateau of the waveform at a moderate receiver bandwidth of 90kHz. Blipped phase encoding of the

imaging echoes were performed during the ramp time between the read gradient plateaus. The combination of a lengthy gradient rise time and moderate receiver bandwidth (and hence moderate read gradient strength) was necessary to maintain a safe acoustic noise level for neonatal imaging (<99dBA with ear protection)[4]. The interleaved EPI period took 22ms to complete, thus giving an effective receiver bandwidth of 46Hz per pixel along the phase encoding direction.

In the interleaved EPI readout period, the seven imaging echoes were acquired by scanning k-space alternately in the positive and negative k_{read} direction. Such a k-space trajectory requires that every other imaging echo in the readout period be reversed prior to image reconstruction and that the imaging echoes be well aligned following the echoes reversal in order to avoid ghosting artefacts. One method of ensuring that the echoes are well aligned following the echo reversal process is to trim the pulse sequence so that the imaging echoes are perfectly centred in the sampling window. However, due to gradient eddy currents and hardware imperfections, the trimming gradients required are often dependent on the slice orientation[5]. Thus, in situations, where the slice orientation is not known *a priori*, sequence trimming either needs to be performed manually for each slice orientation, or done automatically once the hardware imperfections have been fully characterised[5]. As neither of the above processes were trivial, it was decided that for this work, the misalignment of the imaging echoes could be corrected for by acquiring an extra calibration scan and applying a non-linear phase correction to the scan data as described by Bruder et al.[6] (see figure 5.4).

The use of Echo Time Shifting (ETS)[7] has been shown to be effective in reducing much of the ghosting artefacts that can arise from the step changes in T_2* decay between those echoes that are at the boundaries between the first and last echo interleave in a scan (see figure 5.5). Therefore, it would have been desirable to include a facility for ETS in the diffusion-weighted interleaved EPI sequence. However, in order to support echo reacquisition with ETS, a scanner must be capable of altering both the phase encoding gradient and the ETS delay period in the pulse sequence in real-time. Unfortunately, the Bruker Avance scanner did not have this facility and thus ETS was not implemented in this work.

5.3.2 Phantom experiment

To assess the performance of the implemented sequences *in-vitro*, a computer controlled motion phantom was constructed as show in figure 5.6. The phantom was held in equilibrium by an elastic band attached to a fixed anchor. By applying a driving force to the phantom, it can be made to oscillate around an axis at its centre. Although the oscillation is limited to only one axis, all the displacement errors described by Anderson and Gore[8] were reproducible by appropriate selection of the diffusion gradient direction. The driving force required for the oscillation was generated by applying a varying electric current through the wire loop attached to the phantom. In the bore of the scanner, where a magnetic field of 2.4 Tesla was present, the electric current caused an electromagnetic force on the phantom, which then drove the oscillation. By attaching the wire loops to a computer, it was possible to control the start of each oscillation period in the phantom. However, because of the damping time

associated with the phantom oscillation, it was not possible to control the end of the oscillation period with accuracy. In order to end an oscillation period at a specified time, it was necessary to program the computer that controlled the phantom to withdraw the driving force from the phantom at an earlier time point to account for the phantom's damping time. The damping time of the phantom was obtained by scanning the phantom with the diffusion sequence in 'set-up' mode and measuring the time it took for the echo signal to return to normal following the withdrawal of the driving signal.

The performance of the reacquisition algorithm was assessed by setting up the motion phantom to oscillate at random intervals for a fixed percentage of the scanning time. A spherical water phantom was used as the sample in the experiment. The imaging parameters used in the navigated bipolar PGSE DWI sequence for the phantom experiment were as follows: TR = 2 s, TE = 130 ms, FOV = 16 cm x 16 cm, sl = 5 mm, image matrix = 128 x 128, δ = 17 ms, Δ = 49.2 ms. The imaging geometry was set-up so that the sample's axis of rotation was aligned along the read direction and the diffusion gradient was along the slice direction. This geometry ensured that the $\mathbf{dk}_p$ errors were reproduced in the acquired echoes. The imaging parameters used in the isotropic DWI sequence for the phantom experiment were as follows: TR = 2 s, TE = 170 ms, FOV = 16 cm x 16 cm, sl = 5 mm, numbers of interleaves = 16, image matrix = 128 x 112 (zeroed filled to 128 x 128). The diffusion gradients timings were as shown in figure 5.2. The phantom was imaged using both sequences at error rates of 30%, 50% and 70%. The error rate (R) was defined as the ratio of the oscillating period to the total imaging time. At each error rate, six scans at

b-values of 500 s/mm^2 were performed. Both the 'simple' and 'centric' reacquisition algorithms were tested with the navigated bipolar PGSE DWI sequence. Since each interleave EPI readout in the diffusion-weighted interleaved EPI sequence included an imaging echo from a central region of k-space, each interleave was considered to be of equal importance, and thus, only the 'simple' reacquisition algorithm was tested with the interleaved EPI sequence. The reacquisition algorithm was set-up so that it would continue reacquiring echoes until either the scanning period reached a length twice that expected for the error rate or until the maximum differences between the navigator echoes and the reference navigator echo was equal to the estimated noise level. Six control images of the phantom were also obtained by scanning the phantom at rest.

5.3.3 Neonatal imaging

To assess the performance of the reacquisition technique in-vivo, ten neonates, all less than one week old, were scanned in the Bruker Avance 2.4 Tesla scanner using the diffusion-weighted interleaved EPI sequence. All ten neonates were part of an ongoing study of perinatal asphyxia[9;10] and were recruited for the study on the basis of having clinical evidence of perinatal hypoxic-ischaemic brain injury. The neonates were examined head-supine, within a cylindrical Perspex pod mounted on a MR compatible incubator equipped with environmental temperature control[11]. Acoustic noise protection was provided by means of earplugs (E.A.R. Classic, Cabot Safety Ltd, Cheshire, UK) and external ear muffs (Natus MiniMuffs, Natus Medical Inc., CA 94070, USA). Continuous ECG, pulse oximetry, skin temperature and

apnoea monitoring were performed on the neonates throughout the examination and a paediatrician was present at all times during the study to ensure the neonates' safety. To gently restrain the neonates during the scan acquisitions, their heads were placed on top of a plastic bag filled with expanded polythene beads (PRA Plastics Ltd., London, UK). After the bag had been moulded around the neonates' heads, the bag was made semi-rigid by evacuating air from it. As part of their clinical care, the neonates were sedated with either oral or rectal Chloral hydrate (25-50 mg/kg). No additional medications were given as part of the scan procedure. These studies were approved by the University College London Committee on the Ethics of Human Research and informed consent was obtained from parents before each study.

Depending on the time constraints and the clinical judgement of the paediatrician, diffusion-weighted scans of one or more slices of the neonate brain were acquired. In all cases, both the 'high' (b-value = 900 s/mm^2) and 'low' (b-value = 20 s/mm^2) diffusion-weighted scans were acquired. The imaging parameters used in the neonatal imaging protocol were as follows: TR = 2 s, TE = 170 ms, FOV = 16 cm x 16 cm, sl = 5 mm, numbers of interleaves = 16, image matrix = 128 x 112 (zero-filled to 128 x 128). The reacquisition algorithm was set-up for continuous echo reacquisition until the operator terminated the scan. To aid the operator's decision as to when the reacquisition process should be terminated, feedback information was constantly provided to the operator by the algorithm via the console screen (see figure 5.7).

5.4 Results and discussion

5.4.1 Phantom experiment

Figure 5.8 and 5.9 show the typical set of images obtained with the navigated bipolar PGSE DWI sequence using the 'simple' and 'centric' reacquisition algorithm respectively. Also shown on the figures are the total scanning time (that is the time it took to acquire the initial image plus any addition echo reacquisition time) and the normalised Signal to Ghost Ratio (SGR – see chapter 4 for definition) of each of the images. The normalised SGR was defined as follows:

$$\text{Normalised SGR} = \frac{\text{SGR}}{\text{SNR in the final reacquired image}} \qquad (5.2)$$

Normalisation of the SGR was necessary in order to account for the differences in Signal to Noise Ratio (SNR) between different scans. From figure 5.8 and 5.9, it can be seen that there was progressive improvement in image quality during the reacquisition process in both scans. However, it can also be seen that the 'centric' reacquisition algorithm was able to improve the image quality of the scan much more rapidly during the early part of the reacquisition process than the 'simple' reacquisition algorithm. A control image of the still phantom has also been shown on figure 5.8 and 5.9. As can be seen, the image quality of the final reacquired scan in both figures was comparable to that of the control image.

Figure 5.10 shows a typical set of images obtained with the isotropic diffusion-weighted interleaved EPI sequence using the 'simple' reacquisition algorithm.

To prevent ghosting artefacts arising from the lack of ETS, it was necessary to select an off-centred slice of the sphere for the diffusion-weighted interleaved EPI experiment to avoid the large B_0 field inhomogeneity that was present around the air bubble at the top of the sphere phantom. The images in figure 5.10 were thus smaller and slightly different from that shown in figure 5.8 and 5.9. However, as in figure 5.8 and 5.9, a progressive improvement in image quality can be observed throughout the reacquisition period. The image quality of the final reacquired scan in figure 5.10 was also comparable to that of its control image. The SNR in the interleaved EPI sequence was approximately half that observed in the spin-echo sequence. However, this may be accounted for by the larger receiver bandwidth (90kHz vs. 50kHz) and the longer TE time (130ms vs. 170ms) used in the interleaved EPI sequence, and by the T_2* decay that would have been present in six out of the seven echoes in the interleaved EPI readout.

Figure 5.11 shows the mean normalised SGR obtained with the navigated PGSE DWI sequence during the reacquisition process at the three different error rates. The mean SGR of the six control images has also been shown for comparison. After the initial standard scan acquisition (i.e. at the scanning time of 4.3 minutes), the mean normalised SGR for all three error rates were below 0.20. From figure 5.8 and 5.9, it can be seen that such low normalised SGR were typically associated with severe ghosting artefacts. During the echo reacquisition period (i.e. at scanning time > 4.3 minutes) a progressive improvement in the mean normalised SGR can be seen at all error rates and with both the 'simple' and 'centric' reacquisition algorithm. However, it is clear

that the 'centric' reacquisition algorithm was able to improve the corrupted scans substantially faster during the early stages of the reacquisition process than the 'simple' reacquisition algorithm.

Figure 5.12 shows the mean normalised SGR obtained from the diffusion-weighted interleaved EPI sequence during the reacquisition process at the three motion error rates. The mean normalised SGR of the six control images has also been shown for comparison. It can be seen that after the initial standard acquisitions (i.e. at scanning time of 32 seconds) the mean normalised SGR at all three error rates were below 0.30. From figure 5.10, it can be seen that such normalised SGR were typically associated with unusable scans. Following echo reacquisition, substantial improvement in SGR at all error rates was observed and a comparable level of normalised SGR to that in the control images was achieved.

From equation 5.1, the theoretical scanning time required to obtain a scan free of motion error at error rates of 30%, 50% and 70% were calculated as 1.66, 2.34 and 3.75 times the standard scanning time. For the navigated bipolar PGSE DWI sequence, this corresponded to a scanning time of 7.1, 10.0 and 16.0 minutes respectively. From figure 5.11, it can be seen that at approximately these times, the SGR of the reacquired scans were asymptotic for each of the error rates and for both reacquisition algorithms. For the diffusion-weighted interleaved EPI sequence, the theoretical scanning times were 53, 75 and 120 seconds respectively. Inspection of figure 5.12 shows that at these approximate

time points, the SGR of the reacquired scans were also asymptotic for each of the error rates.

Although the reacquisition process was able to improve the image quality of the motion corrupted scans to a comparable level to that of the control scans, it can be seen from figure 5.11 and 5.12 that the SGR of the reacquired scans were always short of that shown by the control scans. Furthermore, it can be seen that the difference in SGR between the control scans and the reacquired scans increased with increasing motion error rates. This difference was probably due to residual motion errors undetectable by the reacquisition algorithm. It was shown in the previous chapter (see section 4.3.4.3) that in cases where motion errors lead to very small changes in the navigator echo signal, such motion errors will remain undetected by the reacquisition algorithm and be retained in the required scan. As the error rate increases, it is expected that the number of undetectable motion errors, and the ghosting artefacts that they produce, will also increase correspondingly. However, despite the presence of residual motion errors in the reacquired scan it can be seen from figure 5.11 that even at the highest expected error rate (i.e. 70%), the reacquisition algorithm was able to improve the corrupted scan to a mean normalised SGR of 0.75. From figure 5.10, it can be seen that such a normalised SGR was typical associated with only a slight amount of ghosting artefact.

5.4.2 Neonatal imaging

A summary of the scans performed in the neonatal imaging experiment is shown in table 5.1. As can be seen, a wide range of image quality was obtained

over the 46 scans. To aid their analysis, the scans were grouped into the following categories:

i) *Category A - This category groups those scans where the initial image quality was considered to be sufficiently free of ghosting artefact not to require any further reacquisition.*

ii) *Category B - This category groups those scans where the initial image quality was sufficient to be used for ADC quantification but where there was sufficient ghosting artefact to require echo reacquisition.*

iii) *Category C - This category groups those scans where the initial image quality was too poor to be of any use and thus echo reacquisition was necessary.*

A summary of the numbers of scans in each of the three above categories, together with their mean scanning time and mean initial and reacquired normalised SGR are presented in table 5.2. Examples of the diffusion-weighted interleaved EPI scans in category A are shown in figure 5.13 together with their SNR and normalised SGR. Two typical T_2-weighted images obtained during the same scanning sessions have also been included for comparison. From the results shown in figure 5.13 and in table 5.1 and 5.2, it can be seen that although scans in category A were considered to be sufficiently free of ghosting artefacts not to require further echo reacquisition, significant ghosting artefact was still present in the scans. However, as a similar level of ghosting artefact was also observed in the T_2-weighted images (the mean normalised SGR in the T_2-weighted scans of the same slice was 0.30, n = 23), the artefact was therefore probably unrelated to the presence of the diffusion-encoding gradient.

Therefore, the decision not to apply the echo reacquisition technique to these scans was apt since the reacquisition technique was only designed to overcome the ghosting artefacts caused by the enhanced motion-sensitivity of the diffusion-encoding gradients. With a mean normalised SGR of 0.68, the diffusion-weighted ($b = 900$ s/mm^2) scans in category A would appear to have a significantly lower ghosting artefact level than either the 'low' diffusion-weighted scans ($b = 20$ s/mm^2) or the T_2-weighted scans. However the high normalised SGR is due to the fact that the SNR in the diffusion-weighted scan was significantly lower than that of either of the other two types of scans rather than a true low level of ghosting artefact.

Examples of the diffusion-weighted interleaved EPI scan in categories B and C are shown in figure 5.14 and 5.15. From the results shown in tables 5.1 and 5.2, it can be seen that improvement in the level of ghosting artefacts was achieved for all scans in both categories B and C following the reacquisition process. However, whilst the increase in mean normalised SGR of 'low' diffusion-weighted and 'high' diffusion-weighted scans in category B were only 24.1% and 16.6% respectively, the increased SGR in category C was a much more substantial 270% and 78% respectively. Of the eleven diffusion-weighted scans in category C, all but two of the scans were improved to a level where they were considered sufficiently free of ghosting artefact to be used for ADC quantification.

The two scans that failed to improve sufficiently to be used for ADC quantification are shown in figure 5.16. Also shown in figure 5.16 are two T_2-

weighted images obtained during the same scanning session. As can be seen, although there was a substantial improvement in the level of ghosting artefact in the scans following the echo reacquisition process, there was still a significant level of image degradation in the scans. However, a similar high level of image degradation was also observed in the T_2-weighted images obtained during the same scanning session. Therefore, the high level of residual ghosting artefact in the reacquired scans was mainly due to the large subject motion that was present during the scanning session rather than the phase errors caused by the presence of the diffusion gradients. In order for the reacquisition technique to be effective, it is essential that the imaging slice remains (fairly) constant throughout the reacquisition period. In the development of the reacquisition algorithm, it was assumed that large subject motion that altered the imaging slice position could be effectively suppressed with gentle restraints (see section 4.2). As this assumption was probably not met during the acquisition of the two scans in figure 5.16, improving the image quality of the scans to an acceptable level was, therefore, not possible.

The mean scanning time of scans in category B and C were, respectively, approximately twice and three times that of the standard scanning time of 32s. The mean normalised SGRs of the scans in category B and C, following the reacquisition process, were improved to a level close to that of the scans in category A. Although the improvement in SGR of scans in category C was much greater than that in category B, the difference in the mean SGR between scans in category C and scans in category A remained greater than that between scans in category B and A. This result is consistent with the result obtained in

the phantom study, which showed that the residual level of ghosting artefact in a scan following the reacquisition process increases with increasing motion error rates.

5.5 Summary and Conclusions

An implementation of the reacquisition algorithm was demonstrated on the Bruker Avance 2.4 Tesla scanner. As the scanner did not officially support real-time modification of the phase encoding gradient, it was not possible to implement the algorithm as designed. However, by using an undocumented feature of the scanner and by modifying the reacquisition algorithm, it was possible to implement a slightly less efficient algorithm.

Using a computer controlled motion phantom, it was demonstrated that the reacquisition algorithm was able to yield high quality images within the theoretically predicted time for a given error rate. Whilst the reacquisition algorithm was able to improve the quality of the reacquired scans to a level similar to that of the control scans, it was not able to match the same image quality. The difference in SGR between the reacquired scans and the control scans increased with increasing motion error rate. However, even at the highest expected motion error rate of 70%, the quality of the reacquired scans was still very good. Both the 'simple' and 'centric' versions of the reacquisition algorithm were assessed. A faster rate of improvement in SGR during the initial phase of the reacquisition process was demonstrated with the 'centric' algorithm during the phantom study. This result is consistent with that obtained in the simulation study described in the previous chapter.

The effectiveness of the reacquisition algorithm was demonstrated by applying the technique to acquire isotropic diffusion-weighted images of neonates in a birth asphyxia study. A wide range of image quality was obtained from neonatal imaging prior to the reacquisition process. In scans where the level of ghosting artefact was sufficient to require echo reacquisition, improvement in ghosting artefacts was always demonstrated following the application of the echo reacquisition process. Whilst the reacquisition process did improve the SGR of the diffusion-weighted scans, a residual level of ghosting artefact was present in all of the scans. However, the residual level of ghosting artefact was similar to that seen in the T_2-weighted images obtained during the same scanning session and was, therefore, probably unrelated to the presence of the diffusion-encoding gradients. All but two of the neonatal scans were of sufficient quality to be used for ADC quantification. In the two scans that failed to be improved sufficiently, the subject motion was so great that even the T_2-weighted images were corrupted beyond use. Therefore, in general, diffusion-weighted imaging using the reacquisition technique is only effective when normal T_2-weighted imaging is also effective.

Reference List

1. Ordidge RJ, Helpern JA, Qing ZX, Knight RA, Nagesh V. Correction of motional artifacts in diffusion-weighted MR images using navigator echoes. **Magnetic Resonance Imaging** 1994; **12**: 455-460.

2. Reese TG, Weisskoff RM, Wedeen VJ. Diffusion NMR facilitated by a refocused eddy-current EPI pulse sequence. **Proc.Sixth Annual Meeting of the Society of Magnetic Resonance in Medicine** 1998; 663

3. Cercignani M, Horsfield MA. An optimized pulse sequence for isotropically weighted diffusion imaging. **Journal Of Magnetic Resonance** 1999; **140**: 58-68.

4. British Standard 5724: Section 2.33. Specification for magnetic resonance equipment for medical diagnosis. 5724. 1996.

5. Reeder SB, Atalar E, Faranesh AZ, McVeigh ER. Referenceless Interleaved Echo-Planar Imaging. **Magnetic Resonance In Medicine** 1999; **41**: 87-94.

6. Bruder H, Fischer H, Reinfelder H-E, Schmitt F. Image reconstruction for echo planar imaging with non-equidistant k-space sampling. **Magnetic Resonance In Medicine** 1992; **23**: 311-323.

7. Feinberg DA, Oshio K. Phase errors in multi-shot echo planar imaging. **Magnetic Resonance In Medicine** 1994; **32**: 535-539.

8. Anderson AW, Gore JC. Analysis and correction of motion artifacts in diffusion weighted imaging. **Magnetic Resonance In Medicine** 1994; **32**: 379-387.

9. Amess, P., Penrice, J., Wylezinska, M., Lorek, A., Townsend, J., Wyatt, J. S., Amiel-Tison, C., Cady, E. B., and Steward, A. Early brain proton magnetic resonance spectroscopy and neonatal neurology related to neurodevelopmental outcome at 1 year in term infants after presumed hypoxic-ischaemic brain injury. Dev.Med.Child.Neurol. (41), 436-445. 1999.

10. Thornton, J. S., Amess, P., Penrice, J., Chong, W. K., Wyatt, J. S., and Ordidge, R. J. Cerebral tissue water spin-spin relaxation times in human neonates at 2.4 Tesla: Methodology and the effects of maturation. Magnetic Resonance Imaging 17(9), 1289-1295. 1999.

11. Chu A, Delpy DT, Thalayasingam S. A transport and life support system for newborn infants during NMR spectroscopy. In: P.Rolfe, ed. *Fetal and Neonatal Physiological Measurements*, London: Butterworths, 1986: 409

Patient	Slice	b-value (s/mm^2)	Initial Normalised SGR	Reacquired Normalised SGR	Scanning Time (s)
1	1	20	0.38	*	32
		900	0.13	0.26	190
2	1	20	0.43	*	32
		900	0.50	0.71	70
	2	20	0.46	*	32
		900	0.63	0.67	52
	3	20	0.30	*	32
		900	0.67	0.70	64
	4	20	0.32	*	32
		900	0.50	0.57	72
3	1	20	0.20	0.20	60
		900	0.15	0.44	90
	2	20	0.30	*	32
		900	0.41	0.63	76
	3	20	0.33	*	32
		900	0.52	0.55	38
	4	20	0.40	*	32
		900	0.62	*	32
4	1	20	0.44	*	32
		900	0.55	0.66	48
	2	20	0.61	*	32
		900	0.48	0.59	64
	3	20	0.43	*	32
		900	0.74	*	32
	4	20	0.28	*	32
		900	0.48	0.59	68
5	1	20	0.07	0.22	54
		900	0.27	0.42	88
6	1	20	0.13	0.36	44
		900	0.20	0.34	60
	2	20	0.33	0.35	84
		900	0.70	0.76	86
7	1	20	0.31	*	32
		900	0.29	0.40	78
	2	20	0.37	0.43	92
		900	0.40	0.54	110
8	1	20	0.50	*	32
		900	0.66	0.73	92
	2	20	0.38	0.41	92
		900	0.22	0.50	68
9	1	20	0.10	0.41	120
		900	0.22	0.46	162
10	1	20	0.51	*	32
		900	0.66	0.72	66
	2	20	0.45	*	32
		900	0.40	0.70	60

Table 5.1 Summary of all neonatal scans image quality and scanning time. * Scans where the echo reacquisition process was not applied.

Scan b-value (s/mm^2)	Scan cate-gory	No of scans	Mean scanning time (s)	Mean initial normalised SGR	Mean reacquired normalised SGR	% Increased in mean normalised SGR
20	A	16	32	0.403	-	-
	B	5	76	0.282	0.350	24.1
	C	2	87	0.085	0.315	271
900	A	2	32	0.680	-	-
	B	12	66	0.563	0.657	16.6
	C	9	100	0.253	0.451	78.1

Table 5.2 Summary of neonatal scan data grouped according to initial scan image quality (see text).

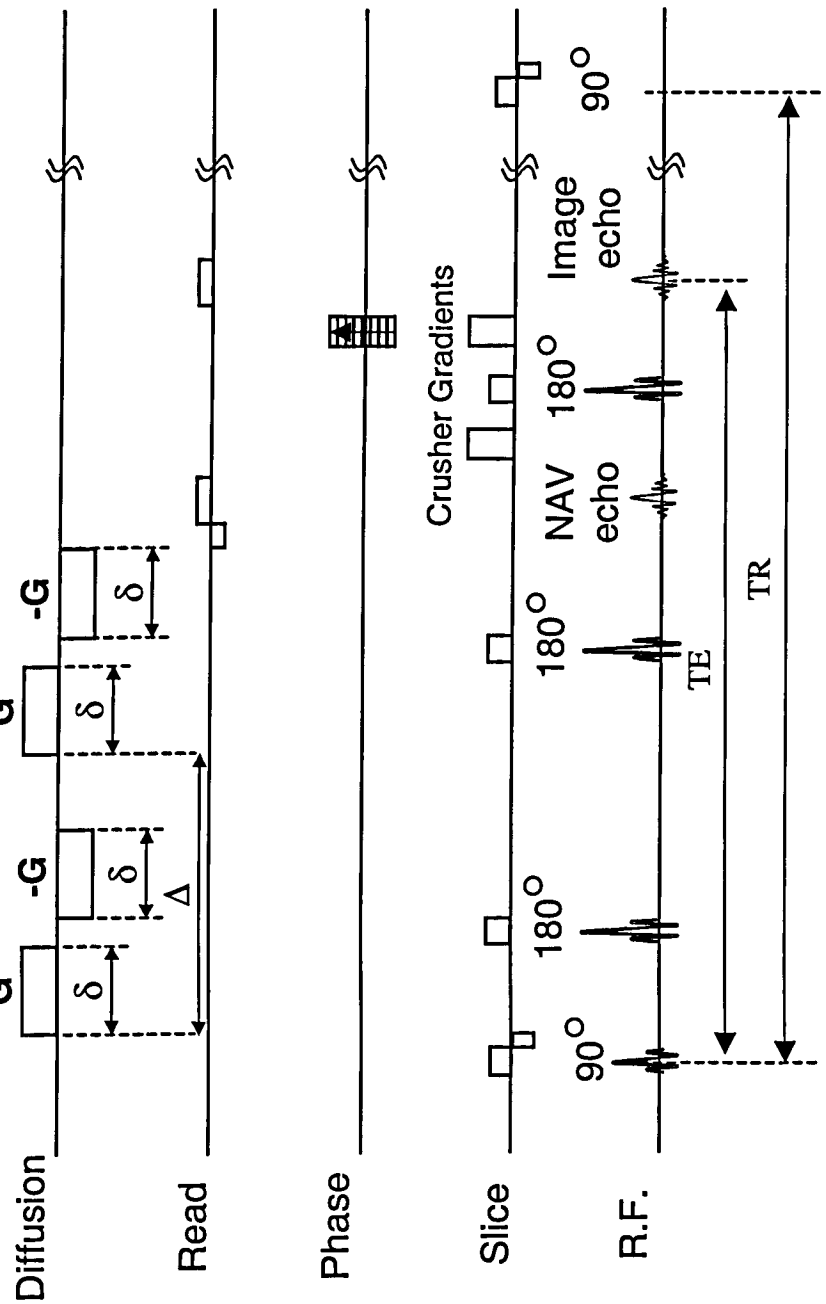

Figure 5.1 Navigated Bipolar PGSE DWI sequence used in the motion phantom study. G is the diffusion gradient strength, δ is the diffusion gradient duration. The bipolar diffusion gradients together with the double 180^0 RF pulses during the diffusion sensitizing period act to minimize unwanted eddy currents from the large diffusion gradients (see text). δ = 17 ms, Δ = 49.2 ms.

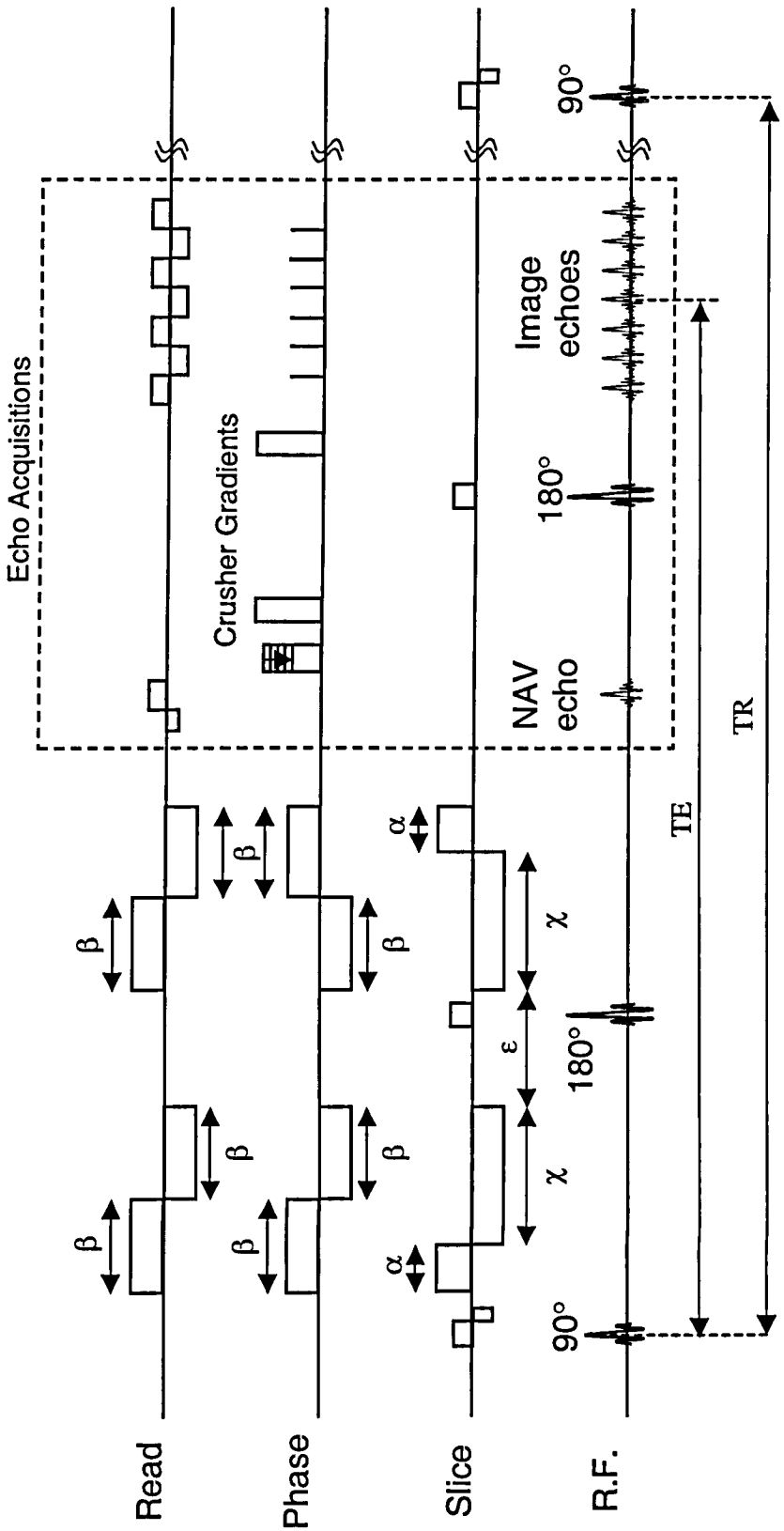

Figure 5.2 Isotropic diffusion weighted interleaved EPI sequence used in the in-vivo imaging study. The bipolar diffusion gradients during the diffusion sensitising period help to minimize unwanted eddy currents from the large diffusion gradients (see text). $\alpha = 10.58$ ms, $\beta = 20.57$ ms, $\chi = 2\beta - \alpha = 30.56$ ms, $\varepsilon = 25.13$ ms. Note that the time axis during the diffusion-encoding period has been scaled differently from that during the echo acquisition period.

(a)

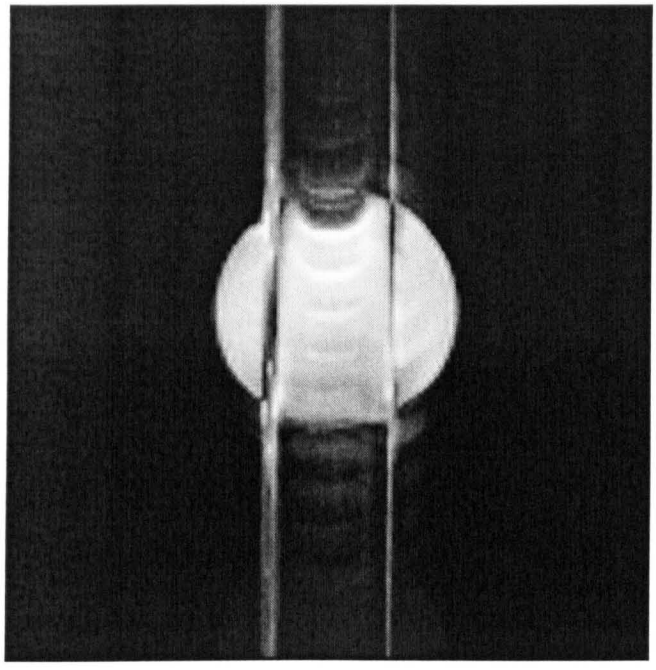

(b)

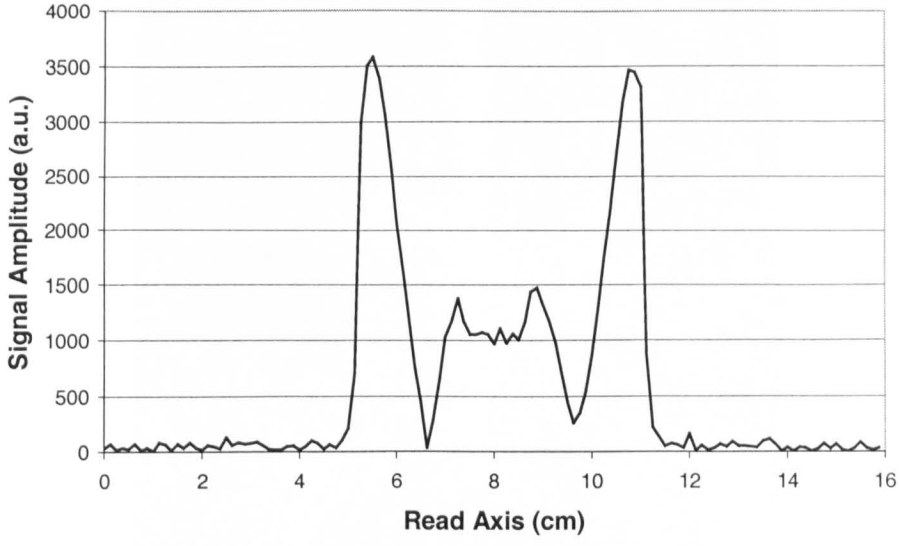

Figure 5.3 (a) Image of a phantom following navigator correction using navigator projection with partial loss of signal. (b) A navigator projection that has lost signal in part of its projection due to eddy current induced phase encoding.

(a)

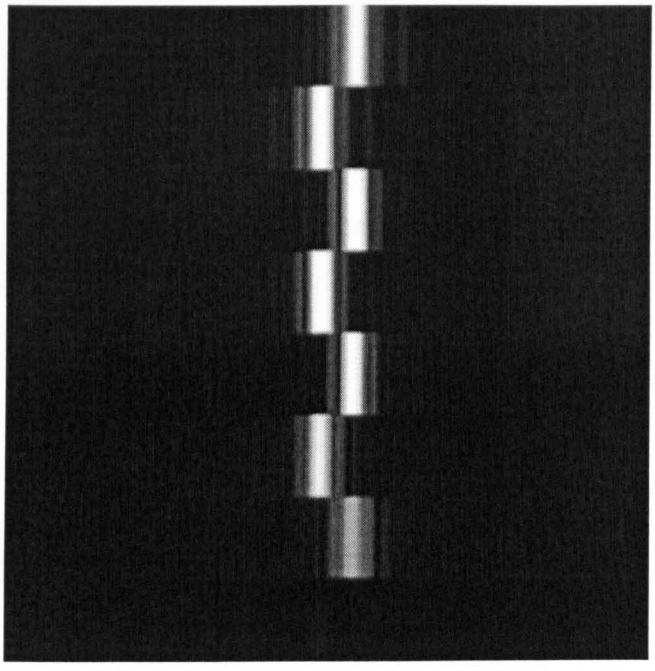

(b)

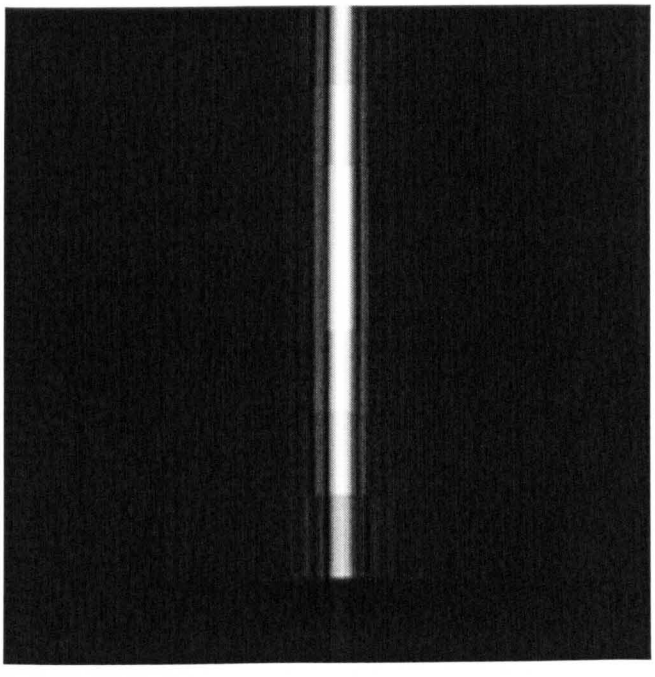

Figure 5.4 Realignment of imaging echoes in the interleaved EPI sequence using calibration scan. (a) An example of the calibration scan showing the misalignment between alternate echoes following the echo reversal process. (b) The calibration scan shown in (a) following realignment with a non-linear phase correction.

(a)

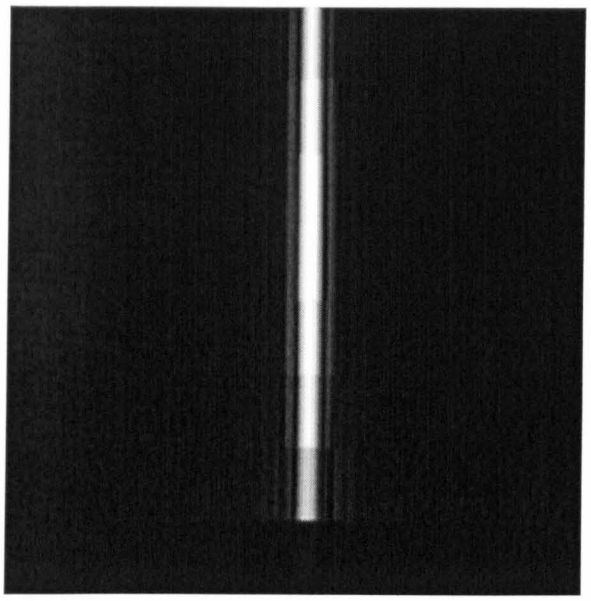

(b)

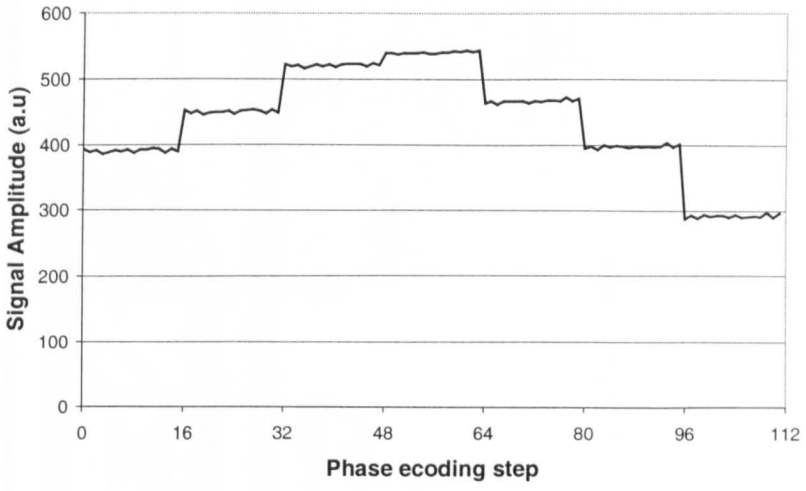

Figure 5.5 Step changes in T_2* decay between echoes at the boundaries between the first and last echo interleave in a scan. (a) Time data of an Interleaved EPI scan with the phase-encoding gradient turned off. (b) Signal amplitude of the time data shown in (a) at the echo peak over all the phase-encoding steps. Note that there are 16 interleaves in each scan and that there are 7 imaging echoes in each interleave. Thus phase-encoding steps 0, 16, 32, 48, 64, 80 and 96 correspond to the first interleave (i.e. interleave 1), whilst phase-encoding steps 15, 31, 47, 63, 79, 95 and 111 correspond to the last interleave (i.e. interleave 16).

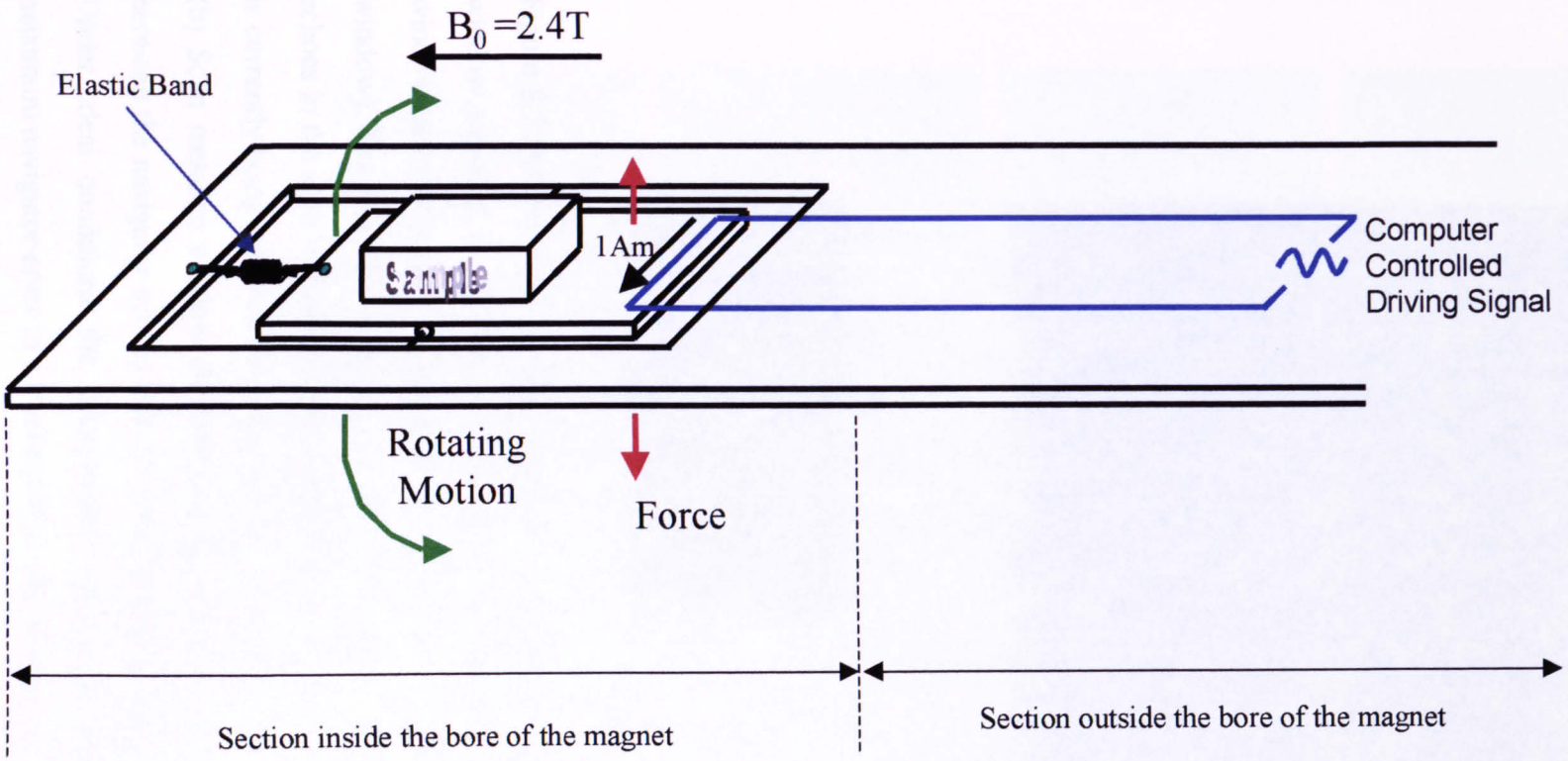

Figure 5.6 Schematic diagram of the computer controlled motion phantom used in the phantom study. The phantom was supported in the bore of the magnet by attaching its outer part to a stand outside the magnet.

(a)

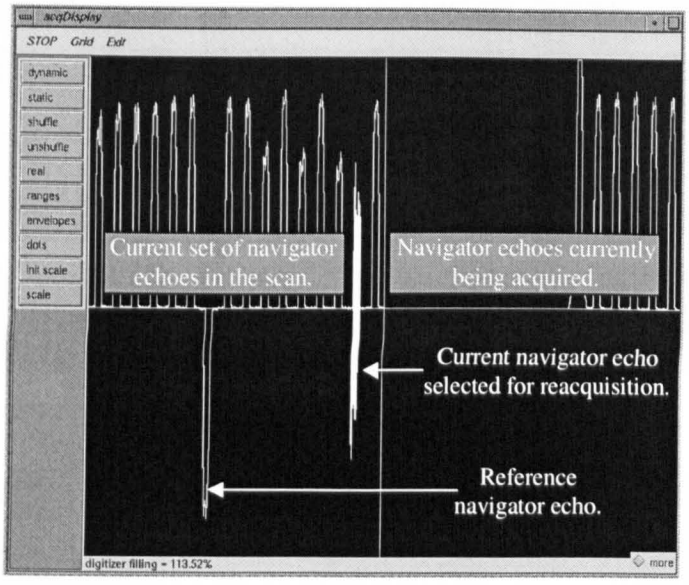

(b)

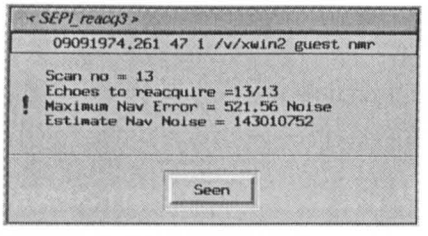

Figure 5.7 Feedback information from the reacquisition algorithm. (a) Scan acquisition window showing the current set of navigator echoes in the scan (left portion of the window) and the current navigator echoes that are being acquired (right portion of the window). The reference navigator has been distinguished from the rest of the navigator echoes in the scan by being shown upside down. To distinguish the navigator echo that is currently being selected for reacquisition, it has been shown as a filled in projection. (b) Scan message window showing amongst other things, the maximum differences between the navigator echoes and the reference navigator echo (Maximum Nav Error). Under ideal conditions the reacquisition process should be able to reduce the maximum navigator error to a level equal to that of the estimated noise.

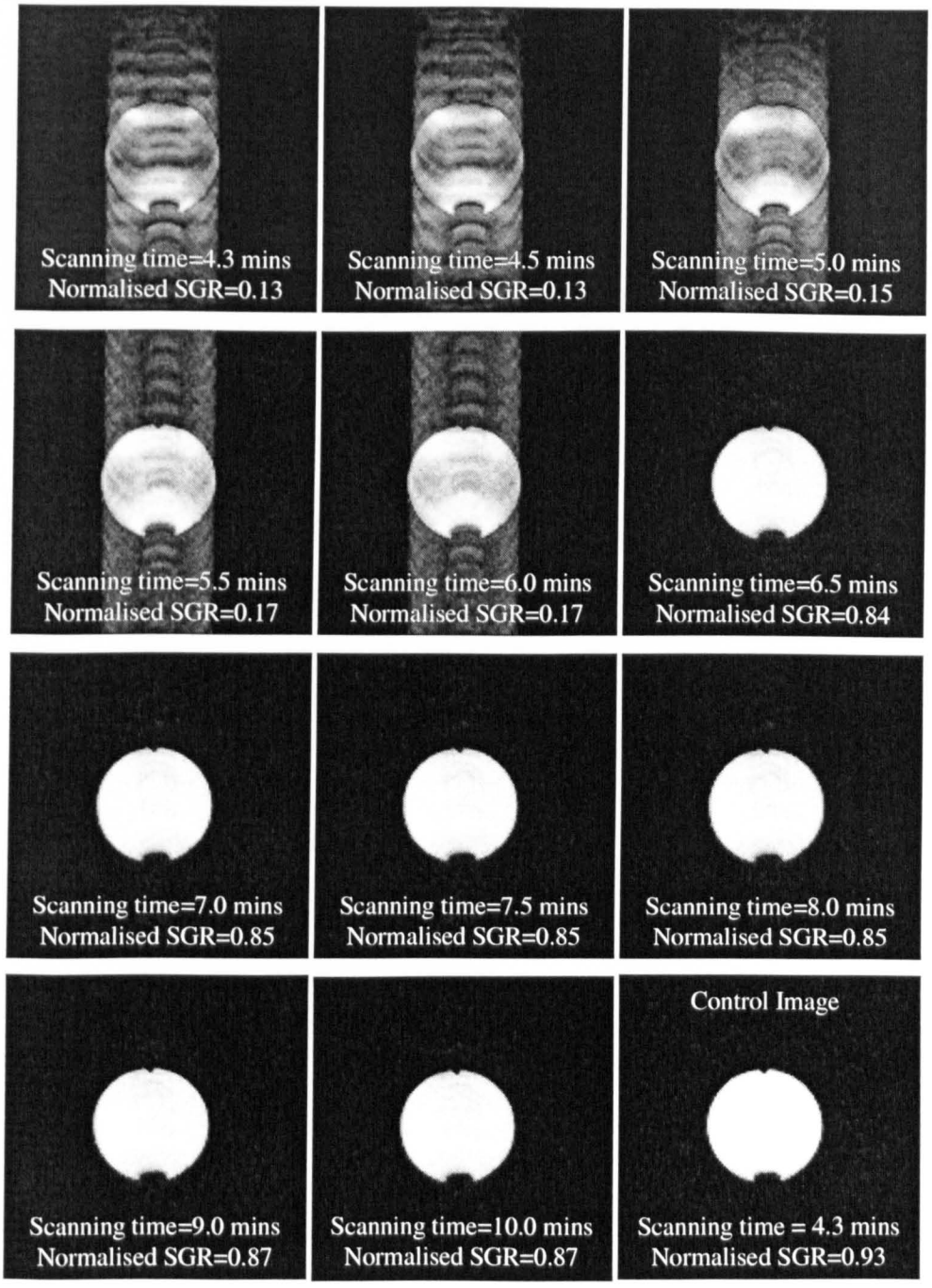

Figure 5.8 Phantom diffusion-weighted imaging with 'simple' echo reacquisition. The modified PGSE diffusion weighted imaging sequence (see figure 5.1) was used for the scan acquisition. The motion error rate was set to 50%. The theoretical scanning time required to remove all motion errors from the scan at an error rate of 50% was 10 minutes. A control image is also shown for comparison. The SNR in the final reacquired scan was 20.0.

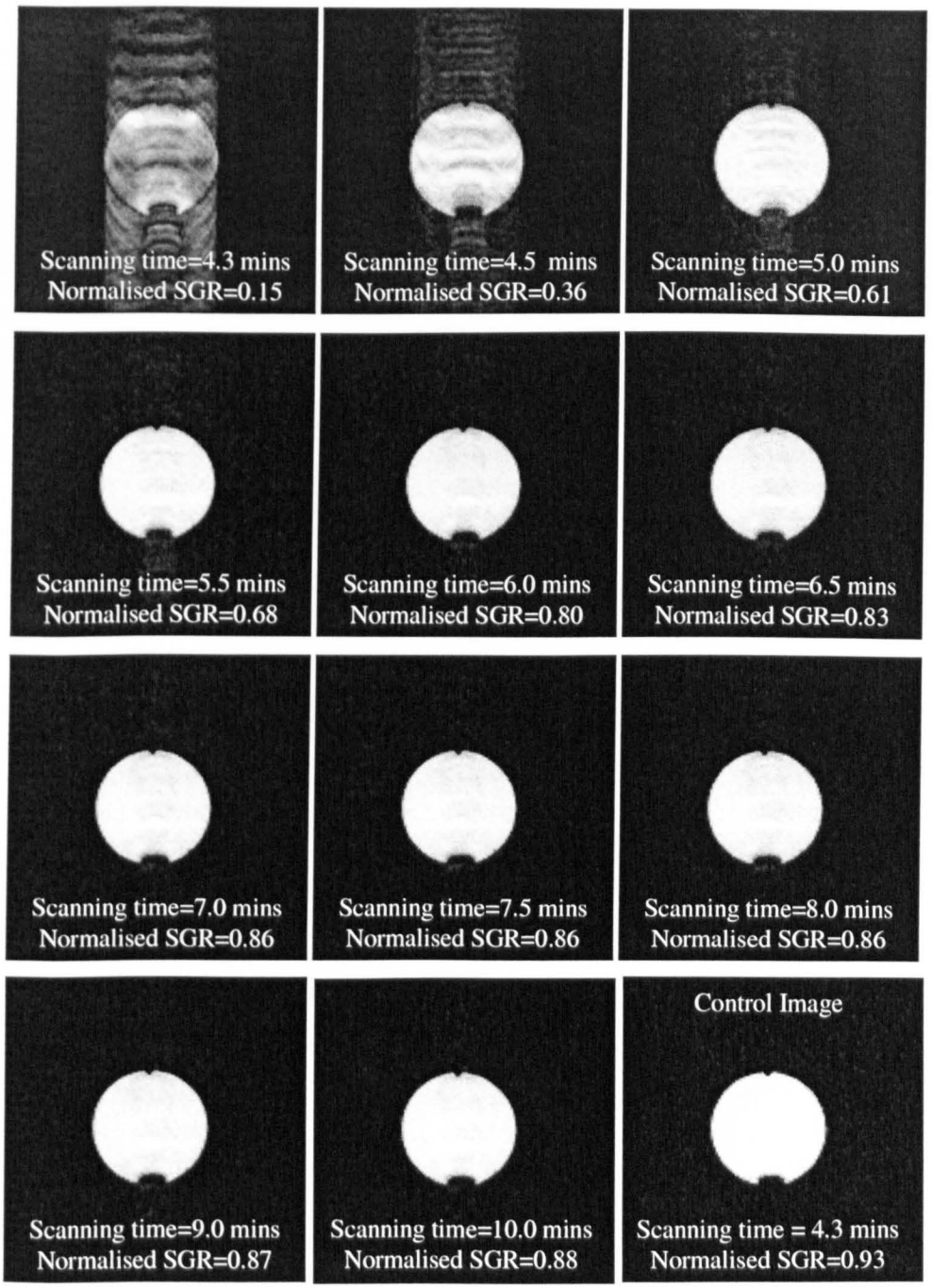

Figure 5.9 Phantom diffusion-weighted imaging with 'centric' echo reacquisition. The modified PGSE diffusion weighted imaging sequence (see figure 5.1) was used for the scan acquisition. The motion error rate was set to 50%. The theoretical scanning time required to remove all motion errors from the scan at an error rate of 50% was 10 minutes. A control image is shown for comparison. The SNR in the final reacquired scan was 19.9.

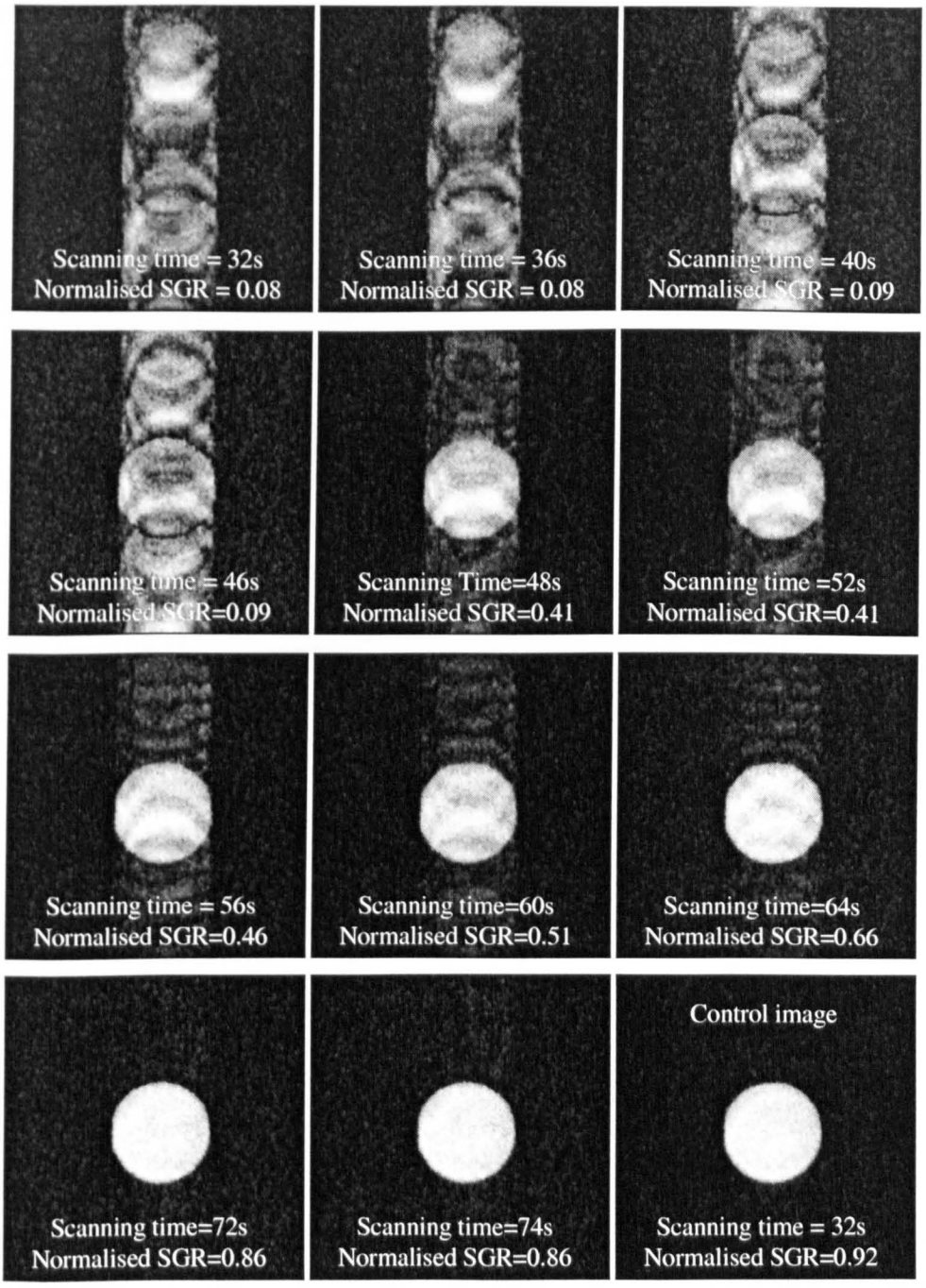

Figure 5.10 Phantom diffusion-weighted interleaved EPI imaging with echo reacquisition. The motion error rate was set to 50%. The diffusion-weighted interleaved EPI imaging sequence shown in figure 5.6 was used for the scan acquisitions. The theoretical total scanning time required to obtain a motion error free scan at an error rate of 50% is 75 seconds. A control image is also shown for comparison. The SNR in the final reacquired scan was 11.14.

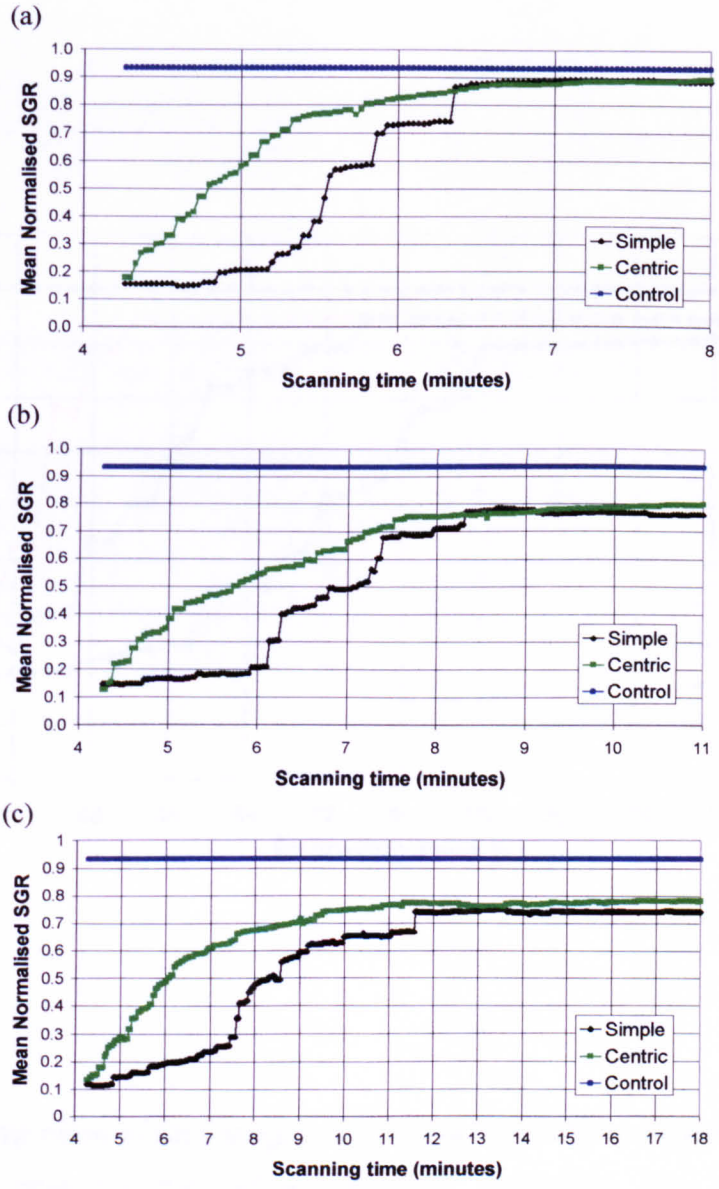

Figure 5.11 Comparison of scan image quality during the reacquisition process using the 'simple' and 'centric' selection methods. The comparison was performed at error rates of (a) 30%, (b) 50% and (c) 70%. Six scans were acquired at each of the error rates. The theoretical scanning times required to remove all irreparable echoes from a scan at an error rate of 30%, 50% and 70% were 7.1, 10.0 and 16.0 minutes respectively. The scan image quality was measured using the mean SGR from the six scans (see text). The SGR was normalised against the SNR of the final image in each scan to account for the variation in SNR that exists between different experiments. The SGR of the control image is also shown for comparison.

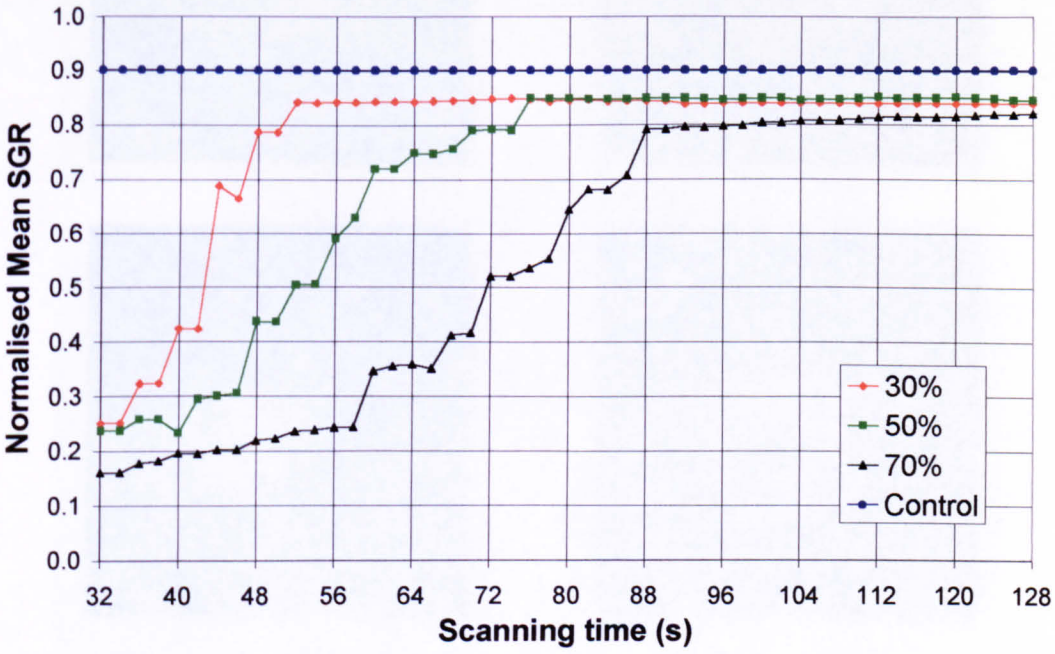

Figure 5.12 Comparison of scan image quality during the echo reacquisition process at different error rates for the diffusion-weighted interleaved EPI sequence. The comparison was performed at error rates of 30%, 50% and 70%. Six scans were acquired at each of the error rates. The theoretical scanning times required to obtain an error free scan at error rates of 30%, 50% and 70% were 53, 75 and 120 seconds respectively. The scan image quality was measured using the mean SGR. The SGR was normalised against the SNR of the final image in each scan to account for the variation in SNR that exists between different experiments. The normalised SGR of the control scans is also shown for comparison.

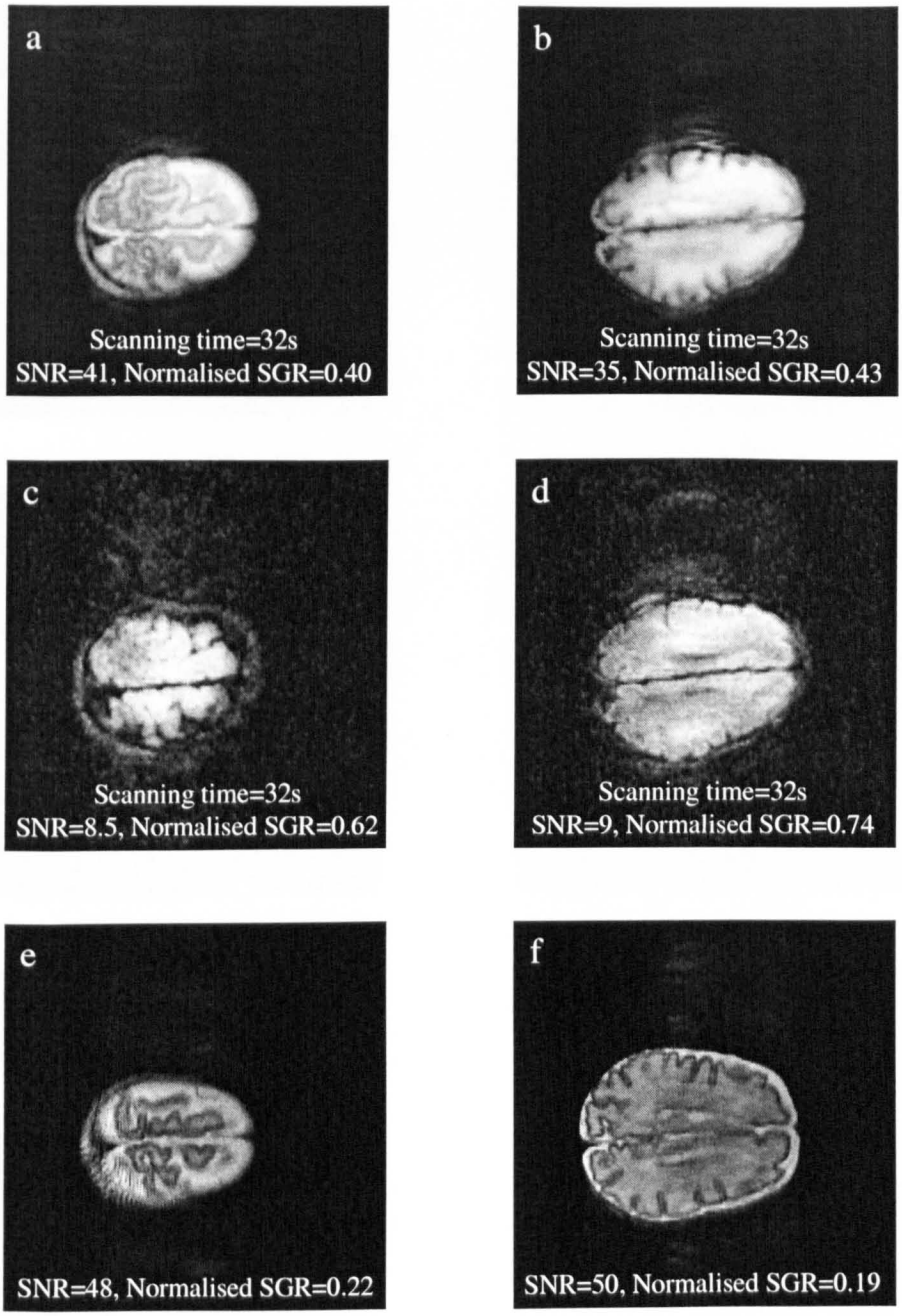

Figure 5.13 Examples of category A diffusion-weighted scans and T_2-weighted scans obtained from the neonatal imaging study: (a) and (b) Typical images from two category A diffusion-weighted scans with a b-value of 20 s/mm2; (c) and (d) typical images from two category A diffusion-weighted scans with a b-value of 900 s/mm2; (e) and (f) typical images from two T_2-weighted scans with an echo time of 200 ms. N.B. category A diffusion-weighted scans are scans where the initial image quality was considered to be sufficient not to require any further reacquisition (see text).

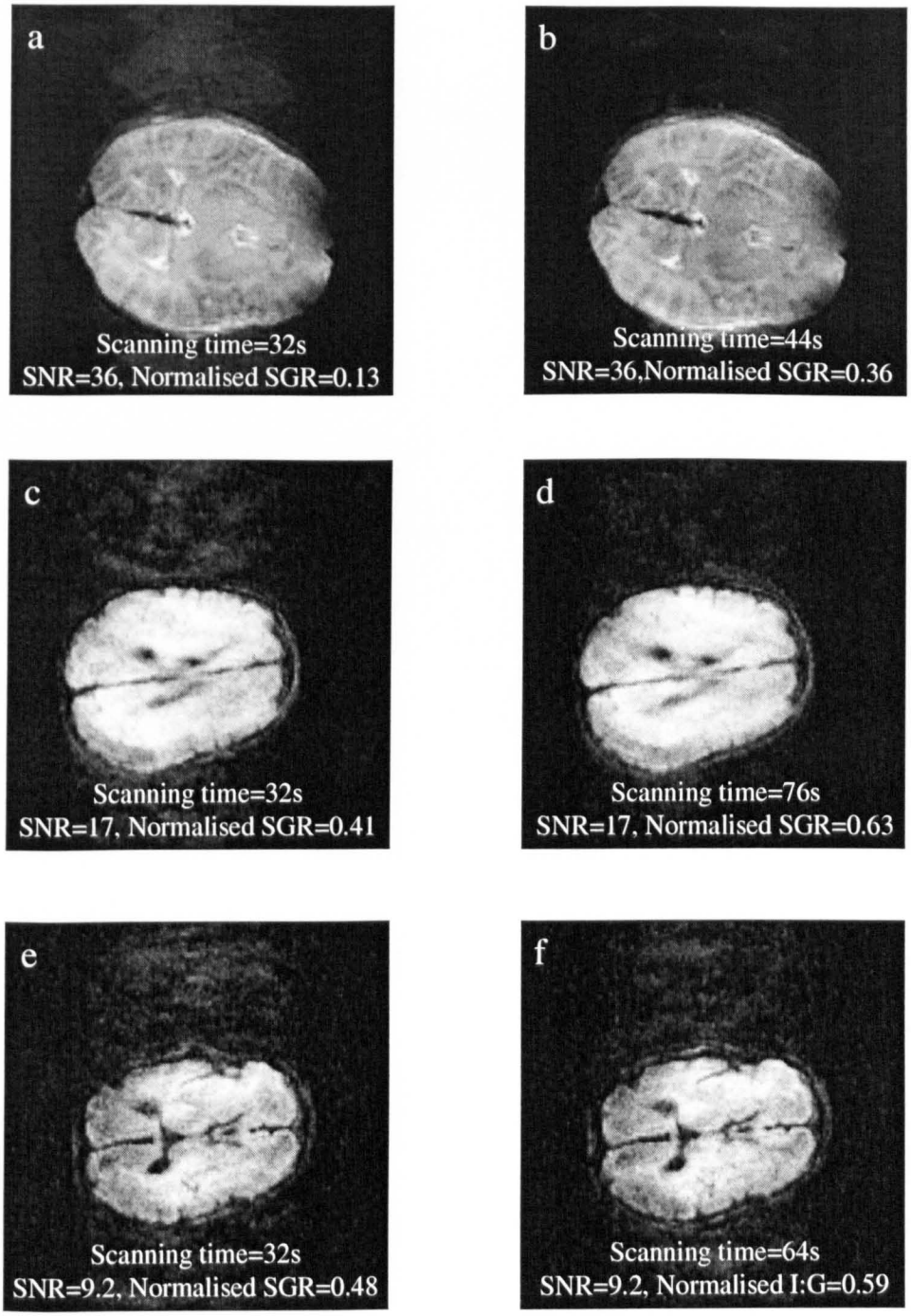

Figure 5.14 Examples of category B diffusion-weighted scans obtained from the neonatal imaging study: (a) and (b) typical images from category B diffusion-weighted scans with b-value of 20 s/mm2 prior to (a) and following (b) the echo reacquisition process; (c) to (f) typical images from category B diffusion-weighted scans with b-value of 900 s/mm2 prior to (c and e) and following (d and f) the echo reacquisition process.

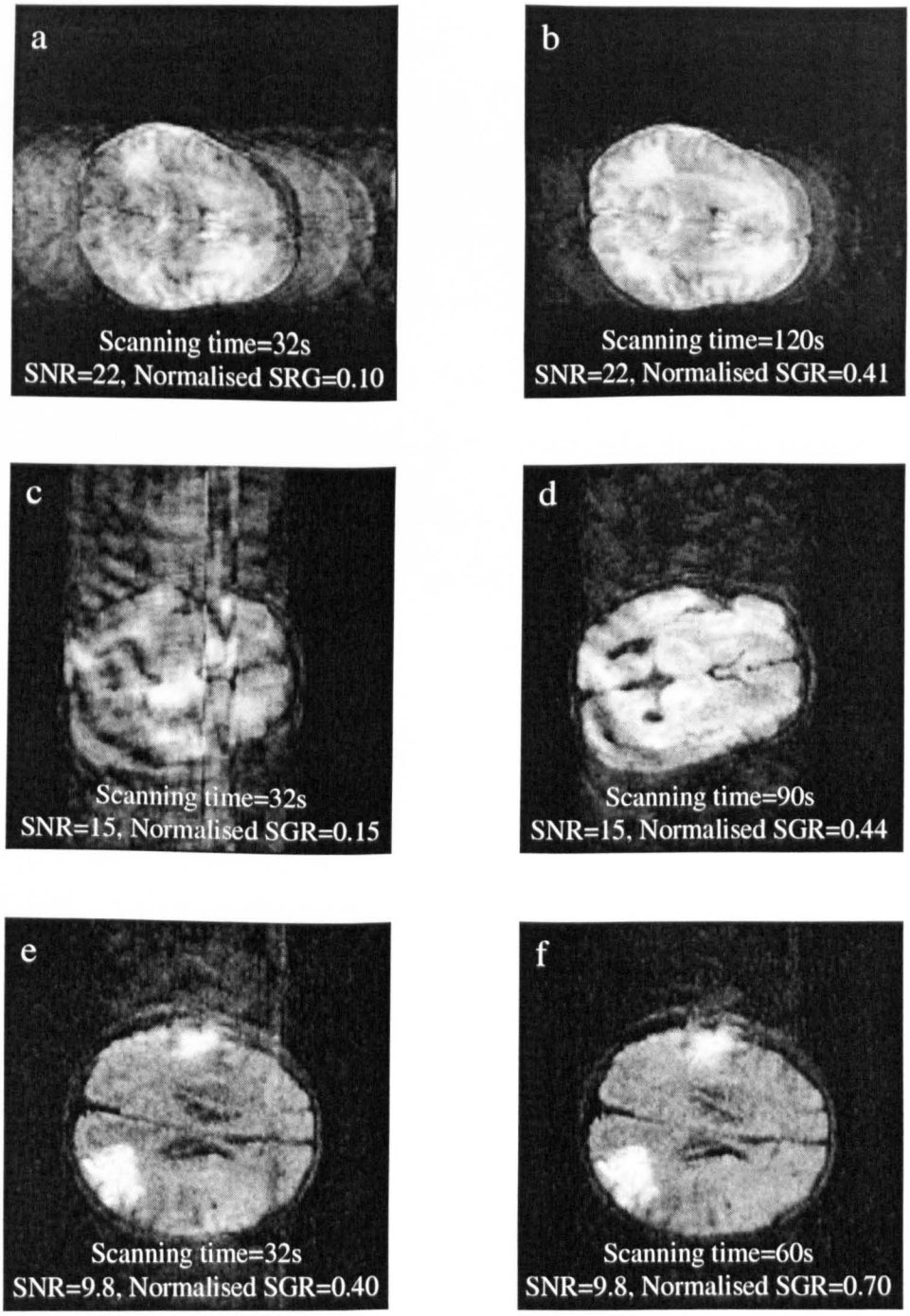

Figure 5.15 Examples of category C diffusion-weighted scans obtained from the neonatal imaging study: (a) and (b) typical images from a category C diffusion-weighted scan with b-value of 20 s/mm2 prior to (a) and following (b) the echo reacquisition process; (c) to (f) typical images from category C diffusion-weighted scans with b-value of 900 s/mm2 prior to (c and e) and following (d and f) the echo reacquisition process.

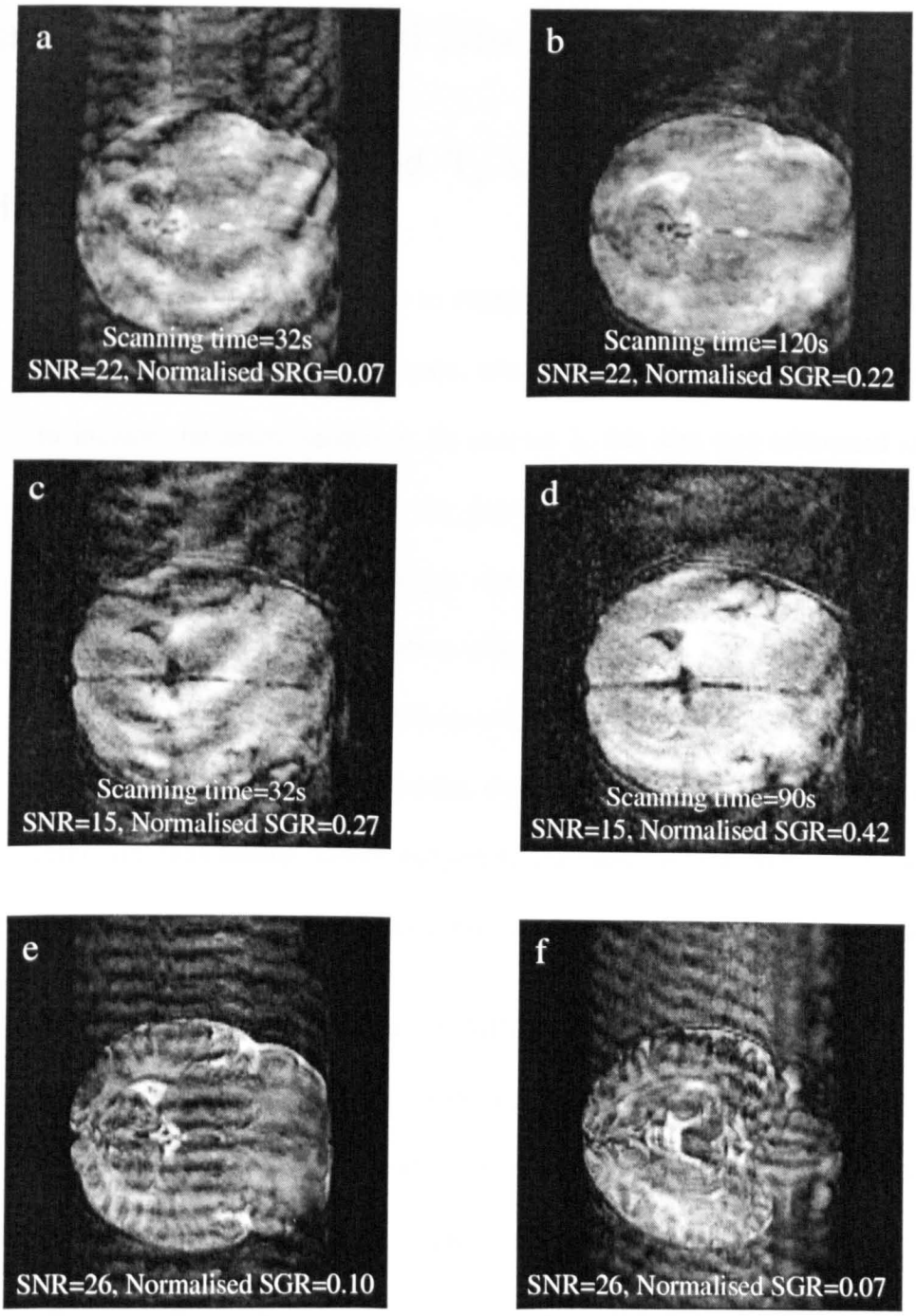

Figure 5.16 Images from the two scans that failed to improve sufficiently for use in ADC quantification. (a) to (d) images from the diffusion-weighted scans prior to (a and b) and following (c and d) the echo reacquisition process. Diffusion b-values of 20 s/mm2 (a and b) and 900 s/mm2 (c and d) were used during the diffusion-weighted scans. (e) and (f) examples of T_2-weighted images obtained during the same scanning session.

Chapter 6 Summary and Discussion

6.1 Quantitative ADC and T_2 study in a piglet model of perinatal asphyxia

The first aim of this thesis was to extend the findings of previous studies in the piglet model of perinatal asphyxia, which were limited to the parietal cortex, to include the entire cerebrum. In chapter 3, this aim was addressed and the results obtained showed that the previous finding in the parietal cortex of delayed derangement in energy metabolism was representative of the cerebrum. The strong correlation observed between the [PCr]/[Pi] and the global averaged Apparent Diffusion Coefficient (ADC_{av}) during secondary energy failure in the parietal studies was also seen in the present study of the cerebrum; thus adding further support to the view that the ADC_{av} may be used as a surrogate marker of cellular energy status during secondary energy failure.

Regional analysis of quantitative MRI data obtained in the present study demonstrated that there was both regional and temporal variation in the cerebral response during secondary energy failure. It was shown that as early as 8 hours post-resuscitation, significant decline in ADC_{av} was observed in both the basal ganglia and parasagittal cortex, regions known clinically to be susceptible to Hypoxic-Ischaemic (HI) injury in perinatal asphyxia[1]. As the global [PCr]/[Pi] did not show a statistically significant decline until 12 hours post-resuscitation, the above result suggests that regional ADC_{av} analysis may be able to provide an even earlier diagnosis of perinatal asphyxia. In the thalamus, internal capsule, periventricular white matter and medial cortex, the

decline in ADC_{av} during secondary energy failure did not reach statistical significance until at least 32 hours post resuscitation. The significance of the delayed decline in ADC_{av} in these regions is unclear at this time but it may indicate that the 'therapeutic window' in these regions is longer than that in the basal ganglia and parasagittal cortex. The degree of ADC_{av} decline approximately two days after the primary HI insult also showed significant variation between anatomical regions. Significantly, regions that showed the earliest decline in ADC_{av} did not necessarily go on to show the greatest decline. Assuming that the degree of ADC_{av} decline reflects the level of cellular compromise, the result suggests that therapeutic intervention may be of greatest benefits to those regions that showed late but severe cellular damage.

In contrast to a previous study of T_2 changes in the parietal cortex during secondary energy failure, very few significant alterations in cerebral T_2 were observed in the present study. The reason for the discrepancy is unclear but it may be related to the used of different echo times between this and the previous study. A significant increased in T_2 was observed in the internal capsule in the present study and this finding is consistent with previous studies in neonates with HI encephalopathy[2]. The significance of the selective T_2 increase in the internal capsule is unclear but it may be related to the myelin component of the internal capsule.

As stated earlier, the aim of the piglet study in this thesis was to extend the findings of previous studies in the parietal cortex and to a large extent this has

been achieved. Discrepancies in T_2 changes exist between this study and a previous study but this may be due to differences in the method of T_2 quantification between the two studies. A wide range of secondary energy failure was obtained in the piglet study and this gave rise to a range of regional and temporal cerebral responses as demonstrated by the ADC_{av} maps. The observed variations in secondary energy failure between the experimental piglets may have reflected their variable susceptibility to HI injury but it is likely that the primary insult was also a contributory factor to the variation seen. Although a consistent insult was attempted on all the experimental piglets, the actual degree of ischaemia achieved during the carotid occlusion is not known. Clinical observations have shown that a short, severe HI insult causes a very different pattern of cerebral injury to that caused by a prolonged but relatively mild insult[3]. Future studies using perfusion imaging to monitor the degree of ischaemia achieved with more frequent ADC and T_2 measurements and better methods of controlling the degree of the primary insult may help shed further light on the susceptibility of different cerebral regions to delayed HI injury and their relationship to the primary insult.

6.2 Reacquisition technique: Development and computer simulations

The strong correlation between cerebral quantitative ADC_{av} MRI and [PCr]/[Pi] during secondary energy failure provided strong motivation for acquiring quantitative ADC_{av} data from neonates with suspected HI brain injury. However, due to the sensitivity of ADC_{av} measurements to subject

motion, this has proved be unfeasible with standard Diffusion-Weighted Imaging (DWI) techniques. Therefore, the second and main aim of this thesis was to develop a novel method of overcoming the problem of motion artefacts in DWI to enable quantitative ADC_{av} data to be obtained from neonates.

In chapter 4, this aim was first addressed by outlining the problem of subject motion in DWI and then proposing a novel technique for overcoming the problem. The novel technique, known as the 'reacquisition' method, involved identifying and reacquiring uncorrectable motion corrupted echoes. Although the need to reacquire echoes leads to an unavoidable increase in scanning time, it was shown theoretically that, provided the motion error rate was not too great, the increase in scanning time was not prohibitive.

To guide the design of the reacquisition method, a computer simulation was set-up to analyse the relationship between the motion errors in a diffusion-weighted image and the resulting ghosting artefacts. It was shown that, for images with a single motion-corrupted echo, the level of ghosting artefacts produced was dependent not only on the size, sign and type of motion error present but also on the intended phase encoding position of the echo affected. In general, it was found that, for a given motion error, the ghosting artefact increased with decreasing level of intended phase encoding in the affected echo. For images with motion errors in multiple echoes, it was demonstrated that the resulting ghosting artefacts were mostly due to a few of the most significant corrupted echoes in the image. The significance of a corrupted echo being defined as the level of ghosting artefact it causes when acting alone.

From this result it was surmised that the design of the reacquisition method should aim to identify and reacquire corrupted echoes in descending order of their significance as this was likely to yield optimal or near optimal reduction in ghosting artefact per unit time.

The design of the reacquisition method was outlined in section 4.3.2. One of the main difficulties with the reacquisition method was the identification of corrupted echoes using 1-D navigator echoes. The approach taken was to identify an ideal uncorrupted reference navigator echo from the scan and then setting a difference threshold from this reference echo beyond which echoes were classified as corrupted. Initial attempts at identifying the reference echo as the largest navigator echo in the scan (on the assumption that uncorrupted echoes were acquired from the centre of k-space) were thwarted by hardware imperfections that caused unintended phase encoding of the navigator echoes. However, by assuming that the motion error rate would not exceed 70%, it was demonstrated using computer simulation that the reference navigator echo could be identified accurately with an algorithm known as the 'clustering method'. By using the navigator echoes to estimate the noise level in the scan to set the difference threshold, it was also shown that corrupted echoes could be identified with high sensitivity and specificity.

Using computer simulation, it was demonstrated that the reacquisition technique was able to eliminate motion artefact from diffusion-weighted scans within the theoretical scanning time. Where the scanning time available was less than the required theoretical scanning time, it was shown that by

reacquiring corrupted echoes in descending order of their significance, near optimal reduction in ghosting artefact per unit time could be achieved. However, because such a reacquisition method was not realisable in real-life, an approximation of the technique, known as the 'centric' reacquisition method, that was realisable in real-life, was developed. Simulation studies showed that although the 'centric' reacquisition method was slightly inferior to the desired reacquisition method, it was superior to a 'simple' reacquisition method that did not consider the significance of the corrupted echoes when deciding the order in which to reacquire them. It was concluded that in the clinical environment, where scanning time is limited, the 'centric' reacquisition method should generally lead to greater motion artefact reduction than the 'simple' reacquisition method.

6.3 Reacquisition technique: Phantom and neonates studies

In chapter 5, the implementation of the reacquisition technique on the Bruker Avance scanner was presented. The implementation process was seriously hampered by the inability of the Avance scanner to alter the phase encoding of a pulse sequence in real-time. However, by using an undocumented feature of the scanner, it was possible to circumvent this limitation to a certain extent and implement a slightly altered version of the proposed reacquisition technique. The reacquisition technique was implemented for both a standard 2DFT spin-echo DWI sequence and an isotropic interleaved EPI sequence. Unfortunately, due to the limitation of the scanner, it was not possible to implement multi-slice imaging or echo time shifting with the reacquisition method. The

effectiveness of the reacquisition technique was assessed firstly with a computer-controlled motion phantom and then with neonates suspected of having suffered HI brain injury. Using the motion phantom, it was demonstrated that high quality diffusion-weighted images could be obtained in the presence of intermittent motion with the aid of the reacquisition method. The increase in scanning time required to achieve high quality diffusion-weighted images was consistent with that predicted theoretically. It was also shown with the standard 2DFT spin-echo DWI sequence that superior ghosting reduction per unit time was achieved with the 'centric' reacquisition method compared to the 'simple' reacquisition method.

Prior to the application of the reacquisition method, a wide range of image quality was obtained from the neonatal imaging experiments. Following the reacquisition process, significant improvement in image quality was achieved in all of the scans. All but two of the scans obtained were considered of sufficient quality to be used for ADC quantification. Of the two scans that did not improve sufficiently, both were obtained during a scanning session when the neonate was so restless that even the T_2-weighted scans were severely corrupted. It was concluded that, in general, the reacquisition method was an effective technique for reducing much of the motion artefacts seen in DWI but it is only effective when the motion errors are sufficiently small to allow standard T_2-weighted scan to be performed. The application of the reacquisition technique during the neonatal study increased the total scanning time to an average of 2 to 3 times that required by a normal scan. With the

interleaved EPI sequence used, this translated to a total scanning time of less than 2 minutes per scan. If multi-slice scanning was possible, whole brain coverage with two b-values could be performed in less than 5 minutes, which should be acceptable for most clinical applications.

The main aim of this thesis was to develop a novel technique to enable quantitative ADC_{av} data to be obtained from neonates. To a large extent this has been achieved and future work will concentrate on acquiring ADC_{av} data from neonates to help establish firstly, the normal ranges of cerebral ADC values in neonates at different ages and secondly, the pattern of cerebral damage in perinatal asphyxia. The inability to perform multi-slice imaging and echo time shifting with the reacquisition method is currently a major obstacle to obtaining a large amount high quality diffusion images from neonates quickly and needs to be overcome. This may need hardware modifications in the Avance scanner but should not pose a major problem on modern scanners where facility for real-time alteration of the phase encoding gradient is available[4].

6.4 Other motion correction techniques

A number of novel motion correction techniques for multi-shot DWI have recently been reported. To compare the different approaches that have been taken and the role of the reacquisition method in the light of these novel techniques, a brief review of the various techniques will be outlined in the following paragraphs.

The most recently published motion correction technique is the 'online motion correction' technique by Norris and Driesel[5]. This technique overcomes the problem of motion artefact in DWI by determining and correcting for motion-induced $\mathbf{dk}_r$ and $\mathbf{dk}_p$ and zero-ordered phase error online immediately following the diffusion-sensitisation period. A pair of orthogonal navigator echoes were used to determine the motion-induced phase errors, whilst short pulses of B_0 and linear gradient magnetic fields were used to correct for the phase errors. By attaching a high-performance, real-time data acquisition processor board (hosted by a personal computer) to the scanner hardware, it was demonstrated that it was possible to acquire the navigator echoes, determine the motion errors and apply the correction pulses in less than 10ms. The effectiveness of the technique was demonstrated on both phantom and human adult volunteers using a RARE DWI sequence. ECG gating was found to be necessary in human studies as approximately 10% of the acquired data were uncorrectable without gating, presumably because of non-rigid pulsatile motion.

An alternative technique of overcoming the problem of motion artefact in DWI is the 'irregular sampling reconstruction' technique. Motion-induced $\mathbf{dk}_p$ errors during a multi-shot DWI scan lead to irregular sampling of k-space along the phase encoding direction. A naïve reconstruction of such data set on a regular sampling grid leads to the familiar ghosting artefacts discussed previously. Rather than avoiding the motion-induced $\mathbf{dk}_p$ errors, the 'irregular sampling reconstruction' technique overcomes such errors by using navigator echoes to determine the irregular sampling grid and then reconstructing the

data set by using either a regridding[6] or matrix inversion[7] technique. Due to the arbitrary nature of the motion errors, the irregular sampling of k-space can often lead to undersampled regions that violate the Nyquist sampling criteria - making the reconstruction process practically impossible. To minimise such eventuality, oversampling of k-space in the phase encoding direction and repeated acquisitions of the data set were found to be necessary. In one human study, it was found that none of the data set satisfied the Nyquist sampling criteria when standard data acquisition was used, whilst only 38% of the data set satisfied the Nyquist sampling criteria when two times oversampling was used[7]. In order to raise the percentage of data sets satisfying the Nyquist sampling criteria to 99%, it was found that two times oversampling and four repeated data acquisitions were required. However, for those data sets that satisfied the Nyquist sampling criteria, high quality images were demonstrated using the 'irregular sampling reconstruction' technique. Some residual artefacts were observed in the ADC maps in the study by Atkinson et al.[7] but these were attributed to the non-rigid pulsatile motion due to ungated data acquisition.

Although yet to be demonstrated with a DWI sequence, the recently reported 'PROPELLER' technique[8] has the potential to obtain high quality motion-tolerant diffusion-weighted images. The 'PROPELLER' technique involves the acquisitions of k-space data in concentric rectangular strips rotated about the k-space origin. Because each data strip contains data from the central region of k-space, navigator data is inherently acquired with each data strip. Using the navigator data and post processing, it was shown that it was possible

to correct for, firstly, multi-voxel in-plane rotation and translational motion between data strips and, secondly, $\mathbf{dk}_r$ and $\mathbf{dk}_p$ errors due to eddy currents and other hardware imperfections. The effectiveness of the technique was demonstrated with an adult human volunteer, who was asked to move his head randomly in all directions for up to a few centimetres, using a turbo-spin echo sequence. Whilst yet to be demonstrated, the ability of the 'PROPELLER' technique to correct for both $\mathbf{dk}_r$ and $\mathbf{dk}_p$ errors due to hardware imperfections suggests that it should also be able to correct for similar errors due to motion in DWI.

Although the three techniques reviewed above have taken very different approaches to motion correction in DWI, they all share a common advantage over the 'standard' navigator correction technique[9] in being able not only to correct for $\mathbf{dk}_r$ and zero-ordered phase errors but also $\mathbf{dk}_p$ errors. As $\mathbf{dk}_p$ error is an important cause of ghosting artefact in diffusion-weighted images, the advantage of being able to correct for it is considerable and, as outlined above, has been demonstrated to yield high quality diffusion-weighted images. However, because the above novel motion-correction techniques are unable to correct for all motion errors (e.g. non-rigid motion and motion causing $\mathbf{dk}_z$ errors), they also share the disadvantage with the 'standard' navigator correction technique of not being able to guarantee consistently high quality images. The 'reacquisition' method described in this thesis has been shown to be able to minimise this disadvantage in the 'standard' navigator correction technique in a time efficient manner and, with suitable modification, should also be effective in combination with the above novel motion-correction

techniques. The use of oversampling and repeated whole-scan acquisition in the 'irregular sampling reconstruction' technique has been shown to be effective in minimising the problem of k-space undersampling. However, it is not a very efficient method of tackling the problem as both adequately sampled and undersampled regions are reacquired. The application of the 'reacquisition' method to selectively reacquire undersampled regions of k-space should lead to considerable improvement in the efficiency of the 'irregular sampling reconstruction' technique.

Multi-shot DWI techniques have a number of advantages over single-shot imaging techniques and are generally preferred in applications where scanning time is not of paramount importance. However, due to the extreme sensitivity of multi-shot DWI to subject motion, clinical uses of multi-shot DWI have been severely limited by motion artefact. To enable multi-shot DWI to be used in the clinical environment, a robust method of overcoming the problem of motion artefact is required. The reacquisition technique described in this thesis offers a novel approach to tackling this problem and has been shown to be effective in combination with the 'standard' navigator correction technique. It is likely that the reacquisition technique will be even more effective when combined with the newer motion-correction techniques. Future work in this direction should eventually lead to multi-shot DWI being a routine imaging technique in the clinical environment.

Reference List

1. Volpe JJ. Neurology of the newborn. Philadelphia: Saunders W.B., 1994; 279-313.

2. Rutherford, M. A., Pennock, J. M., Schweiso, J. E., Cowan, F. M., and Dubowitz, L. M. S. Hypoxic-ischaemic encephalopathy: early and late magnetic resonance imaging findings in relation to outcome. Archives of Disease in Childhood (75), F145-F151. 1996.

3. Wyatt J.S. Hypoxic ischaemic injury of the neonatal brain. **Fetal and Maternal Medicine Review** 1996; 95-108.

4. Weiger M, Bornert P, Proksa R, Schaffter T, Haase A. Motion-adapted gating based on k-Space weighting for reduction of respiratory motion artifacts. **Magnetic Resonance in Medicine** 1997; **38**: 322-333.

5. Norris DG, Driesel W. Online Motion Correction for Diffusion-Weighted Imaging Using Navigator Echoes: Application to RARE Imaging Without Sensitivity Loss. **Magnetic Resonance in Medicine** 2001; **45**: 729-733.

6. Butts K, Pauly J, de Crespigny A, Moseley M. Isotropic Diffusion-Weighted and Spiral-Navigated Interleaved EPI for Routine Imaging of Acute Stroke. **Magnetic Resonance in Medicine** 1997; **38**: 741-749.

7. Atkinson D, Porter D, Hill DLG, Calamante F, Connelly A. Sampling and Reconstruction Effects Due to Motion in Diffusion-Weighted Interleaved Echo Planar Imaging. **Magnetic Resonance in Medicine** 2000; **44**: 101-109.

8. Pipe JG. Motion Correction with PROPELLER MRI: Application to Head Motion and Free-Breathing Cardiac Imaging. **Magnetic Resonance in Medicine** 1999; **42**: 963-969.

9. Anderson AW, Gore JC. Analysis and correction of motion artifacts in diffusion weighted imaging. **Magnetic Resonance in Medicine** 1994; **32**: 379-387.